Charles University in Prague

Faculty of Mathematics and Physics

DOCTORAL THESIS

Martin Pauer

Forward and Inverse Modeling of Planetary Gravity and Topography

Department of Geophysics

Supervisor: Doc. RNDr. Ondřej Čadek, CSc.
Consultant: Prof. Dr. Doris Breuer

Study programme: physics
Specialization: geophysics

Prague 2013

Acknowledgements

Here, I would like to thank first of all both my supervisors: Ondřej Čadek of the Department of Geophysics, Charles University in Prague, and Doris Breuer of the Department of Planetary Physics, Institute of Planetary Research DLR in Berlin. They both helped me to understand better many aspects of planetary physics, and the results presented in this thesis wouldn't be achieved without their support and help. I would like also to thank all the other people from both departments where I stayed; in Prague namely Marie Běhounková, Zdeněk Martinec, Ondřej Šrámek and Jakub Velímský and in Berlin then Matthias Grott, Christian Hüttig, Petr Kabáth, Frank Sohl and Tilman Spohn. Many thanks belong also to Kevin Fleming, for his constructive comments on this thesis and on my English.

This work was supported by the Charles University grant No. 280/2006/B-GEO/MFF and the European Community's Improving Human Potential Programme contract RTN2-2001-00414, MAGE. All figures (unless stated otherwise in the caption) were created using the Generic Mapping Tools of Wessel and Smith [1991]. The biographical data for the footnotes were obtained from Wikipedia, the free encyclopedia (*http://www.wikipedia.org*).

Finally, I want to thank my whole family, namely my parents for their constant support and Martina who managed with all my ups and downs and provided me with a place where I could relax, and with a confidence in my efforts that I did not have myself all the time. Moreover, during my studies our family changed radically as I am experiencing every morning when our dear daughters Klaudie and Thea wake up, and wants me to do so as well. Therefore, I want to also thank them for keeping me rejoicing in the world around us and for their irresistible "tatí" words.

Printed by LaTeX

I declare that I carried out this doctoral thesis independently, and only with the cited sources, literature and other professional sources.

I understand that my work relates to the rights and obligations under the Act No. 121/2000 Coll., the Copyright Act, as amended, in particular the fact that the Charles University in Prague has the right to conclude a license agreement on the use of this work as a school work pursuant to Section 60 paragraph 1 of the Copyright Act.

In Prague on 24th June 2013. .....

Název práce: Přímé a inverzní modelování topografie a gravitačního pole planet
Autor: Martin Pauer
Katedra/Ústav: Katedra geofyziky MFF UK
Vedoucí doktorské práce: Doc. RNDr. Ondřej Čadek, CSc., Katedra geofyziky MFF UK
Abstrakt: Cílem této práce bylo prozkoumat různé mechanismy kompenzace pozorované planetární topografie – izostázi v kůře, elastickou podporu v litosféře a dynamickou podporu působenou tečením v plášti. Tyto zkoumané modely byly následně použity na tři různé planetární problémy. Nejprve jsme aplikovali model dynamické podpory k vysvětlení velkoškálových gravitačních a topografických útvarů na Venuši a zjistili možná rozložení viskozity v jejím plášti. Výsledky modelování ukazují, že k vysvětlení pozorovaných dat lze použít nejen isoviskózní model pláště, ale i model s tuhou litosférou a pozvolným nárůstem viskozity směrem k jádru. V druhém článku jsme se pomocí kombinace různých modelů kompenzace kůry pokusili odhadnout hustotu kůry v oblasti marťanských jižních vysočin. Díky tomu, že různé metody modelování mají na vstupní hustotě odlišnou závislost, podařilo se nám získat maximální odhad hustoty kůry ve studované oblasti. Ve třetí práci jsme studovali intenzitu gravitačního signálu možných topografických útvarů na dně Jupiterova měsíce Europy. Ukazuje se, že pokud budou mít dlouhovlnné topografické útvary výšku aspoň ve stovkách metrů, je dost pravděpodobné, že budeme se současnou technikou schopni jejich gravitační signál zachytit.
Klíčová slova: gravitační pole, topografie, planety, vnitřní stavba

Title: Forward and Inverse Modeling of Planetary Gravity and Topography
Author: Martin Pauer
Department/Institute: Department of Geophysics MFF UK
Supervisor of the doctoral thesis: Doc. RNDr. Ondřej Čadek, CSc., Department of Geophysics MFF UK
Abstract: The aim of this work was to investigate various mechanisms compensating the observed planetary topography – crustal isostasy, elastic support and dynamic support caused by mantle flow. The investigated models were applied to three different planetary problems. Firstly we applied dynamic compensation model to explain today large-scale gravity and topography fields of Venus and investigate its mantle viscosity structure. The results seem to support not only models with constant viscosity structure but also a model with a stiff lithosphere and a gradual increase of viscosity toward a core. In the second paper several crust compensation models were employed to estimate the density of the Martian southern highlands crust. Since the used methods depends differently on crustal density changes, we were able to provide some constraints on the maximum density of the studied region. In the third application, the strength of a possible ocean floor gravity signal of Jupiter's moon Europa was studied. It turned out that if the long wavelength topography reaches height at least a few hundred meters, we will be probably able to detect it with current measurement accuracy.
Keywords: gravity field, topography, planets, internal structure

Contents

A whole is that which has beginning, middle and end.

Aristotle (384 BC–322 BC)

... to Thea, Klaudie, Martina, Jana and Marie.

Chapter 1

Introduction

The 20th century saw a rapid development in all branches of physics, including geophysics. Moreover, upon humanity's venturing into space in the late 1950's, a new field of nature became accessible – the planets and moons of the Solar System. Until that time, the study of these objects was confined largely to the domain of astronomy, but after the first planetary space missions with their continuously developing instrumentation for remote sensing, this topic evolved to the new interdisciplinary field of Planetary Science.

Today, more than 50 years after Sputnik 1, vast amounts of data from various missions have been send back to the Earth. However, with the exception of the ALSEP (Apollo Lunar Surface Experiments Package) [e.g., Wieczorek et al., 2006] the interior of the planets has been studied only by indirect methods: e.g., lunar laser ranging or determination of the tidal response by satellite flybies. One of the methods that allow the investigation of the inner structure is a join analysis of the gravity and topography fields; a method well established for the study of various geophysical problems [e.g., Hager and Clayton, 1989; Peltier, 1989; Mitrovica and Peltier, 1992; Forte et al., 1994; Čadek and Fleitout, 2003]. Due to its nature, it cannot be used to investigate a planet's radial density structure, but instead it provides information about, for instance, the lateral variations in crustal thickness [e.g., Wieczorek and Phillips, 1998; Neumann et al., 2004; Chenet et al., 2006; Wieczorek, 2007] or the rheological structure of the mantle [e.g., Kiefer et al., 1986; Moore and Schubert, 1997; Vezolainen et al., 2004].

As planetary science is a relatively new field of research, the employed models are often very simple. This can, however, result in a substantial error in the derived parameter values (e.g., in the crustal or elastic thickness) [e.g., Wieczorek and Zuber, 2004; Belleguic et al., 2005]. Therefore, there exists a need for more advanced models to better constrain the parameters of interest. Of great importance in particular is the development of models that incorporate more than one of the processes usually studied separately [e.g., Zhong, 2002; Choblet et al., 2007].

This thesis is organized as follows: Chapter 2 describes our current knowledge of planetary gravitational and topographic fields and sets the theoretical basis for the study of gravity associated with processes connected to the compensation of surface structures. In Chapter 3 the models and equations required for studying those processes in detail are derived, with a focus on the behavior of the elastic lithosphere. This model is then applied to the problem of predicting dynamic gravity and topography. In Chapter 4 methods and

concepts such as the geoid-topography ratio, admittance analysis and Bouguer inversion are described, as these are the most commonly used tools in planetary science for the inverse modeling of the gravity field. In addition, the basics of parameterized convection modeling connecting thermal evolution of a planet with the compensation parameters evolution are given.

Most of the tools described in detail in the above mentioned three chapters were used for preparation of three original manuscripts which are attached in Appendix C. First of them is Pauer et al. [2006] which uses gravity and topography fields of Venus to make an estimate of its mantle viscosity structure. It investigates a possibility that a current Venusian mantle can contain a high-viscosity lithosphere and a gradual increase of viscosity through the mantle. The second [Pauer and Breuer, 2008] focuses on a study of Martian crust and places constraints on a maximum density for the southern hemisphere. It further discusses possible implications for the global structure and the planet's evolution. The third manuscript [Pauer et al., 2010] is devoted to forward and inverse modeling of a possible gravity field originating from ocean floor structures of Jupiter's moon Europa. The aim of this paper is to study whether, and under what conditions, a signal from Europa's ocean floor can be detected in future mission.

The last part, Chapter 5, discusses the results presented in this work with an outlook presented for future studies.

Chapter 2

Planetary Gravity and Topography

Many aspects of the thermal and chemical evolution of a planet's interior are connected with the reshaping of planetary surfaces and changes in the internal mass distribution. Therefore, a viable way to study the planets of our Solar System (especially in the case when direct measurements from seismometers are not available, or are not providing the desired coverage and resolution of data) is an inversion of the measured gravity field and the observed surface topography (for a review, see Wieczorek [2007]). This chapter therefore lays down the necessary theoretical basis connecting both observed quantities with regards to the assumed physical processes that have generated them.

2.1 Gravity field

The term *gravity* specifically describes the force attracting one mass object to another mass objects as fully described by Newton's theory[1] (whereas *gravitation* refers to a general tendency of this attractive influence, in other theories it could be explained by different causes other than gravity, e.g. in Einstein's general theory of relativity[2] it is the time-space deformation). In the Earth and planetary sciences, the term gravity (and also gravitation) is, however, often used rather to describe the attraction experienced on the surface of a rotating planet i.e. including the additional factor of the centrifugal force. Since this work aims to deal with the processes occurring at such rotating planets, this factor must also be taken into account. On the other hand, gravity attraction can be divided into the hydrostatic part (which reflects the gravity attraction of a rotating spherically symmetric body in hydrostatic equilibrium) and non-hydrostatic part (which reflects the deviations caused by internal density perturbations). As this work is focused on the signal connected to a nonuniform distribution of topography on the surface and the density perturbations below the surface, only this later part of the gravity field will be examined here.

[1]Named after Sir Isaac Newton (4th January 1643–31st March 1727), English mathematician, physicist, astronomer, alchemist and Master of the Mint, who quantitatively described the gravity attraction in his famous *Philosophiæ Naturalis Principia Mathematica* (1687).

[2]Named after Albert Einstein (14th March 1879–18th April 1955), German born theoretical physicist, who developed the special (1905) and general (1915) theories of relativity.

First, it is necessary to obtain a description of the non-hydrostatic gravity field which will later allow for its modeling and study. As the gravity field is conservative and therefore could be expressed as a gradient of the scalar potential $U(\boldsymbol{r})$ [e.g., Turcotte and Schubert, 2002], where $\boldsymbol{r}$ is a position vector, we start with writing Newton's gravity law for the gravitational acceleration $\boldsymbol{g}(\boldsymbol{r}) = -g(r)\,\boldsymbol{e}_{\mathrm{r}}$ induced by an object of mass M:

$$\boldsymbol{g}(\boldsymbol{r}) = -\frac{GM}{r^2}\boldsymbol{e}_{\mathrm{r}}, \tag{2.1}$$

$$\boldsymbol{g}(\boldsymbol{r}) = \nabla U(\boldsymbol{r}), \tag{2.2}$$

$$U(\boldsymbol{r}) = \frac{GM}{r}, \tag{2.3}$$

where $G = 6.6742 \times 10^{-11}\ \mathrm{m^3\ kg^{-1}\ s^{-2}}$ [Mohr and Taylor, 2005] is the gravitational constant. However, equations (2.1)–(2.3) are only valid for a spherically symmetric body. If the shape of the body is not spherical, or if its density varies laterally, more general relationships must be considered, namely Poisson's equation[3]

$$\nabla^2 U(\boldsymbol{r}) = -4\pi G\rho(\boldsymbol{r}), \tag{2.4}$$

for a region of density ρ, and Laplace's equation[4]

$$\nabla^2 U(\boldsymbol{r}) = 0. \tag{2.5}$$

for regions of $\rho = 0$. [Burša and Pěč, 1993] This invariant form could be written in spherical coordinates (for $\boldsymbol{r} = \boldsymbol{r}(r, \vartheta, \varphi)$) in the following way:

$$\frac{1}{r^2}\frac{\partial}{\partial r}\left(r^2\frac{\partial U}{\partial r}\right) + \frac{1}{r^2\sin\vartheta}\frac{\partial}{\partial\vartheta}\left(\sin\vartheta\frac{\partial U}{\partial\vartheta}\right) + \frac{1}{r^2\sin^2\vartheta}\left(\frac{\partial^2 U}{\partial\varphi^2}\right) = 0, \tag{2.6}$$

whose solution for the unit sphere could be found [e.g., Varshalovich et al., 1988] taking advantage of the method of separation of variables ($U(\boldsymbol{r}) = R(r)S(\vartheta)T(\varphi)$) in two forms:

$$U(\boldsymbol{r}) = \sum_{\ell=0}^{\infty}\sum_{m=0}^{\ell} r^{\ell}[C_{\ell m}\cos m\varphi + S_{\ell m}\sin m\varphi]P_{\ell m}(\cos\vartheta), \qquad \text{for } r < 1, \tag{2.7}$$

$$U(\boldsymbol{r}) = \sum_{\ell=0}^{\infty}\sum_{m=0}^{\ell} \frac{1}{r^{\ell+1}}[C_{\ell m}\cos m\varphi + S_{\ell m}\sin m\varphi]P_{\ell m}(\cos\vartheta), \qquad r \geq 1, \tag{2.8}$$

where $P_{\ell m}(\cos\vartheta)$ stands for the associated Legendre function[5] of first kind (for the definition see the equation (A.5)), ℓ is the harmonic degree, m the harmonic order and $C_{\ell m}$ and $S_{\ell m}$ are

[3]Named after Siméon Denis Poisson (21st June 1781–25th April 1840), Franch mathematician, geometer and physicist, who contributed to electricity, magnetism, celestial mechanics and potential theory.

[4]Named after Pierre-Simon Laplace (23rd March 1749–5th March 1827), French mathematician and astronomer, who first derived spherical harmonic expansion or the theory of potential.

[5]Named after Adrien-Marie Legendre (18th September 1752–10th January 1833), French matematician, who contributed to many field of mathematics (e.g., statistics, algebra and mathematical analysis.

the unknown coefficients. Furthermore, equations (2.7) and (2.8) could be rewritten using a complex notation and the Kronecker delta[6] ($\delta_{km} = 1$ if $k = m$ and 0 otherwise):

$$\hat{U}_{\ell m} = \frac{C_{\ell|m|} - iS_{\ell|m|}}{2 - \delta_{0m}} \qquad |m| \leq \ell, \tag{2.9}$$

$$\hat{Y}_{\ell m}(\vartheta, \varphi) = (\cos|m|\varphi + i \sin|m|\varphi) P_{\ell|m|}(\cos\vartheta) = P_{\ell|m|}(\cos\vartheta) \exp(i|m|\varphi), \tag{2.10}$$

$$U(\boldsymbol{r}) = \Re \sum_{\ell=0}^{\infty} \sum_{m=-\ell}^{\ell} r^{\ell} \hat{U}_{\ell m} \hat{Y}_{\ell m}(\vartheta, \varphi) \qquad \text{for } r < 1, \tag{2.11}$$

$$U(\boldsymbol{r}) = \Re \sum_{\ell=0}^{\infty} \sum_{m=-\ell}^{\ell} \frac{1}{r^{\ell+1}} \hat{U}_{\ell m} \hat{Y}_{\ell m}(\vartheta, \varphi) \qquad r \geq 1, \tag{2.12}$$

which is (omitting the factors r^{ℓ} and $1/r^{\ell+1}$, different normalization of the spherical harmonic functions $Y_{\ell m}$ and the fact that we use only the real part $\Re$) the same expansion as for the scalar spherical harmonics (see formula (A.1) and Appendix A). Equal formulation could be obtained [e.g., Wieczorek, 2007] using an alternative notation:

$$\hat{\hat{U}}_{\ell m} = C_{\ell m} \qquad \hat{\hat{Y}}_{\ell m}(\vartheta, \varphi) = \cos m\varphi \, P_{\ell m}(\vartheta, \varphi) \qquad \text{for } m \geq 0, \tag{2.13}$$

$$\hat{\hat{U}}_{\ell m} = S_{\ell m} \qquad \hat{\hat{Y}}_{\ell m}(\vartheta, \varphi) = \sin m\varphi \, P_{\ell|m|}(\vartheta, \varphi) \qquad m < 0, \tag{2.14}$$

$$U(\boldsymbol{r}) = \sum_{\ell=0}^{\infty} \sum_{m=-\ell}^{\ell} r^{\ell} \hat{\hat{U}}_{\ell m} \hat{\hat{Y}}_{\ell m}(\vartheta, \varphi) \qquad \text{for } r < 1, \tag{2.15}$$

$$U(\boldsymbol{r}) = \sum_{\ell=0}^{\infty} \sum_{m=-\ell}^{\ell} \frac{1}{r^{\ell+1}} \hat{\hat{U}}_{\ell m} \hat{\hat{Y}}_{\ell m}(\vartheta, \varphi) \qquad r \geq 1. \tag{2.16}$$

Throughout this thesis spherical harmonic expansions based on equation (A.1) will be used, but taking into account only the real part which corresponds to the equations stated above. For an overview of the coefficients normalization problematics, see appendix Section A.3.

Using this complex notation, for a given location $\boldsymbol{r} = \boldsymbol{r}(r, \vartheta, \varphi)$ referenced to the same origin as a sphere of radius R_0, the gravitational potential $U(\boldsymbol{r})$ defined by a finite set ($\ell \leq \ell_{\max}$) of coefficients $U_{\ell m}(R_0)$ – i.e. coefficients defining the potential field on the surface of a sphere – could be evaluated as:

$$U(\boldsymbol{r}) = \sum_{\ell=2}^{\ell_{\max}} \sum_{m=-\ell}^{\ell} \left(\frac{r}{R_0}\right)^{\ell} U_{\ell m} Y_{\ell m}(\vartheta, \varphi) \qquad \text{for } r < R_0, \tag{2.17}$$

$$U(\boldsymbol{r}) = \sum_{\ell=2}^{\ell_{\max}} \sum_{m=-\ell}^{\ell} \left(\frac{R_0}{r}\right)^{\ell+1} U_{\ell m} Y_{\ell m}(\vartheta, \varphi) \qquad r \geq R_0. \tag{2.18}$$

Note that in both the equations (2.17) and (2.18) the summation starts with degree $\ell = 2$. This is because in the coordinate system originating in the center-of-mass (CoM) the gravity

[6]Named after Leopold Kronecker (7th December 1823–29th December 1891), German mathematician and logician, who believed that mathematical analysis must be founded on "whole numbers".

coefficients $U_{1m} \equiv 0$ (i.e. there is no displacement of the gravity field from CoM), while the coefficient U_{00} describes only the mean value of gravitational potential.

As mentioned in the beginning of this chapter, the measured gravitational attraction on the surface of any planet includes also the influence of rotation. Since this force is responsible for the flattening of the planetary figure, the whole geopotential must be taken into account when dealing with the global planetary topography and gravity [e.g., Wieczorek, 2007]. If, moreover, one is interested in the study of a planet with a massive moon (or vice versa) an additional term describing the permanent tidal deformation of geopotential has to be included [e.g., Dermott, 1979; Zharkov et al., 1985]. Contrary to this is if the gravity field of a slowly rotating body without a massive natural satellite is being considered or if we are not interested in the degree 2 terms then the basic features of the gravitational field can be lumped into the so-called normal potential (for exact definition see e.g., Novotný [1998]) and we can work then with a residual, or disturbing potential which is obtained by subtracting the normal potential from the observed gravitational signal. This disturbing gravitational potential can then be converted into height anomalies of the equipotential surface undulations relative to the surface mean radius/local ellipsoidal radius – i.e. into the geoid anomalies (while this is a usual name for the equipotential surface of the Earth, this term will be also used for equipotential surfaces of other planets). The relationship between gravitational disturbing potential U and geoid height anomalies h is given to a first approximation by the Bruns formula[7] [e.g., Novotný, 1998; Wieczorek, 2007]:

$$h(\vartheta, \varphi) \approx \frac{U(\vartheta, \varphi)}{g_0}, \tag{2.19}$$

where $g_0 = GM/R_0^2$ is the mean planetary gravitational acceleration. The dimension of the geoid height anomalies is $[h] = \mathrm{m}$.

Instead of the geoid we often use the gravity variations (variations of the gravitational acceleration), which are only another expression of the same physical field. The gravity anomaly $g_\mathrm{r}(r, \vartheta, \varphi)$ could be obtained by evaluating the first radial derivative of the potential U (similarly to the equation (2.2)) starting with the equation (2.18) and employing the convention that the positive gravity anomaly directs downwards:

$$g_\mathrm{r}(r, \vartheta, \varphi) = \sum_{\ell=2}^{\ell_\mathrm{max}} \sum_{m=-\ell}^{\ell} \frac{\ell+1}{R_0} \left(\frac{R_0}{r}\right)^{\ell+2} U_{\ell m} Y_{\ell m}(\vartheta, \varphi) \qquad r \geq R_0. \tag{2.20}$$

The dimension of the gravity anomaly is $[g_\mathrm{r}] = \mathrm{ms}^{-2}$ but the more commonly used unit is *galileo*[8] (1 Gal = 1 cm s^{-2} in CGS units, 10^{-2} m s^{-2} in SI units).

For the Earth, it is usual to evaluate the gravity acceleration anomaly instead of on the reference ellipsoid/sphere (which is the case of equation (2.20)) on the geoid level [e.g., Forte et al., 1994]. This could be for a reference sphere achieved by correcting the above shown formula for the radial gravity anomaly by the change in the mean gravity acceleration

[7] Named after Ernst Heinrich Bruns (4th September 1848–23rd September 1919), German mathematician, physicist and astronomer, who contributed to the development of theoretical geodesy.

[8] Named after Galileo Galilei (15th February 1564–8th Janury 1642), Italian physicist, astronomer and philosopher, who made the first measurements of the acceleration due to gravity.

from the mean planetary radius to the geoid level, which can be approximated as a radial gradient of $g = GM/r^2$ evaluated at the mean planetary radius R_0 multiplied by the local geoid height $h(\vartheta, \varphi)$:

$$\bar{g}_r(R_0, \vartheta, \varphi) \approx g_r(\vartheta, \varphi) + h(\vartheta, \varphi) \frac{\mathrm{d}}{\mathrm{d}r} \frac{GM}{r^2}\bigg|_{R_0}, \tag{2.21}$$

$$\bar{g}_r(R_0, \vartheta, \varphi) \approx g_r(\vartheta, \varphi) - h(\vartheta, \varphi) \frac{2}{R_0} \frac{GM}{R_0^2}, \tag{2.22}$$

$$\bar{g}_r(R_0, \vartheta, \varphi) \approx g_r(\vartheta, \varphi) - \frac{2}{R_0} h(\vartheta, \varphi) g_0, \tag{2.23}$$

and using equations (2.18) and (2.19) we obtain:

$$\bar{g}_r(\vartheta, \varphi) = \sum_{\ell=2}^{\ell_{\max}} \sum_{m=-\ell}^{\ell} \frac{\ell+1}{R_0} U_{\ell m} Y_{\ell m}(\vartheta, \varphi) - \frac{2}{R_0} \sum_{\ell=2}^{\ell_{\max}} \sum_{m=-\ell}^{\ell} U_{\ell m} Y_{\ell m}(\vartheta, \varphi), \tag{2.24}$$

$$\bar{g}_r(\vartheta, \varphi) = \sum_{\ell=2}^{\ell_{\max}} \sum_{m=-\ell}^{\ell} \frac{\ell-1}{R_0} U_{\ell m} Y_{\ell m}(\vartheta, \varphi). \tag{2.25}$$

New measurement techniques (see the Subsection 2.1.1) make use of the gradient of the gravity field ($\nabla \boldsymbol{g}$). This third expression of gravitation (again equivalent to the previous two) describes the spatial changes in the gravity anomaly, and its radial-radial component ($\nabla \boldsymbol{g}$ is a tensor variable) could be obtained from the radial derivation of the equation (2.20):

$$g_{\mathrm{rr}}(r, \vartheta, \varphi) = \sum_{\ell=2}^{\ell_{\max}} \sum_{m=-\ell}^{\ell} \frac{(\ell+1)(\ell+2)}{R_0^2} \left(\frac{R_0}{r}\right)^{\ell+3} U_{\ell m} Y_{\ell m}(\vartheta, \varphi) \qquad r \geq R_0. \tag{2.26}$$

This form is the most sensitive to the small scale gravity features but also the most attenuated with height (see Figure 2.1). The dimension of the gravity gradient is $[g_{rr}] = \mathrm{s}^{-2}$ but more commonly used unit is *eotvos*[9] ($1\,\mathrm{E}{=}10^{-7}\,\mathrm{Gal\,m^{-1}}$ in CGS units, $10^{-9}\,\mathrm{s^{-2}}$ in SI units).

The connection between the density distribution $\rho(\boldsymbol{r}')$ (e.g., a density anomaly in an otherwise homogenous planetary mantle) and the resulting gravity potential $U(\boldsymbol{r})$ can be drawn using the Newton integral which is a solution of the Laplace-Poisson equation:

$$U(\boldsymbol{r}) = G \int_{V'} \frac{\rho(\boldsymbol{r}')}{|\boldsymbol{r} - \boldsymbol{r}'|} \mathrm{d}V'(\boldsymbol{r}'). \tag{2.27}$$

where the integration is carried out over the whole volume V' of a body under consideration. As a next step we transform equation (2.27) into the spectral domain by expanding the terms $\rho(\boldsymbol{r}')$ and $1/|\boldsymbol{r} - \boldsymbol{r}'|$ using the additional theorem [e.g., Burša and Pěč, 1993]:

[9]Named after Loránd Eötvös (27th July 1848–8th April 1919), Hungarian physicist who studied the Earth's gravity field.

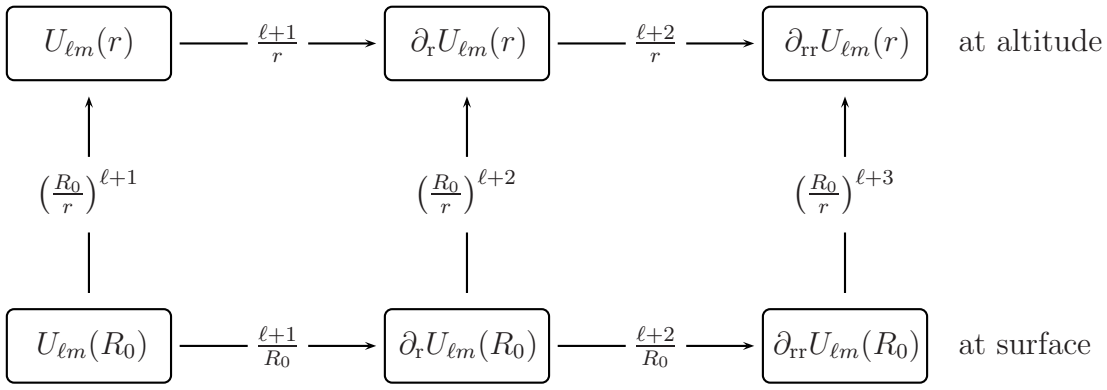

Figure 2.1: *Meissl's spectral scheme for the conversion of the geoid anomaly, gravity anomaly and gravity gradient anomaly evaluated either at the surface (with radius R_0) or at an altitude $r - R_0$ ($r \geq R_0$) (after* Rummel and van Gelderen [1995]*).*

$$\rho(\boldsymbol{r}') = \sum_{\ell,m} \rho_{\ell m}(r') Y_{\ell m}(\vartheta', \varphi'), \tag{2.28}$$

$$\frac{1}{|\boldsymbol{r} - \boldsymbol{r}'|} = \frac{4\pi}{r} \sum_j \frac{1}{2j+1} \left(\frac{r}{r'}\right)^{j+1} \sum_k Y^*_{jk}(\vartheta', \varphi') Y_{jk}(\vartheta, \varphi) \qquad r < r', \tag{2.29}$$

$$\frac{1}{|\boldsymbol{r} - \boldsymbol{r}'|} = \frac{4\pi}{r} \sum_j \frac{1}{2j+1} \left(\frac{r'}{r}\right)^{j} \sum_k Y^*_{jk}(\vartheta', \varphi') Y_{jk}(\vartheta, \varphi) \qquad r \geq r'. \tag{2.30}$$

where asterisk denotes complex conjugation. Together with the relation of orthonormality (A.7) and assuming a spherical body with external radius R_0, we obtain the following equations:

$$U_{int}(\boldsymbol{r}) = \sum_{\ell,m} \left[\frac{4\pi G r}{2\ell+1} \int_{min(r,R_0)}^{R_0} \left(\frac{r}{r'}\right)^{\ell-1} \rho_{\ell m}(r')\, \mathrm{d}r' \right] Y_{\ell m}(\vartheta, \varphi) \qquad r < r', \tag{2.31}$$

$$U_{ext}(\boldsymbol{r}) = \sum_{\ell,m} \left[\frac{4\pi G r}{2\ell+1} \int_{0}^{min(r,R_0)} \left(\frac{r'}{r}\right)^{\ell+2} \rho_{\ell m}(r')\, \mathrm{d}r' \right] Y_{\ell m}(\vartheta, \varphi) \qquad r \geq r', \tag{2.32}$$

$$U(\boldsymbol{r}) = U_{int}(\boldsymbol{r}) + U_{ext}(\boldsymbol{r}), \tag{2.33}$$

which define the resulting spherical harmonic coefficients of the geopotential $U_{\ell m}(r)$.

A common case in geophysics is the consideration of a deformed boundary associated with a density change $\Delta\rho$ that could be described by a set of topographic coefficients $t_{\ell m}$ referenced to a radius D, e.g., surface or crust/mantle interface. In the linear approximation (for details see Section 3.1) we can substitute the real density distribution using the Dirac[10]

[10]Named after Paul Adrien Maurice Dirac (8th August 1902–20th October 1984), English theoretical physicist who contributed to the development of quantum mechanics and quantum electrodynamics.

delta function and the product of the density change and the undulations height $\rho_{\ell m}(r') = \delta(r'-D)\Delta\rho t_{\ell m}$. Then, the resulting geopotential coefficients induced by topographic masses are given by:

$$U_{\ell m}(r) = \frac{4\pi G r}{2\ell+1}\left(\frac{r}{D}\right)^{\ell-1}\Delta\rho t_{\ell m} \qquad r < D, \tag{2.34}$$

$$U_{\ell m}(r) = \frac{4\pi G r}{2\ell+1}\left(\frac{D}{r}\right)^{\ell+2}\Delta\rho t_{\ell m} \qquad r \geq D, \tag{2.35}$$

$$U_{\ell m}(R_0) = \frac{4\pi G R_0}{2\ell+1}\Delta\rho t_{\ell m}, \qquad \text{for the surface topography } (D = R_0). \tag{2.36}$$

This approximation is valid for any topographic feature of degree ℓ for which the vertical dimension is smaller than the given wavelength i.e. $t \ll 2\pi R_0/\ell$ [e.g., Martinec, 1991], otherwise a substantial amount of the topography induced gravity signal could be neglected [e.g., Belleguic et al., 2005]. In such a case, a number of alternative approaches exist [e.g., Martinec and Pěč, 1989; Balmino, 1994; Wieczorek and Phillips, 1998] of which the formulation of Wieczorek and Phillips [1998] is very similar to the equations (2.34)–(2.35):

$$U_{\ell m}(r) = \frac{4\pi G r}{2\ell+1}\left(\frac{r}{D}\right)^{\ell-1} D\Delta\rho \sum_{n=1}^{\ell+3} \frac{{}^n t_{\ell m}}{D^n\, n!} \frac{\prod_{j=1}^{n}(\ell+4-j)}{\ell+3} \qquad r < D, \tag{2.37}$$

$$U_{\ell m}(r) = \frac{4\pi G r}{2\ell+1}\left(\frac{D}{r}\right)^{\ell+2} D\Delta\rho \sum_{n=1}^{\ell+3} \frac{{}^n t_{\ell m}}{D^n\, n!} \frac{\prod_{j=1}^{n}(\ell-3+j)}{\ell-2} \qquad r \geq D, \tag{2.38}$$

where ${}^n t_{\ell m}$ are the spherical harmonic coefficients of the n-th power of topography (for $n = 1$ these equations transform to (2.34) and (2.35)). The sum $\sum_n$ makes the computations very time consuming and therefore in practise it is truncated after the first $n = 5$ terms [e.g., Wieczorek, 2007].

Some authors [e.g., Yuan et al., 2001; McGovern et al., 2002, 2004; Wieczorek, 2007] employ a normalization using the factor GM/R_0 (i.e. the mean value of the geopotential) which then makes e.g. the formula (2.36):

$$\tilde{U}_{\ell m}(R_0) = \frac{4\pi R_0^2}{M(2\ell+1)}\Delta\rho t_{\ell m}, \tag{2.39}$$

which than implies changes in the equations (2.17) and (2.18) and all others:

$$U(\boldsymbol{r}) = \frac{GM}{r}\sum_{\ell=2}^{\ell_{\max}}\sum_{m=-\ell}^{\ell}\left(\frac{r}{D}\right)^{\ell+1}\tilde{U}_{\ell m}Y_{\ell m}(\vartheta,\varphi) \qquad r < D, \tag{2.40}$$

$$U(\boldsymbol{r}) = \frac{GM}{r}\sum_{\ell=2}^{\ell_{\max}}\sum_{m=-\ell}^{\ell}\left(\frac{D}{r}\right)^{\ell}\tilde{U}_{\ell m}Y_{\ell m}(\vartheta,\varphi) \qquad r \geq D. \tag{2.41}$$

2.1.1 Measurement techniques

As an artificial satellite orbits around the planet of interest, its path, which is determined by the orbital (so-called Kepler's) elements and a number of external forces, is modified by

the lateral variations in the planet's gravity field. Of the highest influence is the planetary flattening [e.g., Novotný, 1998] but also other, higher terms, play a role. In this section, a brief overview of the methods used in planetary science to determine the gravity field of a planet is given.

However, before any gravity reconstruction can be undertaken, a precise determination of the satellite's position, taking into account all possible factors, must be done first. Aside from its own dynamic propulsion, there is also the gravitational influence of other planets, tidal forces, the solar wind pressure, atmospheric drag etc. that all must be modeled appropriately. Then, in principle, the radial error δ_{r} (referenced to the Earth observatory) is very small (typically < 1 m) as the distance can be read directly from the 2-way radio communication with the satellite, while today also the along/across-track ($\delta_\vartheta/\delta_\varphi$) error decreases significantly (being typically < 10 m) [e.g., Neumann et al., 2001]. Moreover, employing the technique of altimetery crossovers (i.e. doing the altimetry measurements over one spot multiple-times during different crossing orbits) can improve the orbit geometry determination even more.

Once the position of the satellite in orbit around the planet is known with a sufficient accuracy, we can evaluate the local accelerations of spacecraft (read from the radio signal Doppler tracking) due to the influence of lateral changes in planetary gravity. This along-track varying factor can be studied by the line-of-sight (LOS) accelerations which take advantage of the short-wavelength information content, but suffers from the unknown possible error and only regional coverage [cf. Barnett et al., 2002; McKenzie et al., 2002]. Another and more widely used technique is to stack the information obtained during the Doppler tracking of the spacecraft and invert them later by means of least-square inversion for a global gravity field described by a set of spherical harmonic coefficients and their associated errors [e.g., Konopliv et al., 1999, 2001; Yuan et al., 2001]. This method has several advantages, but on the other hand it suffers from the unequal coverage of the planet, especially in the short-wavelength part of model. This problem is usually solved by applying some a priory constraint for the solution above a certain degree ℓ_{crit} – usually a modified Kaula's rule of thumb [Kaula, 1966] is employed. Additional improvement in the gravity field solution can be achieved using micro-accelerometers on board the spacecraft which provide us with a direct reading of the non-gravitational forces acting on the satellite [e.g. Iess and Boscagli, 2001].

Recently a new method for the investigation of planet's gravity field emerged with the use of the micro-gradiometer [e.g., Koop et al., 2006]. This device, due to its construction (it can be approximated by a pair of accelerometers placed along a desired measurement axis), can sample directly changes in the gravity acceleration which can then be transformed to gravitational potential (see the equation (2.26)). This leads to a progressive improvement of the obtained gravity field, especially over the medium and short-wavelengths, with the maximum possible degree of model even twice or three-times higher than from the use of the Doppler tracking method (for the same orbit height). However, this concept is technically very demanding to implement. Alternatively, such a concept can be realized using two spaceprobes flying apart on the same track with a continuous tracking of their separation by radio ranging (such as the GRACE mission – see e.g., Klokočník et al. [2008]).

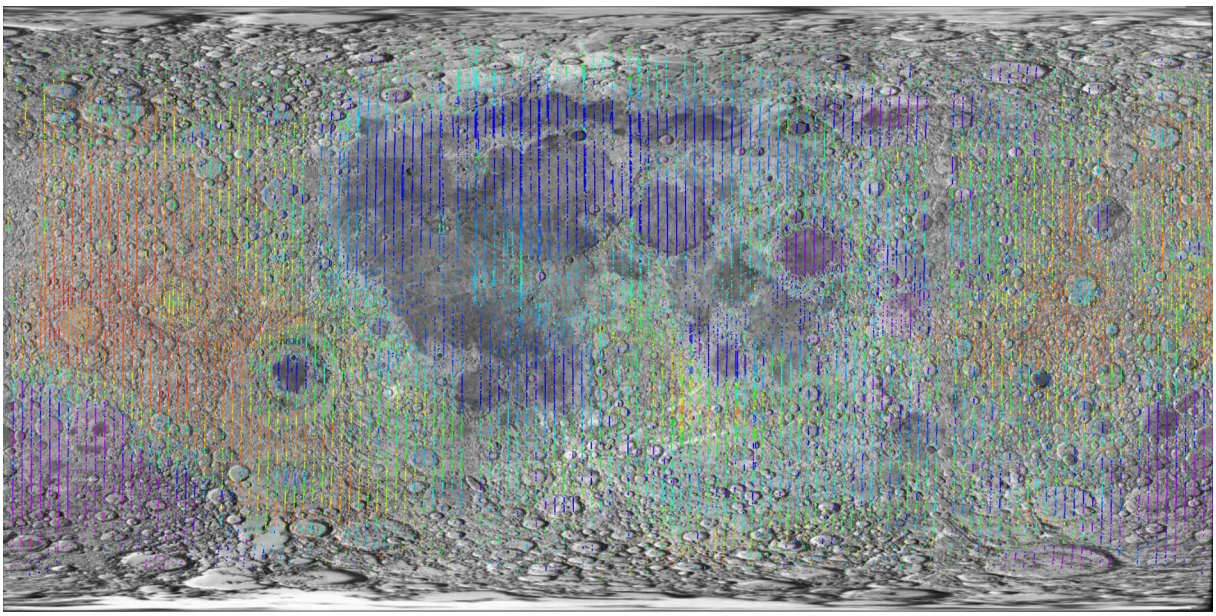

Figure 2.2: *Clementine lidar lunar topography measurements* [Smith et al., 1997] *(freely available at http://pds-geosciences.wustl.edu/missions/clementine/gravtopo.html) superposed on the albedo map of the Moon produced by the Naval Research Laboratory from photographic images obtained by the same spaceprobe.*

2.2 Topography

The second important quantity that can be used to constrain the structure of the planetary subsurface is the surface topography. The most precise way in the terms of the global radius measurements is the radar/lidar (RAdio/LIght Detection And Ranging) altimetry (with the second one achieving much better results) [e.g., Smith et al., 1997; Rappaport et al., 1999; Smith et al., 1999]. The basic principle is simple and is based on a high number of signal shots directed from the spaceprobe towards the planetary surface and measurements of the return-signal arrival time. The resulting digital elevation model (DEM) has a very good coverage along the track, however due to the rotation of the planet and the inclination of the orbit in respect to the planetary polar axis, the longitudinal coverage is irregular and sometimes insufficient (see Figure 2.2 for the a case of lunar topography model). Despite that fact, after a sufficiently long campaign the resulting coverage is usually $1^\circ \times 1^\circ$ or better (e.g., for Mars the final model based on laser altimetry data has a resolution of $1/128^\circ \times 1/128^\circ$ globally – available at *http://pds-geosciences.wustl.edu/missions/mgs/megdr.html*) with measurement accuracy $\sim$1–10 m [cf. Neumann et al., 2001].

To improve the longitudinal resolution of the DEM models, a 3D stereo-camera can be employed, a concept pioneered by the Mars Express mission. This instrument uses (at least) two cameras pointing forward and backward along the track which obtain images of the surface from different angles, allowing for a precise – although local – DEM model. It provides a relatively uniform resolution $\sim$10's meters per pixel depending on the observation height, and vertical determination accuracy $\sim$1 pixel (i.e. also $\sim$10's meters). Apart from

Planet	R_0 [m]	M [kg]	g_0 [ms^{-2}]	$\bar{\rho}$ [kgm^{-3}]	T [days]	$1/\alpha$
Mercury	2439.7×10^3	3.302×10^{23}	3.7	5427	58.646	0
Venus	6051.8×10^3	48.685×10^{23}	8.9	5204	243.018	0
Earth	6371.0×10^3	59.736×10^{23}	9.8	5515	0.997	298.256
Moon	1737.1×10^3	0.735×10^{23}	1.6	3346	27.321	> 825
Mars	3389.5×10^3	6.419×10^{23}	3.7	3934	1.025	169.779
Io	1821.6×10^3	0.893×10^{23}	1.8	3528	1.769	–
Europa	1560.8×10^3	0.480×10^{23}	1.3	2989	3.551	–
Ganymede	2631.2×10^3	1.482×10^{23}	1.4	1942	7.155	–
Callisto	2410.3×10^3	1.076×10^{23}	1.2	1834	16.689	–
Titan	2576.0×10^3	1.345×10^{23}	1.4	1880	15.945	> 5000

Table 2.1: *Compilation of physical characteristics for the terrestrial planets and big moons of the Solar system (based on data published by Anderson et al. [1987]; Sohl et al. [1995]; Konopliv et al. [1999]; Smith et al. [1999]; Rappaport et al. [1999]; Konopliv et al. [2001]; Spohn et al. [2001b]; Schubert et al. [2003]; Jacobson et al. [2006]; Wieczorek et al. [2006]; Seidelmann et al. [2007]; Nimmo et al. [2007]; Zebker et al. [2009]).*

the fact that with such a high resolution the global coverage of a planet's surface is very time demanding, if not impossible because of the typical life-span of a spaceprobe, the main disadvantage comes from the fact that the elevation model is only relative, allowing no radius measurements. Therefore, a combination of the stereo-camera method with the lidar measurements is highly desired [e.g., Blanc et al., 2007]. Various other techniques employing visual observations for the DEM reconstruction exist (e.g., using multiple observations of the same region from different angles and the above mentioned principle or employing the information about the sun-elevation angle and the length of the observed shadows), however, with much lower resolving power and accuracy.

Once a global DEM of the planetary topography (in reality of the planetary shape, since the term topography usually refers to the shape corrected to the geoid) is available, it can be converted into the spectral domain using the formula (A.8) or some other suitable computational approach [cf. Neumann et al., 2004]. Then, with or without the mean planetary radius R_0 normalization, the equation for the spherical harmonic synthesis takes the form:

$$t(\vartheta,\varphi) = \sum_{\ell=0}^{\infty}\sum_{m=-\ell}^{\ell} t_{\ell m}\, Y_{\ell m}(\vartheta,\varphi), \tag{2.42}$$

$$t(\vartheta,\varphi) = R_0 \sum_{\ell=0}^{\infty}\sum_{m=-\ell}^{\ell} \tilde{t}_{\ell m}\, Y_{\ell m}(\vartheta,\varphi), \tag{2.43}$$

Whether or not the supplied data set is normalized by the mean planetary radius can be judged based on the value of $\ell = 0$ coefficient, since $\tilde{t}_{00} \equiv 1$. The mean planetary radii for most important terrestrial objects of the Solar System are listed in Table 2.1.

2.3 Observed planetary gravity and topography

In this section the gravity and topography data obtained for Venus and Mars [Konopliv et al., 1999; Rappaport et al., 1999; Smith et al., 1999; Konopliv et al., 2006] will be presented, together with a short description of their most prominent features and general characteristics. In the following chapters these two objects are often referred to as being typical big and small terrestrial planets. However, first information about the gravity and topography data of other terrestrial objects of the Solar System are shortly reviewed, as they are not the topic of this work and/or we do not have the adequate data for them.

2.3.1 Mercury, Moon and other terrestrial objects

The closest planet to the Sun is Mercury which remains one of the least explored planets of our planetary system. Due to the fact that interplanetary flight in such proximity of the Sun is very fuel consuming, only one spacecraft has explored this planet, Mariner 10, which in the 1970's made three successive flybies. Unfortunately, it was not equipped with any altimetric device and therefore only limited topographic information was obtained using the photometric methods [Cook and Robinson, 2000; André et al., 2005]. Gravity information from the flybies was limited to coefficients C_{20} and C_{22} with quite high uncertainty. However, in the beginning of 2008, the spaceprobe MESSENGER made its first successful flyby around Mercury, which will be followed by an orbital mission starting in 2011. Unfortunately, the chosen orbit is a very eccentric one, which means that only one hemisphere will be investigated in terms of gravity and topography data. Another spaceprobe called BepiColombo is already planned to arrive at Mercury in 2019, promising global topography coverage and a complete spherical harmonic model of gravity field up to degree $\ell \sim 25$ [Milani et al., 2001].

On the other hand, the proximity of our Moon makes it one of the best explored terrestrial objects. Unfortunately its coverage in terms of gravity and topography data is strongly unequal. While the topography of the polar regions is well known thanks to ground-based photometric observation from the Earth, the lidar coverage between the polar regions is quite sparse (see Figure 2.2) [Wieczorek, 2007]. Even more pronounced is the inequality in the gravity data. Despite the fact that radio tracking of both manned and unmanned spacecrafts started already in the 1960's, due to the Moon's tidally locked rotation almost no data were collected directly over the far-side. Therefore, the available data today have very good accuracy on the near-side (information up to degree $\ell \sim 150$) but the far-side data have a large associated error [Konopliv et al., 2001; Hikida and Wieczorek, 2007]. Over the majority of the mare regions were nevertheless already in the first observations found strong positive anomalies caused probably by mass-concentrations (mascons) at or beneath the surface [Muller and Sjogren, 1968; Wieczorek and Phillips, 1998; Konopliv et al., 2001]. The prominent topographic feature is a dichotomy between the near-side mares (big impacts infilled by lava) and the far-side highlands, whose origin is still unclear [Wieczorek et al., 2006]. In recent years an advancement in the knowledge of both lunar gravity and topography was done as three well-equipped spacecraft, Kaguya, Lunar Reconnaissance Orbiter and Grail made very detailed observations of the Moon.

For the other terrestrial objects listed in Table 2.1, we have no data except for those obtained from (numerous) flybies. These are usually sufficient for the derivation of basic structural models but the coverage is not sufficient for the construction of a spherical harmonic model covering the lateral variations in the gravity field [Schubert et al., 2003]. Single point mass anomalies were, however, observed [e.g., Palguta et al., 2006], promising some interesting results once orbital missions are send for continuous observational campaigns. Indeed, with an increasing interest in the exploration of Europa and Titan, there is a promising outlook for orbital missions to those two exceptional moons [e.g., Blanc et al., 2007; Clarke, 2007]. Concerning the topography of the big natural satellites, some information derived using the photometric methods were obtained mainly during the Galileo mission to Jupiter and the Cassini mission to Saturn [e.g., Nimmo et al., 2007], however, for global coverage an orbital mission is still required [Blanc et al., 2007].

2.3.2 Venus

The planet Venus' surface is hidden below a very dense atmosphere which for a long time disabled its observation. The first maps of the planet's topography were made in the 1970's and these effort culminated with the Magellan spaceprobe radar mapping mission in the beginning of 1990's [cf. Wieczorek, 2007]. The obtained topographic map has a resolution $1/20^\circ \times 1/20^\circ$ per pixel and was used to produce a spherical harmonic model GTDR3.2 complete up to degree and order 360 [Rappaport et al., 1999], shown in Figure 2.3. The majority of the surface is covered with shallow lowlands but several features stand above them. First are two elevated highland regions, Ishtar Terra (close to the north pole) and Aphrodite Terra (close to the equator), with the first exhibiting the highest elevation ($\sim$11 km) above the reference radius in the region of the Maxwell mountains. There are also several large volcanic constructs of which the most prominent are in Atla and Beta Regiones (0° N, 200° E and 25° N, 280° E, respectively), that reach heights of several kilometers. The overall characteristic of the Venus' topography is, however, unimodal [e.g., Schubert et al., 2001], suggesting that the elevated landforms are not a consequence of continental crust production processes as in the case of the Earth [e.g., Herrick and Phillips, 1992].

The best today available gravitational field of Venus is a combination of the tracking data from various missions, with the major contribution coming from the Magellan mission. The MGNP180U spherical harmonic model is complete up to degree and order 180 [Konopliv et al., 1999] possessing, however, a substantial error for degrees $\ell > 60$. The uncertainties in the spatially expanded gravity field vary laterally with the lowest error in the equatorial region (see Fig. 3 in Konopliv et al. [1999]). Its representations in the form of first approximation geoid anomalies h and gravity anomalies g_{r} are also depicted in Figure 2.3. The striking feature is a very good correlation with topography, even at the longest wavelengths, which is the opposite of the situation on the Earth [e.g., Wieczorek, 2007]. One of the possible explanations for this phenomena is that at long wavelength the majority of surface topography is connected to the dynamic processes in the mantle [e.g., Kiefer et al., 1986; Pauer et al., 2006]. The highest geoid/gravity anomalies (> 100 m and > 200 mGals, respectively) are associated with the volcanic constructs but the Terra regions also have quite a strong gravity signal. Noticeable also is a small scale signal connected to several ridges with the most prominent one being Artemis Chasma, visible south of Aphrodite Terra.

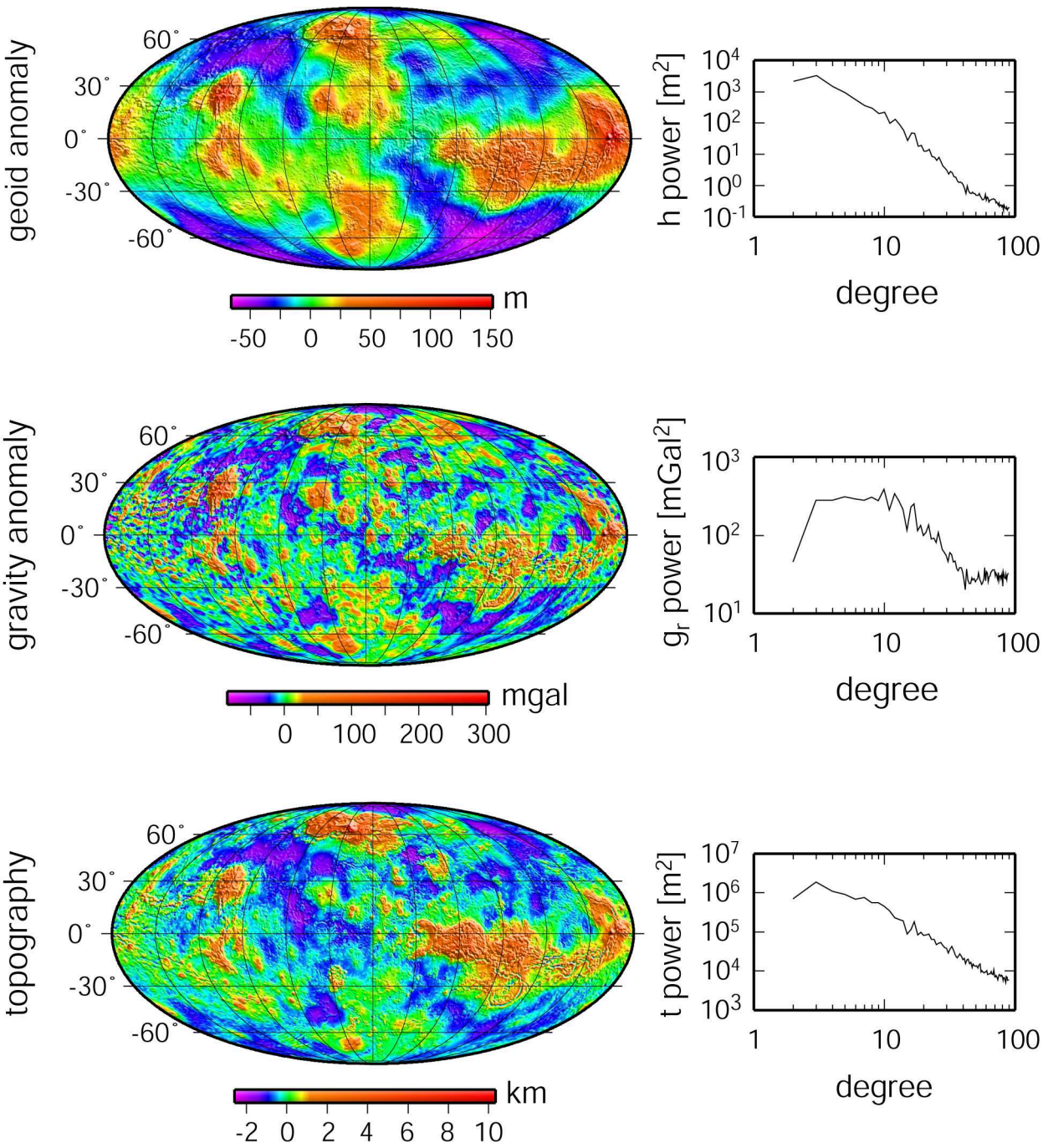

Figure 2.3: *Venus geoid, gravity disturbance anomaly and topography, together with their power spectra computed using eq. (A.10) (ℓ_{max}=90 in all cases). The map images are plotted in Mollweide projection centered at 30°E meridian and the geoid and gravity anomaly are underlaid by the topography gradient image. The depicted topography is referenced to the spherical radius of 6051.8 km.*

2.3.3 Mars

The topography of Mars is known to an unprecedent level thanks to the measurements of MOLA lidar onboard the Mars Global Surveyor spacecraft [Smith et al., 1999]. The resulting data set has attained a uniform coverage of $1/128^\circ \times 1/128^\circ$ and an accuracy of $\sim$1 meter using the crossover technique [Neumann et al., 2001]. Its gridded version with a resolution of 0.25°, named MEG025T, is shown in Figure 2.4. What is not shown here is that the planetary shape has quite a substantial polar flattening ($\sim$20 km difference between the equatorial and polar radii) which is a consequence of relatively fast planetary rotation. The most obvious feature is the north-south dichotomy, in the elevation which remains unexplained, although various models have been proposed e.g., a degree-1 convection [e.g. Zhong and Zuber, 2001] or an enormous impact in the northern hemisphere [e.g., Andrews-Hanna et al., 2008]. In addition, Mars' topography is dominated by a giant volcanic construct Tharsis, which occupies most of the western hemisphere with several prominent volcanoes of which the highest one, Olympus Mons, rises $\sim$22 km above the zero-elevation reference level. Volcanic activity was also present in the eastern hemisphere in the region surrounding Elysium Mons volcano (25° N, 145° E). Other noticeable topographic features are the giant impact basins Hellas, Isidis and Argyre and the vast rift system Valles Marineris, east of the Tharsis region.

The Martian gravity field was also notably improved by the Mars Global Surveyor mission, however, it is still being improved by the fleet of spacecrafts currently orbiting Mars [e.g. Wieczorek, 2007]. The most recent spherical harmonic gravity model field, JGM95J01, is complete up to degree and order 95, with the error reaching the signal strength around degree $\ell \sim 70$ [Konopliv et al., 2006]. The geoid derived from this model is shown in Figure 2.4. After removing the rotation flattening contribution (about 95% of U_{20} coefficient), it is clearly dominated by U_{22} structure connected to the enormous load of Tharsis [Phillips et al., 2001]. Other observable features are geoid heights associated with the biggest volcanoes (with the peak almost 2 km in the region of Olympus Mons) and large impact basins Hellas and Utopia. The radial gravity anomaly shows a little more detail e.g., the negative anomaly connected to Valles Marineris (almost -700 meters) and the mascon signal connected to the Isidis and Argyre impact basins. The short wavelength oscillations, especially in the northern lowlands, can be attributed to a number of subsurface loads connected to the resurfaced impact craters discovered in high-resolution topography data [Frey et al., 2002].

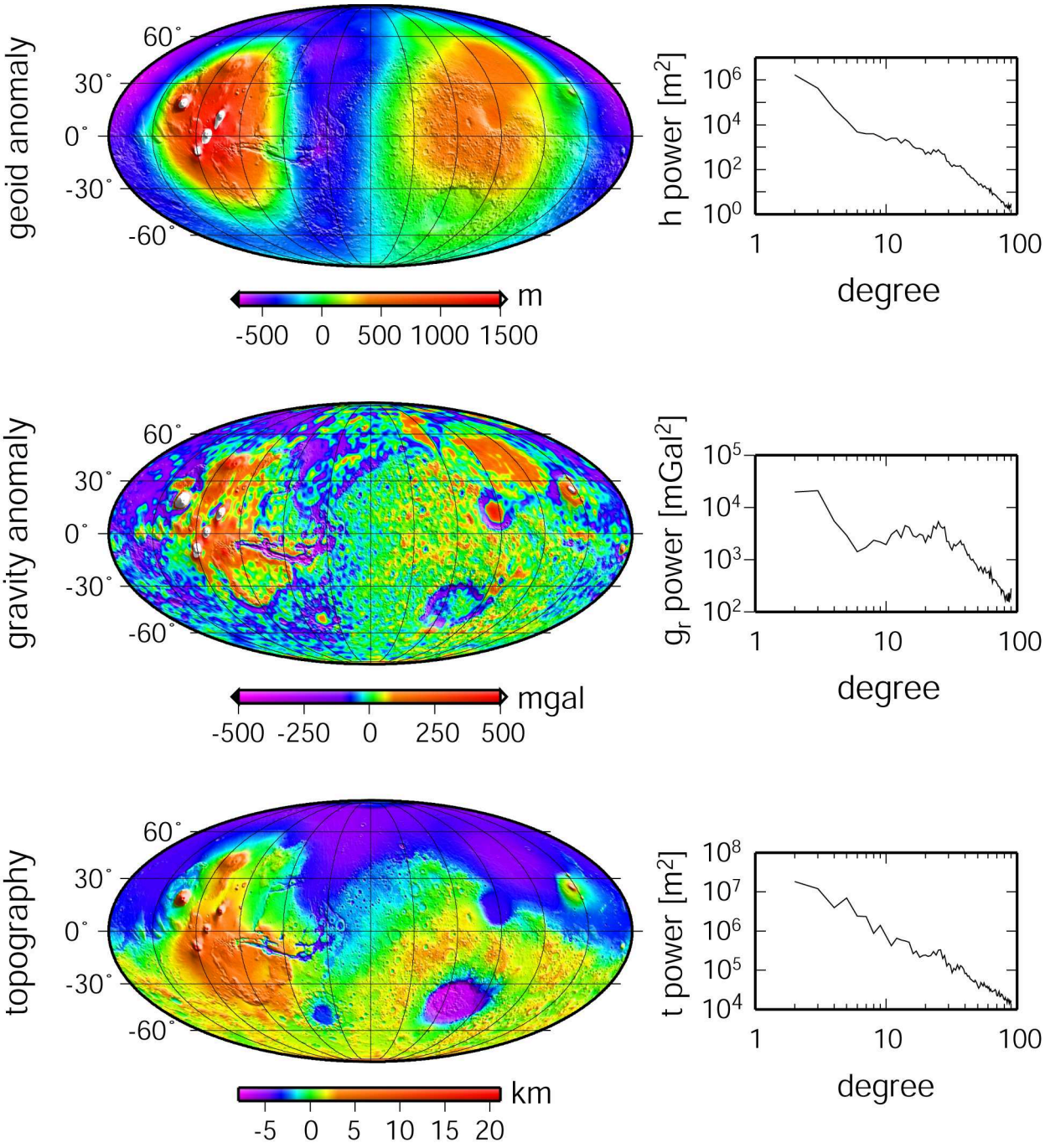

Figure 2.4: *Mars geoid, gravity disturbance anomaly and topography, together with their power spectra computed using eq. (A.10) (ℓ_{max}=90 in all cases). The map images are plotted in Mollweide projection centered at 0° meridian and the geoid and gravity anomaly are underlaid by the topography gradient image. The depicted topography is referenced to the second-order precision geoid, including the rotational term.*

Chapter 3

Forward Modeling of the Gravitational Signal

Any deviation of a planetary surface from its hydrostatic shape in form of positive (or negative) topography causes a mass excess (or deficit), and alters the equilibrium in the lithostatic pressure. Because the crust and underlaying lithosphere are not infinitely rigid, they both deform in a way to achieve again some level of equilibrium. Studying this deformation both quantitatively and qualitatively can provide useful information not only about the loading processes (which emplaced the studied topography on the surface) but also on the properties of the crust and underlaying mantle and eventually even the deeper parts of the planetary interior.

In the case of the Earth, a seismic sounding e.g. in the oceanic volcanic regions, can display the deformation of the crust directly [e.g., Watts, 2001]. However, for the other planets, this observation is not available (though planned in future, cf. Lognonné [2005]) and even for the Earth the deep interior is not well examined due to an insufficient coverage [e.g., Běhounková et al., 2007]. However, we can take advantage of the fact that all density inhomogeneities induced by or supporting the observed topographic features also generate a gravity field that can be observed exterior to the planet (see Section 2.1.1). Joint analysis of both gravity and topography can then provide the desired information if some *a priori* assumptions are made concerning the mechanism of the observed topography compensation [e.g., Mitrovica and Peltier, 1992; Wieczorek and Phillips, 1997; Simons et al., 1997; Čadek and Fleitout, 2003; Vezolainen et al., 2004; Andrews-Hanna et al., 2008].

In this chapter these compensation processes will be studied in detail and, using the theoretical background defined in the previous text, the corresponding gravity signal will be modeled. Throughout this work, several simplifications are adopted, of them the most often used being the assumption of homogeneous crust. This is in contradiction to the observation made on the Earth where the crust is seen to be heterogenous depending on its local origin [e.g., Čadek and Martinec, 1991; Watts, 2001]. However, as a first approximation in the absence of detailed geological and seismological information, this assumption is widely used in planetary science [e.g., Turcotte et al., 1981; McNutt et al., 1988; Smrekar and Phillips, 1991; Neumann et al., 1996; Phillips et al., 2001].

3.1 Crustal isostasy

In the 18th century, a debate arose about whether the shape of the Earth was flatted at the poles or the equator. To solve this questions, two expeditions were send to different latitudes to make the required measurements [e.g., Novotný, 1998]. Among the methods they used was also the determination of the elevation angle of the Polaris star from the horizon, determined using level-bubble tools. One of the participants of the Peru expedition, Pierre Bouguer[1], noted that the deflection of the plumb close to the Andes mountains was not severely influenced by their mass, a result contrary to his expectation based on Newton's gravitational law [e.g., Watts, 2001]. A century later during the geodetic survey in India, a local *deflection of the vertical* was observed and also quantified. John Henry Pratt[2] computed the attraction due to the Himalayas [Pratt, 1855] but arrived at a result three times greater than the observed value. He accounted for this by the large uncertainty in his knowledge of the mountains' shape, whereas George Biddell Airy[3] proposed that this discrepancy came from neglecting the underground mass deficit compensating the mass excess of mountains [Airy, 1855].

Airy had suggested using the analog of an iceberg, where the material underlaying the crust is denser and therefore to compensate the surface mountains additional crustal volume should substitute the mantle material. Today, the physical formulation of his concept is called Airy (sometimes Airy/Heiskanen) isostasy and it assumes that at a certain depth d below the surface with radius R_0, the lithostatic forces are constant (d is chosen such that the local deviation $w(\vartheta, \varphi)$ of the crust-mantle interface (CMI) from the mean crustal thickness D_c always satisfy $D_\mathrm{c} + w(\vartheta, \varphi) < d$). Using a planar approximation (see Figure 3.1a) this concept can be generally formulated as:

$$\int_{R_0-d}^{R_0+t(\vartheta,\varphi)} \rho(r, \vartheta, \varphi) g_0 \, \mathrm{d}r = \text{const.}, \tag{3.1}$$

where $t(\vartheta, \varphi)$ is the topography height referenced to zero level at R_0 and g_0 is a constant approximating gravitational acceleration $g(r)$. In a case of Airy isostasy, i.e. laterally homogeneous crust ($\rho|_{r>R_0-D_\mathrm{c}-w} = \rho_\mathrm{c}$) and mantle ($\rho|_{r<R_0-D_\mathrm{c}-w} = \rho_\mathrm{m}$) it can be substantially simplified [e.g., Turcotte and Schubert, 2002] to:

$$\rho_\mathrm{c} t = (\rho_\mathrm{m} - \rho_\mathrm{c}) w \tag{3.2}$$

$$w = \frac{\rho_\mathrm{c}}{\rho_\mathrm{m} - \rho_\mathrm{c}} t. \tag{3.3}$$

This approximation holds for the case of the Earth where the convergence of the verticals from the surface down to the compensation depth is not an important factor i.e. $R_0 + t \approx R_0 - d$. However, for other planets and moons in the Solar System, this assumption is no

[1] Pierre Bouguer (16th February 1698–15th August 1758), French mathematician and astronomer, who improved significantly naval navigation and architecture.

[2] John Henry Pratt (4th June 1809–28th December 1871), English cleric and mathematician, who first arrived at the principle of crustal balance during his stay in India.

[3] George Biddell Airy (27th July 1801–2nd January 1892), English mathematician and Astronomer Royal (1835–1881), who, among other achievements, established the today used Greenwich meridian.

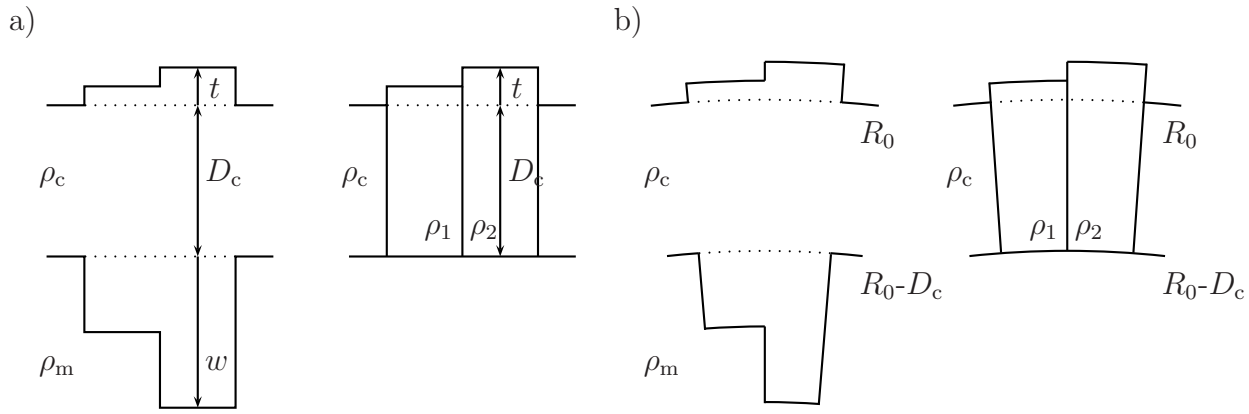

Figure 3.1: *a) Conceptual drawing of Airy (left) and Pratt (right) crustal isostasy in a planar geometry and b) in the spherical geometry (for a description of the parameters, see the text).*

longer valid due to their relatively small radius compared to the Earth (and Venus). Then, each shell of a different radius r has a different surface area and therefore a spherical version of equation (3.1) must be evaluated instead (see Figure 3.1b):

$$\int_{R_0-d}^{R_0+t(\vartheta,\varphi)} \rho(r,\vartheta,\varphi) g_0 r^2 \,\mathrm{d}r = \text{const.} \tag{3.4}$$

Because the load is proportional to the shell radius as r^2, it is not possible to transform equation (3.4) into a form similar to (3.2). To obtain a linear dependency on t, a linear approximation (from equation (3.6) to (3.7)) must be made [e.g., Lambeck, 1988]:

$$\int_{R_0}^{R_0+t} \rho_c r^2 \,\mathrm{d}r = \int_{R_0-D_c-w}^{R_0-D_c} (\rho_m - \rho_c) r^2 \,\mathrm{d}r \tag{3.5}$$

$$\rho_c\Big[(R_0+t)^3 - R_0^3\Big] = (\rho_m-\rho_c)\Big[(R_0-D_c)^3 - (R_0-D_c-w)^3\Big] \tag{3.6}$$

$$\rho_c\Big[R_0^3 + 3R_0^2 t - R_0^3\Big] = (\rho_m-\rho_c)\Big[(R_0-D_c)^3 - (R_0-D_c)^3 + 3(R_0-D_c)^2 w\Big] \tag{3.7}$$

$$\rho_c t R_0^2 = (\rho_m-\rho_c) w (R_0-D_c)^2 \tag{3.8}$$

$$w = \frac{\rho_c}{\rho_m-\rho_c}\left(\frac{R_0}{R_0-D_c}\right)^2 t. \tag{3.9}$$

Today, number of models exists which take into account not only vertical movements in the crust to achieve a state of isostasy but also lateral flow in the lower crust [e.g., Bott, 1999; Nimmo and Stevenson, 2001]. This effect is important particulary in the case of thick crust with comparatively high temperatures at its base. Nevertheless, the vertical adjustment is much faster than this lower crustal flow [Nimmo and Stevenson, 2001] and therefore considered as the primary mechanism to reach isostasy [e.g., Turcotte and Schubert, 2002]. To model the time evolution of crustal compensation, a viscoelastic model with two layers

of distinct viscosities representing the crust and the mantle can be used. The isostatic state is then reached when the degree of compensation c_ℓ (for its definition see equation (3.34)) approaches 1 [Zhong, 1997].

Historically, the second attempt to apply an idea of isostasy to crustal compensation processes comes from Pratt four years later [Pratt, 1859] as a response to Airy's concept. It assumes a different means of topographic mass compensation, where instead of variations in the thickness of the crust it considered variations in the crustal density. Then, the elevation of the column $D_\mathrm{c} + t$ depends on its density ρ. The relationship between topography t and density ρ can be evaluated in a planar approximation (see Fig. 3.1a) using equation (3.1) and assuming constant crustal thickness i.e. $w = 0$ and variable crustal density $\rho = \rho_\mathrm{c} + \delta\rho$ [e.g. Lambeck, 1988; Turcotte and Schubert, 2002]:

$$\rho_\mathrm{c} D_\mathrm{c} = (\rho_\mathrm{c} + \delta\rho)(D_\mathrm{c} + t) \tag{3.10}$$

$$(\rho_\mathrm{c} + \delta\rho) = \frac{D_\mathrm{c}}{D_\mathrm{c} + t}\rho_\mathrm{c} \tag{3.11}$$

$$\delta\rho = -\frac{t}{D_\mathrm{c} + t}\rho_\mathrm{c}. \tag{3.12}$$

In the spherical geometry when the convergence of verticals is taken into account, we have to use again equation (3.4) which, using the linear approximation and the above mentioned assumptions (see Fig. 3.1b), gives [e.g., Tsoulis, 1999]:

$$(\rho_\mathrm{c} + \delta\rho) = \frac{D_\mathrm{c}}{D_\mathrm{c} + t}\left(\frac{R_0}{R_0 - D_\mathrm{c}}\right)^2 \rho_\mathrm{c} \tag{3.13}$$

$$\delta\rho = -\frac{t}{D_\mathrm{c} + t}\rho_\mathrm{c} - \frac{D_\mathrm{c}^2(2R_0 - D_\mathrm{c})}{(D_\mathrm{c} + t)(R_0 - D_\mathrm{c})^2}\rho_\mathrm{c}. \tag{3.14}$$

Pratt (sometimes called Pratt/Hayford) isostasy is not used as much in planetary science as the Airy one, mainly because of the fact that planetary crust is for the highest possible simplicity considered to be homogeneous [e.g., Smrekar and Phillips, 1991; Wieczorek and Phillips, 1998; McGovern et al., 2002; Chenet et al., 2006]. However, on some terrestrial object (Moon, Mars) we can observe whole-planet dichotomy in elevation and in its chemical/geological structure [Smith et al., 1999; Wieczorek et al., 2006]. For those cases, a Pratt isostasy has been advocated as one of the possible mechanism to explain those dichotomies [Wieczorek and Phillips, 1997; Spohn et al., 2001a; Belleguic et al., 2005], however, the majority of the authors do not consider this effect in their works. This can, however, raise some questions about their results when they implicitly assume a different chemical composition or origin. E.g. in the case of the Martian northern lowlands formation via a huge impact that melted the crust and upper mantle, producing new crust in the impact area [Andrews-Hanna et al., 2008]. Employing the Pratt isostasy concept (together with the Airy one which shows itself widely applicable in the planetary research) could therefore improve the quality of future planetary crust models.

The derivation of the gravitational signal of the compensated topography will now follow. Here, only the Airy isostasy, which is simpler and much wider used, will be discussed. For the case of Pratt isostasy, an integration of the signal induced by the density anomalies $\delta\rho$ in the crust is needed, otherwise the procedure is quite similar (for details see Tsoulis [1999]).

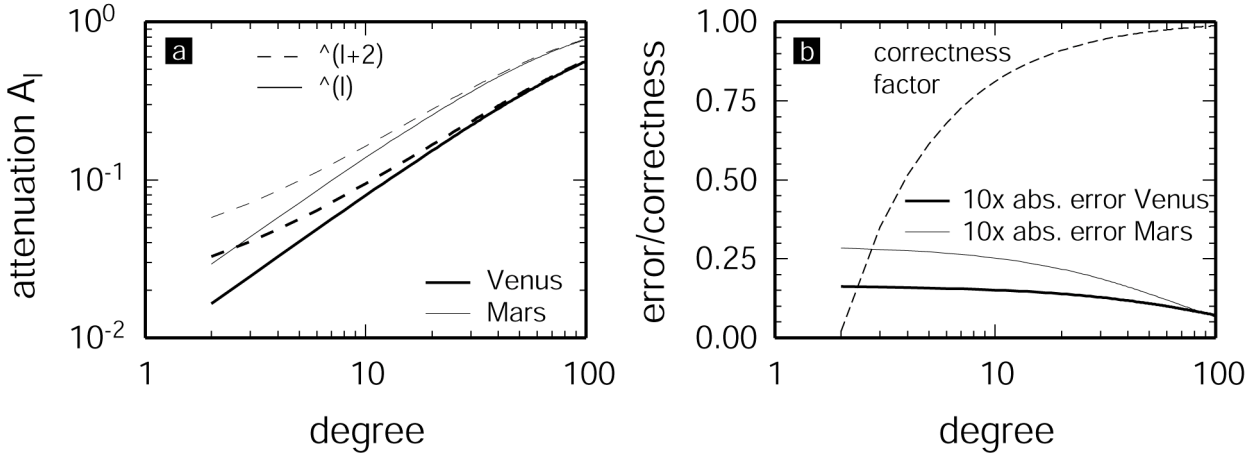

Figure 3.2: *a) Degree attenuation factor for the gravity signal generated by topography compensated by the Airy isostasy mechanism derived using a planar geometry* $A_\ell^{\rm cart} = 1-(\frac{R-D}{R})^{\ell+2}$ *(dashed line) and spherical geometry* $A_\ell^{\rm sph} = 1-(\frac{R-D}{R})^{\ell}$ *(solid line) for planets Venus and Mars with the same fixed crustal thickness* $D_{\rm c} = 50$ *km. b) For comparison the absolute error (multiplied by 10) between both attenuation factors* $\delta = 10 \times |A_\ell^{\rm cart} - A_\ell^{\rm sph}|$ *for Venus and Mars and the "correctness" factor of the planar approximation factor* $1 - |A_\ell^{\rm cart} - A_\ell^{\rm sph}|/A_\ell^{\rm sph}$*, which is typical for both studied cases, is shown.*

The spherical harmonic formalism is used throughout the rest of this chapter. Starting with equation (2.36) for the signal of the surface topography and (2.35) for the one induced by CMI undulations w_ℓ, which is in the case of Airy isostasy evaluated using equation (3.9), we obtain:

$$U_{\ell m} = \frac{4\pi G R_0}{2\ell+1}\left[\rho_{\rm c} t_{\ell m} - (\rho_{\rm m}-\rho_{\rm c}) w_{\ell m}\left(\frac{R_0 - D_{\rm c}}{R_0}\right)^{\ell+2}\right] \tag{3.15}$$

$$w_{\ell m} = \frac{\rho_c}{\rho_m - \rho_c}\left(\frac{R_0}{R_0 - D_{\rm c}}\right)^2 t_{\ell m} \tag{3.16}$$

$$U_{\ell m} = \frac{4\pi G R_0}{2\ell+1}\left[1 - \left(\frac{R - D_{\rm c}}{R}\right)^{\ell}\right] t_{\ell m}. \tag{3.17}$$

In the case where the spherical correction is not applied (i.e. instead of equation (3.9), equation (3.3) is used) the resulting exponent in equation (3.17) is $\ell + 2$ instead of ℓ. This influences in particular the lowermost degree signal below $\ell \sim 20$, as can be seen in Figure 3.2. In both panels, it is obvious that the absolute difference in the attenuation factors increases with decreasing planetary radius, which was already mentioned above, since the convergence of verticals is faster. The interesting point is that the "correctness" of the planar approximation formula given by $1-\delta/A_\ell^{\rm sph}$ (for the definition of δ, see the caption of Figure 3.2) is for both large and small planets the same, with a value of about 1% for degree $\ell = 2$ and approaching 100% for the short degrees (with 90% around degree ~ 20). The same derivation can be done taking into account the finite relief of both topography and CMI using equation (2.38) instead of (2.35) (for details see e.g., Tsoulis [1999]).

3.2 Concept of the elastic lithosphere

When the gravity signal above topographic features on the Earth and other planets is examined, it shows that only some portion of it is generated by the mechanism of Airy isostatic compensation [e.g., Frey et al., 1996; Wieczorek and Phillips, 1997; Watts, 2001; McGovern et al., 2002]. The signal is in fact in the majority of cases stronger than predicted using equation (3.17) which (if we assume that the deflection of the CMI is still caused only by surface loading) means that the lithosphere has some resistance to the deformation. This resistance is attributed to the elasticity of the crust and/or the uppermost part of the mantle – the appropriate model therefore appears to be to an elastic plate/shell deflecting beneath the exerted load [cf. Watts, 2001]. When the rheological parameters are known, then the amount of elastic support given by the thickness of such a plate/shell, usually called elastic (lithosphere) thickness D_e, can be determined. For very small values of D_e, the compensation state approaches the Airy isostasy and for large ones there is almost no compensation (see Figure 3.3).

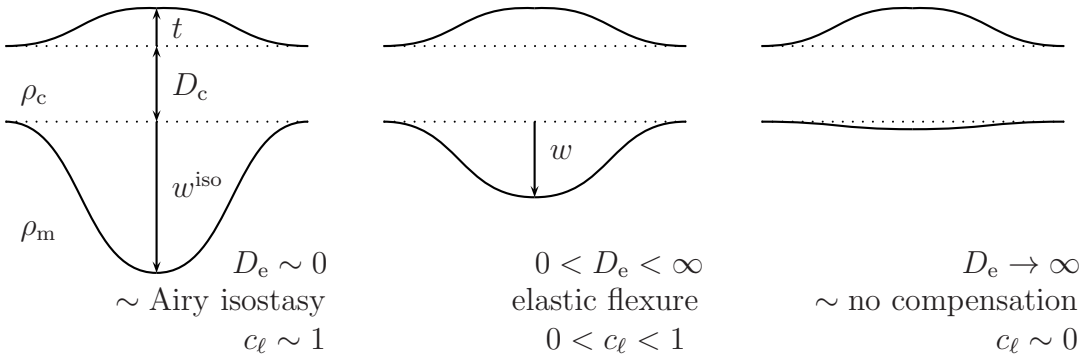

Figure 3.3: *Conceptual sketch of different crustal compensation states depending on the elastic thickness D_e for the same surface load t. If $D_\mathrm{e} > 0$ then the CMI deflection $w < w^\mathrm{iso}$ and the compensation coefficient (see equation (3.34)) $c_\ell < 1$. Note that the load here has the same density as the crust. If these two densities differ then one should take into account the mechanism of loading to adequately estimate the mass of the load.*

Using the compensation models derived later in this chapter, it was found that the deflection of the crust (which depends on the thickness of the supporting elastic layer) varies depending on the age of the loading feature [e.g., Simons et al., 1997; Watts, 2001; McGovern et al., 2002, 2004]. Visco-elasto-plastic models indeed confirmed that the elastic plate "freezes in" its elastic thickness at the time of loading [Albert and Phillips, 2000] which can then be observed by analyzing the gravitational signal of the examined feature. This "formal elastic thickness" depends on the temperature profile across the lithosphere and the rheological parameters of both crust and mantle at the time of loading. Given them and using the yield stress envelope formalism [e.g., McNutt et al., 1988; Watts, 2001] we can compute the stress which can be sustained by the lithosphere before it yields, either by brittle deformation (frictional sliding) or by ductile creep. If the actual stress (here to estimate the

Rheology	B [Pa^{-n} s^{-1}]	n	Q [kJmol^{-1}]	$T(\sigma_y)$ [K]
diabase crust (dry)	1.1×10^{-26}	4.7	488	1029
olivine mantle (dry)	2.4×10^{-16}	3.5	540	1065

Table 3.1: *Rheological parameters used for yield stress envelope calculation of Mercury's elastic lithosphere thickness evolution (see Fig. 3.4)* [Karato et al., 1986; Mackwell et al., 1998]. *For the wet alternatives are (material contains some faction of water) all the parameters different as the water "soften" the material* [cf. Grott and Breuer, 2008].

upper bound the lithostatic pressure $\sigma_{\rm lith}$ is used instead) exceeds any of the critical values of yield brittle stress $\sigma_{\rm B}$ or ductile stress $\sigma_{\rm D}$, the lithosphere beneath this depth does not exhibit elastic behavior anymore. Brittle deformation is considered to be independent of rock type [Byerlee, 1978] and occurs if any of the compressional or extensional stress exceeds the following [e.g., Mueller and Phillips, 1995; Grott and Breuer, 2008]:

$$\sigma_{\rm B}^{\rm ext} = 0.786\sigma_{\rm lith} \qquad \sigma_{\rm lith} \leq 529.9\,{\rm MPa} \tag{3.18}$$

$$\sigma_{\rm B}^{\rm ext} = 56.7\,{\rm MPa} + 0.679\sigma_{\rm lith} \qquad \sigma_{\rm lith} > 529.9\,{\rm MPa} \tag{3.19}$$

$$\sigma_{\rm B}^{\rm comp} = -3.68\sigma_{\rm lith} \qquad \sigma_{\rm lith} \leq 113.2\,{\rm MPa} \tag{3.20}$$

$$\sigma_{\rm B}^{\rm comp} = -176.6\,{\rm MPa} - 2.12\sigma_{\rm lith} \qquad \sigma_{\rm lith} > 113.2\,{\rm MPa}. \tag{3.21}$$

One can see that with increasing lithostatic pressure, the lithosphere becomes more resistant to brittle failure. Contrary to this mechanism, ductile flow depends on the actual rheological parameters of crust/mantle and with increasing temperature (i.e. with the depth below the planetary surface) the strength of the lithosphere $\sigma_{\rm D}$ exponentially decreases according to [e.g., Grott and Breuer, 2008]:

$$\sigma_{\rm D}(T) = \left(\frac{\dot{\varepsilon}}{B}\right)^{1/n} \exp\left(\frac{Q}{nRT}\right), \tag{3.22}$$

where T is temperature, R is the universal gas constant, B, n and Q are the rheological parameters describing behavior of the crust/mantle and $\dot{\varepsilon}$ is the strain rate. Since we do not know the strain rate for the active deformation mechanisms in planetary lithospheres, a typical value of $\dot{\varepsilon} = 10^{-17}$ s^{-1} is assumed [e.g., McGovern et al., 2004; Grott and Breuer, 2008]. To determine the bottom of elastically behaving layer a bounding yield stress must be prescribed, typically taken to be $\sigma_{\rm y} = 15$ MPa [e.g. Burov and Diament, 1995]. Having these parameters for the assumed planetary crust and mantle rheologies (Table 3.1) the critical temperature $T_{\rm y}$ for which $\sigma_{\rm y} = \sigma_{\rm D}$ can be computed using equation (3.22) [Grott and Breuer, 2008]:

$$T_{\rm y}(\sigma_{\rm y}) = \frac{Q}{R}\left[\ln\left(\frac{\sigma_{\rm y}^n B}{\dot{\varepsilon}}\right)\right]^{-1}. \tag{3.23}$$

In Figure 3.4a the yield stress envelopes for three different times are computed, based on the heat flow $q_{\rm s}$ from a parameterized thermal evolution model of Mercury (see Section 4.3) and the rheological parameters listed in Table 3.1. The thermal gradient was assumed

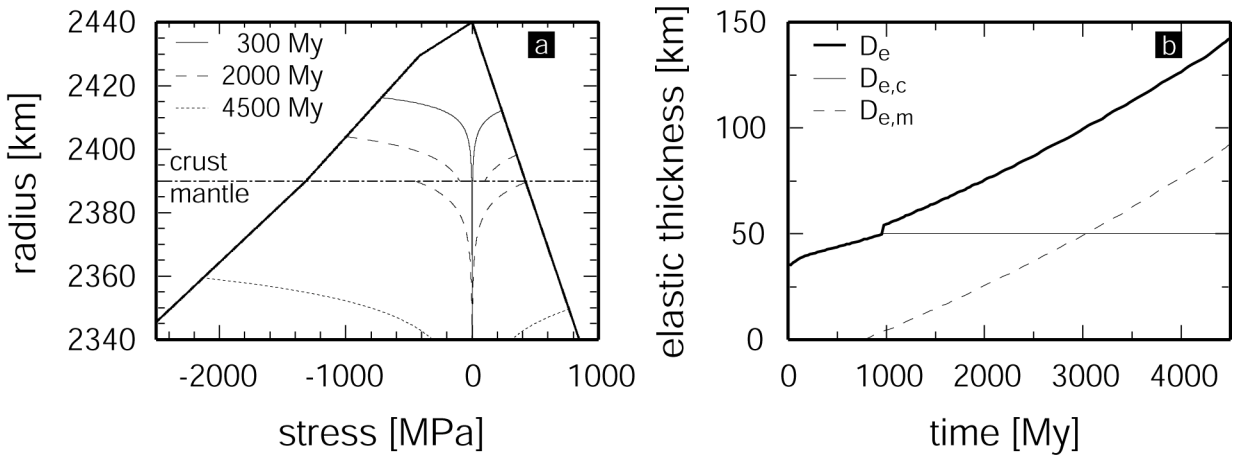

Figure 3.4: *a) Yield stress envelopes for Mercury's lithosphere at times 300 My, 2 Gy and 4.5 Gy, constructed using the heat flow q_s from the parameterized themal evolution model presented in Section 4.3 and the rheological parameters listed in Table 3.1. The thick solid line denotes the brittle yield stress σ_B and the thin lines denote the ductile yield stress σ_D. b) Growth of the elastic thickness D_e based on the yield stress envelope calculations. The crustal elastic thickness $D_{e,c}$ is coincident with D_e until the moment it reaches the whole 50 km around 900 My. The associated jump in D_e is a consequence of the non-zero mantle elastic thickness $D_{e,m}$ at that time (see text for details).*

to be constant with depth, depending only on the thermal conductivity for the crust $k_c = 3\ \mathrm{Wm^{-1}K^{-1}}$ and mantle $k_m = 4\ \mathrm{Wm^{-1}K^{-1}}$. We can see the growth of the elastic lithosphere (i.e. the region bounded by the smaller of the brittle and ductile yield stresses) with time as the planet cools down. As can be seen for the case of 2 Gy, during a certain period of time, the uppermost mantle can withstand higher stresses than the lowermost crust. There is actually a short period of time when the lowermost crust does not behave elastically and the uppermost mantle does [Grott and Breuer, 2008]. This incompetent crust then separates two elastic layers of thicknesses $D_{e,c}$ (for crust) and $D_{e,m}$ (for mantle). The elastic thickness of the whole system can then be computed as [Burov and Diament, 1995]:

$$D_e = (D_{e,c}^3 + D_{e,m}^3)^{1/3}. \tag{3.24}$$

This means that for a situation when $D_{e,m} \ll D_{e,c}$, the resulting elastic thickness $D_e \sim D_{e,c}$ as can be seen for the first 950 My in Figure 3.4b. Then, both separated layers merge into one whose thickness is then the simple sum of the mantle elastic thickness $D_{e,m}$ and the crustal thickness D_c (because the whole crust now behaves elastically):

$$D_e = D_c + D_{e,m}. \tag{3.25}$$

The difference between equation (3.24) and (3.25) causes a jump in the elastic thickness at around 950 My for the given rheological parameters and thermal evolution scenario (for others, this period of rapid elastic thickness growth can differ substantially or not be present at all). Such a rapid increase in the observed elastic thicknesses with time was indeed found for the case of Mars, and its fitting by models based on thermal evolution models provides useful constraints on the rheology of the Martian crust [Grott and Breuer, 2008].

3.3 Elastic shell models

To quantitatively describe the behavior of the elastic lithosphere in the presence of an applied load the basic equations describing the behavior of elastic continuum must be used. For the description of the rheology, in accord with the majority of works, Hooke's law[4] neglecting the thermal dependency is used [Horský et al., 2001]:

$$\boldsymbol{\sigma} = \lambda(\nabla \cdot \boldsymbol{u})\boldsymbol{I} + \mu(\nabla \boldsymbol{u} + \nabla^T \boldsymbol{u}), \tag{3.26}$$

where $\boldsymbol{\sigma}$ is a stress tensor induced by the displacement vector $\boldsymbol{u}$, $\boldsymbol{I}$ is the identity tensor and λ and μ are Lamé coefficients[5] describing the rheology of a given material. An alternative formulation of equation (3.26) employing the bulk modulus (incompressibility coefficient) K is often used:

$$K = \lambda + \frac{2}{3}\mu, \tag{3.27}$$

$$\boldsymbol{\sigma} = K(\nabla \cdot \boldsymbol{u})\boldsymbol{I} + \mu\left(\nabla \boldsymbol{u} + \nabla^T \boldsymbol{u} - \frac{2}{3}(\nabla \cdot \boldsymbol{u})\boldsymbol{I}\right), \tag{3.28}$$

Equation (3.28) must be combined with the continuity equation [e.g., Horský et al., 2001]:

$$\nabla \cdot \boldsymbol{u} + \frac{p}{K} = 0, \tag{3.29}$$

where p is the deviation from the pressure p_0 of the radially symmetric body. The last of the governing equations is the equation of motion which relates the changes in the stress to the body forces vector $\boldsymbol{f}$ [e.g., Horský et al., 2001]:

$$\nabla \cdot \boldsymbol{\sigma} + \boldsymbol{f} = 0. \tag{3.30}$$

For the incompressible case which is sometimes considered as an approximation for the elastic lithospheres in planetary sciences [e.g., Zhong, 2002] the equations (3.28)–(3.30) can be rewritten in the following form:

$$-p\boldsymbol{I} + \mu(\nabla \boldsymbol{u} + \nabla^T \boldsymbol{u}) = \boldsymbol{\sigma}, \tag{3.31}$$

$$\nabla \cdot \boldsymbol{u} = 0, \tag{3.32}$$

$$\nabla \cdot \boldsymbol{\sigma} + \boldsymbol{f} = 0. \tag{3.33}$$

Equations (3.31)–(3.33) have to be considered together with the boundary conditions (BC) applicable to the studied situation (e.g., top load consisting of the surface topography or bottom load by stress generated dynamically in the planetary interior). Additionally, if applicable, self-gravitation can be considered, which describes the change of the elastic shell response caused by the gravity associated with mass heterogeneities induced by this response [e.g. Zhong, 2002].

[4]Named after Robert Hooke (18th July 1635–3rd March 1703), English physicist, biologist (first observation of a cell), chemist, architect and Surveyor to the City of London.

[5]Named after Gabriel Lamé (22th July 1795–1st May 1870), French mathematician, who also worked on many engineering problems (e.g. work on the design of bridges brought him to the study of elasticity).

3.3.1 Thin elastic shell approximation

In most applications of elastic lithosphere modeling [e.g., Simons et al., 1997; McGovern et al., 2002, 2004; Belleguic et al., 2005] it is sufficient to consider a thin elastic shell approximation. This model has a great advantage compared to other approaches since it allows the evaluation of the response of an elastic shell of constant thickness to an exerted load using relatively simple analytical formula [cf. Turcotte et al., 1981]. It starts with the governing equations for elastic continuum (3.28)–(3.30) and adopts several assumptions that later allows the integration of the load-generated stress across the thickness of the assumed elastic layer and approximate it with an infinitely thin layer of corresponding rigidity (for details see Kraus [1967] and Beuthe [2008]). The resulting formula can then be transformed to the spectral domain using the spherical harmonic formalism in the form of only the degree dependent compensation coefficient c_ℓ [Turcotte et al., 1981]:

$$c_\ell = \frac{w_{\ell m}}{w_{\ell m}^{\mathrm{iso}}} \qquad \text{where } w_\ell^{\mathrm{iso}} \text{ is the isostatic deflection – see (3.9)} \tag{3.34}$$

$$c_\ell = \frac{1 - f_{\mathrm{self}}}{(\sigma f_1 + \tau f_2)/f_3 + 1 - f_{\mathrm{self}}}, \tag{3.35}$$

where the self-gravitational term f_{self} and terms f_1, f_2, f_3 are defined as follows:

$$f_{\mathrm{self}} = \frac{3\rho_{\mathrm{m}}}{(2\ell+1)\bar{\rho}}, \tag{3.36}$$

$$f_1 = \ell^3(\ell+1)^3 - 4\ell^2(\ell+1)^2, \tag{3.37}$$

$$f_2 = \ell(\ell+1) - 2, \tag{3.38}$$

$$f_3 = \ell(\ell+1) - (1-\nu), \tag{3.39}$$

with ρ_{m} denoting the mantle density and $\bar{\rho}$ the mean planetary density. The dimensionless parameters τ (the shell rigidity) and σ (the bending rigidity) could be calculated from the following expressions:

$$\tau = \frac{E D_{\mathrm{e}}}{R_0^2 g_0 (\rho_{\mathrm{m}} - \rho_{\mathrm{c}})}, \tag{3.40}$$

$$\sigma = \frac{\tau}{12(1-\nu^2)} \left(\frac{D_{\mathrm{e}}}{R_0} \right)^2, \tag{3.41}$$

where R_0 stands for mean radius of the planetary surface, g_0 is the mean gravitational acceleration, ρ_{c} the crustal thickness and D_{e} the elastic thickness. Young's modulus[6] E and Poisson's ratio ν of the modeled elastic lithosphere relates to the Lamé coefficient μ (shear modulus) and incompressibility K in the following way [e.g., Horský et al., 2001; Turcotte and Schubert, 2002]:

$$E = \frac{9K\mu}{3K+\mu} \qquad \nu = \frac{3K - 2\mu}{2(3K+\mu)}, \tag{3.42}$$

$$\mu = \frac{E}{2(1+\nu)} \qquad K = \frac{E}{3(1-2\nu)}. \tag{3.43}$$

[6]Named after Thomas Young (13th June 1773 –10th May 1829), English physicist, physiologist (developed the theory of physiological optics) and one of the first decipherers of the Egyptian hieroglyphs.

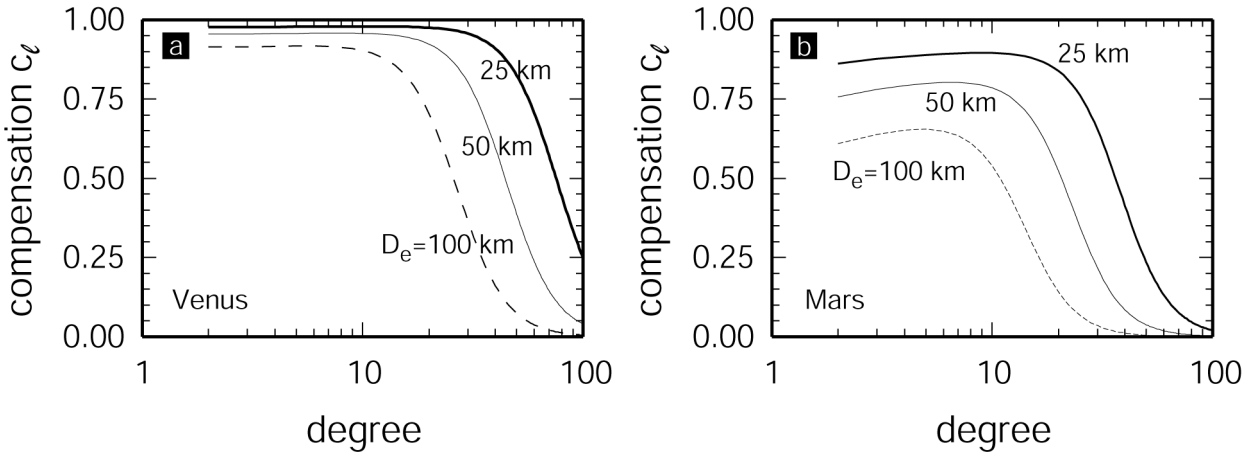

Figure 3.5: *a) Degree compensation coefficient c_ℓ as defined by equation (3.35) for Venus and three elastic thicknesses $D_e = 25, 50, 100$ km. b) The same but for Mars.*

One should note, however, that the self-gravitation term in the equation (3.35) is just a first approximation of this factor. In handling the self-gravitation influence on the amount of exerted load correctly, one arrives at the following equation for applied pressure p caused by the surface load of height t (for the case where the load density is equal to the crustal density ρ_c) [Belleguic et al., 2005]:

$$p = -\rho_c U\Big|_{R_0+t} - (\rho_m - \rho_c)U\Big|_{R_0-D_c-w} \tag{3.44}$$

Using a linear approximation to evaluate the geopotential relative to the values corresponding to the mean surface radius U_s and bottom of the crust U_c gives [Belleguic et al., 2005]:

$$p = -\rho_c\left(U_s + t\frac{\mathrm{d}U}{\mathrm{d}r}\right) - (\rho_m - \rho_c)\left(U_c - w\frac{\mathrm{d}U}{\mathrm{d}r}\right), \tag{3.45}$$

$$p = -\rho_c(h^s g_0 - t g_0) - (\rho_m - \rho_c)(h^c g_0 - w g_0), \tag{3.46}$$

$$p = g_0[\rho_c(t - h^s) - (\rho_m - \rho_c)(w + h^c)], \tag{3.47}$$

$$p \doteq g_0[\rho_c t - \rho_m h^s - (\rho_m - \rho_c)w], \tag{3.48}$$

where the Bruns formula (2.19) was used with the gravitational acceleration g_0 through the whole lithosphere considered to be constant (i.e. $U_s = h^s g_0$ and $U_c = h^c g_0$), assuming also $\mathrm{d}U/\mathrm{d}r$ through the whole lithosphere to be equivalent to $-g_0$ and in the last step (which is equal to equation (3) in Turcotte et al. [1981]) the geoid undulations at the level of CMI were approximated by the value of the surface geoid anomaly $h^c \doteq h^s$.

In Figure 3.5 the compensation coefficient c_ℓ for different elastic thicknesses D_e is computed for Venus (a) and Mars (b), the parameters used in equations (3.35)–(3.41) being listed in Table 3.2. The most obvious feature is that the compensation level for the same harmonic degree ℓ and same elastic thickness differs substantially for each planet. Whereas for Venus even 100 km thick elastic lithosphere does not influence the compensation for $\ell < 10$ by more than 10%, for Mars a 50 km thick elastic lithosphere at this spectral range

Parameter	**Symbol**	**Value**	**Unit**
Young's modulus	E	1×10^{11}	Pas
Poisson's ratio	ν	0.25	–
surface density	ρ_{s}	2900	kgm^{-3}
mantle density of Venus	$\rho_{\mathrm{m}}^{\mathrm{V}}$	3300	kgm^{-3}
mantle density of Mars	$\rho_{\mathrm{m}}^{\mathrm{M}}$	3500	kgm^{-3}
mean density of Venus	$\bar{\rho}^{\mathrm{V}}$	5245	kgm^{-3}
mean density of Mars	$\bar{\rho}^{\mathrm{M}}$	3933	kgm^{-3}
surface radius of Venus	R^{V}	6051.9×10^3	m
surface radius of Mars	R^{M}	3389.5×10^3	m

Table 3.2: *Parameters used for the modeling of the compensation coefficient c_ℓ for Venus and Mars using the thin elastic shell approximation (equation 3.35).*

supports about 20% of the load by its own rigidity. Moreover, for Mars the compensation coefficients for thick elastic lithosphere $D_{\mathrm{e}} > 50$ km approach 0 (i.e. almost no crustal compensation of the surface topography features) already for degrees $\ell \sim 40$ and lower, as compared to Venus where the elastic thickness should be ~ 100 km for c_ℓ to reach a value around 0 before degree 100.

The resulting gravitational signal induced by the surface topography, represented by the spherical harmonic coefficients $t_{\ell m}$, which is compensated by the local crustal variations in the presence of the elastic lithosphere of thickness D_{e}, can be modeled using the equations (3.15), (3.34) and (3.9):

$$w_{\ell m} = c_\ell(D_{\mathrm{e}}) \frac{\rho_c}{\rho_m - \rho_c} \left(\frac{R_0}{R_0 - D_{\mathrm{c}}} \right)^2 t_{\ell m}, \tag{3.49}$$

$$U_{\ell m} = \frac{4\pi G R_0}{2\ell + 1} \left[1 - c_\ell(D_{\mathrm{e}}) \left(\frac{R - D_{\mathrm{c}}}{R} \right)^\ell \right] t_{\ell m}. \tag{3.50}$$

which is a result formally very similar to equation (3.17) for the signal associated with the Airy compensated topography. And indeed, if $D_{\mathrm{e}} = 0$, then both σ and τ are zero as well and equation (3.50) transforms to equation (3.17).

In some works the thin elastic shell model (or some other one adapted to the spherical geometry) is not used, but instead a planar model of an elastic plate is employed [cf. Watts, 2001; Turcotte and Schubert, 2002]. However, such a model has a substantial limitation since it cannot address the membrane stress which is a generic property of the spherical shell. Therefore, it is suitable mainly for the investigation of regions with a relatively thin elastic lithosphere in the case of large planets (Venus, Earth) [Turcotte et al., 1981]. On the other hand, in such a situation, it can be adapted to a variety of more complicated cases that cannot be addressed by the thin elastic shell model, such as a broken elastic plate or subducting tectonic plate, which due to the bending, changes its characteristic elastic behavior [e.g., Watts, 2001].

3.3.2 Thick elastic shell model

The thin elastic shell approximation described above has, however, several disadvantages. Firstly, the results are not sensitive to the crustal thickness D_c which determines the reference radius of the second load on which the associated membrane stress depends. Secondly, it does not take into account the internal density inhomogeneities in the lithosphere caused by the compression (for $\nu < 0.5$) in computing the applied load and therefore it does not allow this factor to be included for the gravity computation (for this, the problems of subsurface loading [e.g., Forsyth, 1985; Belleguic et al., 2005] are related). Furthermore, it cannot accommodate tangential force resulting from mantle flow. Therefore, the more appropriate model of a thick elastic shell is needed [e.g., Janes and Melosh, 1990; Reindler and Arkani-Hamed, 2003].

To do this, the set of equations (3.28)–(3.30) (or the equations (3.31)–(3.33) for the incompressible case) must be supplied with the appropriate BC. For the top loaded elastic lithosphere (topography loading) we require the traction vector $\boldsymbol{s} = \boldsymbol{\sigma} \cdot \boldsymbol{e}_r$ to be zero at the bottom of the lithosphere (stresses from the exerted load are on this boundary already fully relaxed):

$$\boldsymbol{\sigma} \cdot \boldsymbol{e}_r = 0 \tag{3.51}$$

and at the surface the tangential component of $\boldsymbol{s}$ to be also zero (because of no applied tangential loads) and the radial component of $\boldsymbol{s}$ to be equal to the lithostatic pressure induced by the topography t:

$$\boldsymbol{\sigma} \cdot \boldsymbol{e}_r - [(\boldsymbol{\sigma} \cdot \boldsymbol{e}_r) \cdot \boldsymbol{e}_r]\, \boldsymbol{e}_r = 0, \tag{3.52}$$

$$(\boldsymbol{\sigma} \cdot \boldsymbol{e}_r) \cdot \boldsymbol{e}_r = -t\rho_c g_0. \tag{3.53}$$

Note, that in the equation (3.53) the load has implicitly the density equal to the crustal density ρ_c. If this was not the case, and the load density ρ_l differs, then another version of this equation must be used since the subsided load infills the surface deflection of the original crust (see Figure 3.6) [e.g., Belleguic et al., 2005]. Therefore, we obtain:

$$[(\boldsymbol{\sigma} \cdot \boldsymbol{e}_r) \cdot \boldsymbol{e}_r]\, \boldsymbol{e}_r = [t\rho_l - \boldsymbol{u} \cdot \boldsymbol{e}_r(\rho_l - \rho_c)]\boldsymbol{g}. \tag{3.54}$$

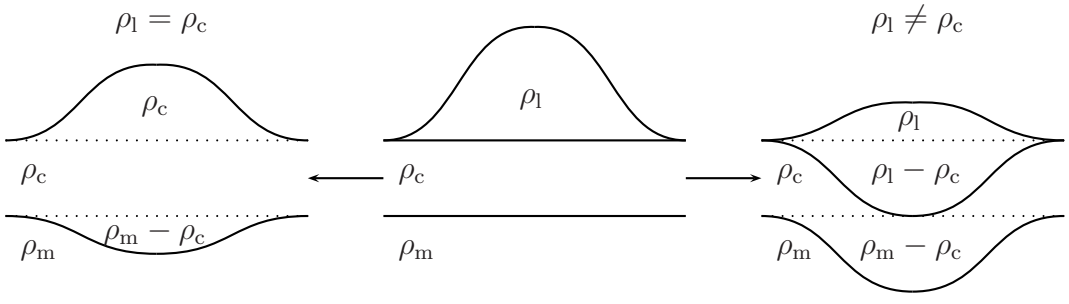

Figure 3.6: *Conceptual sketch of elastic compensation for features with a load density ρ_l equal and different to the crustal density ρ_c – the load consists of the product of deflection amplitude and density anomaly.*

This brings us to the evaluation of the body forces vector $\boldsymbol{f}$ (which again expresses only the deviations from the spherically symmetric state). In the case of an incompressible lithosphere and when no subsurface loads are considered, then the only contribution to $\boldsymbol{f}$ consists of the CMI deflection located at the radius r_{cmi} and the associated buoyancy given by the density contrast between the mantle and crust $\rho_{\mathrm{m}} - \rho_{\mathrm{c}}$:

$$\boldsymbol{f}_{\mathrm{cmi}} = \boldsymbol{g}(\rho_{\mathrm{m}} - \rho_{\mathrm{c}})\boldsymbol{u} \cdot \boldsymbol{e}_{\mathrm{r}}\delta(r - r_{\mathrm{cmi}}). \tag{3.55}$$

If, on the other hand, the elastic lithosphere is considered compressible, an additional contribution describing the effect of the crustal/mantle density inhomogeneities $\delta\rho = \rho - \rho_{\mathrm{c/m}}$ caused by the compression must be added to the internal forces vector $\boldsymbol{f} = \boldsymbol{f}_{\mathrm{cmi}} + \boldsymbol{f}_{\mathrm{K}}$:

$$\boldsymbol{f}_{\mathrm{K}} = \delta\rho\, \boldsymbol{g} = \frac{p}{K}\rho_{\mathrm{c/m}}\boldsymbol{g}, \tag{3.56}$$

where p is the pressure deviation. In addition to this density change, a subsurface loading that acts in a similar manner can be considered. Such a load can e.g., come from a magmatic intrusion in the crust below the surface or consists of extinct magma chamber beneath the crust. In such a case, when we approximate this load by a constant density deviation $\delta\rho_{\mathrm{ss}}$, then the equation (3.56) has to be changed in the following manner:

$$\boldsymbol{f}_{\mathrm{K}} = \left[\frac{p}{K}\rho_{\mathrm{c/m}} + \delta\rho_{\mathrm{ss}}\right]\boldsymbol{g}. \tag{3.57}$$

If the self-gravitation effect is not taken into account, then the gravitational acceleration is assumed to be constant through the whole elastic lithosphere $\boldsymbol{g} = -g_0\boldsymbol{e}_{\mathrm{r}}$. If, on the other hand, we do consider this effect, then the appropriate changes should be applied to all the equations containing this term i.e. to BC and the definition of $\boldsymbol{f}$. In that case, the surface topography has to be referenced to the geoid height h^{s} (see equation (2.19)) instead to the reference radius R_0. More details on a solution with self-gravitation terms included could be found in e.g. Turcotte et al. [1981]. In following text we will deal the body forces vector as $\boldsymbol{f} = \boldsymbol{f}_{\mathrm{cmi}} + \boldsymbol{f}_{\mathrm{K}}$.

The above listed equations describing the behavior of the elastic continuum must now be solved. Since they should describe the behavior of an elastic spherical shell, this will be done in a full spherical geometry using the spherical harmonic expansion approach (see Section A.1). The parameters K, μ and ρ_0 are considered to be only radially dependent. The equation of continuity then reads as [e.g., Čadek, 1989; Matas, 1995]:

$$\sqrt{\frac{\ell}{2\ell+1}}\left(\frac{\mathrm{d}}{\mathrm{d}r} - \frac{\ell+1}{r}\right)u_{\ell m}^{\ell-1}(r) - \sqrt{\frac{\ell+1}{2\ell+1}}\left(\frac{\mathrm{d}}{\mathrm{d}r} + \frac{\ell+2}{r}\right)u_{\ell m}^{\ell+1}(r) + \frac{1}{K(r)}\frac{\sigma_{\ell m}^{\ell 0}(r)}{\sqrt{3}} = 0. \tag{3.58}$$

Next, the constitutive relation is considered. Since there are no lateral variations in the rheological parameters in our model, only the symmetric part of the stress tensor deviator (described by terms $\sigma^{\ell,0}$, $\sigma^{\ell,2}$, $\sigma^{\ell-2,2}$ and $\sigma^{\ell+2,2}$) is nonzero [e.g., Matas, 1995]. The same is true for the spheroidal part of the displacement vector described by terms $u_{\ell m}^{\ell-1}$ and $u_{\ell m}^{\ell-1}$, whereas the toroidal part is zero. Therefore, the rheological equation can be rewritten as

the following three equations:

$$\sigma_{\ell m}^{\ell-2,2}(r) - 2\mu\sqrt{\frac{\ell-1}{2\ell-1}}\left(\frac{\mathrm{d}}{\mathrm{d}r}+\frac{\ell}{r}\right)u_{\ell m}^{\ell-1}(r) = 0, \tag{3.59}$$

$$\begin{aligned}\sigma_{\ell m}^{\ell 2}(r) + 2\mu\sqrt{\frac{(\ell+1)(2\ell+3)}{6(2\ell-1)(2\ell+1)}}\left(\frac{\mathrm{d}}{\mathrm{d}r}-\frac{\ell-1}{r}\right)u_{\ell m}^{\ell-1}(r) &- \\ -2\mu\sqrt{\frac{\ell(2\ell-1)}{6(2\ell+3)(2\ell+1)}}\left(\frac{\mathrm{d}}{\mathrm{d}r}+\frac{\ell+2}{r}\right)u_{\ell m}^{\ell+1}(r) &= 0,\end{aligned} \tag{3.60}$$

$$\sigma_{\ell m}^{\ell+2,2}(r) + 2\mu\sqrt{\frac{\ell+2}{2\ell+3}}\left(\frac{\mathrm{d}}{\mathrm{d}r}-\frac{\ell+1}{r}\right)u_{\ell m}^{\ell+1}(r) = 0. \tag{3.61}$$

The equation of motion can now be written as the following two equations:

$$\begin{aligned}-\sqrt{\frac{\ell}{3(2\ell+1)}}\left(\frac{\mathrm{d}}{\mathrm{d}r}+\frac{\ell+1}{r}\right)\sigma_{\ell m}^{\ell,0}(r) + \sqrt{\frac{\ell-1}{2\ell-1}}\left(\frac{\mathrm{d}}{\mathrm{d}r}-\frac{\ell-2}{r}\right)\sigma_{\ell,m}^{\ell-2,2}(r) &- \\ -\sqrt{\frac{(\ell+1)(2\ell+3)}{6(2\ell-1)(2\ell+1)}}\left(\frac{\mathrm{d}}{\mathrm{d}r}+\frac{\ell+1}{r}\right)\sigma_{\ell m}^{\ell,2}(r) &= -f_{\ell m}^{\ell-1}(r),\end{aligned} \tag{3.62}$$

$$\begin{aligned}\sqrt{\frac{\ell+1}{3(2\ell+1)}}\left(\frac{\mathrm{d}}{\mathrm{d}r}-\frac{\ell}{r}\right)\sigma_{\ell m}^{\ell,0}(r) + \sqrt{\frac{\ell(2\ell-1)}{6(2\ell+3)(2\ell+1)}}\left(\frac{\mathrm{d}}{\mathrm{d}r}-\frac{\ell}{r}\right)\sigma_{\ell m}^{\ell,2}(r) &- \\ -\sqrt{\frac{\ell+2}{2\ell+3}}\left(\frac{\mathrm{d}}{\mathrm{d}r}+\frac{\ell+3}{r}\right)\sigma_{\ell,m}^{\ell+2,2}(r) &= -f_{\ell m}^{\ell+1}(r).\end{aligned} \tag{3.63}$$

The body forces vector $\boldsymbol{f}$ components for the compressible shell with no subsurface loads, but with the crust-mantle interface at radius r_{cmi}, are given by:

$$\begin{aligned}f_{\ell m}^{\ell-1}(r) &= \delta(r-r_{\mathrm{cmi}})(\rho_{\mathrm{m}}-\rho_{\mathrm{c}})g_0\left(-\frac{\ell}{2\ell+1}u_{\ell m}^{\ell-1}(r)+\sqrt{\frac{\ell(\ell+1)}{2\ell+1}}u_{\ell m}^{\ell+1}(r)\right) - \\ &- \frac{\rho_{c/m}(r)}{K(r)}g_0\sqrt{\frac{\ell}{3(2\ell+1)}}\sigma_{\ell m}^{\ell 0} - \sqrt{\frac{\ell}{2\ell+1}}\rho_{\ell m}g_0,\end{aligned} \tag{3.64}$$

$$\begin{aligned}f_{\ell m}^{\ell+1}(r) &= \delta(r-r_{\mathrm{cmi}})(\rho_{\mathrm{m}}-\rho_{\mathrm{c}})g_0\left(\sqrt{\frac{\ell(\ell+1)}{2\ell+1}}u_{\ell m}^{\ell-1}(r)-\frac{\ell+1}{2\ell+1}u_{\ell m}^{\ell+1}(r)\right) + \\ &+ \frac{\rho_{c/m}(r)}{K(r)}g_0\sqrt{\frac{\ell+1}{3(2\ell+1)}}\sigma_{\ell m}^{\ell 0} + \sqrt{\frac{\ell+1}{2\ell+1}}\rho_{\ell m}g_0.\end{aligned} \tag{3.65}$$

Finally, we rewrite the BC equations (3.52) and (3.53) – for details please see Appendix A). We start with the top boundary, as it is somewhat more complicated to describe. Equation (A.34) consists of two terms for $\boldsymbol{Y}^{\ell-1}$ and $\boldsymbol{Y}^{\ell+1}$, however to handle only one of them is sufficient because the spheroidal problem is described by only one tangential component of

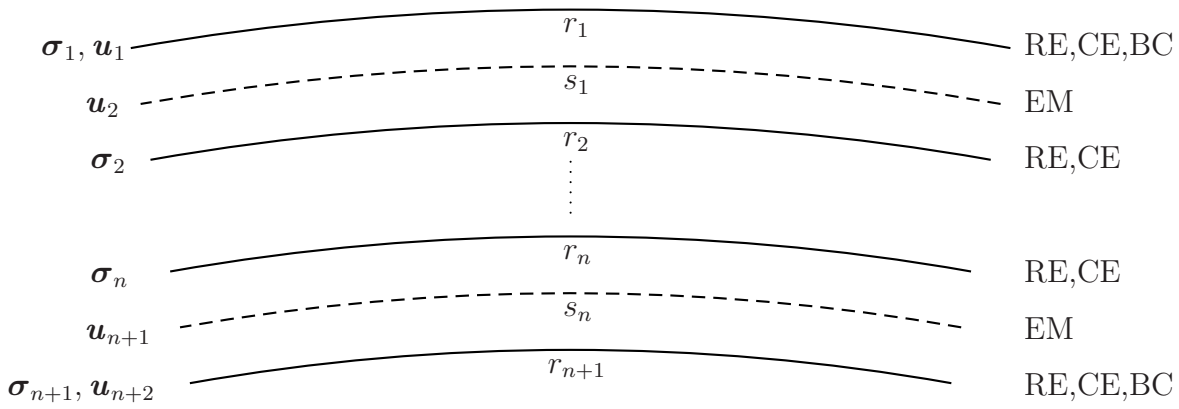

Figure 3.7: *Computational scheme for the thick elastic shell model. The shell, defined by the outer (R_0) and inner ($R_0 - D_\mathrm{e}$) radii, is divided into n layers. For each layer the components of the stress tensor $\boldsymbol{\sigma}$ and displacement vector $\boldsymbol{u}$ are evaluated (at its boundaries and in its middle, respectively). This is done using the rheological equation (RE), constitutional equation (CE), equation of motion (EM) and at the upper and lower boundary the boundary conditions (BC).*

traction. Since we are considering a vector field $\boldsymbol{\sigma} \cdot \boldsymbol{e}_\mathrm{r}$ which is defined by two components, only one additional equation is needed. This can be taken from (A.31):

$$\sqrt{\frac{\ell-1}{2\ell-1}}\sigma_{\ell m}^{\ell-2,2} - \sqrt{\frac{(\ell+1)(2\ell+3)}{6(2\ell+1)(2\ell-1)}}\sigma_{\ell m}^{\ell,2} - \sqrt{\frac{\ell}{3(2\ell+1)}}\sigma_{\ell m}^{\ell,0} = t_{\ell m}\rho_\mathrm{c} g_0 \sqrt{\frac{\ell}{2\ell+1}} \quad (3.66)$$

$$\frac{\ell+1}{2\ell+1}\sqrt{\frac{\ell-1}{2\ell-1}}\sigma_{\ell m}^{\ell-2,2}(r) - \frac{1}{2\ell+1}\sqrt{\frac{\ell(\ell+1)(\ell+2)}{2\ell+3}}\sigma_{\ell m}^{\ell+2,2}(r) - \\ -\sqrt{\frac{3(\ell+1)}{2(2\ell-1)(2\ell+1)(2\ell+3)}}\sigma_{\ell m}^{\ell,2}(r) = 0. \quad (3.67)$$

Considering the lower boundary we can apply the same equations since the constraints are placed on the stress as well, hence only equation (3.66) has to equal to zero.

The last step is to employ the discretization in radius. For that, a finite difference method (see Appendix B) can be used, together with the alternating scheme to increase the stability of the solution [e.g., Kývalová, 1994]. The shell is therefore divided into n layers with a thickness d (bounded by $n+1$ boundaries) in which the governing equations are evaluated. At the boundaries of the layers with radii r_i, the stress tensor $\boldsymbol{\sigma}$ components are defined and in the middle of each layer with radius s_i, the displacement vector $\boldsymbol{u}$ components are defined. The density ρ and rheological parameters K and μ are prescribed for each layer. The BC must also be evaluated at the upper and lower boundary, which means that the displacement vector must also be defined here. The organization of the computational scheme is shown in Figure 3.7. Finally, we have $6n+8$ unknowns and the same number of equations. As they are all m independent, they can be solved for only degree ℓ and this solution can be applied

to all coefficients of the given degree. Therefore, we can write using the matrix notation:

$$\boldsymbol{A}(\ell) \cdot \boldsymbol{x}(\ell) = \boldsymbol{y}(\ell) \tag{3.68}$$

where $\boldsymbol{x}$ is the matrix of unknowns ($\sigma_i^{\ell,0}$, $\sigma_i^{\ell,2}$, $\sigma_i^{\ell-2,2}$, $\sigma_i^{\ell+2,2}$, $u_i^{\ell-1}$ and $u_i^{\ell+1}$), $\boldsymbol{A}$ is a set of coefficients forming the LHS parts of the equations, together with the unknowns, and $\boldsymbol{y}$ is the vector of the RHS consisting of the internal force vector components and the surface topography load. Arranging the elements of matrix $\boldsymbol{A}$ appropriately, we arrive at the band matrix which is easy and fast to invert, thus by the product with $\boldsymbol{y}$ obtaining the solution of $\boldsymbol{x}$.

3.4 Dynamic compensation with a viscous shell

In the case of a viscous shell, the governing equations are of the same kind as for the previous case of the thick elastic shell: equation of motion, continuity equation and rheological equation [e.g., Hager and Clayton, 1989; Čadek and Fleitout, 1999; Matyska, 2005]. Their incompressible forms will be here employed as an approximation for the mantle convecting material. It has been shown that such a simplification can have an impact on predicted quantities such as dynamically generated gravity or surface topography [e.g., Forte and Peltier, 1991; Defraigne et al., 1996], however the influence of compressibility is even for the Earth (which is of the terrestrial planets the biggest one) rather minor, thus this assumption is widely used [e.g. Richards and Hager, 1984; Čadek and Fleitout, 2003; Hüttig and Stemmer, 2008]. For other planets where there are still large uncertainties about their exact internal structure, such a simplification is acceptable [e.g., Spohn et al., 2001a; Zhong, 2002]. The rheology thus simplifies and can be described only by the dynamic viscosity η:

$$\nabla \cdot \boldsymbol{\sigma} + \boldsymbol{f} = 0, \tag{3.69}$$

$$\nabla \cdot \boldsymbol{v} = 0, \tag{3.70}$$

$$-p\boldsymbol{I} + \eta(\nabla \boldsymbol{v} + \nabla^T \boldsymbol{v}) = \boldsymbol{\sigma}, \tag{3.71}$$

where $\boldsymbol{\sigma}$ is the stress tensor, $\boldsymbol{f}$ is the buoyancy force vector driving the mantle flow, $\boldsymbol{v}$ is the velocity of flow and p is the pressure deviation.

As the boundary conditions (BC) at both the upper and lower shell's surfaces are usually prescribed a zero vertical velocity (i.e. no mass flux through these boundaries) and a free slip (i.e. zero tangential stresses) [e.g., Čížková, 1996; Tosi, 2008]:

$$\boldsymbol{v} \cdot \boldsymbol{e}_\mathrm{r} = 0, \tag{3.72}$$

$$\boldsymbol{\sigma} \cdot \boldsymbol{e}_\mathrm{r} - [(\boldsymbol{\sigma} \cdot \boldsymbol{e}_\mathrm{r}) \cdot \boldsymbol{e}_\mathrm{r}]\, \boldsymbol{e}_\mathrm{r} = 0. \tag{3.73}$$

Equation (3.73) can be rewritten using the traction vector $\boldsymbol{s} = \boldsymbol{\sigma} \cdot \boldsymbol{e}_\mathrm{r}$. Its radial component is then not forced to be zero and can be interpreted in terms of dynamically generated topography t associated with the density change $\Delta\rho$, whose pressure balances the dynamically generated stress (formally the same situation as in the case presented in the previous section, where surface topography generates the stress exerted on the elastic shell, however in reverse sense):

$$t = \frac{\boldsymbol{s} \cdot \boldsymbol{e}_\mathrm{r}}{g\Delta\rho}. \tag{3.74}$$

This relationship is valid for both the upper boundary (i.e. the surface with the density contrast $\Delta\rho = \rho_{\mathrm{m}}$ since the thickness of the crust is negligible compared to the thickness of the mantle) and the lower one (i.e. the CMB with the density contrast $\Delta\rho = \rho_{\mathrm{core}} - \rho_{\mathrm{m}}$). The internal force $\boldsymbol{f}$ in the absence of phase transitions (which are important in the Earth's mantle dynamics [e.g., Čadek and Fleitout, 1999] and could also have some importance for the lower mantle of Mars dynamics [e.g., Weinstein, 1995; Breuer et al., 1998]) can be expressed as only the buoyant force caused by the local density deviation $\delta\rho$:

$$\boldsymbol{f} = \delta\rho\, \boldsymbol{g}. \tag{3.75}$$

Using the spherical harmonic formalism, the above stated equations can be again rewritten. The results for the case of only radially changing viscosity $\eta = \eta(r)$, which is considered here, are however very similar to the ones obtained in the previous section, only writing instead of the displacement vector $\boldsymbol{u}$ the velocity vector $\boldsymbol{v}$. In addition, the equation of continuity (3.58) in the viscous case does not have the compressibility term and the rheological equation (3.59)–(3.61) uses instead of the shear modulus μ the dynamic viscosity η. The components of the internal force vector $\boldsymbol{f}$ are therefore:

$$f_{\ell m}^{\ell-1}(r) = -\rho_{\ell m} g_0 \sqrt{\frac{\ell}{2\ell+1}}, \tag{3.76}$$

$$f_{\ell m}^{\ell+1}(r) = \rho_{\ell m} g_0 \sqrt{\frac{\ell+1}{2\ell+1}}. \tag{3.77}$$

The equations of BC (3.72) and (3.73) can then be rewritten as:

$$\sqrt{\ell}\, v_{\ell m}^{\ell-1}(r) - \sqrt{\ell+1}\, v_{\ell m}^{\ell+1}(r) = 0, \tag{3.78}$$

$$\frac{\ell+1}{2\ell+1}\sqrt{\frac{\ell-1}{2\ell-1}}\sigma_{\ell m}^{\ell-2,2}(r) - \frac{1}{2\ell+1}\sqrt{\frac{\ell(\ell+1)(\ell+2)}{2\ell+3}}\sigma_{\ell m}^{\ell+2,2}(r) - \\ -\sqrt{\frac{3(\ell+1)}{2(2\ell-1)(2\ell+1)(2\ell+3)}}\sigma_{\ell m}^{\ell,2}(r) = 0. \tag{3.79}$$

The dynamic topography at the surface t^{s} and CMB t^{cmb} can now be evaluated as:

$$t_{\ell m}^{\mathrm{s}} = -\frac{1}{\rho_{\mathrm{m}} g_0}\left(\frac{1}{\sqrt{3}}\sigma_{\ell m}^{\ell,0} - \sqrt{\frac{\ell(\ell-1)}{(2\ell+1)(2\ell-1)}}\sigma_{\ell m}^{\ell-2,2} - \right. \\ \left. - \sqrt{\frac{(\ell+1)(\ell+2)}{(2\ell+1)(2\ell+3)}}\sigma_{\ell m}^{\ell+2,2} + \sqrt{\frac{2\ell(\ell+1)}{3(2\ell-1)(2\ell+3)}}\sigma_{\ell m}^{\ell,2}\right), \tag{3.80}$$

$$t_{\ell m}^{\mathrm{cmb}} = -\frac{1}{(\rho_{\mathrm{core}} - \rho_{\mathrm{m}}) g_0}\left(\frac{1}{\sqrt{3}}\sigma_{\ell m}^{\ell,0} - \sqrt{\frac{\ell(\ell-1)}{(2\ell+1)(2\ell-1)}}\sigma_{\ell m}^{\ell-2,2} - \right. \\ \left. - \sqrt{\frac{(\ell+1)(\ell+2)}{(2\ell+1)(2\ell+3)}}\sigma_{\ell m}^{\ell+2,2} + \sqrt{\frac{2\ell(\ell+1)}{3(2\ell-1)(2\ell+3)}}\sigma_{\ell m}^{\ell,2}\right). \tag{3.81}$$

Finally, the radial discretization is done again in the same way as for the thick elastic shell model (see Subsection 3.3 and Figure 3.7). Also, the solution of the unknown parameters is obtained as in the previous case.

In Figure 3.8 the dynamic contributions to geoid, surface and CMB topography of Venus from loads at different depths across the mantle in the form of the response functions $h_\ell(r)$, $t_\ell^{\mathrm{s}}(r)$ and $t_\ell^{\mathrm{cmb}}(r)$ for various degrees are shown. The actual amplitudes depend on the thickness of the discretization layer dr, however, the curves' characteristics remain the same. In the left column the isoviscous case is investigated. The results do not depend on the viscosity η absolute value, but it can be shown that it is sensitive to its relative change with depth. The geoid contributions show behavior similar to the skin-effect, when with decreasing wavelength it is less sensitive to the deep perturbations and also the resulting amplitude is smaller. Both the surface and CMB topography contributions increase as the distance of perturbation is getting closer to the respective boundary. However, because all the other planets, except the Earth, are most probably in a so-called stagnant lid regime, when the uppermost part of the mantle is not participating in the thermal convection (c.f. Breuer and Moore [2007]), it is appropriate to consider the stagnant lid viscosity to be several orders of magnitude higher [e.g., Pauer et al., 2006]. The corresponding changes are depicted in the right column of Figure 3.8. The dynamic surface topography contributions remain similar but the CMB topography response for the longest wavelengths decreases throughout most of the mantle. Therefore, the resulting geoid response function $h_\ell(r)$ (to which the signal of CMB undulations also contributes) has somewhat larger amplitudes.

In planetary science we lack the information about the mantle temperature/density structure which is available in case of the Earth [e.g., Čadek and Fleitout, 2003; Běhounková et al., 2007]. Therefore the full 3D density structure must be approximated with some simpler one. For that purpose, laterally changing but radially constant structures can be used, which well approximate the radially averaged density variations. Such a model was shown to allow for the mantle viscosity inversion with acceptable errors by Pauer et al. [2006]. If we accept this approximation, we can stack the response functions into a depth-independent form h_ℓ, t_ℓ^{s} and t_ℓ^{cmb}, that depend on the viscosity profile $\eta(r)$ and the stagnant lid thickness D_{stag}. However, as a shell surface is smaller with decreasing radius r, the density anomaly $\delta\rho$ has to increase as $(R_0/r)^2$ in order to keep the mass anomaly δm constant with depth [Pauer et al., 2006]. In Figure 3.9 a comparison is made of two different cases for Venus and Mars in terms of these stacked response functions. Similarities between the two planets in terms of general trends are obvious, however, the amplitudes of the dynamic topography for Mars are roughly only 1/2 of those for Venus. This seems to be a direct consequence of the much thinner mantle of Mars (1700 km compared to 3000 km of Venus). Nevertheless, the geoid amplitudes remain similar, which gives rise to a higher admittance ratio $g_\ell/t_\ell^{\mathrm{s}}$ in comparison to Venus. Such an admittance ratio can be in principle used to derive the viscosity profile in a planet's mantle [e.g., Richards and Hager, 1984; Kiefer et al., 1986; Forte et al., 1994; Čadek and Fleitout, 2003; Pauer et al., 2006].

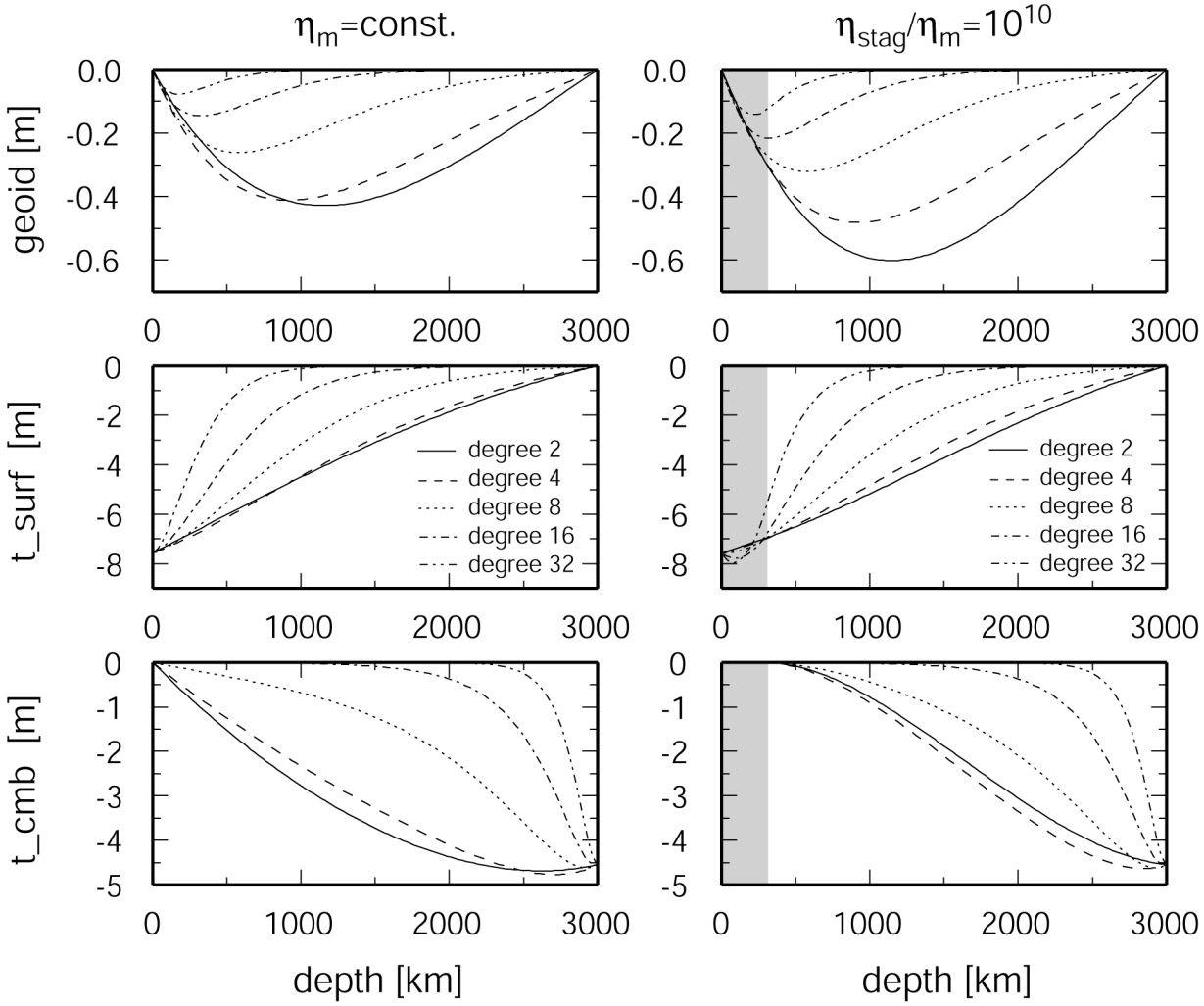

Figure 3.8: *Left column from top to bottom: Dynamically generated geoid, surface topography and CMB topography of Venus for the case of an isoviscous mantle in the form of the response functions* $h_\ell(r)$, $t^{\rm s}_\ell(r)$ *and* $t^{\rm cmb}_\ell(r)$ *(*$\ell = 2, 4, 8, 16, 32$*), respectively. Right column: The same but for the case when a highly viscous stagnant lid* $\eta_{\rm stag}/\eta_{\rm m} = 10^{10}$ *extending to 1/10 of the mantle depth is present (indicated by the shaded regions). The applied load corresponds to the thickness of each discretization layer (see Fig. 3.7) which in this case was 25 km. Since the entire loading shell was considered to possess a unit load across its thickness, the dynamic topography can be evaluated as* $\mathrm{d}r/\Delta\rho$*, where the* $\Delta\rho$ *is the density contrast corresponding to each boundary. For physical dimensions see Table 3.1,* $R_{\rm core}$*=3050 km and* $\Delta\rho^{\rm cmb}$*=5500 kgm*$^{-3}$.

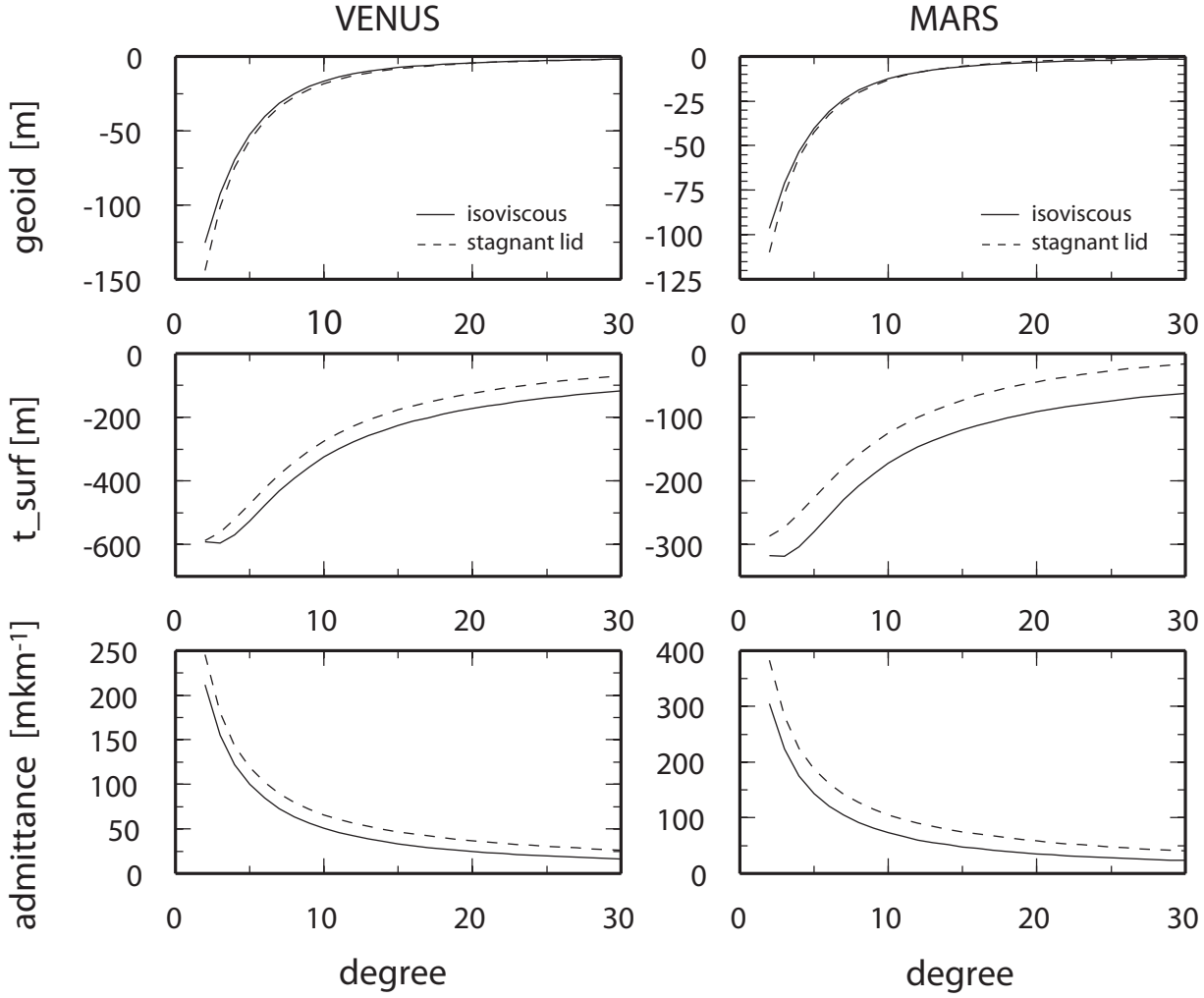

Figure 3.9: *Stacked response functions for dynamic geoid, surface topography and admittance for Venus and Mars. Two investigated cases here were the isoviscous mantle and mantle with a high viscosity stagnant lid with no loading in it.*

Chapter 4

Inverse Modeling

In the previous chapter the methods for deriving the gravity field for given a surface/internal loading and interior structure (i.e. knowing the properties of the crust, lithosphere and mantle) were given. However, our effort in exploring the planets of the Solar System is often exactly opposite to that, in that we have data of the observed gravity and topography fields and we want to derive the past or current internal structure parameters like crustal and elastic thicknesses [e.g., Simons et al., 1997; Wieczorek and Phillips, 1997; Barnett et al., 2002; McGovern et al., 2002, 2004; Belleguic et al., 2005] or mantle viscosity and density structure [e.g., Kiefer et al., 1986; Herrick and Phillips, 1992; Zhong, 2002; Vezolainen et al., 2004; Pauer et al., 2006]. In the following, the most common methods for gravity and topography data inversion are reviewed and also a connection between parameters derived by these methods and thermochemical evolution models of planets is introduced.

4.1 Inversion of gravity and topography data

The resulting value of an unknown parameter vector $\boldsymbol{x}$ which gives the optimum prediction of a modeled quantity directly depends upon the utilized procedure for the inverse modeling. This is often realized by constructing a specific misfit function that is a measure of the discrepancy between the original observed physical quantity and the predicted one. In gravimetric inversions, the quantity which is fitted is usually the geoid h (or gravity anomalies, see Section 2.1), either for the whole power spectrum or for a single degree ℓ:

$$M(\boldsymbol{x}) = \sum_{\ell,m} |h_{\ell m}^{\mathrm{obs}} - h_{\ell m}^{\mathrm{pred}}(\boldsymbol{x})|^2, \tag{4.1}$$

$$M_\ell(\boldsymbol{x}) = \sum_{m} |h_{\ell m}^{\mathrm{obs}} - h_{\ell m}^{\mathrm{pred}}(\boldsymbol{x})|^2. \tag{4.2}$$

In equation (4.1) the employed norm is L_2 which is the most common one in geophysical problems. However, in special cases, other norms could be used [cf. Matas, 1995]. If, however, gravity is not the only modeled field, then the misfit function should be modified accordingly. For instance, in the case of Venus both geoid and topography at long wavelengths seem to be of a dynamic origin, therefore if we try to model dynamic geoid the misfit

function should also include the topography misfit [Pauer et al., 2006]:

$$M^{\mathrm{dyn}}(\boldsymbol{x}) = \sum_{\ell,m} \left[|h_{\ell m}^{\mathrm{obs}} - h_{\ell m}^{\mathrm{pred}}(\boldsymbol{x})|^2 + \lambda_\ell |t_{\ell m}^{\mathrm{obs}} - t_{\ell m}^{\mathrm{pred}}(\boldsymbol{x})|^2 \right], \tag{4.3}$$

$$\lambda_\ell = \sum_m |h_{\ell m}^{\mathrm{obs}}|^2 / \sum_m |t_{\ell m}^{\mathrm{obs}}|^2. \tag{4.4}$$

where λ_ℓ is a weighting function that makes the misfit from gravity and topography equally important. On the other hand, in some models the modeled gravity field depends only on degree ℓ and for all orders m the relation between input and output is constant. In that case we can speed up the inverse modeling procedure by modifying the misfit function accordingly. For example, if we assume that both the observed and the predicted gravity field depend on the observed topography $t_{\ell m}$ and some transfer function Z_ℓ (see Section 4.1.1), then equation (4.1) can be rewritten as:

$$M(\boldsymbol{x}) = \sum_\ell |Z_\ell^{\mathrm{obs}} - Z_\ell^{\mathrm{pred}}(\boldsymbol{x})|^2. \tag{4.5}$$

Equation 4.5 can be replaced by the variance reduction (or percentage of the fitted data) [e.g., Čadek and Fleitout, 2003]:

$$P(\boldsymbol{x}) = \left[1 - \frac{\sum_{\ell,m} |h_{\ell m}^{\mathrm{obs}} - h_{\ell m}^{\mathrm{pred}}(\boldsymbol{x})|^2}{\sum_{\ell,m} |h_{\ell m}^{\mathrm{obs}}|^2} \right] \times 100\%, \tag{4.6}$$

which gives a value between 0% (for a prediction equal to zero) and 100% (for a perfect fit to the observed data). In principle, the variance reduction function for a single degree $P_\ell(\boldsymbol{x})$ can be constructed in the same way as the degree misfit (4.2) from the misfit function (4.1).

All of the above shown examples are constructed for the physical fields represented in the spectral domain by a finite set of spherical harmonic coefficients. Nevertheless, the same can be done in the spatial domain. For instance, the geoid-topography ratio (see Section 4.1.2) one can compute the misfit function simply as a summation of the local misfit over the whole examined region of interest:

$$M(\boldsymbol{x}) = \sum_i |h_i^{\mathrm{obs}} - h_i^{\mathrm{pred}}(\boldsymbol{x})|^2. \tag{4.7}$$

Among the other approaches to inverse modeling, one that is particulary suitable for estimating the most probable value of a single parameter x_i from the unknown vector $\boldsymbol{x}$ is a marginal probability study [e.g., Belleguic et al., 2005], which integrates the misfit between observed and predicted fields over all the other parameters [Tarantola, 1987]. However, for this method a modelization error σ^{pred} must be evaluated. This can be done for some models (e.g. for the top loading where gravity depends only on the observed topography and its crustal compensation) whereas for others this can be very difficult to estimate.

4.1.1 Global methods – admittance study

As shown in Chapter 3, the surface topography generates a contribution to the observed gravity field according to its compensation state. Using again a spectral representation of

both fields, we can determine an admittance factor representing the ratio between the geoid and topography. However, since the real crustal and subcrustal structure is more complicated than our simplified compensation models (meaning there are other contributions to the gravity field that are not taken into account in our models) in practice we determine instead of the ratio for each degree ℓ and order m, an order-averaged ratio Z_ℓ [e.g., Kiefer et al., 1986; Simons et al., 1997; Schubert et al., 2001]. This then defines the gravity signal degree-correlated and degree-uncorrelated ($I_{\ell m}$) to the observed topography $t_{\ell m}$:

$$Z_\ell = \frac{\sum_m h_{\ell m} t^*_{\ell m}}{\sum_m t_{\ell m} t^*_{\ell m}}, \tag{4.8}$$

$$h_{\ell m} = Z_\ell t_{\ell m} + I_{\ell m}. \tag{4.9}$$

where asterisk means complex conjugation and $h_{\ell m}$ again the observed geoid h.

The value of this admittance coefficient Z_ℓ depends not only on the values of the geoid and topography coefficients, but also on how well these two fields are correlated for each degree. To quantify that, a degree of correlation C_ℓ can be defined and equation (4.8) can then be rewritten as a product of this correlation coefficient and the ratio between the geoid (both correlated and uncorrelated parts) and topography power (defined by the equation (A.10)) for a given degree ℓ [e.g., Schubert et al., 2001; Pauer et al., 2006]:

$$C_\ell = \frac{\sum_m h_{\ell m} t^*_{\ell m}}{\sqrt{\sum_m h_{\ell m} h^*_{\ell m} \sum_m t_{\ell m} t^*_{\ell m}}}, \tag{4.10}$$

$$Z_\ell = C_\ell \sqrt{\frac{S_\ell(h)}{S_\ell(t)}}. \tag{4.11}$$

From equation (4.10) one can see that the value of the correlation coefficient does not depend on whether the coefficients of geoid or geopotential/gravity anomaly/gravity gradient are taken into account (contrary to this, the admittance (4.8) does depend on which form of the gravity field is employed). Because for each harmonic degree there is ℓ independent spherical harmonic coefficients $h_{\ell m}$ and $t_{\ell m}$, a statistical measure of the numerical value of C_ℓ must be taken. A so-called confidence level G_ℓ can defined for any desired level of correlation $q \in \langle 0, 1 \rangle$ and degree ℓ [Eckhardt, 1984; Pauer et al., 2006]:

$$G_1(q) = q, \tag{4.12}$$

$$G_\ell(q) = G_{\ell-1}(q) + q(1-q^2)^{\ell-1} \prod_{i=1}^{\ell-1} \frac{2i-1}{2i}. \tag{4.13}$$

In Figure 4.1a the degree correlation coefficients C_ℓ for the gravity and topography of Venus and Mars (see Chapter 2 for details) are displayed, together with the 95% correlation confidence level computed using equations (4.10) and (4.12)–(4.13). In both cases, the correlation starts below the chosen confidence level, however, then for higher degrees it increases well above, until a certain critical degree where it falls below again ($\ell \sim$150 and 70, respectively). This is probably caused by an increasing error present in the gravity field solution which becomes for high degrees an important factor [Wieczorek, 2007]. In Figure 4.1b the corresponding admittances Z_ℓ for geoid and topography are shown, where they both

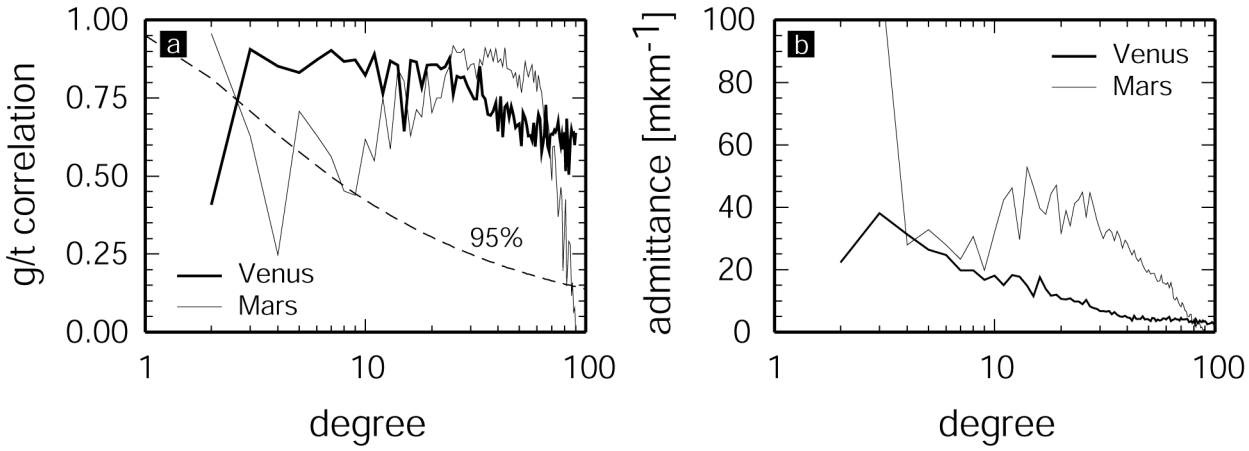

Figure 4.1: *a) Degree correlation between the gravity and topography of Venus and Mars, together with the 95% level of confidence. b) Degree averaged admittance between the geoid and topography of Venus and Mars.*

exhibit anomalous lowermost degree(s) and then relatively uniform behavior. However, for the interpretation of this quantity in terms of compensation mechanisms and appropriate compensation parameter values, an inverse model is needed. For that purpose we use the degree misfit function $M_\ell(D_\mathrm{e}, D_\mathrm{c})$ defined by equation (4.2) in the simplified form derived using the admittance coefficients Z_ℓ as in equation (4.5). These are defined according to equations (3.50) and (4.9), assuming the degree-uncorrelated part $I_{\ell m} = 0$. Values of all the other needed parameters are listed in Table 3.2 at page 40.

In Figure 4.2a the value of the crustal thickness D_c best fitting the observed Venus' gravity field for a given mean elastic thickness D_e and observed topography is shown. The first point to note is the fact that the optimum crustal thickness beyond degree $\ell \sim 40$ stays well below 50 km, independent of the elastic lithosphere thickness. The minimum misfit (denoted with the diamond markers) evaluated separately for each degree moreover shows that at these wavelengths, the optimum elastic thickness D_e is in the range 0–30 km which (see Figure 3.5a), means very little elastic support. Assuming therefore effectively no elastic support (i.e. Airy isostasy – see Section 3.1) and then using a simplified inversion calculating the misfit function $M(D_\mathrm{c})$ for degrees $\ell = 40 - 90$, we arrive to the optimum mean crustal thickness for Venus $D_\mathrm{c} = 35$ km [Pauer et al., 2006]. For degrees $\ell < 40$ on the other hand, we see that the optimum crustal thickness is much higher, reaching values > 100 km for the lowermost degrees. This seems to be an evidence that at this spectral interval another compensation mechanism is employed. Using the dynamic compensation model (see Section 3.4) this part of gravity signal can be explained as being generated by the flow in the mantle of Venus giving moreover constraints on the mantle viscosity structure [Pauer et al., 2006].

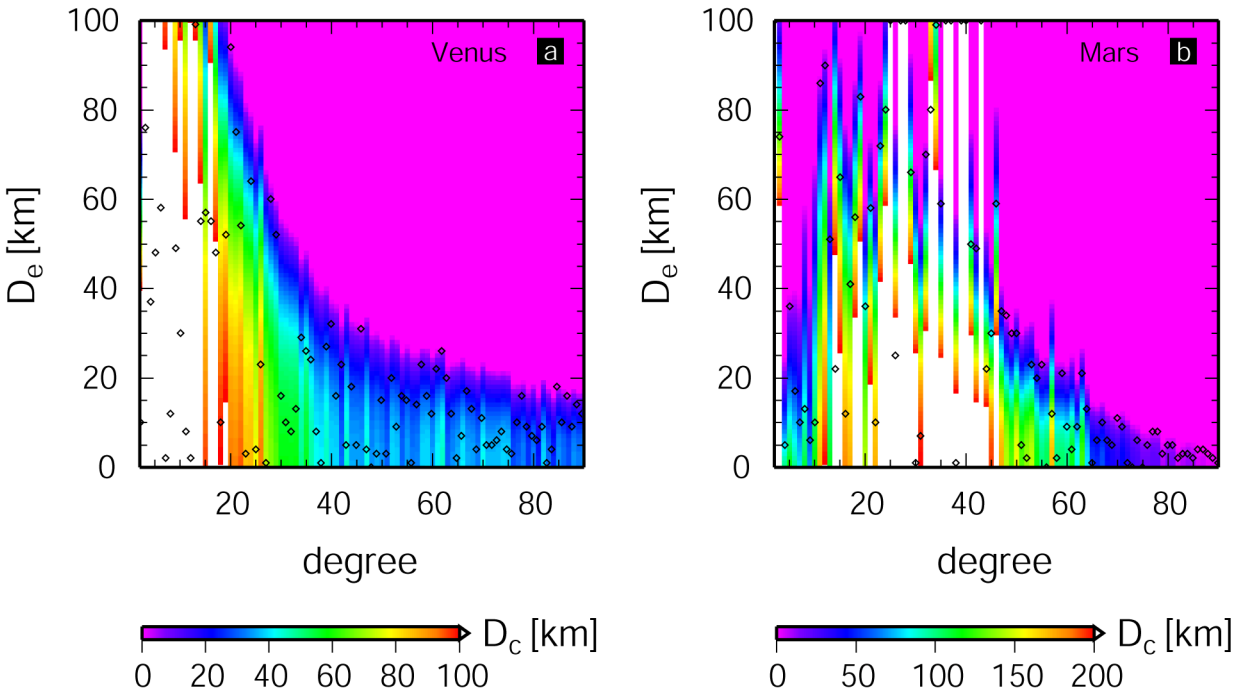

Figure 4.2: *a) An optimum crustal thickness D_c as a function of a degree and elastic lithosphere thickness D_e dermined by the inversion of geoid and topography of Venus. Diamonds mark for each degree ℓ the elastic thickness value that gives (with the appropriate optimum crustal thickness) the minimum value of the misfit $M_\ell(D_e, D_c)$. b) The same but for the case of Mars. The values of the optimum crustal thickness above 100 and 200 km for Venus and Mars, respectively, are not shown (in both panels covered with white color).*

The same misfit function $M_\ell(D_e, D_c)$ is used in Figure 4.2b to analyze the gravity and topography of Mars. The most obvious difference to Figure 4.2a is a shift in the optimum values of the crustal thickness to higher values ($D_c > 200$ km) over the spectral interval $\ell = 10 - 50$. Above this spectral range there is an interval of roughly 15 degrees where the optimum crustal thickness is more-or-less constant for a fixed elastic thickness D_e. However, for smaller elastic thicknesses, the values of this optimum crustal thickness reaches far above 100 km which is presumably the upper limit of the mean crustal thickness of Mars [Nimmo and Stevenson, 2001; Wieczorek and Zuber, 2004]. Results beyond degree $\ell = 65$ are not a subject of our interpretation since the rapid decrease in correlation (Fig. 4.1a) suggest that at these wavelengths the gravity field solution (see Section 2.1.1) is already strongly biased by non-gravitational effects and various sources of error [cf. Konopliv et al., 2006]. These rather confusing results are most probably caused by the fact that in the degree admittance Z_ℓ value are included contributions not only from the uniformly compensated top-loaded features, for which accounts the employed admittance function, but also contains signal from regions containing a substantial portion of the bottom loading [e.g., McGovern et al., 2002, 2004; Belleguic et al., 2005], mascon-style loading [e.g., Neumann et al., 2004; Searls et al., 2006] and top loading which occurs over a large range of elastic thicknesses (i.e. different elastic thicknesses at the time of loading) [e.g. Grott and Breuer, 2008].

4.1.2 Local methods – GTR and localization study

To overcome the problem connected to the global character of the admittance function's definition (4.8) a local geoid-topography ratio GTR can be studied instead by employing the spatial representation of both of the above mentioned fields [e.g., Herrick and Phillips, 1992; Moore and Schubert, 1997; Wieczorek and Phillips, 1997]:

$$GTR(\vartheta,\varphi) = \frac{h(\vartheta,\varphi)}{t(\vartheta,\varphi)} = \frac{\sum\limits_{\ell,m} h_{\ell m} Y_{\ell m}(\vartheta,\varphi)}{\sum\limits_{\ell,m} t_{\ell m} Y_{\ell m}(\vartheta,\varphi)}. \tag{4.14}$$

The choice of a spectral interval $\ell \in \langle \ell_{\min}, \ell_{\max} \rangle$ in such a case influences the resulting value of both the geoid and topography in a nonlinear way and hence the GTR. Therefore, for the purpose of the inverse modeling, the same spectral range as for the analyzed data should be adopted. Because of those contributions to the gravity signal that are not included in our compensation model (compare to the degree averaging for obtaining the admittance coefficient) the widest possible spectral interval satisfying the assumption of the common compensation mechanism should be employed [cf. Wieczorek and Zuber, 2004] to average out the non-correlated parts of the gravity signal.

In order to allow an interpretation of the observed GTR, a theoretical model connecting geoid with the inducing topography depending on a defined compensation state has to be developed. One can use the forward models described in a Chapter 3 together with the observed topography. However, to fully explore the necessary parameter space, this can be quite time consuming. Instead of that, an appropriate analytical formula can be found. In the case of the Earth, it has been shown that for many applications, a simple relationship derived in planar geometry with the assumption of Airy isostasy can be used [Turcotte and Schubert, 2002]. Assuming a crust with a uniform density ρ_{c} and mean thickness D_{c} with the emplaced surface feature of topographic hight $t(\vartheta,\varphi)$, the resulting geoid $h(\vartheta,\varphi)$ is then:

$$h(\vartheta,\varphi) = \frac{\pi G \rho_{\mathrm{c}}}{g_0}\left[2D_{\mathrm{c}}\, t(\vartheta,\varphi) + \frac{\rho_m}{\rho_m - \rho_c} t^2(\vartheta,\varphi)\right]. \tag{4.15}$$

As the resulting geoid depends on the topography in a nonlinear way, a common practise is to omit the second term in brackets (which is acceptable if $D_{\mathrm{c}} \gg t(\vartheta,\varphi)$) which then results in a simple "dipole moment" expression for GTR [Ockendon and Turcotte, 1977; Haxby and Turcotte, 1978]:

$$GTR = \frac{2\pi G \rho_{\mathrm{c}}}{g_0} D_{\mathrm{c}}. \tag{4.16}$$

Similar consideration can be done for Pratt isostasy or for cases when the crust is overlayed by water [Turcotte and Schubert, 2002]. A common premise for all these models, however, is that the "column" of the load has a constant width. That is, the surface element is approximately the same at the surface and crust-mantle interface radii (see Fig. 3.1).

This condition is assumed to be satisfied for the large terrestrial planets i.e. for the Earth and Venus [e.g., Moore and Schubert, 1997; Turcotte and Schubert, 2002], however, for planets with smaller radii the influence of sphericity becomes more important and equation (4.16) must be modified accordingly. This modification was first presented by Wieczorek

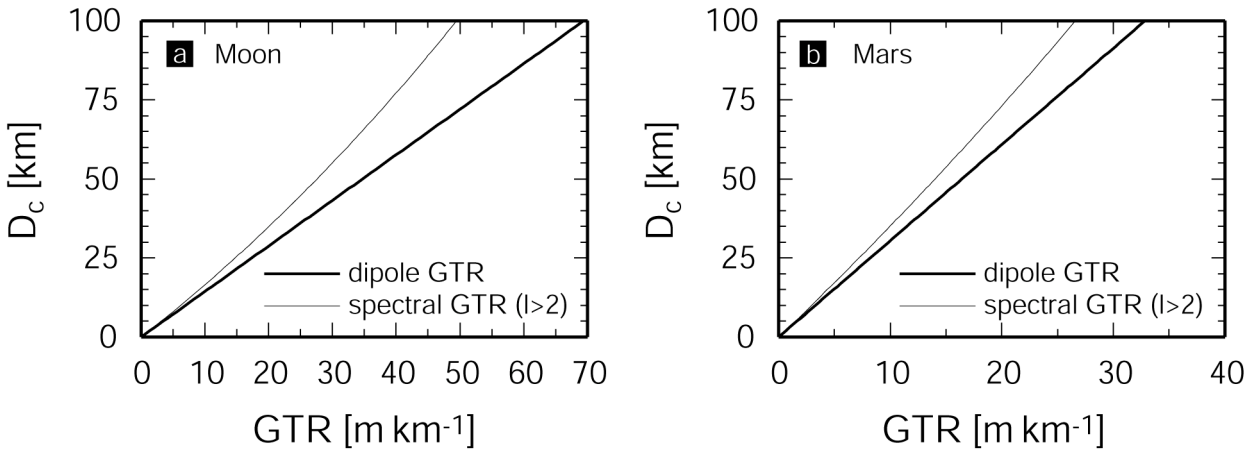

Figure 4.3: *Comparison of GTR for different mean crustal thicknesses D_c computed for a) the Moon ($\rho_c = 2700\ kgm^{-3}$) and b) Mars ($\rho_c = 2900\ kgm^{-3}$) employing the Airy isostasy concept calculated using the dipole moment (equation (4.16), thick line) and spectrally weighted GTR (equation (4.18), thin line) methods. Note that for the latter one, degree 2 was not included since this is connected to fossil bulge resp. rotational flattening* [Wieczorek and Phillips, 1997; Wieczorek and Zuber, 2004].

and Phillips [1997]. Starting with equation (4.14) and assuming that the uncorrelated part of geoid $I_{\ell m} = 0$ (i.e. $h_{\ell m} = Z_\ell t_{\ell m}$), it can be rewritten in the following way, employing a weighting function W_ℓ that describes the fraction of topography at degree ℓ to overall topography at a location (ϑ, φ):

$$GTR(\vartheta,\varphi) = \frac{\sum\limits_{\ell,m} Z_\ell t_{\ell m} Y_{\ell m}(\vartheta,\varphi)}{\sum\limits_{\ell,m} t_{\ell m} Y_{\ell m}(\vartheta,\varphi)} = \sum_\ell Z_\ell W_\ell(\vartheta,\varphi). \tag{4.17}$$

Furthermore, assuming that the GTR is independent of position (ϑ, φ), i.e. for the fixed value of the crustal thickness and compensation mechanism the GTR value is the same, equation (4.17) implies that the weighting function $W_\ell(\vartheta, \varphi)$ also does not depend on the position. The resulting GTR can then be modeled as the sum of the products of the degree admittance Z_ℓ with the degree weighting function W_ℓ:

$$GTR = \sum_\ell W_\ell Z_\ell, \tag{4.18}$$

$$W_\ell = \sum_m t_{\ell m}^2 / \sum_{\ell,m} t_{\ell m}^2. \tag{4.19}$$

Then, for any observed GTR, a mean crustal thickness D_c can be derived. Advantages and disadvantages of this approach are discussed in detail by Wieczorek and Phillips [1997] who first introduced it. The difference between dipole moment GTR and the spectrally weighted one for the Moon and Mars is shown in Figure 4.3 (the employed spectral interval is $\ell = 3 - 60$, since for both planets the degree 2 contains non-hydrostatic contributions).

From the results in Figure 4.3, one can see that the dipole moment formula always tends to underestimate the resulting value of the mean crustal thickness. For the representative values of GTR for the Moon ~ 25 mkm^{-1}, the corresponding value of D_c determined by the spectrally weighted method is ~ 45 km, while the dipole moment formula gives a value almost 10 km smaller. Similarly for Mars, with the typical value of $GTR \sim 15$ mkm^{-1} the derived mean crustal thickness is ~ 55 km and again this is a value around 10 km higher than the one obtained by equation (4.16).

Having the forward model connecting the mean crustal thickness D_c (in fact a product of this and the crustal density ρ_c) with the predicted GTR, an inverse model minimizing the difference between the observed and predicted value of this quantity is needed. To remove the influence of regional inhomogeneities in the crust, an averaging within a fixed radius L_0 can be applied [cf. Wieczorek and Zuber, 2004] and such an averaged GTR is then interpreted in terms of the optimum value of the mean crustal thickness. However, as the regionally averaged topography is not referenced to the mean global reference level but to some regional average t^avg, a correction for this effect is needed. For Airy isostasy with a simple single layer crustal structure, the admittance function and the corresponding correction from the regional mean crustal thickness $D_\mathrm{c}^\mathrm{avg}$ to the global one are given by:

$$Z_\ell = \frac{4\pi G R \rho_\mathrm{c}}{g_0(2\ell+1)}\left[1-\left(\frac{R-D_\mathrm{c}}{R}\right)^\ell\right], \tag{4.20}$$

$$D_\mathrm{c}^\mathrm{avg} = D_\mathrm{c} + t^\mathrm{avg}\left[1+\frac{\rho_\mathrm{c}}{\rho_\mathrm{m}-\rho_\mathrm{c}}\left(\frac{R}{R-D_\mathrm{c}}\right)^2\right]. \tag{4.21}$$

Using the above described approach the mean crustal thickness of the Moon was determined to be $D_\mathrm{c} = 49 \pm 16$ km [Wieczorek et al., 2006], which correlates well with the seismically constrained model giving the thickness 40 ± 5 km [Chenet et al., 2006]), and for Mars where there is a higher uncertainty about the crustal density to be $D_\mathrm{c} = 57 \pm 24$ km [Wieczorek and Zuber, 2004]. For details on modeling more complicated crustal structures (two-layer crust with an upper or lower crust of constant thickness but distinct density) see Wieczorek and Phillips [1997] and Pauer and Breuer [2008] (Section C.2).

Another powerful method to derive local/regional values of the compensation parameters is the spatial-spectral localization of gravity and topography. This method somehow resemble the wavelet analysis [Vescey et al., 2003; Kido et al., 2003], nevertheless it has better defined properties with respect to the spherical harmonic representation of the processed data. This method was already successfully used for the Earth [Simons and Hager, 1995; Simons et al., 2000], Venus [Simons et al., 1997] and Mars [McGovern et al., 2002, 2004; Belleguic et al., 2005], however, using a variety of different approaches. Today, the best developed one is that of Wieczorek and Simons [2005] which supplies the analysis with the full theoretical background needed to estimate the reliability of this method. Using filtering windows well localized both in spatial and spectral domain, Belleguic et al. [2005] used this approach in combination with the admittance function modeling to derive local values of elastic thickness, crustal and load densities and the subsurface loading ratio for major Martian volcanoes. Since this method was not used in this work, the interested reader is referred to Wieczorek and Simons [2005] and Belleguic et al. [2005].

4.2 Bouguer inversion

The previous section was devoted to the derivation of the parameters of a planet's topography compensation state i.e. crustal thickness and density, elastic thickness and/or subsurface loading ratio from the observed gravity and topography under some predefined assumptions, e.g., Airy crustal isostasy or elastic lithosphere flexure. The two above mentioned datasets can also be used without such an *a priori* assumption, but then one must assume that the total gravity field (or almost total, with well defined exceptions) is only due to the surface and crust-mantle interface (CMI) undulations. Then, the Bouguer anomaly, defined as the difference of observed and surface topography generated gravity [e.g., Novotný, 1998; Turcotte and Schubert, 2002] can be expressed by means of geopotential as:

$$U^{\mathrm{BA}}(\rho) = U^{\mathrm{obs}} - U^{\mathrm{s}}(\rho), \tag{4.22}$$

and depends on the density structure of the crust and the topographic loads. As discussed in Chapter 3, the assumption of a homogeneous crust is quite unrealistic, however, because of a lack of other data describing crustal structure, it is usually accepted as a first approximation [e.g., Neumann et al., 1996; Wieczorek and Phillips, 1998; Neumann et al., 2004; Wieczorek, 2007]. Nevertheless, for well studied regions like the lunar mares which contain a substantial mascon loading caused by the lava infill [Muller and Sjogren, 1968; Solomon and Head, 1980; Konopliv et al., 2001] or the Martian polar caps which, while being part of the observed topography, consists of much lighter water and CO_2 ice and dust [Phillips et al., 2008] it is appropriate to model that extra/missing load in the form of regional density anomalies [Wieczorek and Phillips, 1998; Neumann et al., 2004].

Assuming that the density structure is properly modeled, we can evaluate the Bouguer anomaly U^{BA} using equation (2.36). Then, assuming a given value of the mean crustal thickness D_{c}, an inversion for the shape of the CMI can be made easily with the following expression using equation (2.35):

$$w_{\ell m} = \frac{2\ell + 1}{4\pi G R_0 \Delta\rho} \left(\frac{R_0}{R_0 - D_{\mathrm{c}}} \right)^{\ell+2} U^{\mathrm{BA}}_{\ell m}, \tag{4.23}$$

where $\Delta\rho = \rho_{\mathrm{m}} - \rho_{\mathrm{c}}$ is the density contrast at the CMI and R_0 is the mean radius of the planet. The problem appearing in the case of planets is that the high degree signal (which is, according to the equation (4.23), strongly amplified) is often very noisy and leads to a physically unrealistic oscillation in the CMI undulations [Wieczorek and Phillips, 1998; Neumann et al., 2004]. This problem can be avoided either by removing the higher degrees from the solution of the Bouguer inversion (which means lower resolution) or by applying some kind of smoothing filter. This is often done by using a degree-dependent filter λ_ℓ which is for long wavelength 1 but for shorter wavelengths approaches 0. This can be done by either forcing the CMI power spectrum to obey some *a priori* chosen rule [Neumann et al., 2004] or regularizing the obtain solution in some sense (e.g., minimum amplitude or minimum curvature) [Wieczorek and Phillips, 1998].

In Figure 4.4a the surface topography of Venus is depicted together with the names of major regions of interest. Using this topography and the observed geoid (Fig. 2.3) the associated Bouguer anomaly is shown in Figure 4.4b. As expected, the major negative anomalies are connected to the prominent positive topographic structures (Istar Terra, Aphrodite

Terra) whereas the positive anomalies could be observed above the major lowland regions (Atalanta Planitia). Using equation (4.23) to explain this anomaly solely by the signal of the CMI with a density contrast $\Delta\rho = 400$ kgm^{-3}, the crustal thickness variations displayed in Figure 4.4c can be obtained [Wieczorek, 2007]. The crustal thickness at lowland regions then approaches 20 km, while at the highland and volcanic sites it exceeds 70 km. However, if we assume that a substantial contribution to both gravity and topography at the long wavelengths comes from the dynamic flow in Venus' mantle [Kiefer et al., 1986; Pauer et al., 2006] and employ for the inversion only that part of the data not explained by this dynamic model, the resulting crustal thickness variations differ substantially (Fig. 4.4d). While the local thickened crust $D_c^{loc} > 50$ km beneath the highland regions remains, the rest of the planet has a more-or-less constant crustal thickness of 35±5 km (which is the *a priori* chosen value of D_c). Another point of interest is the thinning of the crust beneath

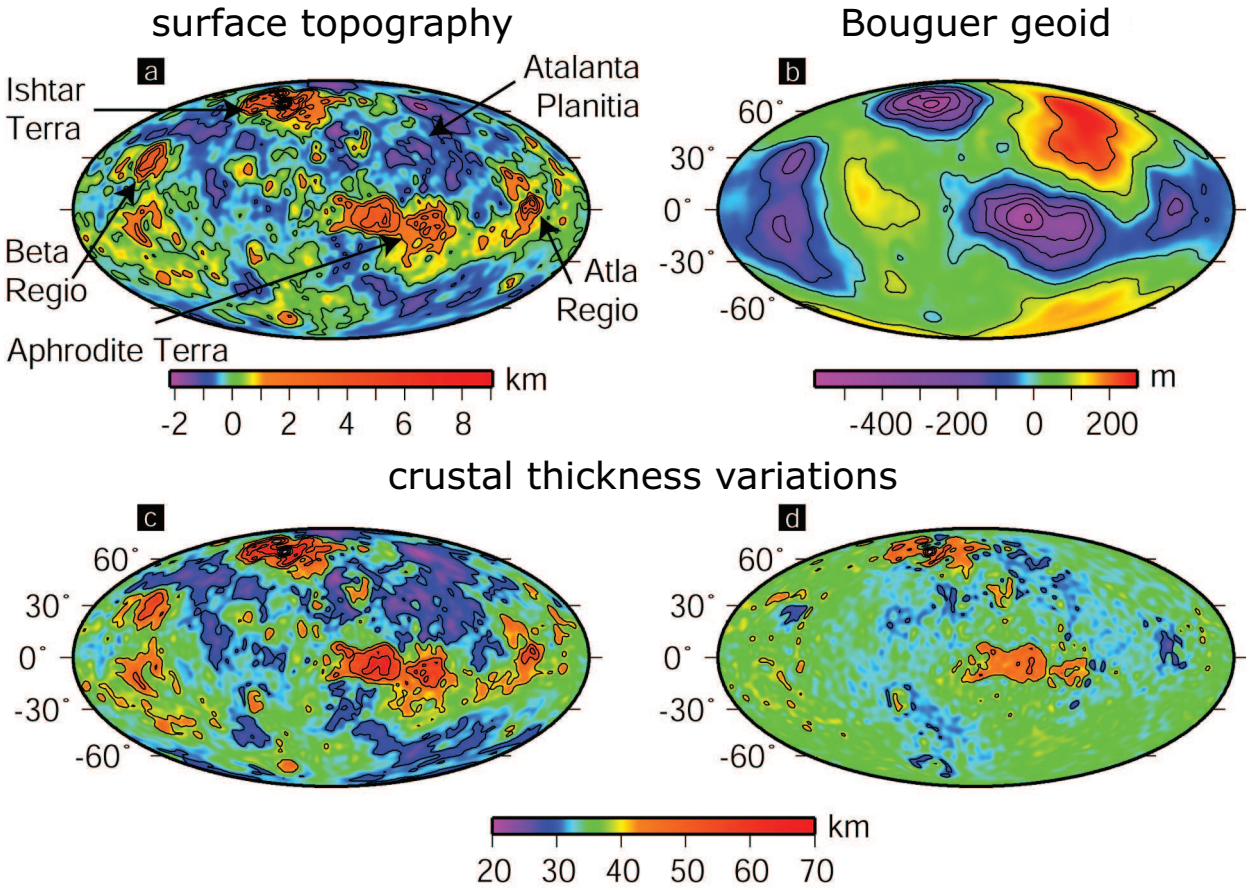

Figure 4.4: *a) Surface topography of Venus with major regions of interest. b) Associated Bouguer anomaly expressed as a geoid height computed by assuming a constant crust density* $\rho_c = 2900$ *kgm*$^{-3}$ *and the spectral interval* $\ell = 2 - 60$. *c) Crustal thickness lateral variations for the given mean crustal thickness* $D_c = 35$ *km and density contrast* $\Delta\rho = 400$ *kgm*$^{-3}$. *The entire Bouguer geoid is explained in terms of the signal of the crust-mantle interface. d) The same as in panel c) but for an inversion that employed only parts of gravity and topography fields not explained by the dynamic model of* Pauer et al. [2006].

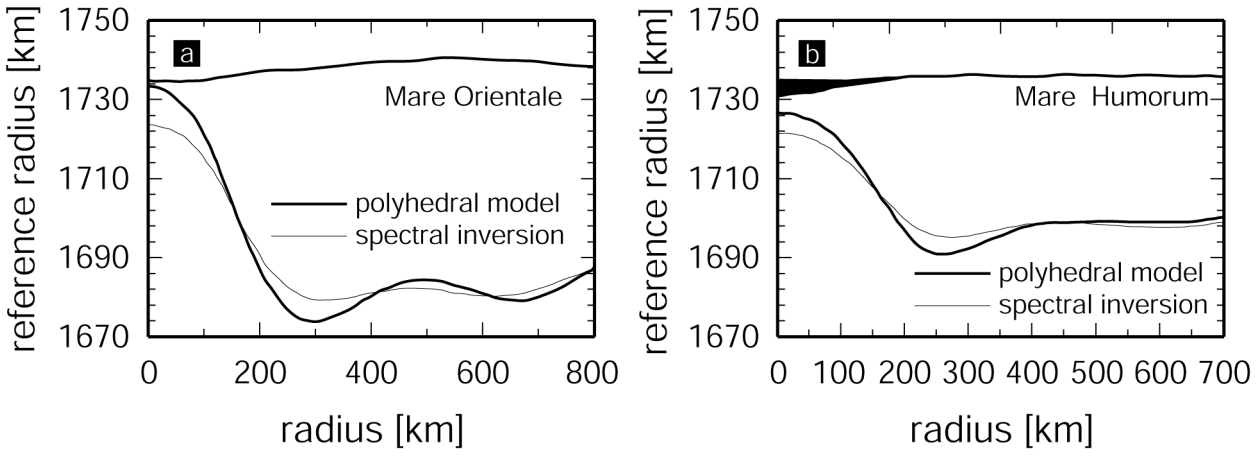

Figure 4.5: *Rotationally averaged crustal structure of two major lunar basins, Mare Orientale and Mare Humorum, obtained by the polyhedral shape model inversion method (solid line) and spherical harmonic inversion (dashed line). Black represents the mare lava infill (redrawn after* Hikida and Wieczorek [2007]*).*

the major volcanic constructs (Atla and Beta Regiones) which is possibly a consequence of too successful dynamic prediction in these regions [cf. Pauer et al., 2006]. Since the dynamic model does not account for crustal thickness variations, it cannot properly model the thickening of the crust due to extensive volcanism. Another more appropriate approach is therefore needed that takes into account both top and internal loading to model the resulting gravity and topography.

In the case of Venus the conditions for the use of the first approximation formula (2.36) are satisfied except for the region of Ishtar Terra, where it introduces an error of a few km [Wieczorek, 2007]. However, for the Moon and Mars, the amplitudes of topography and predicted CMI shape no longer satisfy these conditions. Therefore, a finite relief method to compute the gravity field is needed [e.g., Neumann et al., 1996; Wieczorek and Phillips, 1998]. An inversion using an appropriate equation derived from equation (2.38) is, however, not so straightforward as in the previous case since here the gravity field depends on topography in a nonlinear manner. Therefore, the resulting CMI relief must be modeled iteratively until it satisfies the Bouguer anomaly within an acceptable error. For more on this technique, see Wieczorek and Phillips [1998] or Pauer and Breuer [2008] (Section C.2).

Another approach to Bouguer inversion is modeling the gravity field associated with the observed topography and modeled CMI relief in the spatial domain. For this purpose, a polyhedral model can be employed [e.g., Hikida and Wieczorek, 2007] which profits from the possibility of a denser grid in the regions of interest (which provides more precise results). Such an approach has a clear advantage for the case of laterally varying quality of gravity and/or topography data which is e.g. the case of the Moon [Konopliv et al., 2001]. In such a situation, a polyhedral model can improve the quality of the local crustal thickness models as is demonstrated for two prominent lunar impact basins, Mare Orientale and Mare Humorum, in Figure 4.5. These new predictions of the local crustal variations can then improve the constraints on various planetary processes, e.g. the initial excavation depth/radius ratio of the impact basins [Wieczorek and Phillips, 1999; Hikida and Wieczorek, 2007].

4.3 Thermal evolution of planet

The study of planetary gravity and topography data using the inverse modeling procedures described in the previous sections can provide constraints on the mean crustal thickness and the elastic thickness at the time of loading [cf. Wieczorek, 2007]. These parameters are important for understanding the local compensation processes (and for the case of a large scale load on planets with a small radius, also the global compensation state [Phillips et al., 2001]) as well as for constraining the thermochemical evolution of terrestrial planets [e.g., McGovern et al., 2002, 2004; Breuer and Spohn, 2003; Schumacher and Breuer, 2006; O'Neill et al., 2007; Grott and Breuer, 2008].

There are in general two methods of calculating the thermochemical evolution of a planet using either complex 2D and 3D or parameterized convection models. In the case of 2D and 3D convection models, investigating the full range of possible parameters can be computationally very demanding, both in the sense of the required CPU power and time. Therefore, an alternative approach, the so-called "parameterized convection", is often used [e.g., Stevenson et al., 1983; Schubert et al., 1986; Spohn, 1991; Breuer and Spohn, 2003; Hauck et al., 2004]. This approach uses the results of numerical and laboratory experiments and boundary layer theories [e.g., Turcotte and Oxburgh, 1967; Davaille and Jaupart, 1993; Solomatov, 1995; Grasset and Parmentier, 1998] and is based on simple scaling laws that relate the vigor of convection with the heat loss of a convecting system. For instance, the scaling law for an isovisous convecting mantle is $Nu = aRa^{\beta}$ [e.g., Turcotte and Oxburgh, 1967; Richter, 1978] where Nu is the Nusselt number, i.e., the ratio of the heat transported by convection and the heat transported by conduction, Ra is the Rayleigh number describing the vigor of thermal convection [e.g., Schubert et al., 2001], a is a constant and β is a nondimensional parameter between 1/4 and 1/3, depending on the boundary conditions and geometry of the convecting shell [e.g., Jarvis, 1984; Zebib et al., 1985]. For a temperature dependent viscosity, which is more suitable for a terrestrial mantle [e.g., Weertman and Weertman, 1975], the scaling law is more complicated and depends further on viscosity [cf. Moresi and Solomatov, 1995] since a stagnant lid forms on top of the convecting mantle.

In the following, the general equations describing the thermal evolution of a terrestrial mantle [cf. Breuer and Spohn, 2003; Schumacher and Breuer, 2006; Grott and Breuer, 2008] are presented. This approach separates the stagnant lid and the convecting mantle (see Figure 4.6) and is based on the parameterization of Grasset and Parmentier [1998]. It has the advantage of the possibility to include effects such as the thermal insulation of the crust and the redistribution of radioactive elements from the mantle into the crust. The feedback of these effects on the convecting system cannot be considered if the mantle, including the crust, is treated with one Nu-Ra relationship for the entire system [Breuer and Moore, 2007]. The evolution of the stagnant lid layer can then be determined using the energy balance equation of a growing lithosphere [e.g., Schubert et al., 1979; Spohn, 1991]:

$$\rho_{\mathrm{m}} c_{\mathrm{m}} (T_{\mathrm{m}} - T_{\mathrm{l}}) \frac{\mathrm{d}D_{\mathrm{l}}}{\mathrm{d}t} = q_{\mathrm{m}} - q_{\mathrm{l}} = q_{\mathrm{m}} - k_{\mathrm{m}} \left. \frac{\partial T}{\partial r} \right|_{r=R_{\mathrm{l}}}, \tag{4.24}$$

where ρ_{m} is the mantle density, c_{m} is the specific heat capacity of the mantle, T_{m} and T_{l} are the temperature in the upper mantle and the base of the lithosphere, respectively, D_{l} is the stagnant lid thickness and q_{m} and q_{l} are heat flows out of the mantle and through the

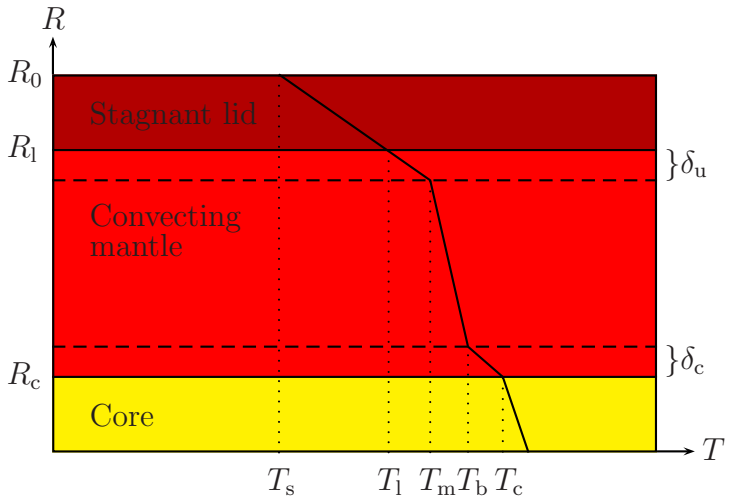

Figure 4.6: *Schematic thermal profile T as a function of radius R with the stagnant lid, convecting mantle and core distinguished by different colors. The mantle is further divided into an upper and lower boundary layer δ_u and δ_c marked by dashed lines.*

lithosphere, respectively. The latter is a product of the mantle thermal conductivity k_m and thermal gradient at the base of the lithosphere.

The temperature at the base of the stagnant lid T_l depends on the temperature of the underlaying upper mantle T_m and the rate of change of viscosity η with temperature T [Davaille and Jaupart, 1993; Grasset and Parmentier, 1998]:

$$T_\mathrm{l} = T_\mathrm{m} - 2.21\left(\frac{\mathrm{d}\ln\eta}{\mathrm{d}T}\right)^{-1}. \tag{4.25}$$

For a strongly temperature dependent viscosity described by:

$$\eta = \eta_0 \exp\left(\frac{A}{RT_\mathrm{m}}\right) \tag{4.26}$$

where η_0 is a reference viscosity, R is the universal gas constant and A is the activation energy for creep [e.g., Weertman and Weertman, 1975], the temperature at the base of the stagnant lid is:

$$T_\mathrm{l} = T_\mathrm{m} - 2.21\left(\frac{RT_\mathrm{m}^2}{A}\right). \tag{4.27}$$

The thermal gradient at the bottom of lithosphere (see equation (4.24)) is calculated by solving the steady state heat conduction equation in the stagnant lid:

$$\frac{1}{r^2}\frac{\partial}{\partial r}\left(r^2 k_\mathrm{l}\frac{\partial T}{\partial r}\right) + Q_\mathrm{l} = 0, \tag{4.28}$$

where k_l is the thermal conductivity of the stagnant lid and Q_l is the heat production rate of the radioactive elements in the lithosphere. The boundary conditions are the temperature at

the surface T_s and at the lithospheric base T_l, the latter is computed using equation (4.27). Solving equation (4.28) with depth dependent parameters also allows the consideration of the thermal insulation of the crust due to its lower thermal conductivity, k_cr, in comparison to the thermal conductivity of the mantle [cf. Schumacher and Breuer, 2006]. Furthermore, it is possible to consider the enrichment of radioactive elements in the crust due to crustal formation processes.

The thermal evolution of the underlying convecting mantle and the core is given by the following energy balance equations:

$$\rho_\mathrm{m} c_\mathrm{m} V_\mathrm{m} \varepsilon_\mathrm{m} \frac{\mathrm{d}T_\mathrm{m}}{\mathrm{d}t} = -q_\mathrm{m} A_\mathrm{m} + q_\mathrm{c} A_\mathrm{c} + Q_\mathrm{m} V_\mathrm{m}, \tag{4.29}$$

$$\rho_\mathrm{c} c_\mathrm{c} V_\mathrm{c} \varepsilon_\mathrm{c} \frac{\mathrm{d}T_\mathrm{c}}{\mathrm{d}t} = -q_\mathrm{c} A_\mathrm{c} + (L + E_\mathrm{g}) \frac{\mathrm{d}m}{\mathrm{d}t}, \tag{4.30}$$

where ρ_m and ρ_c are the densities of the mantle and the core, respectively, c_m and c_c are the specific heat capacities of the mantle and the core, respectively, V_m and V_c are the volumes of the mantle and core, respectively, A_m and A_c are the surface areas of the mantle and the core, respectively, ε_m is the ratio of the mean mantle temperature to the upper mantle temperature and ε_c is the ratio of the mean core temperature to the CMB temperature. L stands for the latent heat and E_g for the gravitational energy both released by the growth of an inner core. The term $\mathrm{d}m/\mathrm{d}t$ describes the growth rate of the inner core, which can be determined by the intersection of the core adiabat and the core liquidus; for details see Stevenson et al. [1983] and Breuer et al. [2007].

The heat production rate in the mantle Q_m is given by:

$$Q_\mathrm{m}(t) = \sum_i Q_i \exp(-\lambda_i t) \left(1 + \frac{V_\mathrm{cr}}{V_\mathrm{m}} (1 - \Lambda) \right), \tag{4.31}$$

where Q_i and λ_i are the heat production rate and the half-life time of i-th radioactive element, respectively, V_cr is the crustal volume and Λ is the crustal enrichment factor with respect to the primitive mantle. Equation (4.31) considers the depletion of radioactive elements in the mantle due to the formation of the crust.

The heat flow out of the mantle q_m and out of the core q_c are given by:

$$q_\mathrm{m} = k_\mathrm{m} \frac{\Delta T_\mathrm{sm}}{\delta_\mathrm{u}}, \tag{4.32}$$

$$q_\mathrm{c} = k_\mathrm{m} \frac{\Delta T_\mathrm{mc}}{\delta_\mathrm{c}}. \tag{4.33}$$

where ΔT_sm is the temperature contrast across the upper boundary layer and ΔT_mc across the lower boundary layer, δ_u and δ_c are the thicknesses of the upper and the lower boundary layers, respectively. To derive the thicknesses of the upper and lower mantle boundary layers δ_u and δ_c, the local stability criterion [Choblet and Sotin, 2000] is used:

$$\delta_\mathrm{u} = \left(\frac{\kappa \eta_\mathrm{m} Ra_{\delta_\mathrm{u}}}{\alpha \rho_\mathrm{m} g_0 \Delta T_\mathrm{sm}} \right)^{1/3}, \tag{4.34}$$

$$\delta_\mathrm{c} = \left(\frac{\kappa \eta_\mathrm{c} Ra_{\delta_\mathrm{c}}}{\alpha \rho_\mathrm{m} g_0 \Delta T_\mathrm{mc}} \right)^{1/3}, \tag{4.35}$$

where κ is the thermal diffusivity of the mantle and α is the thermal expansivity of the mantle. The viscosity in the boundary layers $\eta_{\rm m}$ and $\eta_{\rm c}$ are given by [Richter, 1978]:

$$\eta_{\rm m} = \eta_0 \exp\left[\frac{A}{R(T_{\rm m} - \Delta T_{\rm sm}/2)}\right], \tag{4.36}$$

$$\eta_{\rm c} = \eta_0 \exp\left[\frac{A}{R(T_{\rm c} - \Delta T_{\rm mc}/2)}\right]. \tag{4.37}$$

Parameter	**Symbol**	**Value**	**Unit**
surface radius	R_0	2400×10^3	m
core radius	$R_{\rm c}$	1840×10^3	m
surface temperature	$T_{\rm s}$	440	K
initial temperature at mid-depth	$T_{\rm init}$	1900	K
initial temperature contrast	ΔT	1660	K
initial core temperature	$T_{\rm CMB}$	2100	K
initial internal heating rate	Q_0	5.2373×10^{-8}	$\mathrm{Wm^{-3}}$
crustal enrichment factor	Λ	4	–
radioactive decay rate	λ	0.04951	Gy
gravity acceleration	g_0	3.7	$\mathrm{ms^{-2}}$
density of mantle	$\rho_{\rm m}$	3400	$\mathrm{kgm^{-3}}$
density of core	$\rho_{\rm c}$	8000	$\mathrm{kgm^{-3}}$
heat capacity of mantle	$c_{\rm m}$	1297	$\mathrm{Jkg^{-1}K^{-1}}$
heat capacity of core	$c_{\rm c}$	750	$\mathrm{Jkg^{-1}K^{-1}}$
mantle thermal expansivity	α	2×10^{-5}	$\mathrm{K^{-1}}$
mantle thermal diffusivity	κ	10^{-6}	$\mathrm{m^2s^{-1}}$
mantle thermal conductivity	$k_{\rm m}$	4	$\mathrm{Wm^{-1}K^{-1}}$
crustal thermal conductivity	$k_{\rm cr}$	2	$\mathrm{Wm^{-1}K^{-1}}$
crustal thickness	$D_{\rm c}$	50×10^3	m
universal gas constant	R	8.3144	$\mathrm{Jmol^{-1}K^{-1}}$
activation energy for creep	A	466.07	$\mathrm{kJmol^{-1}}$
reference viscosity	η_0	8.7×10^{22}	Pas
exponent of Nu-Ra relation	β	1/3	–
latent heat	L	250×10^3	$\mathrm{Jkg^{-1}}$
gravitational energy	$E_{\rm g}$	250×10^3	$\mathrm{Jkg^{-1}}$

Table 4.1: *Parameters used for the thermal evolution modeling of Mercury as described in the Section 4.3 (after* Breuer et al. [2007]*).*

Ra_{δ_u} and Ra_{δ_c} are the critical Rayleigh numbers of the respective boundary layer, which can be computed using the internal Rayleigh number Ra_i [Deschamps and Sotin, 2000]:

$$Ra_\mathrm{i} = \frac{\alpha \rho_\mathrm{m} g_0 \Delta T (R_0 - R_\mathrm{c})^3}{\kappa \eta_\mathrm{m}}, \tag{4.38}$$

$$Ra_{\delta_\mathrm{u}} = 2.28 Ra_\mathrm{i}^{0.319}, \tag{4.39}$$

$$Ra_{\delta_\mathrm{c}} = 0.28 Ra_\mathrm{i}^{0.21}, \tag{4.40}$$

with $\Delta T = T_\mathrm{m} - T_\mathrm{s} + \Delta T_\mathrm{mc}$. Finally, the temperature at the base of the mantle T_b, which is needed to compute the temperature increase ΔT_mc across the lower boundary layer, is given by the adiabatic increase of temperature in the mantle T_m [cf. Matyska, 2005]:

$$T_\mathrm{b} = T_\mathrm{m} + \frac{\alpha g_0 T_\mathrm{m}}{c_\mathrm{m}} \Delta R \tag{4.41}$$

with $\Delta R = R_\mathrm{l} - R_\mathrm{c} - \delta_\mathrm{u} - \delta_\mathrm{c}$, where R_l is the radius of the bottom of the stagnant lid and R_c is the radius of the core (see Figure 4.6).

The elastic lithosphere thickness D_e can be derived in each time step of the parameterized convection computation using the strength envelope formalism [McNutt et al., 1988; Grott and Breuer, 2008] (see Section 3.3.2) or, for simplicity, one can define the depth of the elastic lithosphere using a fixed isotherm. The value of the isotherm depends on the rheology of the material, the strain rate and the bounding stress. For a dry olivine rich mantle the isotherm is about 1070 K, assuming a strain rate of 10^{-17} s^{-1} and bounding stress of 15 MPa. This latter approximation further assumes that the whole crust is elastic or that the crustal material has a similar rheology as the mantle material (such as for the case of a crust consisting of a dry diabase and a mantle consisting mainly of dry olivine). Thermochemical evolution models also allow the calculation of the crustal thickness evolution (i.e., evaluating the crustal production rate) – more details on this topic can be found for instance in Breuer and Spohn [2003].

As for the initial conditions of the thermochemical evolution models, an appropriate temperature profile must be adopted. Usually, a profile consistent with the temperature distribution after core formation is chosen. This profile is the consequence of both the planetary accretion, when after a strong meteoritic bombardment the uppermost part of a planet is partially or entirely molten [Elkins-Tanton et al., 2005], and of the core differentiation process [Stevenson, 1990]. It is interesting to note is that the thermal profile during and just after accretion may be stable against thermal convection because the temperature increases toward the surface. It is generally assumed that this temperature profile is inverted by the core formation process due to the release of gravitational energy, hence even a superheated core with respect to the mantle is possible [Stevenson, 1990]. For equations describing temperature profiles after accretion and core differentiation, see e.g., Schubert et al. [1986].

Figure 4.7 shows the results of a typical thermal evolution model of Mercury for a) the mantle temperature, b) the surface heat flow, c) the elastic lithosphere thickness and d) the stagnant lid thickness. These results have been calculated with the parameterized convection model developed by D. Breuer, using the parameter values listed in Table 4.1. The evolution of the mantle temperature T_m (Fig. 4.7a) shows a short period of temperature

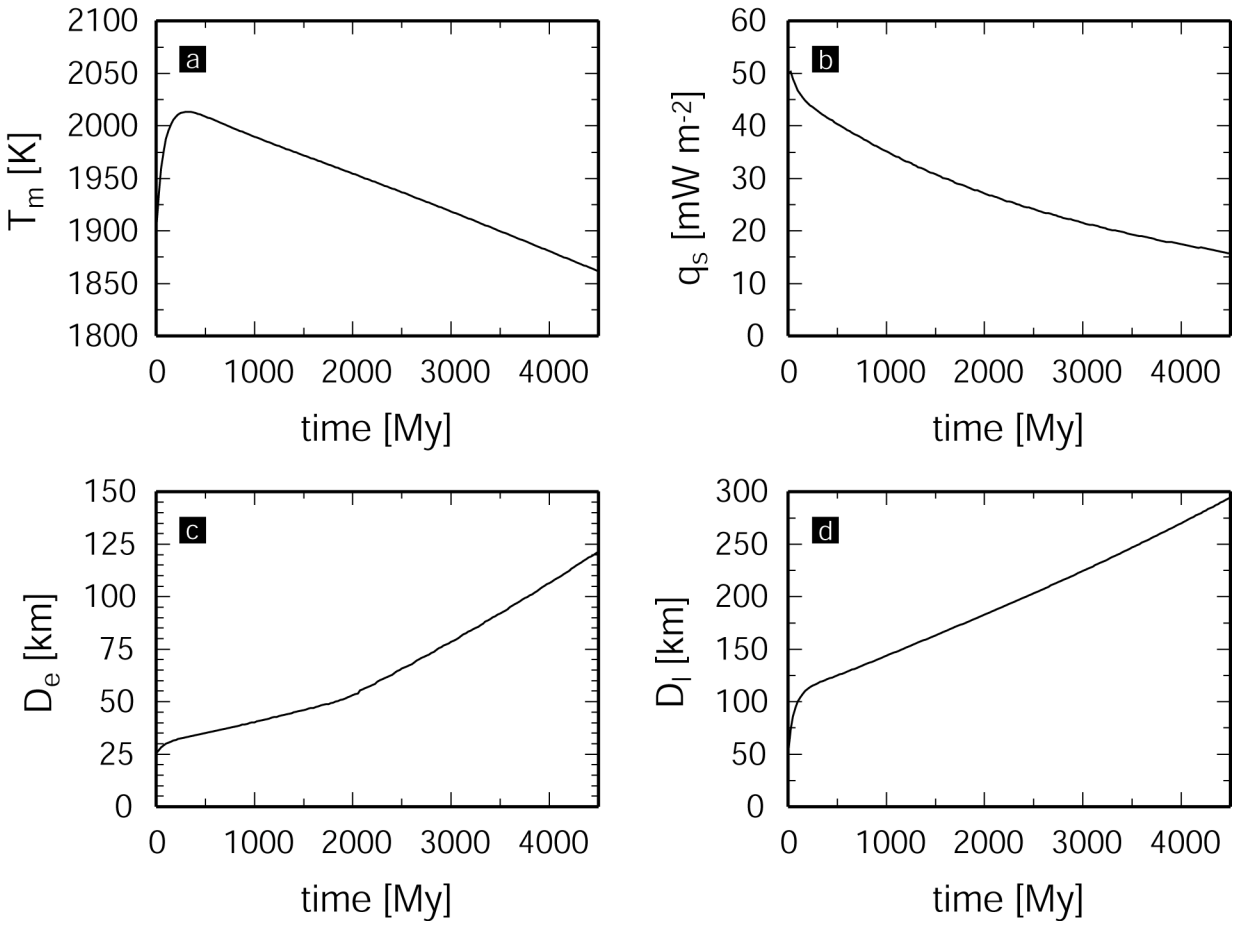

Figure 4.7: *Results for a parameterized model of the thermal evolution of Mercury for the past 4.5 Gy. In panel a) is depicted the evolution of the mantle temperature T_m, b) shows the surface heat flux q_s, c) the elastic thickness D_e and d) the stagnant lid thickness D_l.*

increase ($\sim$ 300 My) connected mainly to the re-adjustment of the system and the heating caused by the radioactive decay in the mantle. After this phase of heating, the mantle cools by about 150 K to a present-day value of about 1850 K. Similarly, the surface heat flow q_s decreases during the entire evolution of the planet (Fig. 4.7b) and the elastic lithosphere thickness increases over time to a present-day value of $\sim$ 125 km (Fig. 4.7c). For the latter, a light kink in the curve can be seen at around 2 Gy. This is the result of the elastic lithosphere thickness becoming greater than the crustal thickness and is a consequence of the different thermal conductivities in the crust and mantle. For this model, an enriched primordial crustal thickness of 50 km is assumed, whereas secondary crust formation is neglected. It is, however, expected that secondary crustal formation is minor for Mercury [Breuer et al., 2007]. The stagnant lid thickness grows to a value of about 300 km (Fig. 4.7d), thus, the present active convection zone is very thin, with a thickness of only 250 km, consistent with 2D and 3D convection models [Spohn et al., 2001a; Breuer et al., 2007]. Note, however, that this is just one possible scenario of Mercury's thermal evolution and it depends strongly on the parameter values chosen, such as the mantle viscosity, the content of radioactive

heat sources in the mantle, and the crustal thermal conductivity (Table 4.1). Only a full exploration of the parameter range can give us sufficient insight into the various possible evolution scenarios of the planet [e.g., Breuer and Spohn, 2003; Hauck et al., 2004; Grott and Breuer, 2008].

Chapter 5

Discussion and Conclusions

In planetary science, a number of concepts taken from the geophysical studies of the Earth are employed to investigate the observed gravity field in relation to the surface topography and its subsurface compensation mechanisms. Sometimes, this has been done without considering the reliability of those methods for the different conditions of use, i.e. for planets with a considerably smaller radius, higher topography, smaller gravitational acceleration or different rheological structure than the Earth. As a consequence, the obtained results in terms of compensation parameters may have large errors. For instance, using only the first approximation method to evaluate the gravitational signal of Martian volcanoes, up to 30% of the real gravity signal can be neglected. This, on the other hand, leads to higher estimates of the thickness of the elastic lithosphere, which supports the volcanic construct [Belleguic et al., 2005].

The aim of this work was to investigate various mechanisms compensating the observed surface topography, i.e. crustal isostasy, elastic support and dynamic support caused by mantle flow. In earlier models, the response of the elastic lithosphere was usually poorly modeled since this complicated mechanism was in most cases handled only by the use of the thin shell approximation [Turcotte et al., 1981]. Therefore, the focus of this work was the derivation of a thick elastic shell model, which would allow for an appropriate implementation of compressibility, subsurface loading and dynamic deformation from the planetary interior. This model decreases the error in the predicted gravity field and, therefore, also of the compensation parameters derived from the inverse models. However, in some cases, if the uncertainty in the observed data to which the predictions are compared is much larger than the modeling error (e.g., see [Pauer and Breuer, 2008]), then the use of the thin elastic shell approximation is still appropriate.

The investigated compensation models were applied to three different planetary problems. Firstly we applied dynamic compensation model to explain today large-scale gravity and topography fields of Venus and investigate for its mantle viscosity structure [Pauer et al., 2006] (Appendix C). Based on investigation of different models with varying number of viscous layers, a whole mantle flow seems to well explain those today observed global fields not only for viscosity structure which is constant but also for a mantle model with a stiff lithosphere and a gradual increase of viscosity toward a core. Exact viscosity structure however was not possible to determine – while three layer models favorite only a week increase in viscosity over the whole mantle (by a factor of 10), four and five layers models

suggest a viscosity structure similar to the one of Earth. An existence of a low viscosity channel beneath a lithosphere cannot be confirmed despite a fact that such a feature has appeared in some more complicated models. Furthermore we have identified regions on the surface which seem to be well fit by means of dynamic compensation model and those where such a fit is poor – i.e. regions which are supported by other mechanisms presumably some kind of crustal/elastic lithospere compensation.

In the second paper the Airy isostasy mechanism, combined with an inverse model based on the spatial geoid-topography ratio, and the Bouguer inversion were employed to estimate the crustal density of the Martian southern highlands [Pauer and Breuer, 2008] (Appendix C). Since the two inverse methods have opposite trends with respect to changes in the crustal density, satisfying both simultaneously may provide constraints on the maximum density of the southern highlands crust, with an estimate of 3020 ± 70 kgm^{-3} obtained for a single-layer crustal model. Using models with a two-layer crust for which one layer has a constant thickness, a maximum density of ~ 3000 kgm^{-3} is also obtained for the compensating crustal layer. These findings, together with the estimates made by other authors on the composition/density of various Martian regions, seem to confirm that the crustal dichotomy is not only in elevation and surface age, but also in the origin of the crustal material. The results indicate either a change in the crustal density with time or two distinct geochemical reservoirs in the mantle, that formed in the early evolution of Mars and are the source regions of the different crustal materials. Furthermore, it is possible that because of this compositional distinctiveness of the Martian crust between the northern and southern hemisphere, Pratt isostasy could be partly responsible for the dichotomy in elevation.

In the third application, the strength of a possible ocean floor gravity signal of Jupiter's moon Europa was studied [Pauer et al., 2010] (Appendix C). This problem – if measured by future missions – will, however, be quite atypical compared to other planetary science problems, since we will have no data on the actual topography of this particular interface. For the forward modeling we must therefore employ a synthetic topography model to estimate the magnitude of its gravity signal. Because of such an approach, using the thin elastic shell model will not introduce a substantial error to the predicted gravity. The magnitude of the predicted signal, depending on the compensation parameters, can be up to 10's of mGals expected at the orbital height. Thus, if the long wavelength topography reaches at least a few hundred meters, we will be able to detect it with the planned measurement precision of 1 mGal. The inversion of the data will be very challenging due to the lack of any topographic measurements of this subsurface interface. Therefore, we invert for the topography amplitudes instead of the compensation parameters. This is possible within c. 25% error due to the substantial elastic support even for relatively thin elastic lithospheres. The contribution to the gravity field of the ice crust overlaying the subsurface ocean is only of the order of $\sim$1 mGal and thus smaller than the ocean floor's gravity field.

In all the above listed applications of the topography compensation modeling undertaken in this work, there exist large uncertainties concerning most of the employed values of the interior structure parameters. This fact, and the non-availability of measurements improving their knowledge today or in the near future, make geophysical modeling in planetary sciences highly uncertain. The major uncertainty in the case of gravity field modeling connected to the compensated surface topography is a very poor knowledge of a planet's crustal composition and structure. We have also only indirect constraints on the crustal

and elastic thicknesses, for instance from thermo-chemical evolution models, which results in additional uncertainties in the compensation models. On the other hand, the continuous iteration of ideas and results, even based on poor knowledge today, leads to a relatively rapid development in terms of the employed models' accuracy improvement and the rejection of contradictory conclusions. Nevertheless, it is generally valid that conclusions drawn in planetary sciences have to be widely discussed (see discussion in all three attached manuscripts in Appendix C) and their implications are weaker than for the case of the Earth, where more data and constraints are available.

Evaluating the benefits of the models presented in this work, one can see that in some cases, the isostatic compensation, thin elastic shell and purely viscous dynamic flow models are adequate for predicting the gravity signal resulting from the compensated topography. However, for a compressible lithosphere or large crustal thickness, the difference between the thick elastic layer model and even those thin elastic layer models handling the loading and the self-gravitation effect appropriately is not negligible because of the basic simplifications used in the thin elastic shell theory. Moreover, our model offers additional possibilities for future enhancements, including a simultaneous inversion for top- and bottom-loading or the introduction of lateral variations in the rheological parameters. For models employing the time evolution of the crustal system, even the thick elastic shell model is insufficient; instead visco-elastic or visco-elasto-plastic rheologies should be adopted. Further improvements in the modeling of the planetary topography compensation and its associated gravity signal can be, in principle, achieved by the careful evaluation of the local compensation properties, instead of employing some globally averaged ones.

Bibliography

Airy, G. B. (1855). On the computation of the effect of the attraction of mountain-masses, as disturbing the apparent astronomical latitude of stations of geodetic surveys. *Phil. Trans. R. Soc.*, 145:101–104.

Albert, R. A. and Phillips, R. J. (2000). Paleoflexure. *Geophys. Res. Lett.*, 27(16):2385–2388.

Anderson, J. D., Colombo, G., Esposito, P. B., Lau, E. L., and Trager, G. B. (1987). Themass, gravity field, and ephemeris of Mercury. *Icarus*, 71:337–349.

André, S. L., Watters, T. R., and Robinson, M. S. (2005). The long wavelength topography of Beethoven and Tolstoj basins, Mercury. *Geophys. Res. Lett.*, 32, L21202, doi:10.1029/2005GL023627.

Andrews-Hanna, J. C., Zuber, M. T., and Banerdt, W. B. (2008). The Borealis basin and the origin of the martian crustal dichotomy. *Nature*, 453:1212–1215, doi:10.1038/nature07011.

Balmino, G. (1994). Gravitational potential harmonics from the shape of an homogeneous body. *Celest. Mech. Dyn. Astron.*, 60:331–364.

Barnett, D. N., Nimmo, F., and McKenzie, D. (2002). Flexure of Venusian lithosphere measured from residual topography and gravity. *J. Geophys. Res.*, 107(E2), 5007, doi:10.1029/2000JE001398.

Belleguic, V., Lognonné, P., and Wieczorek, M. (2005). Constraints on the Martian lithosphere from gravity and topography data. *J. Geophys. Res.*, 110, E11005, doi:10.1029/2005JE002437.

Beuthe, M. (2008). Thin elastic shells with variable thickness for lithospheric flexure of one-plate planets. *Geophys. J. Int.*, 172:817–841, doi:10.1111/j.1365-246X.2007.03671.x.

Blanc, M. et al. (2007). LAPLACE: A mission to Europa and the Jupiter System for ESA's Cosmic Vision Programme.

Bott, M. H. P. (1999). Modeling local crustal isostasy caused by ductile flow in the lower crust. *J. Geophys. Res.*, 104(B9):20,349–20,359.

Breuer, D., Hauck, S. A., Buske, M., Pauer, M., and Spohn, T. (2007). Interior evolution of Mercury. *Space Sci. Rev.*, 132(2-4):229–260, doi:10.1007/s11214-007-9228-9.

Breuer, D. and Moore, W. B. (2007). *Planets and Moons*, volume 10 of *Treatise on Geophysics (Editor-in-Chief G. Schubert)*, chapter Dynamics and thermal history of the terrestrial planets, the Moon, and Io, pages 299–348. Elsevier, Amsterodam.

Breuer, D. and Spohn, T. (2003). Early plate tectonics versus single-plate tectonics on Mars: Evidence from magnetic field history and crust evolution. *J. Geophys. Res.*, 108(E7), 5072, doi:10.1029/2002JE001999.

Breuer, D., Yuen, D. A., Spohn, T., and Zhang, S. (1998). Three dimensional models of martian mantle convection with phase transitions. *Geophys. Res. Lett.*, 25(3):229–232.

Brokešová, J. (2007). Theoretical principles of Fourier spectral analysis. Lecture notes, Charles University in Prague (in Czech).

Burov, E. and Diament, M. (1995). The effective elastic thickness (Te) of continental lithosphere: What does it really mean? *J. Geophys. Res.*, 100(B3):3905–3927.

Burša, M. and Pěč, K. (1993). *Gravity Field and Dynamics of the Earth*. Springer.

Běhounková, M., Čížková, H., Matyska, C., Yuen, D. A., and Wang, M. S. (2007). Resolution tests of three-dimensional convection models by traveltime tomography: effects of Rayleigh number and regular versus irregular parametrization. *Geophys. J. Int.*, 170:401–416, doi:10.1111/j.1365-246X.2007.03458.x.

Byerlee, J. D. (1978). Friction of rocks. *Pure Appl. Geophys.*, 116:615–626.

Chenet, H., Lognonné, P., Wieczorek, M., and Mizutani, H. (2006). Lateral variations of lunar crustal thickness from the Apollo seismic data set. *Earth Planet. Sci. Lett.*, 243:1–14, doi:10.1016/j.epsl.2005.12.017.

Choblet, G. and Sotin, C. (2000). 3D thermal convection with variable viscosity: can transient cooling be described by a quasi-static scaling law? *Phys. Earth Planet. Int.*, 119:321–336.

Choblet, G., Čadek, O., Couturier, F., and Dumoulin, C. (2007). Œdipus: a new tool to study the dynamics of planetary interiors. *Geophys. J. Int.*, 170:9–30, doi:10.1111/j.1365-246X.2007.03419.x.

Clarke, K. B. (2007). Europa Explorer – an exceptional mission using existing technology. In *Aerospace Conference, IEEE proceedings*.

Cook, A. C. and Robinson, M. S. (2000). Mariner 10 stereo image coverage of Mercury. *J. Geophys. Res.*, 105(E4):9429–9443.

Davaille, A. and Jaupart, C. (1993). Transient high-Rayleigh number thermal convection with large viscosity variations. *J. Fluid Mech.*, 253:141–166.

Defraigne, P., Dehant, V., and Wahr, J. M. (1996). Internal loading of an inhomogeneous compressible earth with phase boundaries. *Geophys. J. Int.*, 125(1):173–192.

Dermott, S. F. (1979). Shapes and gravitational moments of satelites and asteroids. *Icarus*, 37:575–586.

Deschamps, F. and Sotin, C. (2000). Inversion of two-dimensional numerical convection experiments for a fluid with a strongly temperature-dependent viscosity. *Geophys. J. Int.*, 143:204–218.

Eckhardt, D. H. (1984). Correlations between global features of terrestrial fields. *Math. Geol.*, 16:155–171.

Edmonds, A. R. (1960). *Angular Momentum in Quantum Mechanics*. Princeton University Press, Princeton.

Elkins-Tanton, L. T., Hess, P. C., and Parmentier, E. M. (2005). Possible formation of ancient crust on Mars through magma ocean processes. *J. Geophys. Res.*, 110, E12S01, doi:10.1029/2005JE002480.

Forsyth, D. W. (1985). Subsurface loading and estimates of the flexural rigidity of continental lithosphere. *J. Geophys. Res.*, 90(B14):12,623–12,632.

Forte, A. M. and Peltier, W. R. (1991). Viscous flow models of global geophysical observables 1. forward problems. *J. Geophys. Res.*, 96(B12):20,131–20,159.

Forte, A. M., Woodward, R. L., and Dziewonski, A. M. (1994). Joint inversions of seismic and geodynamic data for models of three-dimensional mantle heterogeneity. *J. Geophys. Res.*, 99(B11):21,857–21,877.

Frey, H. V., Bills, B. G., Nerem, R. S., and Roark, J. H. (1996). The isostatic state of Martian topography revisited. *Geophys. Res. Lett.*, 23:721724.

Frey, H. V., Roark, J. H., Shockey, K. M., Frey, E. L., and Sakimoto, S. E. H. (2002). Ancient lowlands on Mars. *Geophys. Res. Lett.*, 29(10), 1384, doi:10.1029/2001GL013832.

Grasset, O. and Parmentier, E. M. (1998). Thermal convection in a volumetrically heated, infinite Prandtl number fluid with strongly temperature-dependent viscosity: Implications for planetary thermal evolution. *J. Geophys. Res.*, 103:18,171–18,181.

Grott, M. and Breuer, D. (2008). The evolution of the martian elastic lithosphere and implications for crustal and mantle rheology. *Icarus*, 193:503–515, doi:10.1016/j.icarus.2007.08.015.

Hager, B. H. and Clayton, R. W. (1989). *Mantle Convection: Plate Tectonics and Global Dynamics*, chapter Constraints on the structure of mantle convection using seismic observations, flow models, and the geoid, pages 675–763. Gordon and Breach, New York.

Hauck, S. A., Dombard, A. J., Phillips, R. J., and Solomon, S. C. (2004). Internal and tectonic evolution of Mercury. *Earth Planet. Sci. Lett.*, 222:713–728.

Haxby, W. F. and Turcotte, D. L. (1978). On isostatic geoid anomalies. *J. Geophys. Res.*, 83:5473–5478.

Herrick, R. R. and Phillips, R. J. (1992). Geological correlations with the interior density structure of Venus. *J. Geophys. Res.*, 97(E10):16,017–16,034.

Hikida, H. and Wieczorek, M. A. (2007). Crustal thickness of the Moon: New constraints from gravity inversions using polyhedral shape models. *Icarus*, 192, doi:10.1016/j.icarus.2007.06.015.

Horský, J., Novotný, J., and Štefaník, M. (2001). *Mechanics in Physics*. Academia, Praha (in Czech).

Hüttig, C. and Stemmer, K. (2008). Finite volume discretization for dynamic viscosities on Voronoi grids. *Phys. Earth Planet. Int., in press*, doi:10.1016/j.pepi.2008.07.007.

Iess, L. and Boscagli, G. (2001). Advanced radio science instrumentation for the mission BepiColombo to Mercury. *Planet. Space Sci.*, 49:1597–1608.

Jacobson, R. A., Antreasian, P. G., Bordi, J. J., Criddle, K. E., Ionasescu, R., Jones, J. B., Mackenzie, R. A., Meek, M. C., Parcher, D., Pelletier, F. J., Owen, W. M., Roth, D. C., Roundhill, I. M., and Stauch, J. R. (2006). The gravity field of the Saturnian system from satellite observations and spacecraft tracking data. *Astronom. J.*, 132(6):2520–2526.

Janes, D. M. and Melosh, H. J. (1990). Tectonics of planetary loading – a general model and results. *J. Geophys. Res.*, 95:21,345–21,355.

Jarvis, G. T. (1984). Time-dependent convection in the Earth's mantle. *Phys. Earth Planet. Int.*, 36:305–327.

Jones, M. N. (1985). *Spherical Harmonics and Tensors for Classical Field Theory*. Res. Stud. Press Ltd., Letchworth, U. K.

Karato, S.-I., Paterson, M., and Fitzgerald, J. (1986). Rheology of synthetic olivine aggregates: Influence of grain size and water. *J. Geophys. Res.*, 91:8151–8176.

Kaula, W. M. (1966). *Theory of Satellite Geodesy*. Blaisdell Publication Company, Waltham MA.

Kido, M., Yuen, D. A., and Vincent, A. P. (2003). Continuous wavelet-like filter for a spherical surface and its application to localized admittance function on Mars. *Phys. Earth Planet. Int.*, 135:1–16.

Kiefer, W. S., Richards, M. A., Hager, B. H., and Bills, B. G. (1986). A dynamic model of Venus' gravity field. *Geophys. Res. Lett.*, 13:14–17.

Klokočník, J., Wagner, C. A., Kostelecký, J., Bezděk, A., Novák, P., and McAdoo, D. (2008). Variations in the accuracy of gravity recovery due to ground track variability: GRACE, CHAMP, and GOCE. *J. Geodesy*, doi:10.1007/s00190-008-0222-0.

Konopliv, A. S., Asmar, S. W., Carranza, E., Sjogren, W. L., and Yuan, D.-N. (2001). Recent gravity models as a result of the Lunar Prospector mission. *Icarus*, 150:1–18, doi:10.1006/icar.2000.6573.

Konopliv, A. S., Banerdt, W. B., and Sjogren, W. L. (1999). Venus gravity: 180th degree and order model. *Icarus*, 139:3–18.

Konopliv, A. S., Yoder, C. F., Standish, E. M., Yuan, D.-N., and Sjogren, W. L. (2006). A global solution for the Mars static and seasonal gravity, Mars orientation, Phobos and Deimos masses, and Mars ephemeris. *Icarus*, 182:23–50, doi:10.1016/j.icarus.2005.12.025.

Koop, R., Smit, M., Zegers, T., Bouman, J., Selig, A., Flokstra, J., Cuperus, R., Vermeersen, B., Visser, P., and van den Berg, A. (2006). Prospects for a gradiometry mission for high-resolution mapping of the Martian gravity field. In *European Planetary Science Congress proceedings, abstract no. 00581.*

Kraus, H. (1967). *Thin Elastic Shells*. John Wiley, New York.

Kývalová, H. (1994). Phase transitions and Earth mantle dynamics. Master's thesis, Charles University in Prague (in Czech).

Lambeck, K. (1988). *Geophysical Geodesy*. Oxford Univ. Press, New York.

Lognonné, P. (2005). Planetary seismology. *Annu. Rev. Earth Planet. Sci.*, 33:19.1–19.34.

Mackwell, S., Zimmerman, M., and Kohlstedt, D. (1998). High-temperature deformation of dry diabase with application to tectonics on Venus. *J. Geophys. Res.*, 103(B1):975–984.

Martinec, Z. (1991). On the accuracy of the method of condensation of the Earth's topography. *Manuscripta Geodaetica*, 16:288–294.

Martinec, Z. and Pěč, K.and Burša, M. (1989). The Phobos gravitational field modeled on the basis of its topography. *Earth Moon Planets*, 45:219–235.

Matas, J. (1995). Mantle viscosity and density structure. Master's thesis, Charles University in Prague.

Matyska, C. (2005). Mathematical introduction to geothermics and geodynamics. Lecture notes, Charles University in Prague.

McGovern, P. J., Solomon, S. C., Smith, D. E., Zuber, M. T., Simons, M., Wieczorek, M. A., Phillips, R. J., Neumann, G. A., Aharonson, O., and Head, J. W. (2002). Localized gravity/topography admittance and correlation spectra on Mars: Implications for regional and global evolution. *J. Geophys. Res.*, 107(E12), 5136, doi:10.1029/2002JE001854.

McGovern, P. J., Solomon, S. C., Smith, D. E., Zuber, M. T., Simons, M., Wieczorek, M. A., Phillips, R. J., Neumann, G. A., Aharonson, O., and Head, J. W. (2004). Correction to "Localized gravity/topography admittance and correlation spectra on Mars: Implications for regional and global evolution". *J. Geophys. Res.*, 109(E12), E07007, doi:10.1029/2004JE002286.

McKenzie, D., Barnett, D. N., and Yuan, D.-N. (2002). The relationship between Martian gravity and topography. *Earth Planet. Sci. Lett.*, 195:1–16.

McNutt, M. K., Diament, M., and Kogan, M. G. (1988). Variations of elastic plate thickness at continental thrust belts. *J. Geophys. Res.*, 93:88258838.

Milani, A., Rossi, A., Vokrouhlický, D., Villani, D., and Bonanno, C. (2001). Gravity field and rotation state of Mercury from the BepiColombo Radio Science Experiments. *Planet. Space Sci.*, 49:1579–1596.

Mitrovica, J. X. and Peltier, W. R. (1992). Constraints on mantle viscosity from relative sea level variations in Hudson Bay. *Geophys. Res. Lett.*, 19:1185–1188.

Mohr, P. J. and Taylor, B. N. (2005). CODATA recommended values of the fundamental physical constants: 2002. *Rev. Mod. Phys.*, 77(1):1–107.

Moore, W. B. and Schubert, G. (1997). Venusian crustal and lithospheric properties from nonlinear regressions of highland geoid and topography. *Icarus*, 128(2):415–428, doi:10.1006/icar.1997.5750.

Moresi, L.-N. and Solomatov, V. S. (1995). Numerical investigation of 2D convection with extremly large viscosity variations. *Phys. Fluids*, 7:2154–2162.

Mueller, S. and Phillips, R. J. (1995). On the reliability of lithospheric constraints derived from models of outer-rise exure. *Geophys. J. Int.*, 123:887–902.

Muller, P. M. and Sjogren, W. L. (1968). Mascons: Lunar mass concentrations. *Science*, 161:680–684.

Neumann, G. A., Rowlands, D. D., Lemoine, F. G., Smith, D. E., and Zuber, M. T. (2001). Crossover analysis of Mars Orbiter Laser Altimetry data. *J. Geophys. Res.*, 106(E10):23,753–23,768.

Neumann, G. A., Zuber, M. T., Smith, D. E., and Lemoine, F. G. (1996). The lunar crust: Global structure and signature of major basins. *J. Geophys. Res.*, 101(E7):16,841–16,843.

Neumann, G. A., Zuber, M. T., Wieczorek, M. A., McGovern, P. J., Lemoine, F. G., and Smith, D. E. (2004). Crustal structure of Mars from gravity and topography. *J. Geophys. Res.*, 109, E08002, doi:10.1029/2004JE002262.

Nimmo, F. and Stevenson, D. J. (2001). Estimates of Martian crustal thickness from viscous relaxation of topography. *J. Geophys. Res.*, 106(E3):5085–5098.

Nimmo, F., Thomas, P. C., Pappalardo, R. T., and Moore, W. B. (2007). The global shape of Europa: Constraints on lateral shell thickness variations. *Icarus*, 191:183–192, doi:10.1016/j.icarus.2007.04.021.

Novotný, O. (1998). Motions, gravity field and figure of the Earth. Lecture notes, UFBA, Salvador, Bahia.

Ockendon, J. R. and Turcotte, D. L. (1977). On the gravitational potential and field anomalies due to thin mass layers. *Geophys. J. R. Astron. Soc.*, 48:479–492.

O'Neill, C., Lenardic, A., Jellinek, A. M., and Kiefer, W. S. (2007). Melt propagation and volcanism in mantle convection simulations, with applications for Martian volcanic and atmospheric evolution. *J. Geophys. Res.*, 112(E7), E07003, doi:10.1029/2006JE002799.

Palguta, J., Anderson, J. D., Schubert, G., and Moore, W. B. (2006). Mass anomalies on Ganymede. *Icarus*, 180:428–441, doi:10.1016/j.icarus.2005.08.020.

Pauer, M. and Breuer, D. (2008). Constraints on the maximum crustal density from gravity-topography modeling: Applications to the southern highlands of Mars. *Earth Planet. Sci. Lett.*, 276:253261, doi:10.1016/j.epsl.2008.09.014.

Pauer, M., Fleming, K., and Čadek, O. (2006). Modeling the dynamic component of the geoid and topography of Venus. *J. Geophys. Res.*, 111, E11012, doi:10.1029/2005JE002511.

Pauer, M., Musiol, S., and Breuer, D. (2010). Detectability of the ocean floor topography in the gravity field of Europa. *J. Geophys. Res.*, 115, E12005, doi:10.1029/2010JE003595.

Peltier, W. R. (1989). *Mantle Convection, Plate Tectonics and Global Dynamics*, chapter Mantle viscosity, pages 389–478. Gordon and Breach, New York.

Phillips, R. J., Zuber, M. T., Smrekar, S. E., Mellon, M. T., Head, J. W., Tanaka, K. L., Putzig, N. E., Milkovich, S. M., Campbell, B. A., Plaut, J. J., Safaeinili, A., Seu, R., Biccari, D., Carter, L. M., Picardi, G., Orosei, R., Mohit, P. S., Heggy, E., Zurek, R. W., Egan, A. F., Giacomoni, E., Russo, F., Cutigni, M., Pettinelli, E., Holt, J. W., Leuschen, C. J., and Marinangeli, L. (2008). Mars north polar deposits: Stratigraphy, age, and geodynamical response. *Science*, 320:1182–1185, doi:10.1126/science.1157546.

Phillips, R. J., Zuber, M. T., Solomon, S. C., Golombek, M. P., Jakosky, B. M., Banerdt, W. B., Smith, D. E., Williams, R. M. E., Hynek, B. M., A., A., and Hauck, S. A. (2001). Ancient geodynamics and global-scale hydrology on Mars. *Science*, 291:2587–2591.

Pratt, J. H. (1855). On the attraction of the Himalaya maintains, an of the elevated regions beyond them, upon the plumb line in India. *Phil. Trans. R. Soc.*, 145:53–100.

Pratt, J. H. (1859). On the deflection of the plumb-line in India, caused by the attraction of the Himalaya maintains and of the elevated regions beyond; and its modification by the compensating effect of a deficiency of matter below the mountain mass. *Phil. Trans. R. Soc.*, 149:745–796.

Rappaport, N. J., Konopliv, A. S., and Kucinskas, A. B. (1999). An improved 360 degree and order model of Venus topography. *Icarus*, 139:19–31.

Reindler, L. and Arkani-Hamed, J. (2003). The strength of the lunar lithosphere. *Icarus*, 162:233–241, doi:10.1016/S0019-1035(03)00007-1.

Richards, M. A. and Hager, B. H. (1984). Geoid anomalies in a dynamic Earth. *J. Geophys. Res.*, 89(B7):5987–6002.

Richter, F. M. (1978). Experiments on the stability of convection rolls in fluids whose viscosity depends on temperature. *J. Fluid Mech.*, 89:553–560.

Rummel, R. and van Gelderen, M. (1995). Meissl scheme – spectral characteristics of physical geodesy. *Manuscripta Geodaetica*, 20:379–385.

Schubert, G., Anderson, J. D., Spohn, T., and McKinnon, W. B. (2003). *Jupiter – The Planet, Satellites and Magnetosphere*, chapter Interior composition, structure and dynamics of the Galilean satellites, pages 281–306. Cambridge Univ. Press, Cambridge.

Schubert, G., Cassen, P., and Young, R. (1979). Subsolidus convective cooling histories of terrestrial planets. *Icarus*, 38:192–211.

Schubert, G., Spohn, T., and Reynolds, R. T. (1986). *Satellites*, chapter Thermal histories, compositions, and internal structures of the moons of the solar system, pages 224–292. University of Arizona Press, Tucson.

Schubert, G., Turcote, D. L., and Olson, P. (2001). *Mantle Convection in the Earth and Planets*. Cambridge University Press, Cambridge.

Schumacher, S. and Breuer, D. (2006). Influence of a variable thermal conductivity on the thermochemical evolution of Mars. *J. Geophys. Res.*, 111, E02006, doi:10.1029/2005JE002429.

Searls, M. L., Banerdt, W. B., and Phillips, R. J. (2006). Utopia and Hellas basins, Mars: Twins separated at birth. *J. Geophys. Res.*, 111, E08005, doi:10.1029/2005JE002666.

Seidelmann, P. K., Archinal, B. A., Ahearn, M. F., Conrad, A., Consolmagno, G. J., Hestroffer, D., Hilton, J. L., Krasinsky, G. A., Neumann, G., Oberst, J., Stooke, P., Tedesco, E. F., Tholen, D. J., Thomas, P. C., and Williams, I. P. (2007). Report of the iau/iagworking group on cartographic coordinates and rotational elements: 2006. *Celestial Mech. Dyn. Astr.*, 98:155180, doi:10.1007/s10569-007-9072-y.

Simons, F. J., Zuber, M. T., and Korenaga, J. (2000). Isostatic response of the Australian lithosphere: Estimation of effective elastic thickness and anisotropy using multitaper spectral analyses. *J. Geophys. Res.*, 105(B8):19,163–19,184.

Simons, M. and Hager, B. H. (1995). Localization of the gravity field and the signature of glacial rebound. *Nature*, 390:500–504.

Simons, M., Solomon, S. C., and Hager, B. H. (1997). Localization of gravity and topography: Constraints on the tectonics and mantle dynamics of Venus. *Geophys. J. Int.*, 131:24–44.

Smith, D., Zuber, M., Solomon, S., Phillips, R., Head, J., Garvin, J., Banerdt, W., Muhleman, D., Pettengill, G., Neumann, G., Lemoine, F., Abshire, J., Aharonson, O., Brown, C., Hauck, S., Ivanov, A., McGovern, P., Zwally, H., and Duxbury, T. (1999). The global topography of Mars and implications for surface evolution. *Science*, 284:14951503.

Smith, D. E., Zuber, M. T., Neukum, G. A., and Lemoine, F. G. (1997). Topography of the moon from the Clementine lidar. *J. Geophys. Res.*, 102:1591–1611.

Smrekar, S. E. and Phillips, R. J. (1991). Venusian highlands: geoid to topography ratios and their implications. *Earth Planet. Sci. Lett.*, 107:582–597, doi:10.1016/0012-821X(91)90103-O.

Sohl, F., Sears, W. D., and Lorenz, R. D. (1995). Tidal dissipation on Titan. *Icarus*, 115:278–294.

Solomatov, V. S. (1995). Scaling of temperature- and stress-dependent viscosity. *Phys. Fluids*, 7:266–274.

Solomon, S. C. and Head, J. W. (1980). Lunar mascon basins: Lava filling, tectonics, and evolution of the lithosphere. *Rev. Geophys.*, 18:107–141.

Spohn, T. (1991). Mantle differentiation and thermal evolution of Mars, Mercury and Venus. *Icarus*, 90:222–236.

Spohn, T., Acuña, M. H., Breuer, D., Golombek, M., Greeley, R., Halliday, A., Hauber, E., Jauman, R., and Sohl, F. (2001a). Geophysical constraints on the evolution of Mars. *Space Sci. Rev.*, 96:231–262.

Spohn, T., Konrad, W., Breuer, D., and Ziethe, R. (2001b). The longevity of lunar volcanism: Implications of thermal evolution calculations with 2D and 3D mantle convection models. *Icarus*, 149:54–65, doi:10.1006/icar.2000.6514.

Stevenson, D. J. (1990). *Origin of the Earth*, chapter Fluid dynamics of core formation, pages 231–249. Oxford Univ. Press.

Stevenson, D. J., Spohn, T., and Schubert, G. (1983). Magnetism and thermal evolution of the terrestrial planets. *Icarus*, 54:466–489.

Tarantola, A. (1987). *Inverse Problem Theory: Methods for Data Fitting and Model Parameter Estimation*. Elsevier, New York.

Tosi, N. (2008). *Numerical modeling of present-day mantle convection*. PhD thesis, Charles University in Prague.

Tsoulis, D. (1999). Spherical harmonic computation with topographic/isostatic coefficients. Technical report, Technical University Munich.

Turcotte, D. L. and Oxburgh, E. R. (1967). Finite amplitude convective cells and continental drift. *J. Fluid Mech.*, 28:29–42.

Turcotte, D. L. and Schubert, G. (2002). *Geodynamics*. Cambridge University Press, 2nd edition.

Turcotte, D. L., Willeman, R. J., Haxby, W. F., and Norberry, J. (1981). Role of membrane stresses in the support of planetary topography. *J. Geophys. Res.*, 86(B5):3951–3959.

Varshalovich, D. A., Moskalev, A. N., and Kjersonskii, V. K. (1988). *Quantum Theory of Angular Momentum*. World Scientic, Singapore.

Čadek, O. (1989). Spherical harmonic approach to the solution of the mantle stress problem. *Stud. Geophys. Geod.*, 33:177–197.

Čadek, O. and Fleitout, L. (1999). A global geoid model with imposed plate velocities and partial layering. *J. Geophys. Res.*, 104(B12):29,055–29,075, doi:10.1029/1999JB900150.

Čadek, O. and Fleitout, L. (2003). Effect of lateral viscosity variations in the top 300 km on the geoid and dynamic topography. *Geophys. J. Int.*, 152(3):566–580, doi:10.1046/j.1365-246X.2003.01859.x.

Čadek, O. and Martinec, Z. (1991). Spherical harmonic expansion of the Earth's crust thickness up to degree and order 30. *Studia geoph. et geod.*, 35(3):151–165.

Čížková, H. (1996). *Modelling the dynamical processes in the Earth mantle*. PhD thesis, Charles University in Prague.

Vescey, L., Hier Majumder, C. A., and Yuen, D. A. (2003). Multiresolution tectonic features over the earth inferred from a wavelet transformed geoid. *Vis. Geosci.*, 8(1):26–44, doi:10.1007/s10069-003-0008-8.

Vezolainen, A. V., Solomatov, V. S., Basilevsky, A. T., and Head, J. W. (2004). Uplift of Beta Regio: Three-dimensional models. *J. Geophys. Res.*, 109(E8), E08007, doi:10.1029/2004JE002259.

Watts, A. B. (2001). *Isostasy and Flexure of the Lithosphere*. Cambridge Univ. Press, Cambridge.

Weertman, J. and Weertman, J. R. (1975). High temperature creep of rock and mantle viscosity. *Annu. Rev. Earth Planet. Sci.*, 3:293–315.

Weinstein, S. A. (1995). The effects of a deep mantle endothermic phase change on the structure of thermal convection in silicate planets. *J. Geophys. Res.*, 100:11.719–11,728.

Wessel, P. and Smith, W. H. F. (1991). Free software helps map and display data. *EOS*, 72(41):441.

Wieczorek, M. (2007). *Planets and Moons*, volume 10 of *Treatise on Geophysics (Editor-in-Chief G. Schubert)*, chapter Gravity and Topography of the Terrestrial Planets, pages 165–206. Elsevier, Amsterodam.

Wieczorek, M. A., Jolliff, B. L., Khan, A., Pritchard, M. E., Weiss, B. P., Williams, J. G., Hood, L. L., Righter, K., Neal, C. R., Shearer, C. K., McCallum, I. S., Tompkins, S., Hawke, B. R., Peterson, C., Gillis, J. J., and Bussey, B. (2006). The constitution and structure of the Lunar interior. *Rev. Mineral. Geochem.*, 60:221–364, doi:10.2138/rmg.2006.60.3.

Wieczorek, M. A. and Phillips, R. J. (1997). The structure and compensation of the lunar highland crust. *J. Geophys. Res.*, 102(E5):10,933–10,943.

Wieczorek, M. A. and Phillips, R. J. (1998). Potential anomalies on the sphere: Application to the thickness of the lunar crust. *J. Geophys. Res.*, 103(E1):1715–1724.

Wieczorek, M. A. and Phillips, R. J. (1999). Lunar multiring basins and the cratering process. *Icarus*, 139:246–259, doi:10.1006/icar.1999.6102.

Wieczorek, M. A. and Simons, F. J. (2005). Localized spectral analysis on the sphere. *Geophys. J. Int.*, 162:655–675, doi:10.1111/j.1365-246X.2005.02687.x.

Wieczorek, M. A. and Zuber, M. T. (2004). Thickness of the Martian crust: Improved constraints from geoid-to-topography ratios. *J. Geophys. Res.*, 109, E01009, doi:10.1029/2003JE002153.

Yuan, D.-N., Sjogren, W. L., Konopliv, A. S., and Kucinskas, A. B. (2001). Gravity field of Mars: A 75th degree and order model. *J. Geophys. Res.*, 106:23,377–23,401.

Zebib, A., Goyal, A. K., and Schubert, G. (1985). Convective motion in a spherical shell. *J. Fluid Mech.*, 152:39–48.

Zebker, H. A., Stiles, B., Hensley, S., Lorenz, R., Kirk, R. L., and Lunine, J. (2009). Size and shape of saturn's moon titan. *Sci*, 324(5929):921–923, doi:10.1126/science.1168905.

Zharkov, V. N., Leontjev, V. V., and Kozenko, A. V. (1985). Models, figures and gravitational moments of the Galilean satelites of Jupiter and icy satellites of Saturn. *Icarus*, 61:92–100.

Zhong, S. (1997). Dynamics of crustal compensation and its influence on crustal isostasy. *J. Geophys. Res.*, 102(B7):15,287–15,299.

Zhong, S. (2002). Effects of lithosphere on the long-wavelength gravity anomalies and their implications for the formation of the Tharsis rise on Mars. *J. Geophys. Res.*, 107(E7), doi:10.1029/2001JE001589.

Zhong, S. and Zuber, M. T. (2001). Degree-1 mantle convection and the crustal dichotomy on Mars. *Earth Planet. Sci. Lett.*, 189:75–84, doi:10.1016/S0012-821X(01)00345-4.

List of Figures

List of Tables

List of Abbreviations

2D, 3D	two, three dimensions; two-,three-dimensional
BA	Bouguer anomaly
BC	boundary conditions
CE	constitutional equation
CGS	centimetre gram second system
CMB	core mantle boundary
CMI	crust mantle interface
DEM	digital elevation model
EM	equation of motion
GTR	geod topography ratio
LHS/RHS	left/right hand side
RE	rheological equation
SI	International System of Units

Appendix A

Spherical Harmonics

A.1 Scalar, vector and tensor spherical harmonics

In many mathematical and physical problems, it is useful to study the analyzed signal not only in the spatial domain, but also its spectral transformation. This allows the examination of its properties connected not to some specific region/interval of time, but rather to certain characteristic wavelengths/periods [e.g., Brokešová, 2007]. In the case of data sets referenced to a plane, the Fourier series can be used for this purpose. For the case of data in the spherical geometry, the common choice is a spectral transformation using spherical harmonic functions . Using this approach, a scalar function $f(r, \vartheta, \varphi)$ can be expressed as the sum of spherical harmonic coefficients $f_{\ell m}(r)$ and scalar spherical harmonic functions $Y_{\ell m}(\vartheta, \varphi)$:

$$f(r, \vartheta, \varphi) = \sum_{\ell=0}^{\infty} \sum_{m=-\ell}^{\ell} f_{\ell m}(r) Y_{\ell m}(\vartheta, \varphi), \tag{A.1}$$

where r is radius, $\vartheta \in \langle 0°, 180° \rangle$ is colatitude, $\varphi \in \langle 0°, 360° \rangle$ is longitude, ℓ is the degree (which determines the characteristic wavelength) and m is the order. The scalar spherical harmonics $Y_{\ell m}(\vartheta, \varphi)$ that represent a complete set of basis functions for the spherical surface geometry are defined as a normalized product of the associated Legendre functions $P_{\ell m}$ (dependent on ϑ) and exponential function (dependent on φ):

$$Y_{\ell m}(\vartheta, \varphi) = (-1)^m N_{\ell m} P_{\ell m}(\cos\vartheta) e^{im\varphi} \qquad \ell \geq 0 \quad m \geq 0, \tag{A.2}$$

$$Y_{\ell m}(\vartheta, \varphi) = (-1)^m Y^*_{\ell |m|}(\vartheta, \varphi) \qquad \ell \geq 0 \quad m < 0, \tag{A.3}$$

where asterisk means complex conjugation and the normalization factor $N_{\ell m}$ is given by:

$$N_{\ell m} = \left[\frac{(2\ell + 1)}{4\pi} \frac{(\ell - m)!}{(\ell + m)!} \right]^{\frac{1}{2}}. \tag{A.4}$$

The associated Legendre functions are the solution of the associated Legendre differential equation and can be expressed by the means of Legendre functions $P_\ell(x)$ (which are the solution of the Legendre differential equation):

$$P_{\ell m}(\cos\vartheta) = (1 - \cos^2\vartheta)^{\frac{m}{2}} \frac{\mathrm{d}^m P_\ell(\cos\vartheta)}{\mathrm{d}(\cos\vartheta)^m} = \sin^m\vartheta \frac{\mathrm{d}^m P_\ell(\cos\vartheta)}{\mathrm{d}(\cos\vartheta)^m}, \tag{A.5}$$

$$P_\ell(x) = \frac{1}{2^\ell \ell!} \frac{\mathrm{d}^\ell}{\mathrm{d}x^\ell} (x^2 - 1)^\ell. \tag{A.6}$$

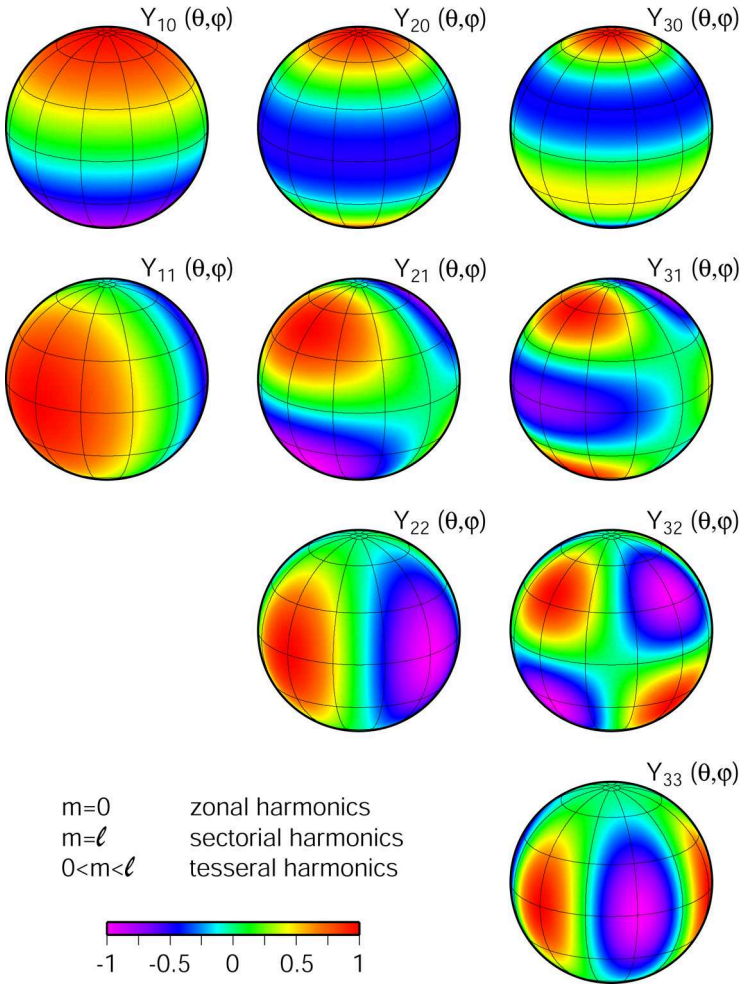

Figure A.1: *Real part of scalar spherical harmonics for degrees ℓ =1, 2, and 3, normalized to the global maximum value 1. Degree $\ell = 0$ (which is not depicted here) represents the global average value i.e. it is constant over the whole sphere. Degree $\ell = 1$ represents the offset from the geometrical center and degree $\ell = 2$ gives the flattening of the sphere. Zonal harmonics ($m = 0$) are always latitudinally symmetric, with ℓ crossings of 0.*

The normalization coefficient $N_{\ell m}$ ensures that the set of basis functions $\{Y_{\ell m}\}$ is orthonormal with respect to the integration over the whole sphere (δ stands for the Kronecker function defined as $\delta_{ij} = 1$ for $i = j$ and 0 otherwise):

$$\int_0^{2\pi}\int_0^{\pi} Y_{\ell m}(\vartheta,\varphi)Y^*_{jk}(\vartheta,\varphi)\sin\vartheta\,\mathrm{d}\vartheta\mathrm{d}\varphi = \delta_{j\ell}\delta_{mk}, \tag{A.7}$$

otherwise it will be only orthogonal (a property that is ensured by definition (A.2)) and additional problem with the normalization of spherical harmonic coefficients appears (see Section A.3). The coefficients $f_{\ell m}(r)$ can be obtained by integrating the product of the function $f(r,\vartheta,\varphi)$ and the corresponding spherical harmonic $Y_{\ell m}(\vartheta,\varphi)$ over the whole sphere:

$$f_{\ell m}(r) = \int_0^{2\pi} \int_0^{\pi} f(r, \vartheta, \varphi) Y^*_{\ell m}(\vartheta, \varphi) \sin\vartheta \, \mathrm{d}\vartheta \, \mathrm{d}\varphi. \tag{A.8}$$

If the integrated function f is real, then one can evaluate the coefficients $f_{\ell m}$ for $m < 0$ using the symmetry from the equation (A.3):

$$f_{\ell,-m}(r) = (-1)^m f^*_{\ell m}(r) \tag{A.9}$$

To examine how important the contribution of each harmonic degree is to the overall signal, the power spectrum of the analyzed function f can be constructed. The power spectrum S_ℓ for any degree ℓ is defined as:

$$S_\ell(f) = \sum_{m=-\ell}^{\ell} f_{\ell m} f^*_{\ell m} \tag{A.10}$$

For a similar case, but this time considering a vector function $\boldsymbol{f}(r, \vartheta, \varphi)$, a series analogous to the equation (A.1) can be employed:

$$\boldsymbol{f}(r, \vartheta, \varphi) = \sum_{\ell=0}^{\infty} \sum_{m=-\ell}^{\ell} \sum_{j=|\ell-1|}^{\ell+1} f^j_{\ell m}(r) \, \boldsymbol{Y}^j_{\ell m}(\vartheta, \varphi), \tag{A.11}$$

where $\boldsymbol{Y}^j_{\ell m}$ are the vector spherical harmonic functions, defined using the so-called cyclic unit vector basis $\boldsymbol{e}_\mu$ ($\mu = -1, 0, 1$). These vectors are constructed in the following way:

$$\boldsymbol{e}_1 = -\frac{1}{\sqrt{2}}(\boldsymbol{e}_\mathrm{x} + i\boldsymbol{e}_\mathrm{y}), \tag{A.12}$$

$$\boldsymbol{e}_0 = \boldsymbol{e}_\mathrm{z}, \tag{A.13}$$

$$\boldsymbol{e}_{-1} = \frac{1}{\sqrt{2}}(\boldsymbol{e}_\mathrm{x} - i\boldsymbol{e}_\mathrm{y}), \tag{A.14}$$

where $\boldsymbol{e}_\mathrm{x}$, $\boldsymbol{e}_\mathrm{y}$, $\boldsymbol{e}_\mathrm{z}$ are the Cartesian basis vectors. The vectors $\boldsymbol{e}_\mu$ have following properties:

$$\boldsymbol{e}^*_\mu = (-1)^\mu \boldsymbol{e}_{-\mu} \tag{A.15}$$

$$\boldsymbol{e}^*_\mu \cdot \boldsymbol{e}_{\mu'} = (-1)^\mu \boldsymbol{e}_{-\mu} \cdot \boldsymbol{e}_{\mu'} = \delta_{\mu\mu'}. \tag{A.16}$$

Employing these basis functions, the vector spherical harmonics $\boldsymbol{Y}^j_{\ell m}$ can be defined in the following way (see e.g., Jones [1985]) to satisfy the condition of orthonormality:

$$\boldsymbol{Y}^j_{\ell m}(\vartheta, \varphi) = \sum_{\mu=-1}^{1} \sum_{\nu=-j}^{j} C^{\ell m}_{j\nu 1\mu} Y_{j\nu}(\vartheta, \varphi) \boldsymbol{e}_\mu, \tag{A.17}$$

$$\int_0^{\pi} \int_0^{2\pi} \boldsymbol{Y}^{j_1}_{\ell_1 m_1}(\vartheta, \varphi) \cdot \boldsymbol{Y}^{j_2\,*}_{\ell_2 m_2}(\vartheta, \varphi) \sin\vartheta \, \mathrm{d}\vartheta \mathrm{d}\varphi = \delta_{\ell_1\ell_2}\delta_{m_1 m_2}\delta_{j_1 j_2}, \tag{A.18}$$

where $C^{\ell m}_{j\nu k\mu}$ are the Clebsh-Gordan coefficients (for their definition see e.g., Varshalovich et al. [1988]). The spherical harmonic coefficients $f^j_{\ell m}(r)$ used in the equation (A.11) can then be derived using relationship similar to equation (A.8):

$$f^j_{\ell m} = \int_0^{\pi} \int_0^{2\pi} \boldsymbol{f}(\vartheta,\varphi) \cdot \boldsymbol{Y}^{j\,*}_{\ell m}(\vartheta,\varphi) \sin\vartheta \,\mathrm{d}\vartheta\mathrm{d}\varphi. \tag{A.19}$$

If the considered vector function $\boldsymbol{f}(r,\vartheta,\varphi)$ is real, then taking advantage of the Clebsh-Gordan coefficients' symmetries, we can again evaluate $\boldsymbol{Y}^{\ell}_{\ell,-m}$ and therefore also $f^j_{\ell,-m}$ using the corresponding terms with $m \geq 0$:

$$\boldsymbol{Y}^{j}_{\ell,-m} = (-1)^{\ell+m+j+1} \boldsymbol{Y}^{j\,*}_{\ell m} \qquad\qquad f^j_{\ell,-m} = (-1)^{\ell+m+j+1} f^{j\,*}_{\ell m} \tag{A.20}$$

If the function $\boldsymbol{f}$ describes a non-divergent field (i.e. $\nabla.\boldsymbol{f} = 0$) then it could be divided into toroidal (for which it holds $\boldsymbol{f}_{\mathrm{T}} \cdot \boldsymbol{e}_{\mathrm{r}} = 0$) and poloidal (for which $(\nabla \times \boldsymbol{f}_{\mathrm{P}}) \cdot \boldsymbol{e}_{\mathrm{r}} = 0$) components. The coefficients $f^{\ell}_{\ell m}$ then describe the toroidal part of the field and the coefficients $f^{\ell\pm1}_{\ell m}$ describe the poloidal part. If the field becomes divergent, then the toroidal field still satisfies $\nabla \cdot \boldsymbol{f}_{\mathrm{T}} = 0$, but the remaining part of the field (called spheroidal) satisfies only $(\nabla \times \boldsymbol{f}_{\mathrm{S}}) \cdot \boldsymbol{e}_{\mathrm{r}} = 0$ [e.g., Matyska, 2005]. These two parts of the vector field can be nevertheless still described by the coefficients $f^{\ell}_{\ell m}$ and $f^{\ell\pm1}_{\ell m}$, respectively [e.g., Jones, 1985].

Finally, the tensor spherical field $\boldsymbol{F}(r,\vartheta,\varphi)$ can also be described by a series similar to the equations (A.1) and (A.11) employing the set of coefficients $F^{jk}_{\ell m}$:

$$\boldsymbol{F}(r,\vartheta,\varphi) = \sum_{\ell=0}^{\infty} \sum_{m=-\ell}^{\ell} \sum_{k=0}^{2} \sum_{j=|\ell-k|}^{\ell+k} F^{jk}_{\ell m}(r)\, \boldsymbol{Y}^{jk}_{\ell m}(\vartheta,\varphi) \tag{A.21}$$

where $\boldsymbol{Y}^{jk}_{\ell m}$ are the tensor spherical harmonic functions defined using the tensor orthogonal basis $\boldsymbol{E}_{k\lambda}$ (which employs again the cyclic unit basis $\boldsymbol{e}_{\mu}$):

$$\boldsymbol{E}_{k\lambda} = \sum_{\mu=-1}^{1} \sum_{\nu=-1}^{1} C^{k\lambda}_{1\mu1\nu} \boldsymbol{e}_{\mu}\boldsymbol{e}_{\nu}. \tag{A.22}$$

Having defined this set of basis functions, the tensor spherical harmonic functions $\boldsymbol{Y}^{jk}_{\ell m}$ are defined by [e.g., Jones, 1985]:

$$\boldsymbol{Y}^{jk}_{\ell m}(\vartheta,\varphi) = \sum_{\mu} \sum_{\nu} C^{\ell m}_{j\nu k\mu} Y_{j\nu}(\vartheta,\varphi) \boldsymbol{E}_{k\mu}, \tag{A.23}$$

which definition satisfies the orthogonality relation:

$$\int_0^{\pi} \int_0^{2\pi} \boldsymbol{Y}^{j_1k_1}_{\ell_1 m_1}(\vartheta,\varphi) : \boldsymbol{Y}^{j_2k_2\,*}_{\ell_2 m_2}(\vartheta,\varphi) \sin\vartheta \,\mathrm{d}\vartheta\mathrm{d}\varphi = \delta_{\ell_1\ell_2}\delta_{m_1m_2}\delta_{j_1j_2}\delta_{k_1k_2}, \tag{A.24}$$

where the : operator denotes the double-dot product (for second order tensors with components A_{ij} and B_{ij} it is defined as $\boldsymbol{A} : \boldsymbol{B} = \sum_i \sum_j A_{ij}B_{ij}$). The coefficients $F^{jk}_{\ell m}$ used in equation (A.21) can be obtained in a similar manner as in the previous two cases (A.8) and (A.19):

$$F^{jk}_{\ell m}(r) = \int_0^{\pi} \int_0^{2\pi} \boldsymbol{F}(r,\vartheta,\varphi) : \boldsymbol{Y}^{jk\,*}_{\ell m}(\vartheta,\varphi) \sin\vartheta \,\mathrm{d}\vartheta\mathrm{d}\varphi. \tag{A.25}$$

If we compare the definition of vector spherical harmonics $\boldsymbol{Y}^{j}_{\ell m}$ (A.17) and tensor spherical harmonics $\boldsymbol{Y}^{jk}_{\ell m}$ (A.23) then we see that the former one are special cases of the latter with $k = 1$ (see also discussion in Jones [1985]). The above described system of orthonormal spherical harmonic functions have moreover an advantage that the coefficients $F^{j0}_{\ell m}$ represent the trace of the tensor function, while $F^{j1}_{\ell m}$ stands for the antisymmetric and $F^{j2}_{\ell m}$ for the deviatoric part of the tensor function $\boldsymbol{F}$.

A.2 Operations with spherical harmonics

Here some useful formulae for the operations with spherical harmonic functions $Y_{\ell m}$, $\boldsymbol{Y}^{j}_{\ell m}$ and $\boldsymbol{Y}^{jk}_{\ell m}$ are listed, which come from Edmonds [1960], Varshalovich et al. [1988] and Čadek [priv. comm.]. First, the products of a unit radial vector and different spherical harmonic basis functions are (the term $\{{}^{\ell_1\ \ell_2\ \ell}_{j_1\ j_2\ j}\}$ stands for 6-j Wigner symbol[1]):

$$\boldsymbol{e}_{\mathrm{r}} Y_{\ell m} = \frac{1}{\sqrt{2\ell+1}}(\sqrt{\ell}\ \delta_{j,\ell-1} - \sqrt{\ell+1}\delta_{j,\ell+1})\,\boldsymbol{Y}^{j}_{\ell m}$$

$$\boldsymbol{e}_{\mathrm{r}} \cdot \boldsymbol{Y}^{j}_{\ell m} = \frac{1}{\sqrt{2\ell+1}}(\sqrt{\ell}\delta_{j,\ell-1} - \sqrt{\ell+1}\delta_{j,\ell+1})Y_{\ell m}$$

$$\boldsymbol{e}_{\mathrm{r}} \cdot \boldsymbol{Y}^{jk}_{\ell m} = (-1)^{\ell+j}\sqrt{2k+1}\left[\sqrt{j+1}\left\{\begin{array}{ccc} j & k & \ell \\ 1 & j+1 & 1 \end{array}\right\}\boldsymbol{Y}^{j+1}_{\ell m} - \sqrt{j}\left\{\begin{array}{ccc} j & k & \ell \\ 1 & j-1 & 1 \end{array}\right\}\boldsymbol{Y}^{j-1}_{\ell m}\right]$$

$$\boldsymbol{e}_{\mathrm{r}} \cdot \boldsymbol{Y}^{\ell,0}_{\ell m} = \frac{1}{\sqrt{3(2\ell+1)}}(\sqrt{\ell+1}\,\boldsymbol{Y}^{\ell+1}_{\ell m} - \sqrt{\ell}\,\boldsymbol{Y}^{\ell-1}_{\ell m})$$

$$\boldsymbol{e}_{\mathrm{r}} \cdot \boldsymbol{Y}^{\ell-2,2}_{\ell m} = \sqrt{\frac{\ell-1}{2\ell-1}}\,\boldsymbol{Y}^{\ell-1}_{\ell m}$$

$$\boldsymbol{e}_{\mathrm{r}} \cdot \boldsymbol{Y}^{\ell-1,2}_{\ell m} = \sqrt{\frac{\ell-1}{2(2\ell+1)}}\,\boldsymbol{Y}^{\ell}_{\ell m}$$

$$\boldsymbol{e}_{\mathrm{r}} \cdot \boldsymbol{Y}^{\ell,2}_{\ell m} = \sqrt{\frac{\ell(2\ell-1)}{2\cdot 3\cdot(2\ell+1)(2\ell+3)}}\,\boldsymbol{Y}^{\ell+1}_{\ell m} - \sqrt{\frac{(\ell+1)(2\ell+3)}{2\cdot 3\cdot(2\ell+1)(2\ell-1)}}\,\boldsymbol{Y}^{\ell-1}_{\ell m}$$

$$\boldsymbol{e}_{\mathrm{r}} \cdot \boldsymbol{Y}^{\ell+1,2}_{\ell m} = -\sqrt{\frac{\ell+2}{2(2\ell+1)}}\,\boldsymbol{Y}^{\ell}_{\ell m}$$

$$\boldsymbol{e}_{\mathrm{r}} \cdot \boldsymbol{Y}^{\ell+2,2}_{\ell m} = -\sqrt{\frac{\ell+2}{2\ell+3}}\,\boldsymbol{Y}^{\ell+1}_{\ell m}$$

[1]Named after Jenö Pál Wigner (17th November 1902–1st January 1995), Hungarian born physicist and mathematician, who received the Nobel Prize in Physics (1963) for his contributions to nuclear physics.

$$(\boldsymbol{f}\cdot\boldsymbol{e}_{\rm r})\boldsymbol{e}_{\rm r}=\sum_{\ell m}\frac{1}{2\ell+1}\times$$

$$\times\left\{\left[\ell f_{\ell m}^{\ell-1}-\sqrt{\ell(\ell+1)}f_{\ell m}^{\ell+1}\right]\boldsymbol{Y}_{\ell m}^{\ell-1}-\left[\sqrt{\ell(\ell+1)}f_{\ell m}^{\ell-1}-(\ell+1)f_{\ell m}^{\ell+1}\right]\boldsymbol{Y}_{\ell m}^{\ell+1}\right\}$$

$$\boldsymbol{f}-(\boldsymbol{f}\cdot\boldsymbol{e}_{\rm r})\boldsymbol{e}_{\rm r}=\sum_{\ell m}f_{\ell m}^{\ell}\,\boldsymbol{Y}_{\ell m}^{\ell}+$$

$$+\sum_{\ell m}\frac{1}{2\ell+1}\left\{\left[(\ell+1)f_{\ell m}^{\ell-1}+\sqrt{\ell(\ell+1)}f_{\ell m}^{\ell+1}\right]\boldsymbol{Y}_{\ell m}^{\ell-1}+\left[\sqrt{\ell(\ell+1)}f_{\ell m}^{\ell-1}+\ell f_{\ell m}^{\ell+1}\right]\boldsymbol{Y}_{\ell m}^{\ell+1}\right\}$$

Next, some formulae evaluating the results of differential operators acting on the spherical harmonic functions $Y_{\ell m}$, $\boldsymbol{Y}_{\ell m}^{j}$ and $\boldsymbol{Y}_{\ell m}^{jk}$ are presented:

$$\Delta\left[f(r)Y_{\ell m}\right]=\left[\frac{{\rm d}^2f(r)}{{\rm d}r^2}+\frac{2}{r}\frac{{\rm d}f(r)}{{\rm d}r}-\frac{\ell(\ell+1)f(r)}{r^2}\right]Y_{\ell m}$$

$$\nabla\left[f(r)Y_{\ell m}\right]=\frac{1}{\sqrt{2\ell+1}}\left[\sqrt{\ell}\left(\frac{\rm d}{{\rm d}r}+\frac{\ell+1}{r}\right)f(r)\,\boldsymbol{Y}_{\ell m}^{\ell-1}-\sqrt{\ell+1}\left(\frac{\rm d}{{\rm d}r}-\frac{\ell}{r}\right)f(r)\,\boldsymbol{Y}_{\ell m}^{\ell+1}\right]$$

$$\begin{aligned}\nabla\left[f(r)\,\boldsymbol{Y}_{\ell m}^{j}\right] &= (-1)^{\ell+j+1}\sum_k\sqrt{2k+1}\sqrt{j}\begin{Bmatrix}1 & 1 & k\\ \ell & j-1 & j\end{Bmatrix}\left(\frac{\rm d}{{\rm d}r}+\frac{j+1}{r}\right)f(r)\,\boldsymbol{Y}_{\ell m}^{j-1,k}+\\ &+ (-1)^{\ell+j}\sum_k\sqrt{2k+1}\sqrt{j+1}\begin{Bmatrix}1 & 1 & k\\ \ell & j+1 & j\end{Bmatrix}\left(\frac{\rm d}{{\rm d}r}-\frac{j}{r}\right)f(r)\,\boldsymbol{Y}_{\ell m}^{j+1,k}\end{aligned}$$

$$\nabla\cdot f(r)\,\boldsymbol{Y}_{\ell m}^{j}=\frac{1}{\sqrt{2\ell+1}}\left[\sqrt{\ell}\left(\frac{\rm d}{{\rm d}r}-\frac{\ell-1}{r}\right)\delta_{j,\ell-1}-\sqrt{\ell+1}\left(\frac{\rm d}{{\rm d}r}+\frac{\ell+2}{r}\right)\delta_{j,\ell+1}\right]f(r)Y_{\ell m}$$

$$\begin{aligned}\nabla\times f(r)\,\boldsymbol{Y}_{\ell m}^{j} = &- i\sqrt{6}(-1)^{\ell+j}\sqrt{j+1}\begin{Bmatrix}j & \ell & 1\\ 1 & 1 & j+1\end{Bmatrix}\left(\frac{j}{r}-\frac{\rm d}{{\rm d}r}\right)f(r)\,\boldsymbol{Y}_{\ell m}^{j+1}-\\ &- i\sqrt{6}(-1)^{\ell+j}\sqrt{j}\begin{Bmatrix}j & \ell & 1\\ 1 & 1 & j-1\end{Bmatrix}\left(\frac{j+1}{r}+\frac{\rm d}{{\rm d}r}\right)f(r)\,\boldsymbol{Y}_{\ell m}^{j-1}\end{aligned}$$

$$\Delta\left[f(r)\,\boldsymbol{Y}_{\ell m}^{j}\right]=\left[\frac{{\rm d}^2f(r)}{{\rm d}r^2}+\frac{2}{r}\frac{{\rm d}f(r)}{{\rm d}r}-\frac{j(j+1)f(r)}{r^2}\right]\boldsymbol{Y}_{\ell m}^{j}$$

$$\Delta\left[f(r)\,\boldsymbol{Y}_{\ell m}^{jk}\right]=\left[\frac{{\rm d}^2f(r)}{{\rm d}r^2}+\frac{2}{r}\frac{{\rm d}f(r)}{{\rm d}r}-\frac{j(j+1)f(r)}{r^2}\right]\boldsymbol{Y}_{\ell m}^{jk}$$

$$\nabla\cdot\left[f(r)\,\boldsymbol{Y}_{\ell m}^{jk}\right]=(-1)^{\ell+j}\sqrt{2k+1}\times$$

$$\times\left[\sqrt{j+1}\begin{Bmatrix}1 & j & j+1\\ \ell & 1 & k\end{Bmatrix}\left(\frac{\rm d}{{\rm d}r}-\frac{j}{r}\right)f(r)\,\boldsymbol{Y}_{\ell m}^{j+1}-\sqrt{j}\begin{Bmatrix}1 & j & j-1\\ \ell & 1 & k\end{Bmatrix}\left(\frac{\rm d}{{\rm d}r}+\frac{j+1}{r}\right)f(r)\,\boldsymbol{Y}_{\ell m}^{j-1}\right]$$

A.3 Normalization of the scalar spherical harmonic coefficients

Various works using spherical harmonic formalism make use of different normalization for spherical harmonic functions $Y_{\ell m}(\vartheta, \varphi)$ [e.g., Wieczorek, 2007]. For planetary research purposes, there are two main systems: geophysical (described in Section A.1) and geodetic (also called "4π normalization"). The latter one uses a normalization factor different to (A.4):

$$\bar{N}_{\ell m} = \left[(2 - \delta_{0m})(2\ell + 1)\frac{(\ell - m)!}{(\ell + m)!}\right]^{\frac{1}{2}}, \tag{A.27}$$

which makes the spherical harmonic functions $\bar{Y}_{\ell m}(\vartheta, \varphi)$ only orthogonal, i.e.:

$$\int_0^{2\pi}\int_0^{\pi} \bar{Y}_{\ell m}(\vartheta, \varphi)\bar{Y}^*_{jk}(\vartheta, \varphi)\sin\vartheta \,\mathrm{d}\vartheta \,\mathrm{d}\varphi = 4\pi\delta_{\ell j}\delta_{mk}, \tag{A.28}$$

and subsequently also changes the spherical harmonic analysis formula (A.8) to:

$$\bar{f}_{\ell m}(r) = \frac{1}{4\pi}\int_0^{2\pi}\int_0^{\pi} f(r, \vartheta, \varphi)\bar{Y}^*_{\ell m}(\vartheta, \varphi)\sin\vartheta \,\mathrm{d}\vartheta \,\mathrm{d}\varphi. \tag{A.29}$$

When we then compare formulae (A.29) and (A.8), it is easy to arrive at a relationship between coefficients $f_{\ell m}$ and $\bar{f}_{\ell m}$. This conversion is needed when geodetic normalized coefficients (e.g., data from *Planetary Data System* available on *http://pds-geosciences.wustl.edu/*) are used with geophysically normalized spherical harmonic functions:

$$f_{\ell m} = \sqrt{\frac{4\pi}{2 - \delta_{0m}}}\bar{f}_{\ell m}. \tag{A.30}$$

Another normalization that could be used when working with publicly available data sets is a physical one, where each coefficient is divided by the average value of the studied physical field. For the applications of this approach on the geopotential and shape/topography planetary fields, see the equations (2.41) and (2.43).

A.4 Stress components in spherical harmonic notation

Omitting the toroidal component of the stress tensor $\boldsymbol{\sigma}$ (see Section A.1) we arrive at an expression for stress acting on plane perpendicular to the radial direction ($\boldsymbol{e}_\mathrm{r}$ is a normal vector):

$$\begin{aligned}\boldsymbol{\sigma}\cdot\boldsymbol{e}_\mathrm{r} \;=\; & \sum_{\ell,m}\left(\sigma^{\ell-2,2}_{\ell m}\sqrt{\frac{\ell-1}{2\ell-1}} - \sigma^{\ell,2}_{\ell m}\sqrt{\frac{(\ell+1)(2\ell+3)}{6(2\ell+1)(2\ell-1)}} - \sigma^{\ell,0}_{\ell m}\sqrt{\frac{\ell}{3(2\ell+1)}}\right)\boldsymbol{Y}^{\ell-1}_{\ell m} + \\ & + \left(\sigma^{\ell,2}_{\ell m}\sqrt{\frac{\ell(2\ell-1)}{6(2\ell+1)(2\ell+3)}} + \sigma^{\ell,0}_{\ell m}\sqrt{\frac{\ell+1}{3(2\ell+1)}} - \sigma^{\ell+2,2}_{\ell m}\sqrt{\frac{\ell+2}{2\ell+3}}\right)\boldsymbol{Y}^{\ell+1}_{\ell m},\end{aligned} \tag{A.31}$$

which gives directly the coefficients of the corresponding traction vector $s_{\ell m}^{\ell-1}$ and $s_{\ell m}^{\ell+1}$. If we are interested in the radial component of this vector $(\boldsymbol{\sigma}\cdot\boldsymbol{e}_{\mathrm{r}})\cdot\boldsymbol{e}_{\mathrm{r}}$, it could be evaluated as:

$$\begin{aligned}(\boldsymbol{\sigma}\cdot\boldsymbol{e}_{\mathrm{r}})\cdot\boldsymbol{e}_{\mathrm{r}} &= -\sum_{\ell,m}\left(\frac{1}{\sqrt{3}}\sigma_{\ell m}^{\ell,0}-\sqrt{\frac{\ell(\ell-1)}{(2\ell+1)(2\ell-1)}}\sigma_{\ell m}^{\ell-2,2}-\right. \\ &- \left.\sqrt{\frac{(\ell+1)(\ell+2)}{(2\ell+1)(2\ell+3)}}\sigma_{\ell m}^{\ell+2,2}+\sqrt{\frac{2\ell(\ell+1)}{3(2\ell-1)(2\ell+3)}}\sigma_{\ell m}^{\ell,2}\right)Y_{\ell m}\end{aligned} \tag{A.32}$$

which gives directly the radial traction coefficients ${}^{\mathrm{r}}s_{\ell m}$ (this can be used for the computation of dynamic topography) and also formula for computing the pressure variations $p=\sum_{\ell,m}\frac{1}{\sqrt{3}}\sigma_{\ell m}^{\ell,0}Y_{\ell m}$ (since $\sigma_{\ell m}^{\ell,0}$ represents the trace of tensor $\boldsymbol{\sigma}$). The following term:

$$\begin{aligned}((\boldsymbol{\sigma}\cdot\boldsymbol{e}_{\mathrm{r}})\cdot\boldsymbol{e}_{\mathrm{r}})\boldsymbol{e}_{\mathrm{r}} &= -\sum_{\ell,m}\left(\sqrt{\frac{\ell}{3(2\ell+1)}}\sigma_{\ell m}^{\ell,0}+\ell\sqrt{\frac{2(\ell+1)}{3(2\ell-1)(2\ell+1)(2\ell+3)}}\sigma_{\ell m}^{\ell,2}-\right. \\ &- \frac{\ell}{2\ell+1}\sqrt{\frac{\ell-1}{2\ell-1}}\sigma_{\ell m}^{\ell-2,2}-\frac{1}{2\ell+1}\left.\sqrt{\frac{\ell(\ell+1)(\ell+2)}{2\ell+3}}\sigma_{\ell m}^{\ell+2,2}\right)\boldsymbol{Y}_{\ell m}^{\ell-1}- \\ &- \left(\sqrt{\frac{\ell+1}{3(2\ell+1)}}\sigma_{\ell m}^{\ell,0}+(\ell+1)\sqrt{\frac{2\ell}{3(2\ell-1)(2\ell+1)(2\ell+3)}}\sigma_{\ell m}^{\ell,2}-\right. \\ &- \left.\frac{1}{2\ell+1}\sqrt{\frac{\ell(\ell-1)(\ell+1)}{2\ell-1}}\sigma_{\ell m}^{\ell-2,2}-\frac{\ell+1}{2\ell+1}\sqrt{\frac{\ell+2}{2\ell+3}}\sigma_{\ell m}^{\ell+2,2}\right)\boldsymbol{Y}_{\ell m}^{\ell+1}\end{aligned} \tag{A.33}$$

represents the radial component of the traction vector acting on the spherical surface and the tangential component could be evaluated as:

$$\begin{aligned}\boldsymbol{\sigma}\cdot\boldsymbol{e}_{\mathrm{r}}-((\boldsymbol{\sigma}\cdot\boldsymbol{e}_{\mathrm{r}})\cdot\boldsymbol{e}_{\mathrm{r}})\boldsymbol{e}_{\mathrm{r}} &= \sum_{\ell,m}\left(\frac{\ell+1}{2\ell+1}\sqrt{\frac{\ell-1}{2\ell-1}}\sigma_{\ell m}^{\ell-2,2}-\frac{1}{2\ell+1}\sqrt{\frac{\ell(\ell+1)(\ell+2)}{2\ell+3}}\sigma_{\ell m}^{\ell+2,2}-\right. \\ &- \left.\sqrt{\frac{3(\ell+1)}{2(2\ell-1)(2\ell+1)(2\ell+3)}}\sigma_{\ell m}^{\ell,2}\right)\boldsymbol{Y}_{\ell m}^{\ell-1}- \\ &- \left(\frac{1}{2\ell+1}\sqrt{\frac{\ell(\ell-1)(\ell+1)}{2\ell-1}}\sigma_{\ell m}^{\ell,2}-\frac{\ell}{2\ell+1}\sqrt{\frac{\ell+2}{2\ell+3}}\sigma_{\ell m}^{\ell-2,2}-\right. \\ &- \left.\sqrt{\frac{3\ell}{2(2\ell-1)(2\ell+1)(2\ell+3)}}\sigma_{\ell m}^{\ell+2,2}\right)\boldsymbol{Y}_{\ell m}^{\ell+1}.\end{aligned} \tag{A.34}$$

Appendix B

Finite Difference Approach

If one is interested in solving a set of ordinary differential equations, the way how to approximate derivatives from these equations must be found. One common way to do this is the use of the finite difference method. This method evaluates the derivative of an evenly sampled quantity (with step h) to the desired degree of error ($O(h^n)$). We can make use of three different kinds of differences: forward, backward and central one. These are defined respectively in the following way:

$$\begin{aligned} \triangle_+ f(r) &= f(r+h) - f(r), & \text{(B.1)} \\ \triangle_- f(r) &= f(r) - f(r-h), & \text{(B.2)} \\ \delta f(r) &= f(r+h/2) - f(r-h/2). & \text{(B.3)} \end{aligned}$$

The first two could be related to the derivation by quite simply using a derivation operator D and Taylor series expansion[1] $f(x-a) = \sum_{n=0}^{\infty} \frac{f^{(n)}(a)}{n!}(x-a)^n$:

$$\begin{aligned} \Delta_+ &= hD + \frac{1}{2}h^2D^2 + \frac{1}{3!}h^3D^3 + \cdots = \mathrm{e}^{hD} - 1, & \text{(B.4)} \\ \Delta_- &= hD - \frac{1}{2}h^2D^2 + \frac{1}{3!}h^3D^3 - \cdots = 1 - \mathrm{e}^{-hD}, & \text{(B.5)} \end{aligned}$$

which could be formally inverted and using again Taylor's expansion we obtain:

$$\begin{aligned} hD &= \log(1+\Delta_+) = \Delta_+ - \frac{1}{2}\Delta_+^2 + \frac{1}{3}\Delta_+^3 - \cdots, & \text{(B.6)} \\ hD &= -\log(1-\Delta_-) = \Delta_- + \frac{1}{2}\Delta_-^2 + \frac{1}{3}\Delta_-^3 + \cdots. & \text{(B.7)} \end{aligned}$$

This relationships allows us to approximate a first forward/backward derivation to any desired order of error, e.g., the finite difference approximations of the second order are:

$$D_+ f(r) = \frac{\Delta_+ f(r) - \frac{1}{2}\Delta_+^2 f(r) + O(h^3)}{h} = -\frac{f(r+2h) - 4f(r+h) + 3f(r)}{2h} + O(h^2), \quad \text{(B.8)}$$

$$D_- f(r) = \frac{\Delta_- f(r) + \frac{1}{2}\Delta_-^2 f(r) + O(h^3)}{h} = \frac{f(r-2h) - 4f(r-h) + 3f(r)}{2h} + O(h^2). \quad \text{(B.9)}$$

[1] Named after Brook Taylor (18th August 1685–30th November 1731), English mathematician.

If we need to evaluate a second (or any higher) forward/backward derivation, an analogous approach based on (B.6) and (B.7) could be used:

$$h^2D^2 = \Delta_+^2 - \Delta_+^3 + \frac{11}{12}\Delta_+^4 - \cdots, \tag{B.10}$$

$$h^2D^2 = \Delta_-^2 + \Delta_-^3 + \frac{11}{12}\Delta_+^4 + \cdots, \tag{B.11}$$

which gives in the finite difference approximation of the first order the following expressions for the second derivative:

$$D_+^2 f(r) = \frac{\Delta_+^2 f(r) + O(h^3)}{h^2} = \frac{f(r+2h) - 2f(r+h) + f(r)}{h^2} + O(h), \tag{B.12}$$

$$D_-^2 f(r) = \frac{\Delta_-^2 f(r) + O(h^3)}{h^2} = \frac{f(r-2h) - 2f(r-h) + f(r)}{h^2} + O(h). \tag{B.13}$$

Returning back to the last of the above mentioned differences, the central one, the following properties could be used for its evaluation in a similar way as for the other cases:

$$\Delta_+ + \Delta_- = \exp(hD) - \exp(-hD) = 2\sinh(hD), \tag{B.14}$$

$$\delta = 2\sinh\left(\frac{hD}{2}\right) \qquad \text{for step } h \to \frac{h}{2}, \tag{B.15}$$

$$hD = 2\,\mathrm{arcsinh}\left(\frac{\delta}{2}\right) = \delta - \frac{1}{24}\delta^3 - \frac{3}{640}\delta^5 - \cdots, \tag{B.16}$$

$$Df(r) = \frac{\delta f(r) + O(h^3)}{h}\Big|_{\frac{h}{2}\to h} = \frac{f(r+h) - f(r-h)}{2h} + O(h^2), \tag{B.17}$$

$$D^2 f(r) = \frac{\delta^2 f(r) + O(h^4)}{h^2} = \frac{f(r+h) - 2f(r) + f(r-h)}{h^2} + O(h^2). \tag{B.18}$$

Appendix C

Published Papers

This chapter contains texts of three papers prepared during the work on this dissertation. These papers include analysis of long-wavelength gravity and topography of Venus [Pauer et al., 2006], inverse modeling of Martian gravity and topography [Pauer and Breuer, 2008] and forward models simulating a possible gravity field of Europa with prospects for its inversion [Pauer et al., 2010].

C.1 Modeling the dynamic component of the geoid and topography of Venus

C.1.1 Abstract

We analyze the Venusian geoid and topography to determine the relative importance of isostatic, elastic and dynamic compensation mechanisms over different degree ranges. The geoid power spectrum plotted on a log-log scale shows a significant change in its slope at about degree 40, suggesting a transition from a predominantly dynamic compensation mechanism at lower degrees to an isostatic and/or elastic mechanism at higher degrees. We focus on the dynamic compensation in the lower-degree interval. We assume that (1) the flow is whole mantle in style, (2) the long-wavelength geoid and topography are of purely dynamic origin, and (3) the density structure of Venus' mantle can be approximated by a model in which the mass anomaly distribution does not vary with depth. Solving the inverse problem for viscosity within the framework of internal loading theory, we determine the families of viscosity models that are consistent with the observed geoid and topography between degrees 2 and 40. We find that a good fit to the data can be obtained not only for an isoviscous mantle without a pronounced lithosphere, as suggested in some previous studies, but also for models with a high-viscosity lithosphere and a gradual increase in viscosity with depth in the mantle. The overall viscosity increase across the mantle found for the latter group of models is only partially resolved, but profiles with a ∼100-km-thick lithosphere and a viscosity increasing with depth by a factor of 10–80, hence similar to viscosity profiles expected in the Earth's mantle, are among the best fitting models.[1]

[1]published as: Pauer, M., K. Fleming, and O. Čadek (2006), Modeling the dynamic component of the geoid and topography of Venus, J. Geophys. Res., 111, E11012, doi:10.1029/2005JE002511.

C.1.2 Introduction

Two potentially important sources of information about the internal structure and dynamics of planetary bodies are the geoid and topography. A number of efforts have been made to explain the relationship between these datasets for Venus, either using the concept of isostasy [e.g., *Bowin*, 1983; *Smrekar and Phillips*, 1991; *Kucinskas and Turcotte*, 1994; *Arkani-Hamed*, 1996], elasticity [e.g., *Sandwell and Schubert*, 1992; *Johnson and Sandwell*, 1994; *Barnett et al.*, 2002], or within the framework of internal-loading theory [e.g., *Kiefer et al.*, 1986; *Herrick and Phillips*, 1992; *Simons et al.*, 1994] and thermal-convection modeling [e.g., *Kiefer and Hager*, 1991a,1992; *Moresi and Parsons*, 1995; *Ratcliff et al.*, 1995; *Solomatov and Moresi*, 1996; *Kiefer and Kellogg*, 1998; *Dubuffet et al.*, 2000]. Such studies have been carried out both regionally [*Herrick et al.*, 1989; *Smrekar and Phillips*, 1991; *Grimm and Phillips*, 1991, 1992; *Phillips*, 1994; *Moore and Schubert*, 1995] and globally [*Kiefer et al.*, 1986; *Simons et al.*, 1994; *McKenzie*, 1994; *Smrekar*, 1994; *Arkani-Hamed*, 1996; *Simons et al.*, 1997], with the aim of determining which topographic features are maintained by forces within the lithosphere, and which require dynamic support from the deeper mantle. Some of the above studies have also provided estimates of the average thickness of the thermal-boundary layer on Venus, with values ranging between a few tens of kilometers up to 300 km.

In the present paper, we analyze the relationship between the geoid and topography on Venus over a global scale, examining the relative importance of three end-member compensation mechanisms: Airy isostasy, elasticity and mantle flow driven by internal loads. As demonstrated in previous studies [e.g., *Simons et al.*, 1997], there is a high correlation between the geoid and topography of Venus, with a large admittance at low degrees that decays rapidly with increasing degree. Such behavior cannot be explained by a simple Airy model with a single depth of compensation [*Kiefer et al.*, 1986; *Arkani-Hamed*, 1996; *Simons et al.*, 1997]. Elastic flexure is potentially important on a regional scale [e.g., *Barnett et al.*, 2002], but its role at long wavelengths is probably limited. In the present paper, we first reexamine the applicability of the Airy isostatic and elastic mechanisms on a global scale, and compare our results with previously published studies. Our focus will then turn to the importance of dynamic mantle processes for lower-degree observations. This will allow us to place some constraints on the mantle viscosity structure of Venus, one of the planet's least-known characteristics.

Our work is motivated by similar efforts that have been carried out for the Earth [e.g., *Hager and Clayton*, 1989; *Ricard et al.*, 1993; *Forte et al.*, 1994; *King*, 1995a; *Čadek and Fleitout*, 1999]. It has been shown that the Earth's geoid at low degrees is dynamic in origin [*Ricard et al.*, 1984; *Richards and Hager*, 1984]. Our understanding of the relatiornship between the long-wavelength non-hydrostatic geoid and the dynamic processes in the mantle has been facilitated by seismic tomographic imaging that provides important information about the internal structure of the Earth [e.g.,*van der Hilst et al.* 1997; *Bijwaard et al.*, 1998; *Montelli et al.*, 2004]. The analysis of the observed geoid in conjunction with seismic tomographic information allows constraints to be placed on the viscosity variations in the Earth's mantle, and the style of mantle convection in general [e.g., *Ricard et al.*, 1993; *Le Stunff and Ricard*, 1997; *Čadek and Fleitout*, 2003]. The mantle flow also deforms the surface of the Earth and thus contributes to its long-wavelength surface topography. However, the

interpretation of the observed topography is difficult since most of it is related to the isostatic compensation of continental lithosphere (for further discussion of the dynamic topography on the Earth, see e.g., *Colin and Fleitout* [1990], *Gurnis* [1990], *Forte et al.* [1993b], *Le Stunff and Ricard* [1995], *Čadek and Fleitout* [1999,2003], *Panasyuk and Hager* [2000]).

Unfortunately, there is no seismological information about the internal structure of Venus. To overcome the lack of such data, we must adopt several simplifications. First, we will assume that the observed long-wavelength geoid and topography are of a purely dynamic origin at low degrees. In other words, we will assume that the long-wavelength geoid on Venus has a similar nature to the Earth. In contrast to the Earth, however, we will also assume that the long-wavelength surface topography is maintained dynamically. This assumption is motivated by the high values of admittance at low degrees and justified by the presumed absence of plate tectonics, and the probable lack of Earth-like continents on Venus. Second, we assume that the lateral distribution of mass anomalies in Venus' mantle does not change with depth. In other words, we will use a density model averaged between the surface and the core-mantle boundary. This is clearly an oversimplification, but we should remember that the order of this simplification is similar to that for the case of Airy isostasy where all density anomalies within the lithosphere are approximated by a surface mass located at a single depth. Moreover, if plumes play an important role in the mantle dynamics of Venus, as has been suggested by some authors [e.g., *Phillips et al.*, 1991; *Bindschadler et al.*, 1992; *Kiefer and Hager*, 1992; *Phillips and Hansen*, 1998; *Vezolainen et al.*, 2004], then the effect this assumption has on our final results may not be too significant.

In contrast to previous works [e.g. *Kiefer et al.*, 1986], we will also test models with a stiff lithosphere, and in addition will examine the effect of two prominent topographic features, Ishtar Terra and Aphrodite Terra, on the solution of the inverse problem. Based on these analyses, we will (i) determine whether a dynamic model can explain the observed geoid and topography at lower degrees and (ii) infer a family of viscosity profiles that are compatible with the long-wavelength geoid and topography on Venus.

We proceed as follows. In section 2, we compare and contrast the geoid and topography fields of Venus with those of the Earth. Then in section 3, we reexamine the applicability of simple Airy isostatic and elasticity models to explain the relationship between the geoid and topography. In section 4, we present a dynamic model of the long-wavelength geoid and topography of Venus, and attempt to infer feasible mantle viscosity profiles. The plausibility of the dynamic model and the inferred viscosity profiles is discussed in section 5 where we also give a summary of our findings. The formulas required for the spectral analysis and an assessment of the consequence of our assumption of depth-independent density anomalies are provided in the appendices.

C.1.3 Geoid and Topography of Venus

The input data of this study are spherical harmonic models of the Venusian geoid and topography, namely the geoid model MGNP180U [*Konopliv et al.*, 1999] and the topography model shtjv360.a02 [*Rappaport et al.*, 1999] (available at http://pds-geosciences.wustl.edu). These models were originally provided up to spherical harmonic degree 180 (geoid) and 360 (topography). In the present study, we will only employ them up to degree 90 because of potentially large uncertainties in determining the geoid coefficients at higher degrees (see

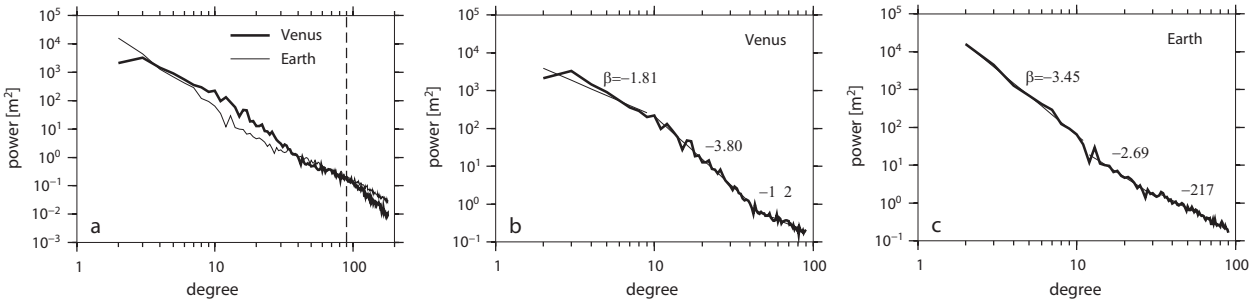

Figure C.1.1: *a) Comparing the geoid power spectra of Venus and the Earth. For the normalization of the spectra, see Appendix A. The vertical dashed line marks the upper bound of the spectral interval considered in the present paper ($\ell_{\max} = 90$). b) Power spectrum of Venus' geoid. The decay of the spectrum can be approximated by three linear segments of different slopes β (equation 1). c) The same as b) but for the Earth's non-hydrostatic geoid.*

Fig. 6 in *Konopliv et al.* [1999]). Over this spectral interval ($\ell = 2-90$), the new models do not differ significantly from earlier models of the Venusian topography and geoid [*Konopliv and Sjogren*, 1994; *Rappaport and Plaut*, 1994], whose properties, including their relationship to Venus' surface tectonics, have been extensively discussed in the literature [e.g. *Simons et al.*, 1997].

The power spectra of the geoid of Venus and the Earth are compared in Figure 1 (for the definition of the spectra, see Appendix A). The decay of the power of the Venusian geoid with increasing degree is similar to that observed for the Earth (Figure 1a). However, in contrast to the Earth, the Venusian geoid shows a smaller amplitude at degree 2 and higher amplitudes in the intermediate-degree range ($\ell = 8 - 30$). To a first approximation, the power spectrum, S_ℓ, decays with degree ℓ in a power-law manner,

$$S_\ell \sim \ell^\beta \tag{1}$$

where $\beta = -3.03$ over the degree range $2 - 90$. However, a more detailed analysis shows that the decay is not uniform, but can be divided into three intervals (Figure 1b) with logarithmic slopes of -1.81 ($\ell = 2-9$), -3.80 ($10-40$) and -1.82 ($41-90$). The change in the slope around degree 10 remains significant even if the anomalous degree 2 is excluded from the analysis, resulting in the slopes for the first two intervals being now -2.48 for $\ell = 3-11$ and -3.89 for $\ell = 12 - 40$. The changes in the slope may be an indication that different mechanisms are responsible for the generation of the geoid at different wavelengths. For the case of the Earth (Figure 1c), the slope of the spectrum changes at around degrees 10 and 30 [*Čížková et al.*, 1996]. It has been shown that the Earth's geoid at the lowermost degrees is predominantly generated by flows in the deep mantle [*Ricard et al.*, 1984; *Richards and Hager*, 1984]. Lithospheric contributions dominate the geoid signal above degree 30, while for ℓ between 10 and 30, both dynamic and lithospheric contributions may be important [*LeStunff and Ricard*, 1995; *Kido and Čadek*, 1997]. The question therefore arises as to whether the changes in slope found in the Venusian geoid spectrum can be interpreted in a similar manner. It is tempting to speculate that the Venusian geoid is of a purely dynamic origin at low degrees and of a predominantly lithospheric origin above degree ~ 40. One

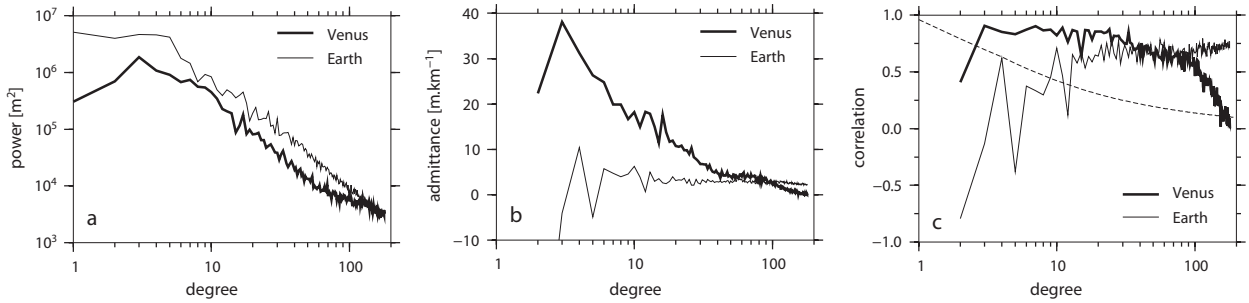

Figure C.1.2: *a) Comparing the power spectra of the topography of Venus and the equivalent-rock topography of the Earth. b) The admittance ratios (equation A9) for Venus and the Earth. c) Degree-by-degree correlation (equation A6) between the geoid and topography for Venus and the Earth. The dotted line marks the 95% confidence level (equation A7).*

must, however, keep in mind that the slope of the spectrum may be influenced by the damping applied during the construction of the spherical harmonic model. The shape of the power spectrum and other spectral characteristics (see Figure 2, discussed below) indeed indicate that the regularization and data uncertainties may have influenced the spherical harmonic coefficients at degrees higher than ~ 90. It is not fully clear, however, how much the lower-degree coefficients are affected.

The topography of Venus is significantly smaller than that of the Earth. As illustrated in Figure 2a, the total power of topography is approximately three times smaller on Venus than on the Earth. Since the geoid anomalies on both planets are comparable in magnitude, the admittance ratio (equation A9) is significantly higher for Venus than for the Earth (Figure 2b). Note that the slope of the admittance curve changes sharply at degrees 40 and 90. While the change around degree 90 may be an artifact associated with the construction of the spherical harmonic models, the change of slope at degree 40 probably reflects a transition between two different mechanisms generating the gravity field of Venus. The topography on Venus is well correlated with the geoid (Figure 2c) up to degree ~ 100, after which the slope of the correlation curve changes, such that by degree 150 it falls below the 95% confidence level. Unlike for the Earth, the correlation is also significant at lower degrees ($\ell \geq 3$). The low correlation between the geoid and topography at low degrees for the Earth is usually attributed to the continents, which contribute the most to the long-wavelength topographic signal, but induce negligible undulations in the low-degree geoid since they are very close to isostatic equilibrium. The long-wavelength geoid is thus mostly related to the dynamic processes driven by density anomalies in the deep mantle [*Ricard et al.*, 1984; *Richards and Hager*, 1984]. For Venus, the significant correlation between the geoid and topography at low degrees, together with a relatively high admittance ratio, may indicate that a significant portion of the long-wavelength topography has a dynamic origin.

C.1.4 Airy Isostasy and Elastic Flexure

The concept of isostasy is based on the assumption that the lithostatic pressure at some depth, usually called the depth of compensation, is laterally homogeneous. In other words,

at any point (θ, ϕ) it holds that,

$$\int_{a-d}^{a+t(\theta,\phi)} \rho(r,\theta,\phi) r^2 \mathrm{d}r = \text{const.} \tag{2}$$

where a is the mean radius of the planet, d is the depth of compensation, t is the topographic height at a point (θ, ϕ) relative to the mean radius of the planet and ρ is the density. Since the density structure of Venus is poorly known, equation (2) is usually written in the simplified form corresponding to the standard Airy isostatic model [*Lambeck*, 1988]. For any degree $\ell > 0$, equation (2) can be rewritten in the following form:

$$\rho_\mathrm{s} t_{\ell m} a^2 + \Delta\rho w_{\ell m} (a - d_\mathrm{ADC})^2 = 0 \tag{3}$$

where ρ_s is the density of surface rocks, $t_{\ell m}$ is the spherical harmonic coefficient of the surface topography, $w_{\ell m}$ is the spherical harmonic coefficient of the topography of a density interface located at a depth d_ADC, also often termed the apparent depth of compensation (ADC), and $\Delta\rho$ is the density contrast across this interface. The value of d_ADC is usually interpreted as the crustal thickness. In equation (3), the depth-dependent density ρ in the integrand of equation (2) has been replaced by the masses $\rho_\mathrm{s} t_{\ell m}$ and $w_{\ell m}\Delta\rho$, approximating the real topographic anomalies. The geoid anomalies h induced by such an isostatically compensated system only depend upon the density ρ_s and the apparent depth of compensation d_ADC [*Lambeck*, 1988],

$$h_{\ell m} = \frac{4\pi a G \rho_\mathrm{s}}{g_0 (2\ell + 1)} \left[1 - \left(\frac{a - d_\mathrm{ADC}}{a} \right)^\ell \right] t_{\ell m} \tag{4}$$

where G is the gravitational constant and g_0 is the mean value of gravitational acceleration on the surface. The simple relationship between the geoid and the depth of compensation has been used in a number of studies that aimed to determine whether a single value of d_ADC can explain the observed geoid over the whole degree range available [*Kiefer et al.*, 1986; *Arkani-Hamed*, 1996; *Simons et al.*, 1997]. We will repeat this inversion for the most recent models of Venus' geoid and topography now available. We assume that $\rho_\mathrm{s} = 2900$ kg m^{-3}, and determine the value of d_ADC that best predicts the observed geoid for each degree. The inverse problem is formulated as a degree-by-degree minimization of the misfit

$$M_\ell^\mathrm{iso}(d_\mathrm{ADC}) = \sum_{m=-\ell}^{\ell} |h_{\ell m}^\mathrm{obs} - h_{\ell m}^\mathrm{pred}(d_\mathrm{ADC})|^2 \tag{5}$$

where $h_{\ell m}^\mathrm{obs}$ and $h_{\ell m}^\mathrm{pred}$ are the spherical harmonic coefficients of the observed geoid and the geoid predicted for the apparent depth of compensation d_ADC, respectively. To determine $h_{\ell m}^\mathrm{pred}$, we use equation (4). This equation does not include the viscous adjustment due to selfgravitation that was considered by *Kiefer et al.*, [1986]. We note, however, that the results of this inversion do not differ significantly from those that would be obtained if the effect of selfgravitation were taken into account.

The optimum values of ADC as a function of degree ℓ obtained by the minimization of equation (5) are presented in Figure 3a. These results are generally in agreement with similar, previously published analyses [*Kiefer et al.*, 1986; *Arkani-Hamed*, 1996; *Simons*

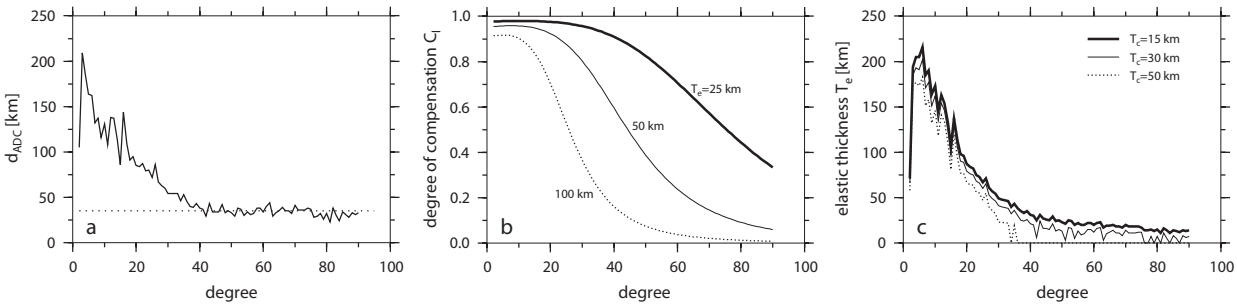

Figure C.1.3: *a) The apparent depth of compensation $d_{\rm ADC}$ of the surface topography on Venus as a function of spherical harmonic degree ℓ. b) The degree of compensation for an elastic lithosphere of various thicknesses. c) The optimum elastic lithosphere thickness as a function of spherical harmonic degree ℓ computed for three values of crustal thickness T_c.*

et al., 1997]. We therefore conclude that the geoid and topographic data in the spectral interval under consideration are inconsistent with a single ADC. This is most apparent between degrees 2 and 40, where a gradual decrease in the ADC is observed, from a value greater than 200 km at degree 3 to less than 50 km for $\ell > 35$. From degree ~ 40, the ADC values stabilize and more or less randomly vary between 25 and 50 km. The geoid spectrum can therefore be divided into two parts. The first corresponds to degrees 2-40, where the geoid signal cannot be explained by an Airy isostasy model with a single ADC. The second part ($\ell > 40$) suggests that an Airy isostatic model with $d_{\rm ADC} = 35$ km is a feasible explanation for a significant part of the geoid signal at higher degrees.

As mentioned in the introduction, a number of studies have attempted to explain the relationship between the geoid and topography using the concept of an elastic lithosphere [e.g., *Sandwell and Schubert*, 1992; *Johnson and Sandwell*, 1994]. *Barnett et al.* [2002] estimated the elastic lithosphere thickness for profiles across various locations on Venus corresponding to different geological features, and found that a value of 25 km fits almost all observed profiles within uncertainty for a crustal thickness of 16 km. They also found that this result was only weakly dependent upon crustal thickness, with elastic thickness varying by only 5 km when crustal thickness was increased to 25-30 km. We will now consider the effect of elasticity on the relationship between the geoid and topography over a global scale, using a similar spectral technique as applied to the isostatic case. We use the formula for the deformation of a thin spherical shell derived by *Turcotte et al.* [1981]. First, we rewrite equation (3) for the Airy isostasy in the more general form:

$$C_\ell \rho_{\rm s} t_{\ell m} a^2 + \Delta\rho w_{\ell m} (a - d_{\rm ADC})^2 = 0 \qquad (6)$$

where C_ℓ is the degree of compensation at degree ℓ ($0 \le C_\ell \le 1$). If the lithosphere is rigid, the deflection w due to the surface topographic loading is zero and $C = 0$. In contrast, if the lithosphere has no strength, $C = 1$, and equation (6) reduces to simple Airy isostasy. For the case where the lithosphere is elastic, we can calculate C_ℓ using formula (27) in *Turcotte et al.* [1981]. This formula takes into account both flexural and membrane stresses and is especially useful for bodies with a smaller radius, such as Mars, where the role of membrane stress is larger [*Turcotte et al.* 1981, 2002]. For Venus on the other hand, due to its larger

radius, membrane stresses are not so important, and we find that C_ℓ is greater than 0.9 between degrees 2–40 for the elastic lithosphere thickness of 25 km found by *Barnett et al.* [2002] (Figure 3b). This means that at low degrees, the effect of an elastic lithosphere of this thickness would not differ much from pure Airy isostasy.

Using equation (6) instead of (3) and replacing d_{ADC} by a crustal thickness T_{c}, we can modify equation (4) to obtain the formula for the geoid heights induced by surface topography t for the case of an elastic lithosphere thickness T_{e} [cf. *Turcotte et al.*, 1981]:

$$h_{\ell m} = \frac{4\pi a G \rho_{\mathrm{s}}}{g_0(2\ell+1)} \left[1 - C_\ell(T_e) \left(\frac{a - T_c}{a}\right)^\ell\right] t_{\ell m} \tag{7}$$

Applying equation (7) and following a similar inverse procedure as for isostasy, we determine the optimum thickness of the elastic lithosphere degree by degree. We use the same elastic parameters as *Barnett et al.* [2002], and consider three different values of T_{c}: 15 km (close to the 16 km used by *Barnett et al.* [2002]), 30 km and 50 km. The results of this inversion are shown in Figure 3c, where we find that, as with the isostatic results, no single value of T_{e} is optimal between degrees $\ell = 2$ and 40, with values becoming more or less consistent for $\ell > 40$. The most consistent solution for degrees $\ell > 40$ is found for $T_{\mathrm{c}} = 15$ km, with T_{e} ranging between 10 and 30 km, which is close to the result of *Barnett et al.* [2002]. We therefore conclude that the purely isostatic and elasticity end-member compensation mechanisms cannot explain the observed geoid and topography at low degrees ($\ell < 40$). This now leads us to the next section where we apply a dynamic mechanism of compensation.

C.1.5 Dynamic Model of Venus' Geoid and Topography

In our analysis of the forces maintaining surface topography, we have so far neglected the stresses due to viscous flow in the mantle. We have seen, however, that such simple models cannot account for the observed geoid and topography at degrees lower than ~ 40. In this section, we propose an alternative interpretation of the low- and intermediate-degree geoid and topography on Venus, based on mantle flow modeling.

In a viscous mantle, density heterogeneities induce flow. The stresses arising from this flow deform all density interfaces, most importantly the surface and the core-mantle boundary. The gravitational signal due to mantle heterogeneities is therefore a superposition of the contributions from the density anomalies themselves and from the deformation of boundaries, or dynamic topographies, associated with the induced flow [*Richards and Hager*, 1984; *Ricard et al.*, 1984]. The deformation of the density interfaces, that is the shapes and amplitudes of the dynamic topographies, strongly depend upon how the viscosity varies with depth. Predicting the geoid of a dynamic planet therefore requires knowledge of the density and viscosity structure of its mantle. Vice versa, if the geoid is known and an *a priori* density model is available, variations of viscosity with depth can be estimated from inverse modeling [e.g., *Hager and Clayton*, 1989; *Ricard et al.*, 1993; *Forte et al.*, 1994; *King*, 1995a; *Čadek and Fleitout*, 1999].

The major problem in interpreting the Venusian data in terms of a mantle flow model is the absence of information about the planet's internal density structure. To avoid this problem, some authors have studied the relationship between the topography and geoid of

Venus in a selfconsistent manner, using numerical simulations of thermal convection [e.g., *Kiefer and Hager*, 1991a,1992; *Moresi and Parsons*, 1995; *Ratcliff et al.*, 1995; *Solomatov and Moresi*, 1996; *Kiefer and Kellogg*, 1998; *Dubuffet et al.*, 2000], while others have considered simplified (depth-independent) or synthetic (random) density distributions [*Kiefer et al.*, 1986; *Herrick and Phillips*, 1992; *Simons et al.*, 1994] and analyzed the geoid and topography within the framework of internal-loading theory. In this work, we will use the latter approach and will attempt to infer a simple model of the density and viscosity structure of Venus' mantle that can explain the observed geoid and topography at low and intermediate ($\ell < 40$) degrees. We will assume that (i) the geoid and topography in this degree range are of a purely dynamic origin, and (ii) the distribution of the mass anomalies does not vary with depth. We will furthermore assume that (iii) the mantle material is incompressible, (iv) obeys the Newtonian constitutive law, (v) viscosity is only radially dependent, and (vi) both the surface and the core-mantle boundary can be treated as free-slip boundaries. As discussed in the introduction, the assumption of depth-independent mass anomalies is clearly an oversimplification, although it may not be too far from reality. As has been shown for the Earth, the most significant up- and downwellings, namely plumes and slabs, penetrate the mantle more or less vertically [e.g., *Grand*, 1994; *Bijwaard et al.*, 1998; *Montelli et al.*, 2004], suggesting that our depth-independent density model may be a reasonable first approximation. Moreover, if plumes play an important role in the mantle dynamics of Venus, as suggested by some authors [ie.g., *Phillips et al.*, 1991; *Bindschadler et al.*, 1992; *Kiefer and Hager*, 1992; *Phillips and Hansen*, 1998; *Vezolainen et al.*, 2004], the effect such an assumption has on our final results may not be too significant. A test of the validity of this assumption employing tomographic information about the Earth's mantle is given in Appendix B.

We formulate the inverse problem as a minimization of the misfit function $M^{\rm dyn}$, defined as,

$$M^{\rm dyn}(\eta, \delta m) = \sum_{\ell=2}^{40} M_\ell^{\rm dyn}(\eta, \delta m) \tag{8}$$

where

$$M_\ell^{\rm dyn}(\eta, \delta m) = \sum_{m=-\ell}^{\ell} \left[|h_{\ell m}^{\rm obs} - h_{\ell m}^{\rm pred}(\eta, \delta m)|^2 + \lambda_\ell |t_{\ell m}^{\rm obs} - t_{\ell m}^{\rm pred}(\eta, \delta m)|^2 \right] \tag{9}$$

In equation (9), $h_{\ell m}^{\rm pred}$ and $t_{\ell m}^{\rm pred}$ denote the spherical harmonic coefficients of the geoid and topography predicted for a viscosity structure η and mass anomalies δm. The weighting factor λ_ℓ is chosen such that both terms on the right-hand side of equation (9) are equally important and is expressed as:

$$\lambda_\ell = \sum_{m=-\ell}^{\ell} |h_{\ell m}^{\rm obs}|^2 / \sum_{m=-\ell}^{\ell} |t_{\ell m}^{\rm obs}|^2 \tag{10}$$

In other words, we search for a density and viscosity structure that satisfies the assumptions described above and predicts the geoid and topography that are as close as possible to the observed ones in the sense of the norm given by equations (8)-(10). The summation in equation (8) is considered up to degree 40. This value is chosen to be roughly in agreement

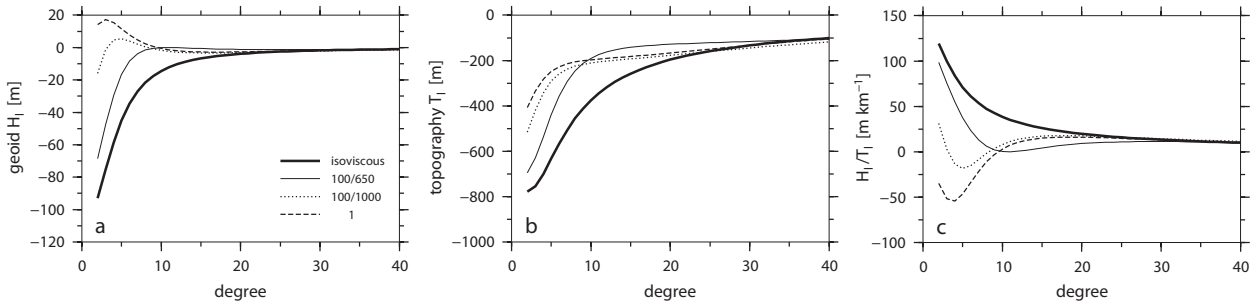

Figure C.1.4: *a) The geoid response function $\mathcal{H}_\ell$ (equation 12) as a function of degree ℓ for different viscosity profiles. b) The same as a) but for the topography response function $\mathcal{T}_\ell$ (equation 13). c) The ratio of the geoid and topography response functions as a function of degree ℓ. The viscosity models tested are an isoviscous model and three models with $\eta_{\rm UM} = 0.01\eta_{\rm lith}$ and $\eta_{\rm LM} = 30\eta_{\rm UM}$ (UM – upper mantle, LM – lower mantle) differing in the thickness of the lithosphere and the depth of the upper/lower mantle boundary (for the values of these parameters in km, see the legend in the top panel).*

with the results presented in sections 2 and 3 (see Figures 1b, 2b and 3a). We note that the exact value of the cut-off degree is not important, since the same results are essentially obtained for any cut-off degree close to 40.

Since the power of the geoid decays with increasing degree, the minimization of $M^{\rm dyn}$ will mainly take into account the behavior of the geoid and topography at lower degrees. To examine the impact of higher-degree terms on the inversion solution, we will also use a misfit function in which the geoid is replaced by the free-air gravity [*Forte et al.,* 1994]. This function can easily be derived from equation (8) by multiplying $M_\ell^{\rm dyn}$ by a factor $(g_0/a)^2(\ell-1)^2$:

$$M_{\rm gr}^{\rm dyn}(\eta,\delta m) = (g_0/a)^2 \sum_{\ell=2}^{40} (\ell-1)^2\, M_\ell^{\rm dyn}(\eta,\delta m) \tag{11}$$

Although the predicted geoid and topography are nonlinear functions of η, their dependence on δm is linear, which implies that they can be expressed in terms of response functions [e.g., *Ricard et al.*, 1984; *Hager and Clayton*, 1989]. Since δm does not depend on radius and $\eta = \eta(r)$, we can write

$$h_{\ell m}^{\rm pred} = \delta m_{\ell m} \mathcal{H}_\ell(\eta(r)) \tag{12}$$

$$t_{\ell m}^{\rm pred} = \delta m_{\ell m} \mathcal{T}_\ell(\eta(r)) \tag{13}$$

where the response functions $\mathcal{H}_\ell$ and $\mathcal{T}_\ell$ only depend on η, and can be determined by solving the Stokes equation together with the Poisson equation degree by degree for fixed $\delta m_{\ell 0} = 1$ and an appropriate viscosity profile. For details of the internal loading theory, the reader is referred to the extensive literature [e.g., *Ricard et al.*, 1984; *Hager and Clayton*, 1989; *King*, 1995b].

The sensitivity of the geoid and topography predictions to the defined viscosity profile is illustrated in Figure 4, where $\mathcal{H}_\ell$, $\mathcal{T}_\ell$ and the ratio $\mathcal{H}_\ell/\mathcal{T}_\ell$ are plotted as functions of degree ℓ for four different viscosity profiles. Note that the sensitivity of the response functions

to viscosity structure decreases with increasing degree. This means that the geoid and topographic data in the transitional degree range (ℓ greater than ~ 30), which may partly be of a non-dynamic origin, play only a minor role in searching for the viscosity profile that minimizes $M^{\rm dyn}$ and $M^{\rm dyn}_{\rm gr}$. At the same time, one can see that our dynamic model cannot properly explain the admittance observed in this degree range (compare Figures 2b and 4c). While the observed admittance at the transitional degrees is about 5 m km^{-1}, our dynamic models converge to a value of $\mathcal{H}_\ell/\mathcal{T}_\ell$, which is approximately twice as large.

Using equations (9), (12) and (13), equation (8) can be rewritten in the form,

$$M^{\rm dyn}(\eta,\delta m)=\sum_{\ell=2}^{40}\sum_{m=-\ell}^{\ell}\left[|h^{\rm obs}_{\ell m}-\delta m_{\ell m}\mathcal{H}_\ell(\eta)|^2+\lambda_\ell|t^{\rm obs}_{\ell m}-\delta m_{\ell m}\mathcal{T}_\ell(\eta)|^2\right] \tag{14}$$

If the viscosity profile, η, is fixed, we can easily find the mass anomaly coefficients that yield the minimum misfits $M^{\rm dyn}$. By solving the equation $\partial M^{\rm dyn}/\partial(\delta m_{\ell m})=0$, we obtain,

$$\delta m_{\ell m}=\frac{\mathcal{H}_\ell h^{\rm obs}_{\ell m}+\lambda_\ell\mathcal{T}_\ell t^{\rm obs}_{\ell m}}{\mathcal{H}^2_\ell+\lambda_\ell\mathcal{T}^2_\ell} \tag{15}$$

Substituting equation (15) into (14) results in $M^{\rm dyn}$ being a function of only viscosity:

$$M^{\rm dyn}(\eta)=\sum_{\ell=2}^{40}\frac{\lambda_\ell}{\mathcal{H}^2_\ell+\lambda_\ell\mathcal{T}^2_\ell}\sum_{m=-\ell}^{\ell}|h^{\rm obs}_{\ell m}\mathcal{T}_\ell(\eta)-t^{\rm obs}_{\ell m}\mathcal{H}_\ell(\eta)|^2 \tag{16}$$

and analogously for the free-air gravity:

$$M^{\rm dyn}_{\rm gr}(\eta)=(g_0/a)^2\sum_{\ell=2}^{40}\frac{(l-1)^2\lambda_\ell}{\mathcal{H}^2_\ell+\lambda_\ell\mathcal{T}^2_\ell}\sum_{m=-\ell}^{\ell}|h^{\rm obs}_{\ell m}\mathcal{T}_\ell(\eta)-t^{\rm obs}_{\ell m}\mathcal{H}_\ell(\eta)|^2 \tag{17}$$

Although $M^{\rm dyn}$ and $M^{\rm dyn}_{\rm gr}$ depend on viscosity in a nonlinear way, finding their minimum is straightforward, especially if the number of parameters characterizing the viscosity model is relatively small. In this study, the viscosity structure is parameterized in terms of n layers of constant viscosity. Since the geoid and topography are only sensitive to relative changes of viscosity [*Hager and Clayton*, 1989], the total number of parameters characterizing the viscosity model is $2n-2$, where $n-1$ parameters describe the relative viscosity and the same number of parameters is needed to specify the positions of interfaces between the layers. To find the minimum of $M^{\rm dyn}(\eta)$ and $M^{\rm dyn}_{\rm gr}(\eta)$, we have applied the technique of a systematic exploration of the model space for $n\le 4$ and a Monte-Carlo method for $n\ge 5$. These global techniques have allowed us to map the whole model space and to estimate the sensitivity of the solution to individual parameters.

C.1.6 Viscosity Structure of Venus' Mantle

The misfit functions, $M^{\rm dyn}$ and $M^{\rm dyn}_{\rm gr}$, obtained for a two-layer model, are presented in Figure 5 as a function of the viscosity contrast and the depth of the interface between the layers. The misfit is expressed in m^2 for the geoid and in mgal^2 for the free-air gravity. To

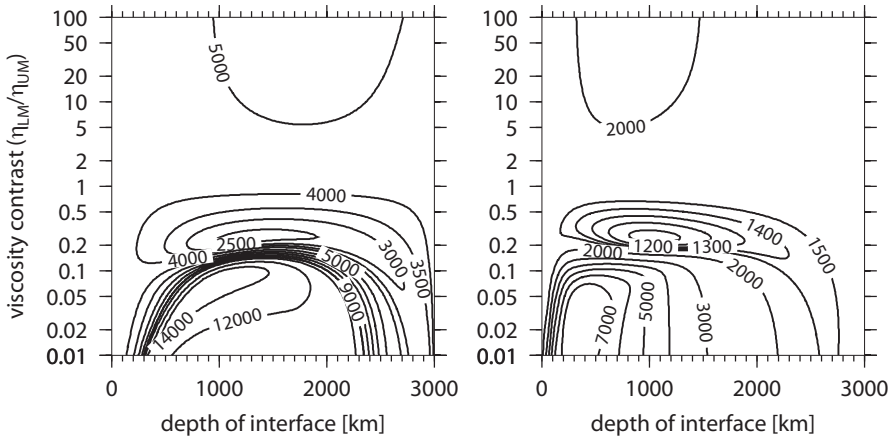

Figure C.1.5: *Left: The misfit function M^{dyn} (equation 16), obtained for a two-layer model of Venus. The misfit (in m^2) is shown as a function of the depth of the interface and the viscosity contrast between the layers. Right: The same, but for the misfit function $M^{\mathrm{dyn}}_{\mathrm{gr}}$ (equation 17) in mgals^2.*

obtain an estimate of the mean accuracy of the geoid or free-air gravity predictions, we can replace the misfit M by an average value $\sqrt{M/8\pi}$ (note that, according to equations 8-10, the gravitational signal represents only one half of the misfit). For example, a misfit of 2500 m^2 means that the average difference between the observed and predicted geoids is 10 m. In spite of some differences, both the geoid and gravity data prefer models with a weak decrease in viscosity with depth ($\eta_{\mathrm{LM}}/\eta_{\mathrm{UM}} \sim 0.3$). However, such a viscosity profile would be unrealistic, since the effect of increasing pressure with depth should cause an increase, not a decrease, in viscosity. The other possible interpretation of this result is that the more viscous top layer corresponds in reality to a very thick thermal boundary layer [e.g., *Parmentier and Hess*, 1992; *Turcotte*, 1995; *Moresi and Solomatov*, 1998; *Vezolainen et al.*, 2004]. We note that the results shown in Figure 5 are in agreement with the first inferences of viscosity from the Venusian geoid [*Kiefer et al.*, 1986] that suggested only small changes in viscosity with depth in the mantle of Venus.

The main drawback of the two-layer model is the absence of a lithosphere, a highly viscous thermal boundary layer common to convecting systems with a temperature-dependent viscosity. As the next step, we investigate viscosity models with a highly viscous upper layer and another two layers that correspond approximately to the upper and lower mantles. The relative viscosity, η_{lith}, of the first layer is fixed at a value of 1. The upper- and lower-mantle viscosities, η_{UM} and η_{LM}, respectively, are assumed to be smaller than η_{lith}. The values of η_{UM} and η_{LM} are set to vary by five orders of magnitude, i.e. from 10^{-5} to 1, and both increasing ($\eta_{\mathrm{UM}} \leq \eta_{\mathrm{LM}}$) and decreasing ($\eta_{\mathrm{UM}} > \eta_{\mathrm{LM}}$) viscosity-with-depth options are considered. The base of the lithosphere is expected to be located within a depth interval of 20-500 km, while the depth of the interface between layers 2 and 3 is varied from 500 to 2500 km depth. The results of the inversion, again obtained by a systematic exploration of the parameter space, are illustrated for three lithosphere thicknesses in Figures 6 and 7.

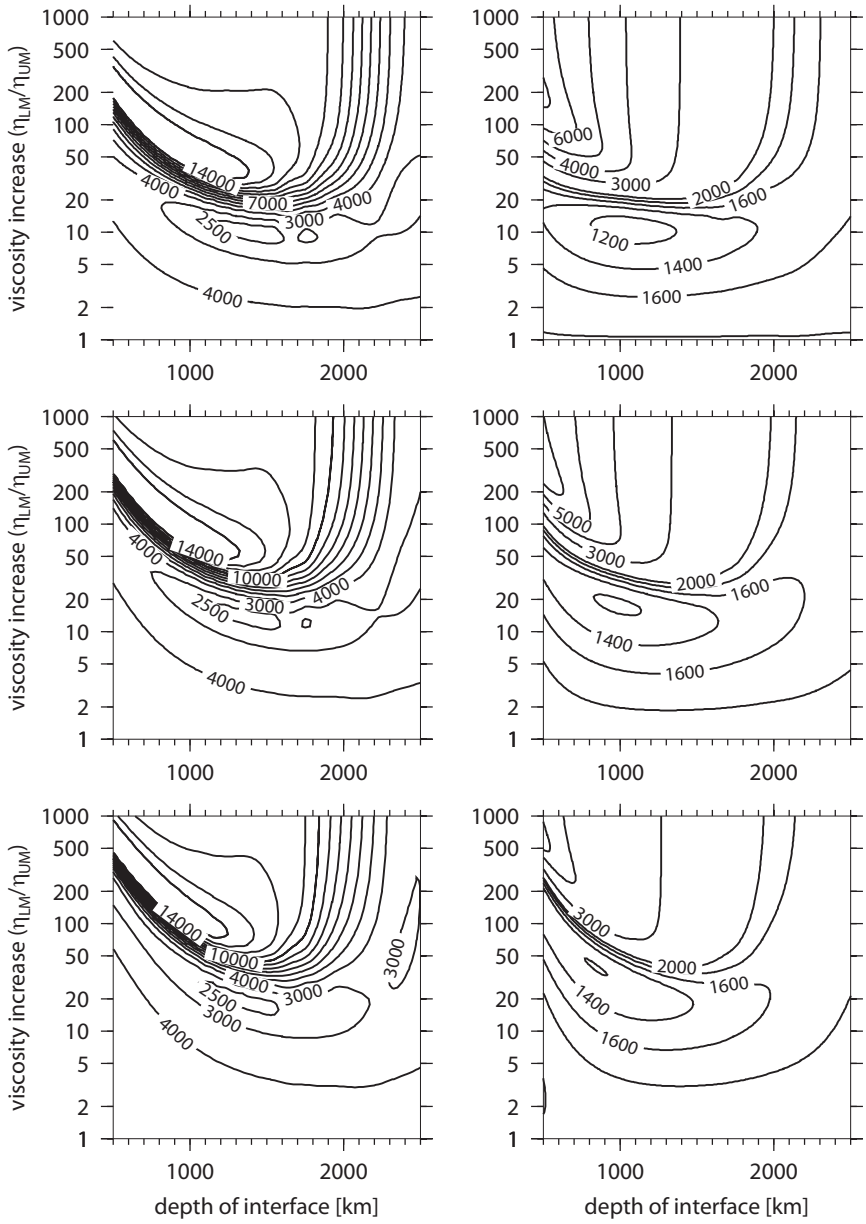

Figure C.1.6: *The misfit functions M^{dyn} (left panels) and $M^{\mathrm{dyn}}_{\mathrm{gr}}$ (right panels) computed for a three-layer model of Venus' mantle assuming that $\eta_{\mathrm{UM}} = 0.01\eta_{\mathrm{lith}}$. The misfits are presented as functions of the viscosity contrast $\eta_{\mathrm{LM}}/\eta_{\mathrm{UM}}$ between the upper and lower mantle and the position of the upper/lower mantle interface. Three different lithosphere thicknesses are considered: 100 km (top), 200 km (middle) and 300 km (bottom).*

Figure 6 shows the misfit functions $M^{\rm dyn}$ and $M^{\rm dyn}_{\rm gr}$ obtained for $\eta_{\rm UM} = 0.01\eta_{\rm lith}$ as a function of the depth of interface between the upper and lower mantle and the viscosity contrast $\eta_{\rm LM}/\eta_{\rm UM}$. Since no minimum is found for $\eta_{\rm LM}/\eta_{\rm UM} < 1$, only results from models with increasing viscosity with depth are presented. The top, middle and bottom panels correspond to lithosphere thicknesses of 100, 200 and 300 km, respectively. Figure 7 is the same as Figure 6, but for $\eta_{\rm UM} = 0.001\eta_{\rm lith}$. Although the minimum values of $M^{\rm dyn}$ and $M^{\rm dyn}_{\rm gr}$ in Figures 6 and 7 do not differ much from those shown in Figure 5, the best predictions of the geoid and topography are obtained for viscosity profiles that are significantly different from those inferred using a two-layer model. That is, the optimum 3-layer viscosity models show increasing viscosity with depth, not decreasing. The minimum misfit values correspond to viscosity increases ranging from 10 to 40, with the larger values obtained for models with a thicker lithosphere. It is obvious from Figures 6 and 7 that the inversion solution is nonunique, and that some of the model parameters, namely lithosphere thickness and the depth of the interface between the upper and lower mantle, are not well resolved.

Typical families of the best-fitting viscosity profiles obtained for models with four and five layers are shown in Figure 8. The presented models are those whose misfit does not exceed the absolute minimum by more than 1% ($M^{\rm dyn} < 2270$ m^2 and $M^{\rm dyn}_{gr} < 1040$ mgal^2). Again, we assume that the lithosphere viscosity is higher than for the rest of the mantle. The viscosity of the lithosphere is fixed at a value of 1, while the relative viscosities in the underlying layers are varied between 10^{-3} and 1. The resulting best-fitting models show certain common features, the most significant of which is a gradual increase in viscosity with depth which is comparable in magnitude to that expected in the Earth's mantle [e.g., *Ricard et al.*, 1993; *Peltier and Jiang*, 1996; *Kaufmann and Lambeck*, 2000; *Čadek and Fleitout*, 2003; *Karato*, 2003; *Mitrovica and Forte*, 2004]. Again, the thickness of the lithosphere is not well resolved and any value between 20 and 200 km is feasible. A narrow (100-km thick) low-viscosity channel beneath the lithosphere is found only for some five-layer models when considering the free-air gravity misfit function. While the data can be equally well fitted without such a feature, it is still interesting to see that such models are feasible, although they are rejected in most studies [e.g., *Smrekar and Phillips*, 1991; *Nimmo and McKenzie*, 1998]. It should be mentioned, however, that the low-viscosity channel obtained here for Venus is less pronounced than the asthenosphere beneath oceanic plates on the Earth [e.g., *Dumoulin et al.*, 1999; *Čadek and Fleitout*, 2003].

For the case of models with five layers and more, a good fit to the data was also obtained for viscosity profiles strongly oscillating with depth. These profiles are usually characterized by two viscosity minima, one beneath the lithosphere and the other in the mid-mantle. Similar oscillating profiles have been obtained for the Earth's mantle when carrying out inversions using higher numbers of layers [*King*, 1995b; *Čadek et al.*, 1997]. Since they are likely to be an artifact of over-parameterization, we have excluded them from this discussion. We note, however, that the concept of a low-viscosity zone above or below the upper/lower mantle interface cannot, in general, be rejected [e.g., *Forte et al.*, 1993a; *Kido and Čadek*, 1997].

The absolute minimum of the misfit attained by the viscosity models that incorporate a pronounced lithosphere and increasing viscosity with depth (Figures 6-8, see also the discussion above) are only slightly smaller than the misfit values obtained for the best-fitting two-layer model (Figure 5) that exhibits a weak decrease in viscosity with depth.

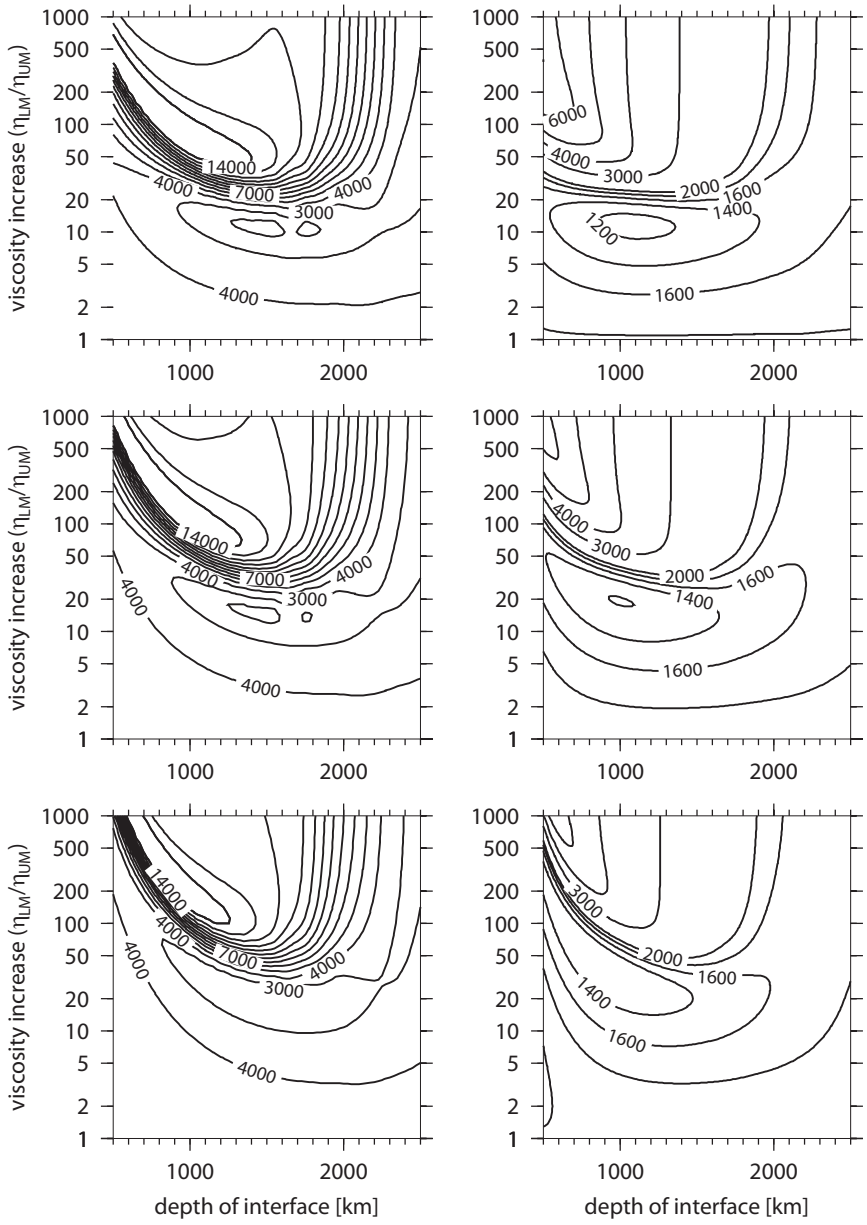

Figure C.1.7: *The same as in Figure 6, but for* $\eta_{\mathrm{UM}} = 0.001\eta_{\mathrm{lith}}$.

The question therefore arises as to whether such a small difference in the misfit is sufficient for the two-layer viscosity models to be excluded from further discussion of Venus' mantle structure. To answer this question, we have investigated general three- and four-layer models with no a priori constraint imposed on $\eta_{\rm lith}$. Solving the inverse problem for these cases, we indeed find two prominent families of best-fitting models. The first family corresponds to the models discussed above, where the viscosity profiles are characterized by a lithosphere of relatively high viscosity, underlaid by a mantle that exhibits an increase in viscosity with depth. The other family includes models with an indistinct lithosphere and usually only small changes in viscosity with depth. The minimum values of the misfit obtained for the two families of the models are almost identical, with both groups of models equally probable. From a formal statistical point of view, the latter family of models thus cannot be excluded. Nevertheless, the authors of this paper prefer the models with a pronounced lithosphere, since a high-viscosity thermal boundary layer is a common feature of all models of thermal convection that include a realistic rheology.

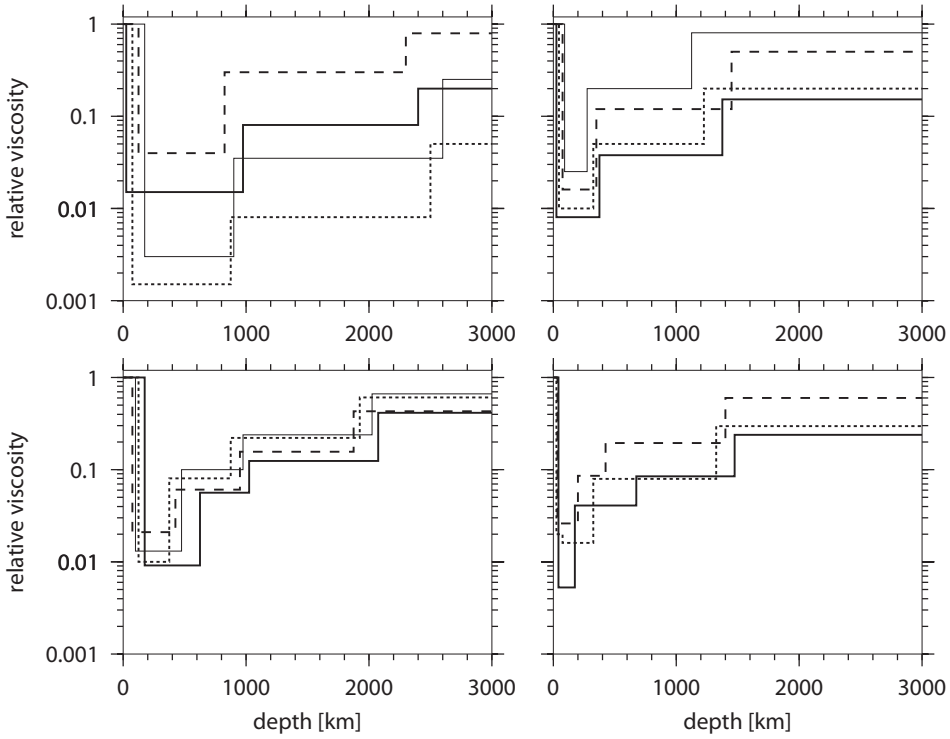

Figure C.1.8: *Viscosity profiles obtained from the inversion of gravitational and topography data for four- (top panels) and five- (bottom panels) layer models of Venus. The results shown on the left are based on the misfit function $M^{\rm dyn}$, while the profiles on the right are based on the misfit function $M_{\rm gr}^{\rm dyn}$.*

The quality of the dynamic predictions of the geoid and topography for spherical harmonic degrees 2-40 is illustrated in Figure 9. For the geoid, the differences between the observed and predicted values locally exceed 35 m, but are usually less than 10 m. A good agreement between the observed and predicted geoid is obtained for the highland rises (e.g. Atla Regio and Beta Regio), while relatively large differences are found for Ishtar Terra and

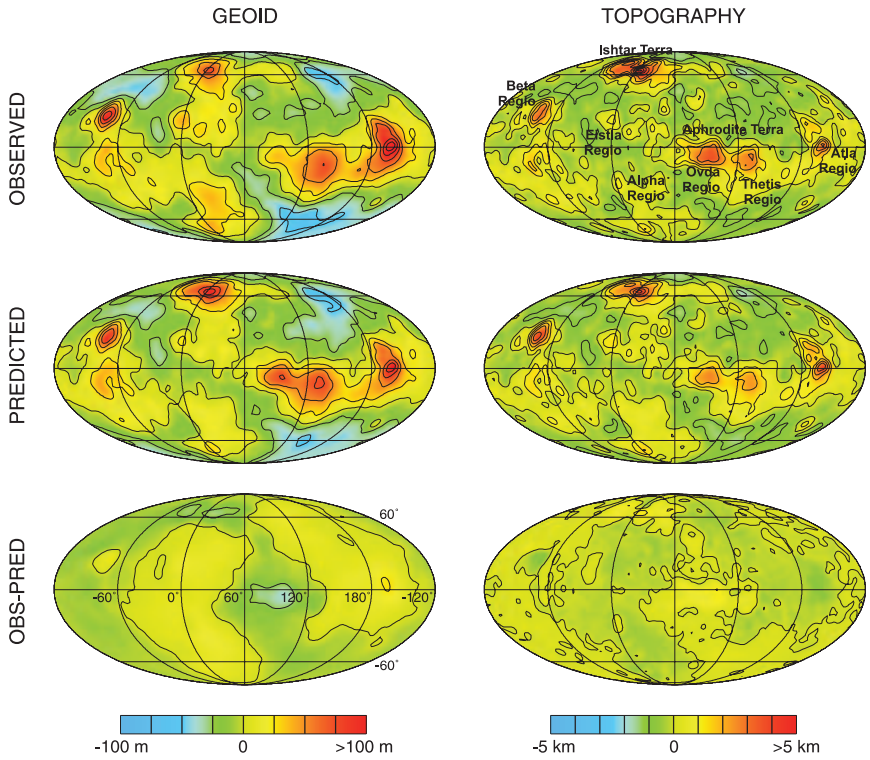

Figure C.1.9: *Top: Observed geoid and topography truncated at harmonic degree 40. Middle: Geoid and topography predicted for the same degree range from an optimum five-layer dynamic model of Venus. Bottom: The difference between the observed and the predicted quantities. The projection is a Mollweide centered at the* 60°*E meridian.*

western Aphrodite Terra. To estimate the effect the latter regions have on the resultant viscosity profiles, we have repeated the inversion for viscosity described above but using geoid and topography data where the signal associated with the above mentioned terrae is filtered out. The viscosity profiles found for the new data set (not shown here) are similar to those described above. The best-fitting 3-layer model shows an increase in viscosity by a factor of ~ 10, while inferred models with four and five layers show a gradual increase in viscosity with depth similar to that illustrated in Figure 8.

The distribution of mass anomalies (Figure 10), obtained as a by-product of our inversion for viscosity, shows negative density anomalies beneath all surface structures with a pronounced positive topography [cf. *Herrick and Phillips*, 1992]. The existence of such plume-like upwellings beneath the equatorial highlands was proposed by *Morgan and Phillips* [1983] and is generally accepted today [e.g., *Vezolainen et al.*, 2004], although the opposite view, relating Alpha, Ovda and Thetis Regio with mantle downwelling, has also been presented [*Bindschadler et al.*, 1992].

Our density model also gives a negative density anomaly beneath the Ishtar Terra region. Scenarios of the tectonic evolution of this region, based on the observed gravity and topography fields, include regional compression, local mantle downwelling as well as local mantle upwelling [*Roberts and Head*, 1990; *Bindschadler and Parmentier*, 1990; *Grimm*

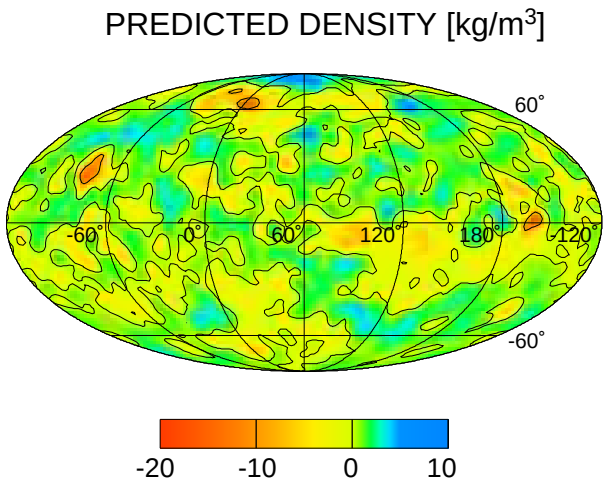

Figure C.1.10: *Density anomalies at a depth of 100 km obtained from the inversion of the geoid and topography data. Since we assume that the mass anomaly δm does not change with depth, the amplitude of the density anomaly increases with decreasing radius as r^{-2}. The projection is a Mollweide centered at the 60°E meridian.*

and Phillips, 1991]. The structure of Ishtar Terra is obviously very complex, and shows similarities to continental structures on Earth, and so it could hardly be explained by a single evolutionary mechanism [*Kiefer and Hager,* 1991b; *Kaula et al.*, 1997; *Schubert et al.*, 2001]. Figure 11 presents the predicted and observed geoid of this region, divided into the contributions from ℓ = 2-40, and 41-90. As discussed above, in this region our dynamically predicted geoid differs the most from the observations (Figure 11a,b). In contrast, an isostatic model with T_c = 35 km gives a very good fit to the data for spherical harmonic degrees 41-90 (Figure 11c,d). The quality of the isostatic predictions for Ishtar Terra stands

out in contrast with the same predictions for regions such as Atla and Beta Regio. This is shown by Figure 12, where we again compare observations and predictions of the geoid arising from ℓ = 2-40 and 41-90. We note that the dynamic predictions at degrees 2-40 work very well in this region, while the signal at degrees 41-90 is strongly underestimated relative to the observations if an isostatic model is used.

Besides the models described in this section, we also tested dynamic models that mimic a stagnant-lid regime of mantle convection on Venus, as suggested by some authors [e.g., *Moore and Schubert*, 1997]. We have assumed that $\eta_{\rm lith}/\eta_{\rm UM} \rightarrow \infty$ and we have omitted the mass heterogeneities inside the lithosphere. The results obtained for this model do not differ much from those illustrated in Figures 6-8, and hence we can conclude that considering a stiff lithosphere without mass anomalies has only a minor effect on the inversion solution.

C.1.7 Discussion and Conclusions

In previous works, the large admittance ratios on Venus have mostly been interpreted as a consequence of the dynamic support of topographic structures and relatively constant viscosity [*Kiefer et al.*, 1986; *Smrekar and Phillips*, 1991; *Simons et al.*, 1994]. However, this interpretation does not appear to be unique. From a study of two highland regions,

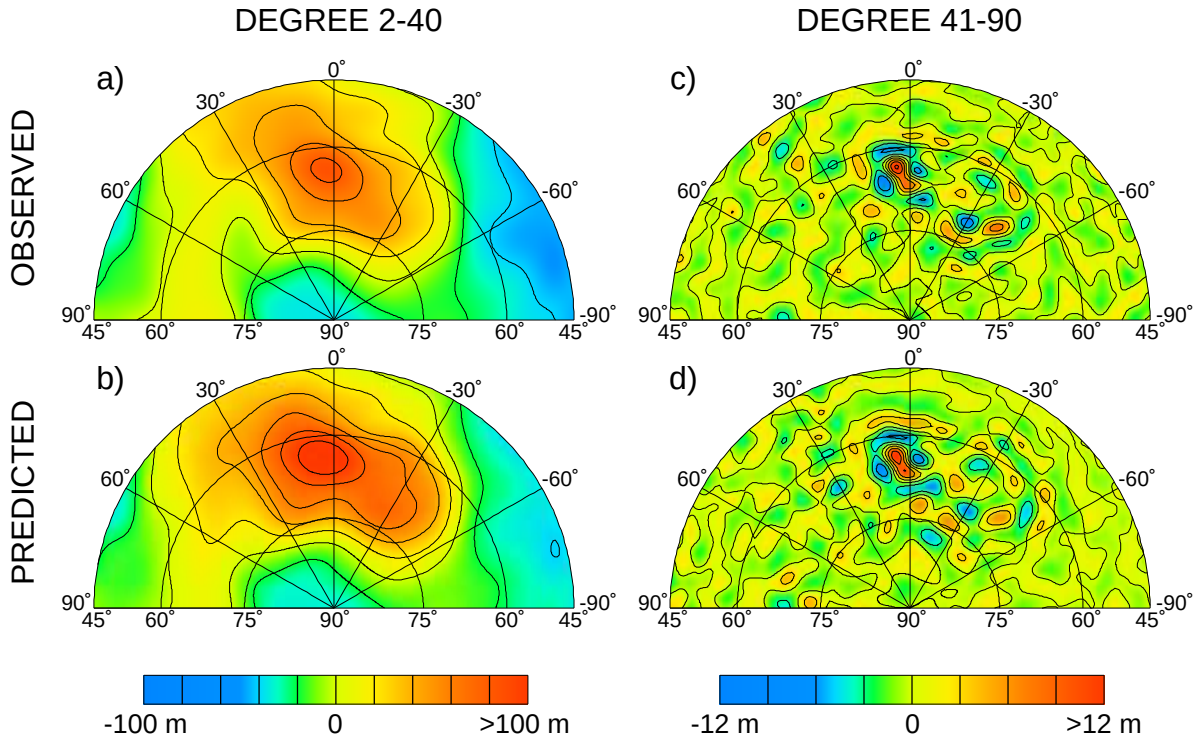

Figure C.1.11: *Distribution of the observed and predicted geoid anomalies in the Ishtar Terra region. The top panels show the observed geoid for the degree range* $\ell = 2 - 40$ *(left) and* $41 - 90$ *(right). The bottom panels show the dynamic (left) and isostatic (right) predictions for the same degree ranges. The dynamic prediction has been obtained for an optimum five-layer viscosity profile of Venus' mantle while an apparent depth of compensation of 35 km has been considered in the case of the isostatic compensation model. The isoline interval is 25 meters for the long-wavelength maps and 2 meters for the short-wavelength maps. The projection is orthographic with the projection center at the north pole.*

Atla Regio and Beta Regio, *Kiefer and Hager* [1991a] showed that cylindrical axisymmetric convection plume models may fit the observed data not only for a constant viscosity and a Rayleigh number of $\sim 10^6$, but also for a significantly higher Rayleigh number (10^7) and a viscosity contrast of 10 between the upper and lower mantle. The latter view has been supported by numerical simulations of thermal convection in a 3d Cartesian geometry [*Dubuffet et al.* 2000] that suggests that the tectonic pattern on Venus is better predicted for models with a stepwise increase in viscosity by a factor of 10 or 100 between the upper and lower mantle, rather than for isoviscous models. In the present study, we find that both classes of viscosity profiles explain well the geoid and topography between degrees 2-40. While an isoviscous mantle is the only acceptable solution of the inverse problem for the case of a two-layer parameterization, an increase in viscosity with depth is obtained for models with three or more layers. The four- and five-layer models usually prefer a viscosity increase across the mantle which is similar to or somewhat smaller than that expected for the Earth. These models are consistent with the concept of strongly pressure-dependent creep and, as shown by *Dubuffet et al.* [2000], they are also acceptable from the viewpoint

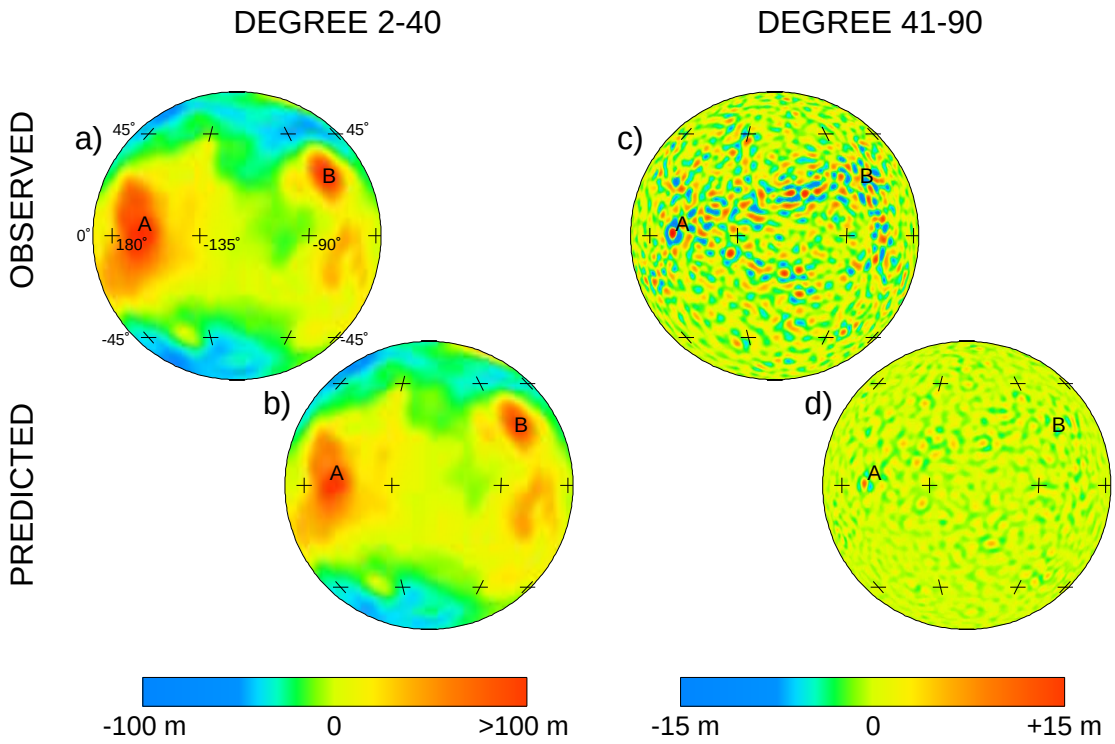

Figure C.1.12: *The same as in Figure 13 but for an equatorial projection. Letters A and B denote the locations of Atla Regio and Beta Regio, respectively.*

of thermal convection modeling.

The results obtained in this paper for the spherical harmonic models of Venus' geoid and topography truncated at degree 90 are summarized as follows:

1. The slope of the geoid log-log spectrum significantly changes around degree 10 and 40 (Figure 1). These changes can also be recognized by the degree dependence of the admittance ratio (Figure 2). The change in the geoid-spectrum behavior at degree 40 may suggest a change in the mechanism responsible for maintaining the surface topography. This view is supported by a degree-by-degree analysis of the apparent depth of compensation and elastic lithosphere thickness (Figure 3).

2. The geoid and topography spectra between degrees 2-40 can be well explained by whole-mantle flow models. A good fit to data is obtained not only for the isoviscous model without a pronounced lithosphere, as suggested, e.g., by *Kiefer et al.* [1986], but also for models including a highly viscous and relatively thin (∼100-km thick) lithosphere and a significant increase of viscosity with depth across the mantle. While the best-fitting 3-layer model shows only a weak (by a factor of ∼10) increase in viscosity, an increase of viscosity similar to that expected in the Earth mantle is obtained for the best-fitting 4- and 5-layer models (see Figure 8). The existence of a thin low-viscosity channel mechanically decoupling the lithosphere from the rest of the mantle cannot be excluded on the basis of our modeling. Howevever, a narrow (less than 200-km thick) low-viscosity zone beneath the lithosphere is found only for

some of the best fitting 5-layer models when analysing the free-air gravity (see right bottom panel of Figure 8).

3. The dynamic models predict well the long-wavelength ($\ell \leq 40$) geoid and topography in regions of highland rises, such as Atla Regio and Beta Regio (figure 12). A somewhat worse prediction is obtained for highland plateaus, such as Ishtar Terra, where the isostatic component may be significant (Figure 11).

4. The removal from the geoid and topographic data of the signal from two major topographic features, Ishtar Terra and Aphrodite Terra, was found to have little effect on the inferred viscosities. The inversion is also rather robust with respect to physical conditions expected close to the upper surface. We find that models with a stiff lithosphere without mass anomalies give a similar viscosity increase across the mantle as the models with a lithosphere of finite viscosity including mass anomalies.

Finally, we again mention that the inferred viscosity models presented in this paper may be influenced by the assumptions adopted in solving the inverse problem. The most important of these is the assumption of the pattern of mass anomalies remaining constant with depth. Such a condition is suggested by the numerical modeling of the geoid and topography due to mantle plumes on Venus [e.g., *Kiefer and Hager*, 1991a; *Vezolainen et al.*, 2004], and tomographic studies on Earth that have indicated the predominantly vertical penetration of plumes and slabs through the Earth's mantle [*Bijwaard et al.*, 1998; *Montelli et al.*, 2004]. Therefore, this assumption is believed to be not very significant, a statement supported by the test results presented in Appendix B.

C.1.8 Appendix A

In the present paper, we use a complex spherical harmonic basis $\{Y_{\ell m}(\theta, \phi)\}$ normalized so that

$$\int_0^{2\pi} \int_0^{\pi} Y_{\ell_1 m_1} Y^*_{\ell_2 m_2} \sin\theta \mathrm{d}\theta \mathrm{d}\phi = \delta_{\ell_1 \ell_2} \delta_{m_1 m_2} \qquad (A1)$$

where θ is the co-latitude, ϕ is the longitude and the asterisk denotes complex conjugation. Any sufficiently smooth function f defined on a sphere may then be expressed in terms of the following spherical harmonic expansion

$$f(\theta, \phi) = \sum_{\ell=0}^{\infty} \sum_{m=-\ell}^{\ell} f_{\ell m} Y_{\ell m}(\theta, \phi) \qquad (A2)$$

where

$$f_{\ell m} = \int_0^{2\pi} \int_0^{\pi} f(\theta, \phi) Y^*_{\ell m}(\theta, \phi) \sin\theta \mathrm{d}\theta \mathrm{d}\phi \qquad (A3)$$

(for more details, see, e.g., *Jones* [1985] or *Varshalovich et al.* [1989]). The power S_ℓ of the function f at degree ℓ is defined in terms of the L_2-norm of the function at a given wavelength,

$$S_\ell(f) = |f_\ell|^2_{L_2} = \int_0^{2\pi} \int_0^{\pi} f_\ell f^*_\ell \sin\theta \mathrm{d}\theta \mathrm{d}\phi = \sum_{m=-\ell}^{\ell} f_{\ell m} f^*_{\ell m} \qquad (A4)$$

where

$$f_\ell(\theta,\phi) = \sum_{m=-\ell}^{\ell} f_{\ell m} Y_{\ell m}(\theta,\phi) \tag{A5}$$

Let $h_{\ell m}$ and $t_{\ell m}$ be the complex spherical harmonic coefficients of the geoid, h, and topography, t, respectively. The correlation between functions h and t at degree ℓ can be evaluated as a scalar product of the normalized functions f_ℓ and g_ℓ,

$$c_\ell = \frac{1}{\sqrt{S_\ell(h)S_\ell(t)}} \int_0^{2\pi}\int_0^{\pi} h_\ell t_\ell^* \sin\theta \mathrm{d}\theta\mathrm{d}\phi = \frac{\sum_{m=-\ell}^{\ell} h_{\ell m} t_{\ell m}^*}{\sqrt{\sum_{m=-\ell}^{\ell} h_{\ell m} h_{\ell m}^*}\sqrt{\sum_{m=-\ell}^{\ell} t_{\ell m} t_{\ell m}^*}} \tag{A6}$$

where we used equation (A4) to express the powers $S_\ell(h)$ and $S_\ell(t)$ of functions h and t at degree ℓ. The statistical meaning of the correlation depends on the number of free parameters, i.e. the number of spherical harmonic coefficients at a given degree, and is usually expressed in terms of a confidence level. The confidence level $G_\ell(q)$ at degree ℓ corresponding to a correlation coefficient of value q can be evaluated using the following recurrent formula [*Eckhardt*, 1984, *Weisstein*, 2006]:

$$G_1(q) = q$$

$$G_\ell(q) = G_{\ell-1}(q) + q(1-q^2)^{\ell-1} \prod_{i=1}^{\ell-1} (2i-1)/2i \tag{A7}$$

The relationship between the geoid and topography is often characterized by the admittance A_ℓ [*Kiefer et al.*, 1986; *Simons et al.*, 1997; *Schubert et al.*, 2001].

$$h_{\ell m} = A_\ell t_{\ell m} + u_{\ell m} \tag{A8}$$

where

$$A_\ell = \frac{\sum_{m=-\ell}^{\ell} h_{\ell m} t_{\ell m}^*}{\sum_{m=-\ell}^{\ell} t_{\ell m} t_{\ell m}^*} = c_\ell \sqrt{\frac{S_\ell(h)}{S_\ell(t)}} \tag{A9}$$

and $u_{\ell m}$ is the part of the geoid that is not correlated with topography.

C.1.9 Appendix B

An assumption made in our dynamic modeling is that the mass anomaly pattern does not vary with depth. This condition, together with the assumption of a dynamic origin of the geoid and topography at low degrees, plays a crucial role in our inversion for viscosity. Using tomographic information available for the Earth, we will now test whether the application of this simplified density structure can still lead to realistic viscosity profiles. Our procedure consists of the following three steps.

First, we use the S-wave seismic tomographic model of the mantle "smean" [*Becker and Boschi*, 2002] and translate it into a global 3d density model. We assume that the seismic velocity anomalies reflect temperature variations in the mantle and we compute the relative density anomalies $\delta\rho/\rho$ in the mantle using a simple linear relationship:

$$\frac{\delta\rho}{\rho} = C\frac{\delta V}{V} \tag{B1}$$

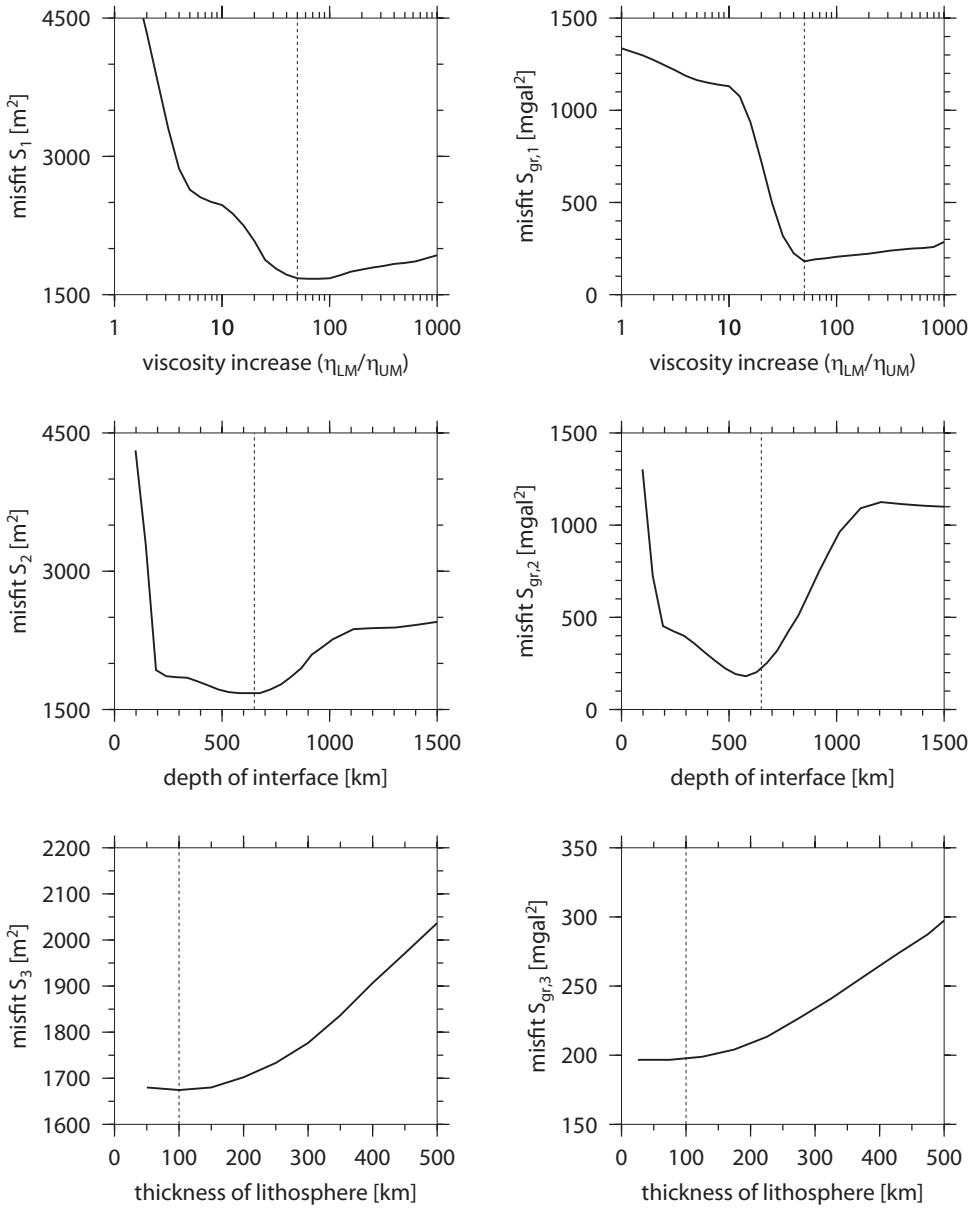

Figure C.1.13: *The misfit functions for the geoid (M_1, M_2 and M_3, left panels) and free-air gravity ($M_{\mathrm{gr},1}$, $M_{\mathrm{gr},2}$ and $M_{\mathrm{gr},3}$, right panels) defined by equations B2, B3 and B4 (Appendix B). The minima of these curves indicate the values of model parameters inferred from synthetic data under the assumption of depth-independent mass anomalies. The vertical lines indicate the values used to generate the synthetic data.*

where C is the seismic velocity-to-density scaling factor ($C = \partial ln\rho / \partial \ln V$) and $\delta V/V$ is the relative S-wave seismic velocity anomaly. We choose $C = 0.2$ for most of the mantle [cf. *Karato*, 1993], except for the top 300 km where C is set to zero. Neglecting the density anomaly in the uppermost mantle is justified by the fact that most of the seismic anomalies in this part of the mantle are associated with petrological rather than thermal variations. The lateral resolution of the density model is given by the cut-off degree of the "smean" model, which is 31, thus not too different from the degree range considered in our analysis presented in section 4.

In the second step, we use this density model to generate synthetic dynamic geoid and topography data for low and intermediate degrees ($2 \leq \ell \leq 31$). We consider the case of a three-layer viscosity model with a stiff lithosphere ($\eta_{\rm lith}/\eta_{\rm UM} = 10^{10}$) and a viscosity increase of a factor of 50 at a depth of 650 km. Such a viscosity model is a reasonable first-order approximation of the Earth's mantle-viscosity structure [*Ricard et al.*, 1993] which ensures that our predictions of the geoid are not far from the observations.

For the third step, we use the synthetic data generated in the previous step as input for the inversion described in section 4. We emphasize that no seismic tomographic information is used in this step and the lack of information about the mantle is only compensated by the assumption of mass anomalies being constant with depth as described in section 4. The inversion is then solved by minimizing the misfit $M^{\rm dyn}$ (equation 16), and $M^{\rm dyn}_{\rm gr}$ (equation 17), which is a function of three free parameters: the thickness of the lithosphere, $d_{\rm lith}$, the depth of interface between the upper and lower mantle, $d_{\rm int}$, and the viscosity increase at this interface, $\eta_{\rm LM}/\eta_{\rm UM}$. For simplicity, we assume that the lithosphere is perfectly stiff and we omit density anomalies inside it.

Comparing the values of the model parameters obtained from the inversion (i.e. those that minimize $M^{\rm dyn}$ and $M^{\rm dyn}_{\rm gr}$) with those used to generate the synthetic data provides information about the behavior of the inversion process and, especially, the plausibility of our assumption of depth-independent mass anomalies. This comparison is shown in Figure B1 where we depict the minimum values of $M^{\rm dyn}$ and $M^{\rm dyn}_{\rm gr}$ as functions of the free parameters. The functions M_1, M_2 and M_3 plotted in Figure B1 are defined as follows:

$$M_1(\eta_{\rm LM}/\eta_{\rm UM}) = \min_{d_{\rm lith}, d_{\rm int}} M^{\rm dyn}(d_{\rm lith}, d_{\rm int}, \eta_{\rm LM}/\eta_{\rm UM}) \qquad (B2)$$

$$M_2(d_{\rm int}) = \min_{\eta_{\rm LM}/\eta_{\rm UM}, d_{\rm lith}} M^{\rm dyn}(d_{\rm lith}, d_{\rm int}, \eta_{\rm LM}/\eta_{\rm UM}) \qquad (B3)$$

$$M_3(d_{\rm lith}) = \min_{\eta_{\rm LM}/\eta_{\rm UM}, d_{\rm int}} M^{\rm dyn}(d_{\rm lith}, d_{\rm int}, \eta_{\rm LM}/\eta_{\rm UM}) \qquad (B4)$$

and analogously for the free-air gravity misfit functions $M_{\rm gr,1}$, $M_{\rm gr,2}$ and $M_{\rm gr,3}$. The values used to generate the synthetic data are marked by the vertical lines.

An inspection of Figure B1 indicates that the inverse procedure used in section 4, along with the assumption of depth-independent mass anomalies, can give reasonable estimates of the parameters describing the Earth's viscosity structure. We see that the minima of the functions depicted in Figure B1 are very close to the correct values. However, the resolution of the inversion is limited. We can reject all viscosity profiles where $\eta_{\rm LM}/\eta_{\rm UM} < 10$, but any increase of viscosity at 650 km greater than ~ 30 is acceptable. The depth of the interface between the upper and lower mantle is rather well resolved if free-air gravity is used, but the minimum is rather flat for the case of the geoid misfit function. The thickness of the

lithosphere is poorly resolved from both geoid and free-air gravity data, although in both cases the positions of the minima of M_3 and $M_{\mathrm{gr},3}$ do not differ from the correct value by more than 25 km.

C.1.10 Acknowledgments

We thank F. Nimmo, M. Wieczorek and an anonymous reviewer for their positive criticisms and helpful comments. This work has been supported by the European Community's Improving Human Potential Programme under contract RTN2-2001-00414, MAGE, and the Charles University grant 280/2006/B-GEO/MFF. K. F.'s visits to Prague for meetings were supported by the MAGMA program (European Commission project EVG3-CT-2002-80006).

C.1.11 References

Arkani-Hamed, J. (1996), Analysis and interpretation of the surface topography and gravitational potential of Venus, J. Geophys. Res., 101(E2), 4711–4724.
Barnett, D. N., F. Nimmo, and D. McKenzie (2002), Flexure of Venusian lithosphere measured from residual topography and gravity, J. Geophys. Res., 107(E2), 5007, doi:10.1029/2000JE001398.
Becker, T. W., and L. Boschi (2002), A comparison of tomographic and geodynamic mantle models, Geochem. Geophys. Geosyst., 3(1), 1003, doi:10.1029/2001GC000168.
Bijwaard, H., W. Spakman, and E. R. Engdahl (1998), Closing the gap between regional and global travel time tomography, J. Geophys. Res., 103(B12), 30,055–30,078.
Bindschadler, D. L., and E. M. Parmentier (1990), Mantle flow tectonics: The influence of a ductile lower crust and implications for the formation of the large-scale features on Venus, J. Geophys. Res., 95(B13), 21,329– 21,344.
Bindschadler, D. L., G. Schubert, and W. M. Kaula (1992), Coldspots and hotspots: Global tectonics and mantle dynamics of Venus, J. Geophys. Res., 97(E8), 13,495–13,532.
Bowin, C. (1983), Gravity, topography, and crustal evolution of Venus, Icarus, 56, 345–371.
Čadek, O., and L. Fleitout (1999), A global geoid model with imposed plate velocities and partial layering, J. Geophys. Res., 104(B12), 29,055– 29,075.
Čadek, O., and L. Fleitout (2003), Effect of lateral viscosity variations in the top 300 km on the geoid and dynamic topography, Geophys. J. Int., 152(3), 566–580, doi:10.1046/j.1365-246X.2003.01859.x.
Čadek, O., H. Čížková, and D. A. Yuen (1997), Can long-wavelength dynamical signature be compatible with layered mantle convection?, Geophys. Res. Lett., 24(16), 2091–2094.
Čížková, H., O. Čadek, D. A. Yuen, and H. W. Zhou (1996), Slope of the geoid spectrum and constraints on mantle viscosity stratification, Geophys. Res. Lett., 23(21), 3063–3066.
Colin, P., and L. Fleitout (1990), Topography of the ocean floor: Thermal evolution of the lithosphere and interaction of deep mantle heterogeneities with the lithosphere, Geophys. Res. Lett., 17(11), 1961–1964.
Dubuffet, F., M. Rabinowicz, and M. Monnereau (2000), Multiple-scales in mantle convection, Earth Planet. Sci. Lett., 178, 351–366.
Dumoulin, C., M.-P. Doin, and L. Fleitout (1999), Heat transport in stagnant lid convection with temperature- and pressure-dependent Newtonian or non-Newtonian rheology, J.

Geophys. Res., 104(B6), 12,759–12,777.
Eckhardt, D. H. (1984), Correlations between global features of terrestrial fields, Math. Geol., 16, 155–171.
Forte, A. M., A. M. Dziewonski, and R. L. Woodward (1993a), Aspherical structure of the mantle, tectonic plate motions, nonhydrostatic geoid, and topography of the core-mantle boundary, in Dynamics of the Earth's Deep Interior and Earth Rotation, Geophys. Monogr. Ser., vol. 72, edited by J.-L. Le Mouel, D. E. Smylie, and T. Herring, pp. 135–166, AGU, Washington, D. C.
Forte, A. M., W. R. Peltier, A. M. Dziewonski, and R. L. Woodward (1993b), Dynamic surface topographyA new interpretation based upon mantle flow models derived from seismic tomography, Geophys. Res. Lett., 20(3), 225–228.
Forte, A. M., R. L. Woodward, and A. M. Dziewonski (1994), Joint inversions of seismic and geodynamic data for models of three-dimensional mantle heterogeneity, J. Geophys. Res., 99(B11), 21,857–21,877.
Grand, S. P. (1994), Mantle shear structure beneath the Americas and surrounding oceans, J. Geophys. Res., 99(B6), 11,591–11,621.
Grimm, R. E., and R. J. Phillips (1991), Gravity anomalies, compensation mechanisms, and the geodynamics of Western Ishtar Terra, Venus, J. Geophys. Res., 96(B5), 8305–8324.
Grimm, R. E., and R. J. Phillips (1992), Anatomy of a Venusian hot spot: Geology, gravity, and mantle dynamics of Eistla Regio, J. Geophys. Res., 97(E10), 16,035–16,054.
Gurnis, M. (1990), Bounds on global dynamic topography from Phanerozoic flooding of continental platforms, Nature, 344, 754–756.
Hager, B. H., and R. W. Clayton (1989), Constraints on the structure of mantle convection using seismic observations, flow models, and the geoid, in Mantle Convection: Plate Tectonics and Global Dynamics, edited by W. R. Peltier, pp. 675–763, Gordon and Breach, New York.
Herrick, R. R., and R. J. Phillips (1992), Geological correlations with the interior density structure of Venus, J. Geophys. Res., 97(E10), 16,017–16,034.
Herrick, R. R., B. G. Bills, and S. A. Hall (1989), Variations in effective compensation depth across Aphrodite Terra, Venus, Geophys. Res. Lett., 16(6), 543–546.
Johnson, C. L., and D. T. Sandwell (1994), Lithospheric flexure on Venus, Geophys. J. Int., 119, 627–647.
Jones, M. N. (1985), Spherical Harmonics and Tensors for Classical Field Theory, Res. Stud. Press Ltd., Letchworth, U. K.
Karato, S. (1993), Importance of anelasticity in the interpretation of seismic tomography, Geophys. Res. Lett., 20(15), 1623–1626.
Karato, S. (2003), Dynamic Structure of the Deep Earth: An Interdisciplinary Approach, Princeton Univ. Press, Princeton, N. J.
Kaufmann, G., and K. Lambeck (2000), Mantle dynamics, postglacial rebound and the radial viscosity profile, Phys. Earth Planet. Inter., 121, 301–324.
Kaula, W. M., A. Lenardic, D. L. Bindschadler, and J. Arkani-Hamed (1997), Ishtar Terra, in Venus IIGeology, Geophysics, Atmosphere, and Solar Wind Environment, edited by S. W. Bougher, D. M. Hunten, and R. J. Phillips, pp. 879–900, Univ. of Ariz. Press, Tucson.
Kido, M., and O. Čadek (1997), Inferences of viscosity from the oceanic geoid: Indication of a low viscosity zone below the 660-km discontinuity, Earth Planet. Sci. Lett., 151, 125–137,

doi:10.1016/S0012-821X (97)81843-2.
Kiefer, W. S., and B. H. Hager (1991a), A mantle plume model for the equatorial highlands of Venus, J. Geophys. Res., 96(E4), 20,947–20,966.
Kiefer, W. S., and B. H. Hager (1991b), Mantle downwelling and crustal convergence: A model for Ishtar Terra, Venus, J. Geophys. Res., 96(E4), 20,967–20,980.
Kiefer, W. S., and B. H. Hager (1992), Geoid anomalies and dynamic topography from convection in cylindrical geometry: Application to mantle plumes on Earth and Venus, Geophys. J. Int., 108(1), 198–214.
Kiefer, W. S., and L. H. Kellogg (1998), Geoid anomalies and dynamic topography from time-dependent, spherical axisymmetric mantle convection, Phys. Earth Planet. Inter., 106, 237–256.
Kiefer, W. S., M. A. Richards, B. H. Hager, and B. G. Bills (1986), A dynamic model of Venus' gravity field, Geophys. Res. Lett., 13(1), 14–17.
King, S. D. (1995a), Models of mantle viscosity, in Mineral Physics and Crystallography: A Handbook of Physical Constants, AGU Ref. Shelf, vol. 2, edited by T. J. Ahrens, pp. 227–236, AGU, Washington, D. C.
King, S. D. (1995b), Radial models of mantle viscosityResults from a genetic algorithm, Geophys. J. Int., 122, 725–734.
Konopliv, A. S., and W. L. Sjogren (1994), Venus spherical harmonic gravity model to degree and order 60, Icarus, 112(1), 42–54, doi:10.1006/icar.1994.1169.
Konopliv, A. S., W. B. Banerdt, and W. L. Sjogren (1999), Venus gravity: 180th degree and order model, Icarus, 139, 3–18, doi:10.1006/ icar.1999.6086.
Kucinskas, A. B., and D. L. Turcotte (1994), Isostatic compensation of equatorial highlands on Venus, Icarus, 112(1), 104–116, doi:10.1006/ icar.1994.1172.
Lambeck, K. (1988), Geophysical Geodesy, Oxford Univ. Press, New York.
Le Stunff, Y., and Y. Ricard (1995), Topography and geoid due to lithospheric mass anomalies, Geophys. J. Int., 122, 982–990.
Le Stunff, Y., and Y. Ricard (1997), Partial advection of equidensity: A solution for the dynamic topography problem?, J. Geophys. Res., 102(B11), 24,655–24,677.
McKenzie, D. (1994), The relationship between topography and gravity on Earth and Venus, Icarus, 112(1), 55–88, doi:10.1006/icar.1994.1170.
Mitrovica, J. X., and A. M. Forte (2004), A new inference of mantle viscosity based upon joint inversion of convection and glacial isostatic adjustment data, Earth Planet. Sci. Lett., 225, 177–189.
Montelli, R., G. Nolet, N. A. Dahlen, G. Masters, E. R. Engdahl, and S.-H. Hung (2004), Finite-frequency tomography reveals a variety of plumes in the mantle, Science, 303, 338–343, doi:10.1126/science.1092485.
Moore, W. B., and G. Schubert (1995), Lithospheric thickness and mantle density contrast beneath Beta Regio, Venus, Geophys. Res. Lett., 22(4), 429–432.
Moore, W. B., and G. Schubert (1997), Venusian crustal and lithospheric properties from nonlinear regressions of highland geoid and topography, Icarus, 128(2), 415–428.
Moresi, L., and B. Parsons (1995), Interpreting gravity, geoid, and topography for convection with temperature-dependent viscosity: Application to surface features on Venus, J. Geophys. Res., 100(E10), 21,155–21,171.
Moresi, L., and V. Solomatov (1998), Mantle convection with a brittle lithosphere: Thoughts

on the global tectonic styles of the Earth and Venus, Geophys. J. Int., 133, 669–682.
Morgan, P., and R. J. Phillips (1983), Hot spot heat transfer: Its application to Venus and implications to Venus and Earth, J. Geophys. Res., 88(B10), 8305–8317.
Nimmo, F., and D. McKenzie (1998), Volcanism and tectonics on Venus, Annu. Rev. Earth Planet Sci., 26, 23–53, doi:10.1146/annurev. earth.26.1.23.
Panasyuk, S. V., and B. H. Hager (2000), Models of isostatic and dynamic topography, geoid anomalies, and their uncertainties, J. Geophys. Res., 105(B12), 28,199–28,209.
Parmentier, E. M., and P. C. Hess (1992), Chemical differentiation of a convecting planetary interior: Consequences for a one plate planet such as Venus, Geophys. Res. Lett., 19(20), 2015–2018.
Peltier, W. R., and X. Jiang (1996), Glacial isostatic adjustment and Earth rotation: Refined constraints on the viscosity of the deepest mantle, J. Geophys. Res., 101(B2), 3269–3290.
Phillips, R. J. (1994), Estimating lithospheric properties at Atla Regio, Venus, Icarus, 112(1), 147–170.
Phillips, R. J., and V. L. Hansen (1998), Geological evolution of Venus: Rises, plains, plumes, and plateaus, Science, 279, 1492–1497, doi:10.1126/science.279.5356.1492.
Phillips, R. J., R. E. Grimm, and M. C. Malin (1991), Hot-spot evolution and the global tectonics of Venus, Science, 252, 651–658.
Rappaport, N. J., and J. J. Plaut (1994), A 360-degree and 360-order model of Venus topography, Icarus, 112(1), 27–33.
Rappaport, N. J., A. S. Konopliv, and A. B. Kucinskas (1999), An improved 360 degree and order model of Venus topography, Icarus, 139(1), 19–31, doi:10.1006/icar.1999.6081.
Ratcliff, J. T., G. Schubert, and A. Zebib (1995), Three-dimensional variable viscosity convection of an infinite Prandtl number Boussinesq fluid in a spherical shell, Geophys. Res. Lett., 22(16), 2227–2230.
Ricard, Y., L. Fleitout, and C. Froidevaux (1984), Geoid heights and lithospheric stresses for a dynamic Earth, Ann. Geophys., 2, 267–285.
Ricard, Y., M. A. Richards, C. Lithgow-Bertelloni, and Y. LeStunff (1993), A geodynamic model of mantle density heterogeneity, J. Geophys. Res., 98(B12), 21,895–21,909.
Richards, M. A., and B. H. Hager (1984), Geoid anomalies in a dynamic Earth, J. Geophys. Res., 89(B7), 5987–6002.
Roberts, K. M., and J. W. Head (1990), Western Ishtar Terra and Lakshmi Planum, Venus: Models of formation and evolution, Geophys. Res. Lett., 17(9), 1341–1344.
Sandwell, D. T., and G. Schubert (1992), Flexural ridges, trenches, and outer rises around coronae on Venus, J. Geophys. Res., 97(E10), 16,069–16,083.
Schubert, G., D. L. Turcotte, and P. Olson (2001), Mantle Convection in the Earth and Planets, Cambridge Univ. Press, New York.
Simons, M., B. H. Hager, and S. C. Solomon (1994), Global variations in geoid/topography admittances of Venus, Science, 256, 798–803.
Simons, M., S. C. Solomon, and B. H. Hager (1997), Localization of gravity and topography: Constraints on the tectonics and mantle dynamics of Venus, Geophys. J. Int., 131, 24–44.
Smrekar, S. E. (1994), Evidence for active hotspots on Venus from analysis of Magellan gravity data, Icarus, 112(1), 2–26.

Smrekar, S. E., and R. J. Phillips (1991), Venusian highlands: Geoid to topography ratios and their implications, Earth Planet. Sci. Lett., 107, 582–597, doi:10.1016/0012-821X(91)90103-O.
Solomatov, V. S., and L. N. Moresi (1996), Stagnant lid convection on Venus, J. Geophys. Res., 101(E2), 4737–4753.
Turcotte, D. L. (1995), How does Venus lose heat?, J. Geophys. Res., 100(E8), 16,931–16,940.
Turcotte, D. L., R. J. Willemann, W. F. Haxby, and J. Norberry (1981), Role of membrane stresses in the support of planetary topography, J. Geophys. Res., 86(B5), 3951–3959.
Turcotte, D. L., R. Scherbakov, B. D. Malamud, and A. B. Kucinskas (2002), Is the Martian crust also the Martian lithosphere?, J. Geophys. Res., 107(E11), 5091, doi:10.1029/2001JE001594.
van der Hilst, R. D., S. Widiyantoro, and E. R. Engdahl (1997), Evidence for deep mantle circulation from global tomography, Nature, 386, 578–584, doi:10.1038/386578a0.
Varshalovich, D. A., A. N. Moskalev, and V. K. Khersonski (1989), Quantum Theory of Angular Momentum, World Sci., Hackensack, N. J.
Vezolainen, A. V., V. S. Solomatov, A. T. Basilevsky, and J. W. Head (2004), Uplift of Beta Regio: Three-dimensional models, J. Geophys. Res., 109, E08007, doi:10.1029/2004JE002259.

C.2 Constraints on the maximum crustal density from gravity-topography modeling: Applications to the southern highlands of Mars

C.2.1 Abstract

Gravimetric methods commonly used to constrain crustal parameters such as the mean crustal thickness and density are ambiguous with a noted trade-off between these parameters. However, combining two different methods, the geoid-topography ratio and Bouguer inversion, in regions that are homogeneous with respect to lateral density variations and compensation state can help to constrain a maximum density of the crust. For the Martian Noachian southern highlands a combination of these methods gives us a maximum crustal density of 3020 ± 70 kg m^{-3}, assuming a single-layer crustal structure. We also test various two-layer crustal structures to check how they influence the results. We find a possibility to fit the observed data with a crust having a dense uniformly thick lower crust, but in these models the upper crustal density was also limited to ~ 3000 kg m^{-3}. The obtained results together with the findings on crustal densities (and composition) of other regions on Mars are consistent with various scenarios of crustal evolution: a temporal increase in the crustal density or a large scale density variation that has been already manifested in the early evolution during the formation of the crustal dichotomy.[2]

[2]published as: Pauer, M., Breuer, D., 2008. Constraints on the maximum crustal density from gravity-topography modeling: Applications to the southern highlands of Mars. Earth Planet. Sci. Lett. 276, 253–261. doi:10.1016/j.epsl.2008.09.014.

C.2.2 Introduction

The mean thickness and the bulk density of the crust are important parameters for constraining the inner structure and thermo-chemical evolution of a planet [e.g., Spohn et al., 2001; Breuer and Spohn, 2003; Elkins-Tanton et al., 2005a; Nimmo, 2005; Sohl et al., 2005; Schumacher and Breuer, 2006]. Without samples of crustal material or seismic data that are suitable to derive these parameters directly [e.g., Lognonné, 2005], estimates of these quantities can be still gained by gravity-topography analysis [e.g., Wieczorek and Phillips, 1997; Neumann et al., 2004; Belleguic et al., 2005]. The solution of the gravimetric methods, however, is non-unique as the results show a trade-off between the crustal density and the mean crustal thickness. Thus, with none of these quantities known, the observed data can be fitted with a wide range of parameter values.

Two important methods of studying gravity and topography data are the Bouguer inversion and the analysis of the geoid-topography ratio (GTR). For the case of the Bouguer inversion, one assumes that the observed gravity signal is simply caused by the topography and the undulations of the crust-mantle interface (CMI). Using an assumed mean crustal thickness, the variations in crustal thickness can then be modeled with a high accuracy [e.g., Wieczorek and Phillips, 1998; Neumann et al., 2004; Chenet et al., 2006]. Such an approach is,however, not possible where the long-wavelength part of the observed geoid is generated dynamically in the mantle as in the case of the Earth [e.g., Hager and Clayton, 1989; adek and Fleitout, 1999] or as suggested for Venus [e.g., Kiefer et al.,1986; Pauer et al., 2006]. The Bouguer inversion also allows an estimate of the minimum mean (or zero-elevation) crustal thickness if deep impacts are present and the crust-mantle interface is everywhere below the surface, i.e. mantle material is not exposed at the surface [e.g., Zuber et al., 2000; Neumann et al., 2004]. The analysis of the GTR by either a spatial or spectral comparison of the observed and predicted admittance function [e.g., Simons et al., 1997; Wieczorek and Phillips, 1997; Wieczorek and Zuber, 2004] allows an estimation of the mean crustal thickness if a certain type of compensation mechanism like Airy isostasy can be applied globally, or to a sufficiently large surface unit. However, both methods, i.e., the Bouguer inversion and the GTR analysis, depend strongly on the assumed crustal density.

In the present paper, we show that applying both methods to the same region provides a constraint on the upper bound of the crustal density. This is possible because the minimum mean crustal thickness increases with increasing crustal density for the Bouguer inversion [e.g., Neumann et al., 2004] whereas the mean crustal thickness decreases with increasing crustal density for the GTR analysis [e.g., Wieczorek and Zuber, 2004]. The application of both methods, however, requires some specific conditions for the considered region: a homogeneous unit with respect to lateral density variations and compensation state (Airy isostasy) as well as no, or only minor, influence on the gravity signal from internal dynamic processes or sub-crustal density interfaces.

We apply this method to the Martian southern highlands, which, in contrast to the northern lowlands, seem to fulfill the above mentioned requirements [Frey et al., 1996; McGovern et al., 2002; Wieczorek and Zuber, 2004]. The most prominent feature of the highland region is the Hellas basin, which serves in our study as an anchoring-point to determine the minimum mean crustal thickness. To test the influence of the crustal structure on the results, we consider in addition to a simple single-layer crustal structure also two-layer

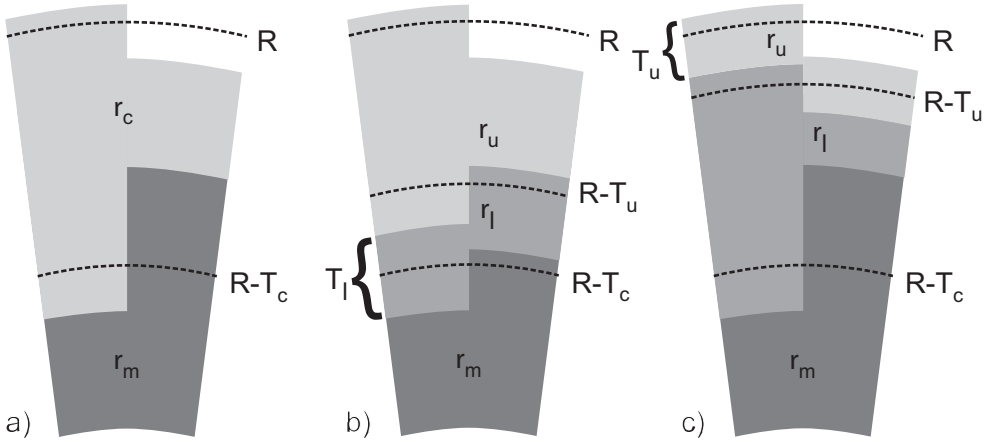

Figure C.2.1: *Sketch of the crustal models considered in this study: a) single-layer crust of a mean thickness T_c and a homogeneous density ρ_c, b) two-layer crust with a lower crust of a constant thickness T_l and a density ρ_l (the upper crust has a density ρ_u and mean thickness T_u) and c) two-layer crust with an upper crust of constant thickness T_u and density ρ_u (lower crust has a density ρ_l and mean thickness T_l).*

structures (Fig. 1). It will be demonstrated that the maximum density of the compensating crustal layer (i.e. the layer in which lateral variations of thickness occur) in the southern highlands can be constrained to 3020 ± 70 kg m^{-3}.

C.2.3 Methods

In the following section, the methods of the GTR analyses and the Bouguer inversion are described. The relevant equations are derived for three different crustal structures:

1. A simple single-layer crustal structure (Fig. 1a).
2. A two-layer crustal structure with a lower crust of constant thickness and an upper crust of variable thickness (Fig. 1b). A possible formation scenario for this crustal structure may be due to the redistribution of surface material (i.e. only the upper crust) caused by large impacts such as the Hellas impact in the considered region of the southern highlands. This scenario implies that the crust was already layered before the large impact happened.
3. A two-layer crustal structure with an upper crust of constant thickness and a lower crust of variable thickness (Fig. 1c). This type of crustal structure may be a consequence of laterally homogeneous fracturing of the upper crust by impacting and thereby decreasing its density due to the increase in porosity. Another mechanism can be related to endogenic processes in which the lower crust thickness varies due to crustal underplating, and/or erosion and the redistribution of lower-crustal material by vigorous mantle convection [e.g., Wise et al., 1979; Zhong and Zuber, 2001].

In the GTR analysis both the surface topography and the CMI relief are modeled to a first approximation, i.e. the mass anomalies connected to volcanoes or impacts are approximated

by the density anomalies at a given radius. Therefore, the resulting values of a mean global crustal thickness T_c for the observed data can be any positive value dependent on the input crustal density. However, the existence of deep impact structures and their CMI anti-roots posses a problem to this concept. That is, the sum of these two "depths" gives a global minimum crustal thickness $T_c^{\min}$, which must be always smaller than the mean crustal thickness T_c. To model the shape of the CMI relief and to obtain the global minimum crustal thickness, we use the Bouguer inversion method [Neumann et al., 2004] with a fixed minimum local thickness (i.e. thickness of crust between the bottom of the impact basin and the top of its anti-root).

GTR analysis

To infer the optimum global mean crustal thickness T_c we use the method of the spatial geoid-topography ratio which has been adapted the spherical geometry by Wieczorek and Phillips [1997]. The Cartesian version of this method, which is often applied to Earth [e.g., Turcotte and Schubert, 2002] and Venus [e.g., Smrekar and Phillips, 1991], is not valid for smaller objects like the Moon or Mars [Wieczorek and Phillips, 1997; Wieczorek and Zuber, 2004].

The derivation of a spherical form of GTR is straightforward and in detail described by Wieczorek and Phillips [1997], therefore we list only the key relationships used in our study. Both the gravitational potential U (which can be easily converted to the geoid height H using the Bruns theorem $H = U/g_0$ where g_0 stands for the mean gravity acceleration, see e.g., Lambeck, 1988) and the topography T of the planet are employed in the form of their spherical harmonic representation. These two fields are used not only in a form of harmonic coefficients ($C_{\ell m}$ and $t_{\ell m}$ for potential and topography coefficients respectively – ℓ denotes the harmonic degree and m the harmonic order) but also as spatial expansions referenced to the planetary radius R:

$$\begin{aligned} U(\theta,\phi) &= \frac{GM}{R}\sum_{\ell,m} U_{\ell m} Y_{\ell m}(\theta,\phi) \\ T(\theta,\phi) &= \sum_{\ell,m} t_{\ell m} Y_{\ell m}(\theta,\phi), \end{aligned}$$

where G is the gravitational constant, M is the planetary mass and $Y_{\ell m}(\theta,\phi)$ is the spherical harmonic function for a given colatitude θ and longitude ϕ (for the definition of spherical harmonic formalism see e.g., Wieczorek, 2007).

A regional observed value of GTR averaged over a circle of radius L_0 can be fitted by a combination of the appropriate admittance model Z_ℓ, where the density and the thickness of the crust are input parameters, and a weighting factor W_ℓ which reflects the considered spherical harmonic interval $\ell_{\min}$–$\ell_{\max}$:

$$GTR = R \sum_{\ell=\ell_{\min}}^{\ell_{\max}} W_\ell Z_\ell \qquad (1)$$

$$W_\ell = \frac{S_\ell^{tt}}{\sum\limits_{j=\ell_{\min}}^{\ell_{\max}} S_j^{tt}}, \tag{2}$$

where S_ℓ^{tt} is the power spectrum of the topography for the degree ℓ.

For the single-layer crust with the global zero-elevation thickness T_c and a constant crustal density ρ_c, the admittance function between the potential and topography is [e.g., Lambeck, 1988]:

$$Z_\ell = \frac{C_{\ell m}}{t_{\ell m}} = \frac{4\pi\rho_\mathrm{c}R^2}{M(2\ell+1)}\left[1-\left(\frac{R-T_\mathrm{c}}{R}\right)^\ell\right] \tag{3}$$

This spectral relationship is valid for the entire planet as it employs the global zero-elevation crustal thickness. In practice, however, we deal with some regional-average elevation-based topography t_avg. The correction to obtain the global mean crustal thickness T_c from the regional mean crustal thickness $T_\mathrm{c}^\mathrm{avg}$ for the single-layer model depends on both the density of the crust ρ_c and the mantle ρ_m (e.g., Wieczorek and Phillips, 1997):

$$T_\mathrm{c}^\mathrm{avg} = T_\mathrm{c} + t^\mathrm{avg}\left[1+\frac{\rho_\mathrm{c}}{\rho_\mathrm{m}-\rho_\mathrm{c}}\left(\frac{R}{R-T_\mathrm{c}}\right)^2\right]. \tag{4}$$

For the two-layer crust cases with either the upper or the lower crust of a uniform thickness, Eqs. (14)–(17) from Wieczorek and Phillips (1997) provide the admittance and the correction functions, but mistakenly they were switched. The correct equations for the case of a two-layer crustal structure with an upper crust of constant thickness T_u and constant density ρ_u and a lower crust with variable thickness and constant density ρ_l (Fig. 1c) are:

$$Z_\ell = \frac{4\pi\rho_\mathrm{u}R^2}{M(2\ell+1)}\left\{1+\frac{\rho_\mathrm{l}-\rho_\mathrm{u}}{\rho_\mathrm{u}}\left(\frac{R-T_\mathrm{u}}{R}\right)^{\ell+2} - \left(\frac{R-T_\mathrm{c}}{R}\right)^\ell\left[1+\frac{\rho_\mathrm{l}-\rho_\mathrm{u}}{\rho_\mathrm{u}}\left(\frac{R-T_\mathrm{u}}{R}\right)^2\right]\right\} \tag{5}$$

$$T_\mathrm{c}^\mathrm{avg} = T_\mathrm{c} + t^\mathrm{avg}\left[1+\frac{\rho_\mathrm{u}+(\rho_\mathrm{l}-\rho_\mathrm{u})\left(\frac{R-T_\mathrm{u}}{R}\right)^2}{(\rho_\mathrm{m}-\rho_\mathrm{l})\left(\frac{R-T_\mathrm{c}}{R}\right)^2}\right] \tag{6}$$

while for a two-layer crustal structure with a lower crust of a constant thickness T_l and a variable upper crust with an average thickness $T_\mathrm{u} = T_\mathrm{c} - T_\mathrm{l}$ (Fig. 1b) these equations are:

$$Z_\ell = \frac{4\pi\rho_\mathrm{u}R^2}{M(2\ell+1)}\left\{1-\left(\frac{R-T_\mathrm{u}}{R}\right)^\ell\left[1+\frac{\rho_\mathrm{m}-\rho_\mathrm{l}}{\rho_\mathrm{l}-\rho_\mathrm{u}}\left(\frac{R-T_\mathrm{c}}{R-T_\mathrm{u}}\right)^2\right]^{-1} - \left(\frac{R-T_\mathrm{c}}{R}\right)^\ell\left[1+\frac{\rho_\mathrm{l}-\rho_\mathrm{u}}{\rho_\mathrm{m}-\rho_\mathrm{l}}\left(\frac{R-T_\mathrm{u}}{R-T_\mathrm{c}}\right)^2\right]^{-1}\right\} \tag{7}$$

$$T_\mathrm{c}^\mathrm{avg} = T_\mathrm{c} + t^\mathrm{avg}\left[1+\frac{\rho_\mathrm{u}+(\rho_\mathrm{l}-\rho_\mathrm{u})\left(\frac{R-T_\mathrm{u}}{R}\right)^2}{(\rho_\mathrm{m}-\rho_\mathrm{l})\left(\frac{R-T_\mathrm{c}}{R}\right)^2}\right] \tag{8}$$

To obtain an appropriate value of T_c, a global non-isostatic signature needs to be removed from the analyzed data prior to the analysis itself [Turcotte et al., 2002; Wieczorek and

Zuber, 2004]. For objects like the Moon or Mars, the degree 2 distortion must be removed [e.g., Wieczorek and Phillips, 1997] and for the case of some global-scale lithospheric-loading deformation, such as the Tharsis load for Mars, some other low degree terms should be removed [e.g., Zuber and Smith,1997]. Concerning the error analysis, we consider the 1σ error-bar for the GTR analysis following previous studies [Wieczorek and Phillips, 1997; Wieczorek and Zuber, 2004].

Bouguer inversion

We use the Bouguer inversion to obtain the minimum mean crustal thickness. The approach is based on the assumption that the observed gravity signal (and not only the correlated part as in the case of GTR analysis [e.g., Smrekar and Phillips, 1991; Turcotte et al., 2002; Wieczorek and Zuber, 2004]) is explained only by the contributions from the surface topography masses and the subsurface crustal interface(s) [e.g., Neumann et al., 1996; Wieczorek and Phillips, 1998; Zuber et al., 2000; Neumann et al., 2004]. Technically, the Bouguer anomaly, i.e. the observed gravity signal minus the surface topography signal [e.g., Turcotte and Schubert, 2002] is fitted by the gravity signal of the iteratively adjusted CMI [Wieczorek and Phillips, 1998] or the CMI and intra-crustal interface (ICI) for the case of a two-layer crustal structure. Depending on the input densities and crustal thickness(es), we obtain the lateral variation of the crustal thickness which corresponds to the observed gravity signal. The minimum mean (or zero elevation) crustal thickness is then obtained using the assumption that the local crustal thickness is always non-negative, i.e., the CMI relief is everywhere below the surface [e.g., Zuber et al., 2000; Neumann et al., 2004]. Here, we set the minimum local thickness in accord with other studies [e.g., Neumann et al., 2004] to be 5 km. Using this constraint as an input for the Bouguer inversion we can calculate the appropriate minimum mean crustal thickness T_{c} min. For two-layer crustal structures this assumption is implemented by keeping the minimum local thickness of the non-constant layer also at a value of 5 km.

The approach used in this study for evaluating the gravity signal of the density interface(s) with a fixed shape as well as of the iteratively adjusted CMI relief uses the higher order approximation formalism based on the work of Wieczorek and Phillips [1998]. The potential signal of an interface with the undulations represented by coefficients $h_{\ell m}$, with a constant density contrast $\Delta\rho$, referenced to a spherical radius D and evaluated at the planetary radius R can be for the case $R \geq D$ written as:

$$C_{\ell m} = \frac{4\pi\Delta\rho D^3}{M(2\ell+1)}\left(\frac{D}{R}\right)^{\ell}\sum_{n=1}^{\ell+3}\frac{{}^{n}h_{\ell m}}{D^n n!}\frac{\prod_{j=1}^{n}(\ell+4-j)}{\ell+3} \tag{9}$$

where ${}^{n}h_{\ell m}$ is the spherical harmonic coefficient of the n-th power of the interface undulations h. The calculation of the term $\sum_{n=1}^{\ell+3}$ is very demanding with respect to computational power for higher degrees ℓ. In practice, the term is therefore replaced by $\sum_{n=1}^{5}$ which has been shown to represent the potential signal sufficiently [McKenzie et al., 2002; Wieczorek, 2007].

The resulting Bouguer anomaly $C_{\ell m}^{\mathrm{BA}}$ for a single-layer crustal model (and also for the two-layer crust model with a lower crust of constant thickness) is computed as the difference between the observed potential $C_{\ell m}^{\mathrm{obs}}$ and the surface relief potential signal $C_{\ell m}^{\mathrm{s}}$ which is

obtained by using Eq. (9) with $\Delta\rho = \rho_c$ (or ρ_u), $D = R$ and $h_{\ell m} = t_{\ell m}$ (topography spherical harmonic coefficients referenced to a spherical datum of the mean planetary radius):

$$C_{\ell m}^{BA} = C_{\ell m}^{obs} - C_{\ell m}^{s} \tag{10}$$

For the two-layer crustal model with an upper crust of constant thickness (where the ICI shape and amplitudes are identical to the topography) this should be modified by subtracting also the potential contribution of ICI, $C_{\ell m}^{ICI}$, (using Eq. 9) with $\Delta\rho = \rho_l - \rho_u$, $D = R - T_u$ and $h_{\ell m} = t_{\ell m}$):

$$C_{\ell m}^{BA} = C_{\ell m}^{obs} - C_{\ell m}^{s} - C_{\ell m}^{ICI} \tag{11}$$

For the cases of the single-layer crust and two-layer crust with constant upper layer thickness, the CMI relief $h_{\ell m}$ with $\Delta\rho = \rho_m - \rho_c$ (or $\rho_m - \rho_l$) and referenced to the radius $D = R - T_c$ can be derived iteratively using the following relationship [Wieczorek and Phillips, 1998]:

$$h_{\ell m} = w_\ell \left[\frac{C_{\ell m}^{BA} M (2\ell + 1)}{4\pi \Delta\rho_{CMI} D^2} \left(\frac{R}{D} \right)^\ell - D \sum_{n=2}^{\ell+3} \frac{{}^n h_{\ell m}}{D^n n!} \frac{\prod_{j=1}^{n} (\ell + 4 - j)}{\ell + 3} \right]. \tag{12}$$

The first solution of $h_{\ell m}$ for the iterative process is derived analytically from the first approximation (using the above formula, but omitting completely the second term).

In the case of the two-layer crust with a constant lower crust thickness, the relief of the ICI (referenced to the radius $D_i = D + T_l$ with $D = R - T_c$) is iteratively determined together with the shape of CMI since the Bouguer anomaly $C_{\ell m}^{BA}$ must be fitted by the sum of the potential signals from both interfaces. Therefore, we arrive at the more complicated relationship:

$$h_{\ell m} = \frac{w_\ell}{\gamma_\ell} \left[\frac{C_{\ell m}^{BA} M (2\ell + 1) R^\ell}{4\pi} - \Delta\rho_{ICI} D_i^{\ell+3} \sum_{n=2}^{\ell+3} \frac{{}^n h_{\ell m}}{D_i^n n!} \frac{\prod_{j=1}^{n} (\ell + 4 - j)}{\ell + 3} - \right.$$
$$\left. - \Delta\rho_{CMI} D^{\ell+3} \sum_{n=2}^{\ell+3} \frac{{}^n h_{\ell m}}{D^n n!} \frac{\prod_{j=1}^{n} (\ell + 4 - j)}{\ell + 3} \right] \tag{13}$$

with

$$\gamma_\ell = \Delta\rho_{ICI} D_i^{\ell+2} + \Delta\rho_{CMI} D^{\ell+2} \tag{14}$$

For the limiting case when $T_l = 0$ i.e. $\Delta\rho_{ICI} = 0$, Eq. (13) is equal to Eq. (12).

In both Eqs. (12) and (13) a weighting factor w_ℓ is introduced to stabilize the downward continuation process [Wieczorek and Phillips, 1998]. The inversion of the gravity data causes an amplification of the short-wavelength noise and the density inhomogeneities signal which is increasing with depth (i.e. with decreasing CMI reference radius D), thus this part of the data can significantly influence the solution. The w_ℓ filter compensates this effect by continuous decreasing from unity for long wavelengths to zero for a given short wavelength.

C.2.4 Results for Martian highlands

We analyze the southern highland region of Mars, which is a sufficiently large area [Wieczorek and Zuber, 2004], displaying homogeneity with respect to stratigraphy and geochemistry [Nimmo and Tanaka, 2005] and presumably mostly in Airy isostasy [Frey et al., 1996; McGovernet al., 2002]. In addition, it contains the Hellas basin which is the deepest impact structure on the planet [Smith et al., 1999] with an elevation of the floor of −6.81 km [Wieczorek and Zuber, 2004]. Gravity analysis of the Hellas basin also suggest that no significant mascon loading, mantle exposure nor remnants of dense impactor material influences the gravimetric inversion [Frey et al., 1996; McGovern et al., 2002; Neumann et al., 2004]. The exact definition of the examined highland area follows closely the region selected by Wieczorek and Zuber [2004] and excludes in the same way all inappropriate parts of the surface (for details see their Fig. 5 and the corresponding discussion in Section 4). We also use an averaging radius L_0 of 2000 km for the GTR analysis, which has been shown to resolve T_c correctly for Mars [Wieczorek and Zuber, 2004].

We use the spherical harmonic model *Mars2000.shape* (referenced to the IAU2000 standard) for the Martian topography and the recent gravity field model *jgm95j01* (downloaded from Geosciences node of Planetary Data Archive). However, some modifications of the data are required for both methods. For the Bouguer inversion, a subtraction of 2% of the degree 2 zonal harmonic potential due to the flattening of the core is needed, in accord with a setup of Neumann et al. (2004). Since our study is not aimed of dealing with subtle local variations in the crustal distribution, we choose as a stabilization filter w_ℓ for simplicity a step-like function equivalent to cutting out degrees higher than ℓ=30. We have checked that for our application the use of this filter will not significantly flaw the obtained results. On the contrary, it decreases the minimum crustal thickness value by a few km which gives a slightly higher and thus more conservative estimate on ρ_c max. For the GTR analysis, we remove the global non-isostatic signature of Tharsis, following the method of Wieczorek and Zuber (2004), which involved removing the lowermost degrees of both the gravity and topography signal. However, the resulting estimate of a mean global crustal thickness T_c depends on the exact cut-off degree. We have chosen to study the signal between ℓ=11–60, which gives among several other cut-off degrees the highest estimate for the value of T_c [Wieczorek and Zuber, 2004] and therefore a conservative value for the maximum crustal density. The maximum spherical harmonic degree was chosen to be ℓ=60 in accord with Wieczorek and Zuber [2004] because of increasing uncertainty of the gravity model at the short wavelengths.

The only free parameters in the current study are the densities of the mantle and the crustal layers. For the mantle we use a density of 3500 kg m^{-3}; a value obtained from geochemical and interior structure models [e.g., Bertka and Fei, 1997; Sohl and Spohn, 1997]. The crust densities have been varied between 2400 and 3200 kg m^{-3} (3000–3200 kg m^{-3} for the lower crust) to study all possible cases and also the general trends.

The results for the single-layered crustal model are shown in Fig. 2. The mean crustal thickness derived by the GTR analysis (depicted with 1σ error-bar) decreases almost linearly with increasing crustal density as indicated by Wieczorek and Zuber [2004]. On the other hand, the minimum crustal thickness derived by the Bouguer inversion increases with increasing density, with a stronger increase for crustal densities higher than 2900 kg m^{-3}.

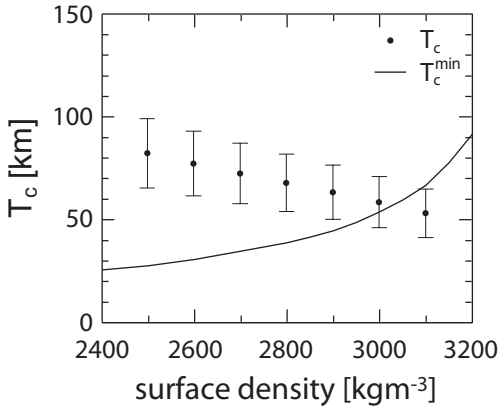

Figure C.2.2: *Results of the joint gravity-topography analysis for the Martian southern highland using a single-layer crustal model. For various crustal densities* ρ_c *the mean crustal thickness* T_c *is obtained by the GTR analysis (dots with error-bars) and the minimum mean crustal thickness* T_c^{min} *by the Bouguer inversion (solid line). The maximum crustal density* ρ_c^{max} *is determined by the crossing of these two trends.*

To satisfy the constraint that the mean crustal thickness should be larger or equal to the minimum crustal thickness, a maximum crustal density of 3020±70 kg m^{-3} is obtained. The admissible mean crustal thickness in this case ranges between 50 and 100 km consistent with previous studies [e.g., Nimmo and Stevenson, 2001; McGovern et al., 2002; Wieczorek and Zuber, 2004].

For the two-layer crustal model with a lower crust of constant thickness, we test two different cases with T_l equal to 10 and 20 km. The results for both the GTR analysis and the Bouguer inversion are sensitive to the density of the upper crust ρ_u, but not as much to variations in the lower crust density ρ_l (Fig. 3). The mean crustal thickness derived by the GTR analysis decreases with increasing surface crustal density and the minimum crustal thickness derived by the Bouguer inversion increases with increasing surface crustal density, similar to single-layer crustal model. The maximum crustal density of the compensating (upper crustal) layer ρ_u is about 3000 kg m^{-3}, as for the single-layer structure, but decreases slightly for increasing upper crustal layer thickness.

For the second two-layer crustal model with a constant thickness of the upper crust, we vary T_u between 10 and 20 km. Similar to the previous model, results for both the GTR analysis and the Bouguer inversion depend mainly on the density of the compensating layer, which is in this case the lower-crustal density ρ_l and not much on the upper crust density ρ_u. The joint analysis of both methods shows that for the structural parameters considered, the observed gravity and topography data cannot be explained with lower crust (compensating layer) densities larger than 3000 kg m^{-3} (Fig. 4). As the results are insensitive to the upper crust density ρ_u, we find for $\rho_l < 3000$ kg m^{-3} a wide range of acceptable models with an upper crust density higher than the lower crust density. Note, however, that with decreasing thickness of the upper crust, the results again become similar to the single-layer crustal structure with a maximum lower crust density of about 3000 kg m^{-3}.

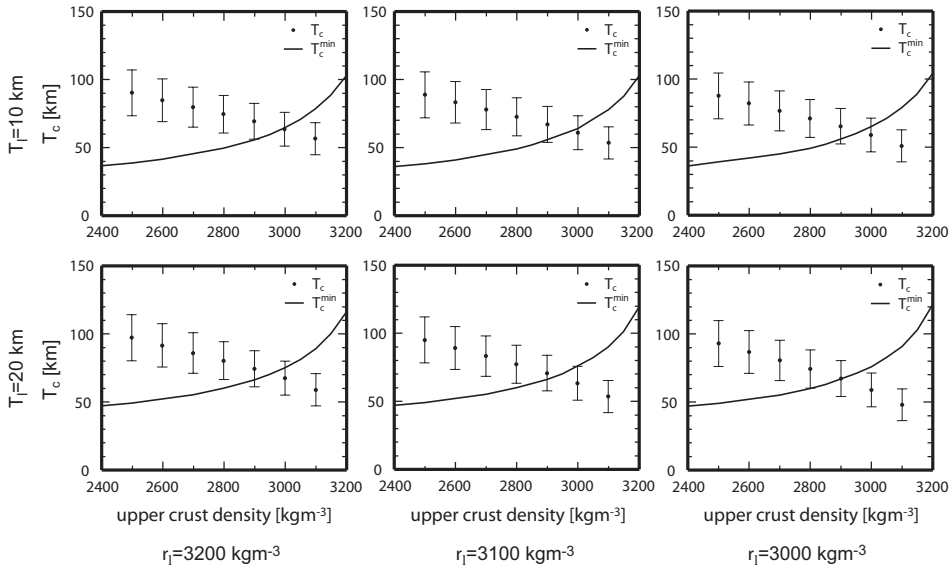

Figure C.2.3: *As for Fig. 2 but using a two-layer crust model with a lower crust of constant thickness* T_l.

C.2.5 Conclusions and discussion

The combination of the GTR analysis and the Bouguer inversion allows to constrain the maximum crustal density for a homogeneously compensated region with a significantly deep impact structure. In comparison to the studies of Wieczorek and Phillips [1997] and Wieczorek and Phillips [1998], we have rederived Eqs. (5)–(8) and modified the equations for the CMI relief inversion for the case of a two layer crustal structure (Eqs. (13) and (14)). Applying both methods simultaneously to the gravity and topography data of the Martian southern highlands, a maximum crustal density 3020±70 kg m^{-3} is obtained. For layered crustal structures, the admissible maximum density of the compensating layer (i.e. the layer with lateral variations in thickness) is also about 3000 kg m^{-3}, but decreases with increasing thickness of the layer of constant thickness.

Assuming that in general the density of the upper layer cannot be higher than the density of the lower-crustal layer, the current results suggest that the upper crustal density ρ_u is less than about 3000 kg m^{-3}, whereas the lower-crustal density can be up to 3200 kg m^{-3} or higher for the models with the compensation in the upper crust. Without such a restriction on the density stratification, models with a constant upper crust thickness could also fit the observed data,with the upper crustal density of ∼3200 kg m^{-3} or higher being denser than the lower crust with a density $\rho_\mathrm{l} < 3000$ kg m^{-3}. However, we believe that this structure is unlikely for the southern crust for the following reason: the old southern crust has been fractured due to impacts during the last 4 Ga. That process resulted in a decrease in the surface density due to the increase in porosity. At a certain depth the pores are closed and the density is consistent with compact material due to lithostatic pressure. Although there is evidence by high-resolution images that part of the fractures are cemented due to fluids [Okubo and McEwan, 2007] and by data from the OMEGA spectrometer for pervasive

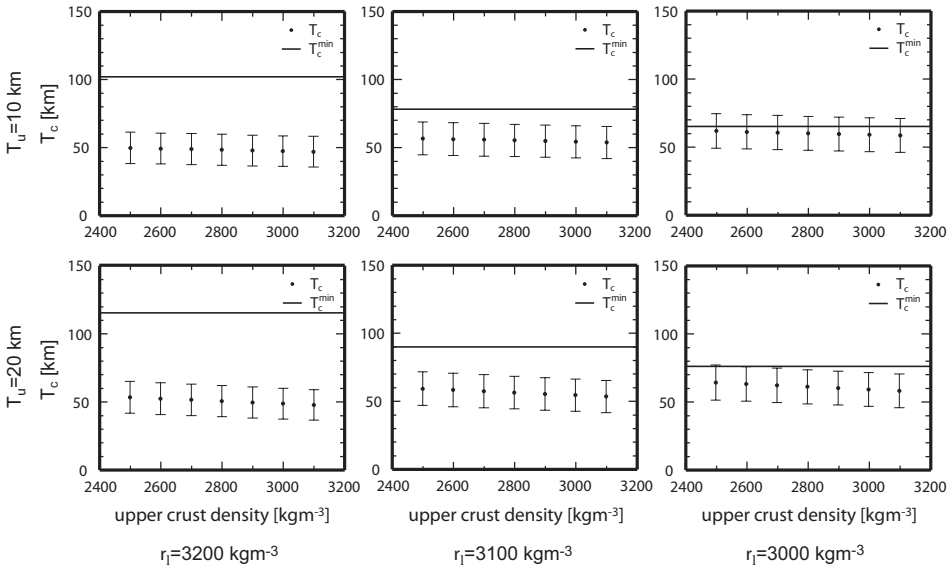

Figure C.2.4: *Fig. 4. As for Fig. 2 but using a two-layer crust model with an upper crust of constant thickness* $T_{\rm u}$.

sulfates and phyllosilicates throughout the southern highlands [Poulet et al., 2005; Bibring et al., 2006], the density of this cemented crust might still be slightly lower than that of compact basaltic material. The consequence is that the density of the lower crust should be in general higher than the surface density. One possible scenario for a denser upper crust in comparison to the lower crust is e.g. observed at the Moon in mascons. Here, secondary (extrusive) volcanism transported dense material towards the surface. While, such a structure might be possible locally, a homogeneous distribution of dense volcanic material on lighter older crust seems unlikely. In fact, it is likely that the crustal structure is formed by a combination of various processes. In that case the structures may not be described simply by a constant thickness of one crustal layer. In any case, as long as we have no additional constraints on crustal structure, the present results provide an upper limit on the compensating crustal layer density of about 3000 kg m^{-3}.

The results of the Bouguer inversion are sensitive to variations in mantle density. A mantle density of 3500 kg m^{-3} has been used throughout our study. This value has been derived from interior structure models [e.g., Sohl and Spohn,1997; Fei et al.,1995, Sohl et al., 2005] and is also in agreement with other gravity and topography studies [e.g., Nimmo and Stevenson, 2001; McKenzie et al., 2002; McGovern et al., 2002; Neumann et al., 2004]. Only the study by Wieczorek and Zuber [2004] uses a slightly higher upper bound for $\rho_{\rm m}$ of 3550 kg m^{-3} but the influence on the results is negligible. On the contrary, it has been suggested that the mantle may be layered with a depleted upper mantle layer (harzburgite layer) as a consequence of partial melting [Schott et al., 2001]. This depleted layer could have a density of about 3300 kg m^{-3}. Assuming an upper mantle of this density will result in an increase of $T_{\rm c}^{\rm min}$ for the Bouguer inversion. As the influence of $\rho_{\rm m}$ on the results for the GTR analysis is minor, the maximum density of the crust decreases to 2870±70 kg m^{-3}. Another factor which influences the results of Bouguer inversion is the minimum assumed

crustal thickness, which was considered in our work to be 5 km in accord with Neumann et al. [2004] – however changing this value to 1 km would result in an increase of the maximum crustal density only by ∼30 kg m^{-3}.

The present results correspond to the findings of the maximum pore-free rock density of 3060 kg m^{-3} derived by Neumann et al. [2004] based on Mars Pathfinder Alpha Proton X-ray Spectrometer measurements [Brückner et al., 2003]. The landing site of Mars Pathfinder was located in an outflow channel that originates within the highlands and therefore rocks found at this site may have an origin from the ancient highlands of Mars. Considering that the upper crustal layer is in general fractured by impacting over the last 4 Ga, the surface density should be even lower (see above). Estimates by gravitational considerations suggest a decrease from a typical surface porosity of about 35% to about 1% at a depth of 10 km [e.g., Clifford and Parker, 2001]. This can be approximated by an average column porosity of about 10 vol.%, suggesting a reduction of the mean surface layer density of about 300 kg m^{-3}. However, if the pore space is filled with liquid water or ice, the bulk density would only be reduced by about 200 kg m^{-3}. Thus, a mega-regolith layer 10 km in thickness consisting entirely of rock measured by Mars Pathfinder may have an average density between 2760 and 2860 kg m^{-3}. However, the situation can be different if a large part of the pore space is cemented due to fluids or by sulfates and phyllosilicates. In that case, the density of the megaregolith layer is only minor reduced in comparison to solid material. Low densities for the southern crust have been suggested by Nimmo [2002] who examined an area at the dichotomy boundary region and suggested a best fitting surface density of 2500 kg m^{-3}. This result is, however, somehow questionable since the employed compensation model was not shown to match the observed coherence and the assumption that both the highland and the lowland regions in the selected area have common properties is also problematic.

Volcanoes such as Elysium, Olympus, Pavonis, Arsia and Ascraeus Mons that have been studied with gravity/topography analysis show load densities of 3200±100 kg m^{-3} [Mc Govern et al., 2004; Belleguic et al., 2005] – much higher than the maximum density obtained for the southern crust. The recent activity of these volcanoes is of Amazonian age [Werner, 2005]. It should be noted, however, that the bulk of the volcanic constructs have been formed earlier, i.e. at least since the Early Hesperian [Werner, 2005]. This in fact would indicate on high density volcanism since that time. High density volcanism is also supported by the SNC meteorites. The latter show pore-free densities between 3220 and 3390 kg m^{-3} and are believed to have a crystallization age of less than 1.3 Ga [Papanastassiou and Wasserburg, 1974]. Even if one considers a porosity of about 5%, a value typical for the Martian meteorites [Britt and Consolmagno, 2003], the density of the meteorites are reduced by about 100 to 150 kg m^{-3} depending whether the pore space is filled with water or air, respectively. Comparing the high densities of the volcanic structures with the comparatively lower density of the ancient southern hemispheric crust suggests an increase of the density. The 'temporal' increase probably results from different formation mechanisms or possibly from a change in composition of the basaltic magmas over time. The increase in density is supported by the observation of the Fe concentration from Mars Odyssey Gamma Ray Spectrometer, with higher Fe abundances in the superficial younger northern lowlands and lower Fe abundances in the ancient southern lowlands [Boynton et al., 2007]. In general, an increase in Fe concentration of 12% between the Noachian and Hesperian has been observed

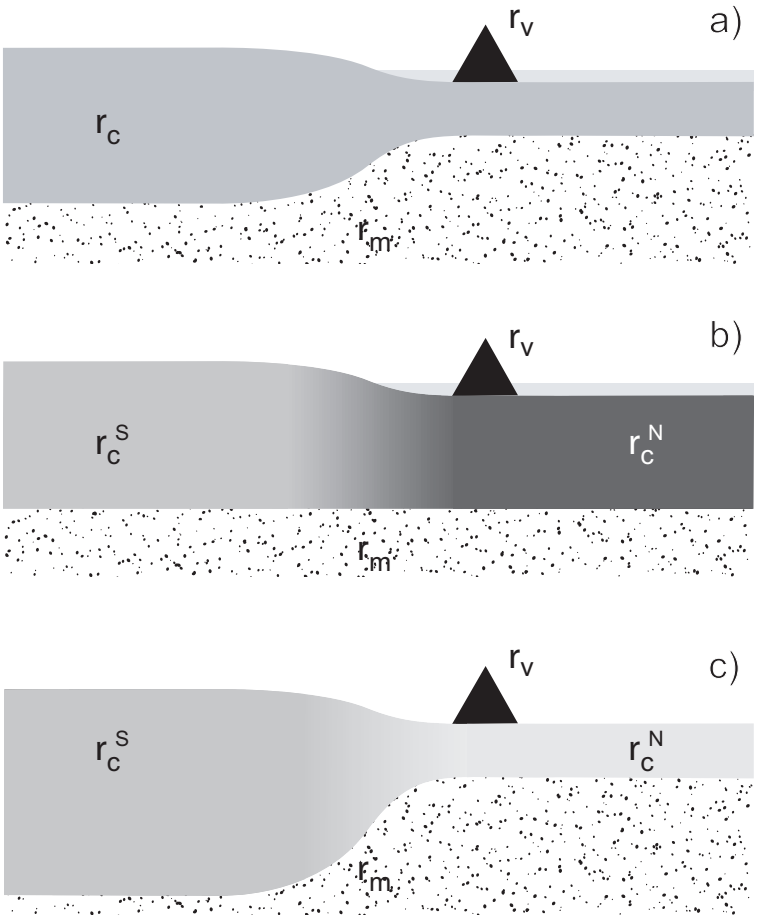

Figure C.2.5: *Schematic sketch of different models of the hemispheric crustal dichotomy (see Section 4): a) with uniform density* ρ_c *of both hemispheres underlain by a mantle with density* ρ_m*. The crustal dichotomy is compensated by Airy isostasy. The superficial young northern hemisphere consists of a thin layer of altered crust and volcanic constructs with density* ρ_v*. b) The same as in a) but the crustal dichotomy is reflected also in a crustal density variation with the density of southern highland crust* ρ_c^S *lower than the density of northern lowland crust* ρ_c^N*. The compensation mechanism in this case is Pratt isostasy. c) The same as in b) but with* $\rho_c^S > \rho_c^N$ *– in that case the compensation mechanism is a combination of Airy and Pratt isostasy. The grayscale of the crustal material reflects its density; the lighter the color is the lower is the density.*

[Hahn et al., 2007]. However, the cause of this dichotomy in Fe concentration cannot be uniquely interpreted as igneous origin, surface alteration process, or a combination of both. A change in primary igneous magma compositions could lead to an increase of iron and thus an increase in the density, thus supporting the temporal change in density. Alternatively, Fe could have been leached out of the southern highlands and been deposited onto the Northern lowlands through significant long-term circulation of water [e.g., Scott et al.,1995; Fairén et al., 2003; Tanaka et al., 2003]. Given the early Noachian age of the Martian lowlands below the superficial younger surface [Frey et al., 2002], the density of the lower crust of the Northern lowlands should have a similar density as the crust of the early Noachian southern hemisphere (Fig. 5a). As a consequence, the bulk of the crust has the same density. For that assumption, a Bouguer inversion of the gravity data can be applied to obtain crust thickness variations. The results suggest the generally accepted dichotomy in the crustal thickness with a thick crust of about 70 km underneath the southern hemisphere and a thinner crust of about 30 km below the northern hemisphere [Zuber et al., 2000; Neumann et al., 2004].

The variation in the crustal density, however, can also be associated with a hemispheric dichotomy, although the implications for such a scenario are less well constrained. For the Elysium region it is suggested that even the surrounding crustal density is similar to the load density with a value of 3270±150 kg m^{-3} [Belleguic et al., 2005]. Assuming the finding of the Elysium crust is representative for the entire Northern lowlands, then this implies that the density and composition of the northern hemisphere crust is different than that of the southern highlands. Such an assumption is highly speculative as the formation of the volcanic Elysium region can be completely different to the formation of the Martian lowlands. However, a high density of the entire northern lowlands can not completely be excluded; therefore, the possibility for a Pratt mechanism appears as an explanation for the elevation difference between north and south as already suggested by Spohn et al. [2001] and Belleguic et al. [2005]. With Pratt isostasy the density variation $\Delta\rho$ to support a given topography variation Δt is $\rho'(z'/\Delta t + 1)^{-1}$ where z' and ρ' are the average crust thickness and density, respectively. Assuming z'=50 km, ρ'=3100 kg m^{-3} and taking the topography variations to be ±3 km thereby ignoring the largest variations associated with large impact basins and volcanoes, we require a $\Delta\rho$ of ±175 kg m^{-3}. This would bring the density of lowland crust close to the densities of the northern crust of 3270±150 kg m^{-3} [Belleguic et al., 2005] and would require a density in the highland crust of 2925 kg m^{-3}. As a further consequence, the crustal thickness variations would be small, about equal to the topography variations and thus crust-mantle interface undulations negligible (Fig. 5b).

A compositional dichotomy is supported by the findings of the Thermal Emission Spectrometer (TES) of Mars Global Surveyor. TES mapped two distinct spectral signatures on the Martin surface dividing the northern and southern hemisphere [Christensen et al., 2000; Bandfield et al., 2000]. The surface type 1 on the southern hemisphere has been interpreted as basalt [Christensen et al., 2000; Bandfield et al., 2000]. There are, however, several competing mineralogical models for surface type 2, which is found primarily in the northern lowlands. The spectra indicate that the surface type 2 is either basalt plus weathering products or andesite [McSween et al., 2003] or a material originating from a compositionally distinct mantle source than surface type 1 [Karunatillake et al., 2006]. In the former case, the crust of both hemispheres would most likely be produced by a similar mechanism and later modified by aqueous processesthis is consistent with the scenario described above

assuming a temporal evolution of the density manifested in the high density of the Amazonian volcanic regions (Fig. 5a). In the two latter cases, the origin of the andesites is by igneous processes and given the early Noachian age of the Martian lowlands [Frey et al., 2002], this compositional difference that is most likely associated with a density difference must have been formed during the early evolution of Mars. Possible scenarios are either early plate tectonics operating in the Northern lowlands (i.e., the northern crust represents 'oceanic' basaltic crust and the southern crust represents 'continental' andesitic crust) or a fundamental asymmetry in the primary differentiation of this planet as suggested e.g. by a large scale instability of the differentiated magma ocean [Elkins-Tanton et al., 2005a,b] or by a large impact, a theory recently rejuvenated by Andrews-Hanna et al. [2008], Nimmo et al. [2008] and Marinova et al. [2008]. Both two latter cases support the assumption that the surface type 2 may originate from a compositional distinct mantle source [Karunatillake et al., 2006].

Although the TES data support a compositional dichotomy and, therefore, also a density dichotomy, the characteristics of the two surface types are not compatible with the assumption of a low crustal density of the southern hemisphere in comparison to a higher crustal density of the northern hemisphere. Basalt has in general a higher density than andesite, therefore, the spectral data suggest a density distribution vice versa. Accepting the observed compositional distribution from TES being the result of igneous processes, the high densities of volcanic material of Amazonian age and the present results of a maximal density of the southern crust of about 3000 kg m^{-3}, the general density variation of the Martian crust can be even threefold: a density dichotomy that separates the Noachian crust of the southern and northern hemisphere with a higher density of the southern basaltic crust and a comparatively lower density of the northern crust. In the subsequent evolution, basaltic volcanism is formed that is enriched in iron and has a higher density than the Noachian crust of the southern highlands. The consequence is even larger crust-mantle interface undulations as compared to the model with Bouguer inversion assuming a constant crust density (Fig. 5c).

C.2.6 Summary

The combination of the GTR analysis and the Bouguer inversion allows to constrain the maximum surface crustal density for the Martian southern highlands to be about 3020±70 kg m^{-3}. The comparison of this maximum crustal density of the southern highlands with crustal densities (and composition) of other regions on Mars, can help to better understand the planetary evolution and results in the following three different evolution scenarios (Fig. 5): 1) A temporal evolution in the densities with low densities of the ancient crust and comparatively higher densities of the young (Amazonianera) volcanic material. 2) The density variation is already manifested in the early evolution during the formation of the crustal dichotomy, i.e. the Noachian crust of the northern lowlands has a different density than the Noachian southern highland crust. The ancient northern hemisphere might have a higher density than the crust of the ancient southern hemisphere, assuming the high density crust of the Elysium region being representative for the entire Northern lowlands. If correct, this also suggests a much lower crust-mantle undulation as generally assumed [Zuber et al., 2000; Neumann et al., 2004]. 3) As in case 2, the density variation is already manifested in the early evolution during the formation of the crustal dichotomy. However, in contrast to

case 2, the ancient northern hemisphere has a lower density than the crust of the ancient southern hemisphere as suggested by TES data. The spectra can be interpreted as basalt in the southern hemisphere and andesite in the northern hemisphere. A consequence of that density variation is a stronger crust-mantle undulation than assumed by Bouguer inversion with constant crust density [Zuber et al., 2000; Neumann et al., 2004]. In the subsequent evolution of dichotomy formation and bulk crust formation, the volcanism in Elysium and Tharsis becomes more enriched in iron and therefore shows an increasing density.

C.2.7 Acknowledgments

We thank G. A. Neumann who kindly provided us the access to the MOLA spherical harmonic models and K. Fleming and anonymous reviewers for their comments on the manuscript. Some parts of our spherical harmonic analyses were performed using the freely available software archive SHTOOLS (available at http://www.ipgp.jussieu.fr/ wieczor/SHTOOLS/SHTOOLS.html). This work was financially supported through the European Community's Improving Human Potential Programme under contract RTN2-2001-00414, MAGE and the Charles University grant 280/2006/B-GEO/MFF.

C.2.8 References

Andrews-Hanna, J.C., Zuber, M.T., Banerdt,W.B., 2008. The Borealis basin and the origin of the Martian crustal dichotomy. Nature 453, 1212–1215. doi:10.1038/nature07011.

Bandfield, J.L., Hamilton, V.E., Christensen, P.R., 2000. A global view of Martian surface compositions from MGS-TES. Science 287, 1626-1630.

Belleguic, V., Lognonné, P., Wieczorek, M., 2005. Constraints on theMartian lithosphere from gravity and topography data. J. Geophys. Res.110, E11005. doi:10.1029/2005JE002437.

Bertka, C.M., Fei, Y., 1997. Mineralogy of the Martian interior up to core-mantle boundary pressures. J. Geophys. Res. 102, 5251-5264.

Bibring, J., Langevin, Y., Mustard, J.F., Poulet, F., Arvidson, R., Gendrin, A., Gondet, B., Mangold, N., Pinet, P., Forget, F., the OMEGA team, 2006. Global mineralogical and aqueous Mars history derived from OMEGA/Mars express data. Science 312, 400-404. doi:10.1126/science.1122659.

Boynton, W.V., Taylor, G.J.,Evans, L.G.,Reedy, R.C., Starr, R., Janes, D.M., Kerry, K.E., Drake, D.M., Kim, K.J., Williams, R.M.S., Crombie, M.K., Dohm, J.M., Baker, V., Metzger, A.E., Karunatillake, S., Keller, J.M., Newsom, H.E., Arnold, J.R., Brückner, J., Englert, P.A.J., Gasnault, O., Sprague, A.L., Mitrofanov, I., Squyres, S.W., Trombka, J.I., d'Uston, L., Wänke, H., Hamara, D.K., 2007. Concentration of H, Si, Cl, K, Fe, and Th in the low- and midlatitude regions of Mars. J. Geophys. Res. 112 (E12), E12S99. doi:10.1029/2007JE002887.

Breuer, D., Spohn, T., 2003. Early plate tectonics versus single-plate tectonics on Mars: evidence from magnetic field history and crust evolution. J. Geophys. Res. 108 (E7), 5072. doi:10.1029/20002JE001999.

Britt, D.T., Consolmagno, G.J., 2003. Stony meteorite porosities and densities: a reviewof the data through 2001. Meteorit. Planet. Sci. 38, 1161–1180.

Brückner, J., Dreibus, G., Rieder, R., Wänke, H., 2003. Refined data of alpha proton

X-ray spectrometer analyses of soils and rocks at the Mars Pathfinder site: implications for surface chemistry. J. Geophys. Res. 108 (E12), 8094. doi:10.1029/2003JE002060.
Clifford, S.M., Parker, T.J., 2001. The evolution of the Martian hydrosphere: implications for the fate of a primordial ocean and the current state of the northern plains. Icarus 154, 40–79. doi:10.1006/icar.2001.6671.
Čadek, O., Fleitout, L., 1999. A global geoid model with imposed plate velocities and partial layering. J. Geophys. Res. 104 (B12), 29,055–29,075. doi:10.1029/1999JB900150.
Chenet, H., Lognonné, P., Wieczorek, M., Mizutani, H., 2006. Lateral variations of lunar crustal thickness from the Apollo seismic data set. Earth Planet. Sci. Lett. 243, 1–14. doi:10.1016/j.epsl.2005.12.017.
Christensen, P.R., Bandfield, J.L., Clark, R.N., Edgett, K.S., Hamilton, V.E., Hoefen, T., Kieffer, H.H., Kuzmin, R.O., Lane, M.D., Malin, M.C., Morris, R.V., Pearl, J.C., Pearson, R., Roush, T.L., Ruff, S.W., Smith, M.D., 2000. Detection of crystalline hematite mineralization on Mars by the Thermal Emission Spectrometer: evidence for near surface water. J. Geophys. Res. 105 (E4), 9623–9642. doi:10.1029/1999JE001093.
Elkins-Tanton, L.T., Hess, P.C., Parmentier, E.M., 2005a. Possible formation of ancient crust on Mars through magma ocean processes. J. Geophys. Res. 110, E12S01. doi:10.1029/2005JE002480.
Elkins-Tanton, L.T., Zaranek, S.E., Parmentier, E.M., Hess, P.C., 2005b. Early magnetic field and magmatic activity on Mars from magma ocean cumulate overturn. Earth Planet. Sci. Lett. 236, 1–12. doi:10.1016/j.epsl.2005.04.044.
Fairén, A.G., Dohm, J.M., Baker, V.R., de Pablo, M.A., Ruiz, J., Ferris, J.C., Anderson, R.C., 2003. Episodic flood inundations of the northern plains of Mars. Icarus 165, 53–67. doi:10.1016/S0019-1035(03)00144-1.
Fei, Y., Prewitt, C.T., Mao, H., Bertka, C.M., 1995. Structure and density of FeS at high pressure and high temperature and the internal structure of Mars. Science 268, 1892–1894.
Frey, H.V., Bills, B.G., Nerem, R.S., Roark, J.H., 1996. The isostatic state of Martian topography revisited. Geophys. Res. Lett. 23, 721–724.
Frey, H.V., Roark, J.H., Shockey, K.M., Frey, E.L., Sakimoto, S.E.H., 2002. Ancient lowlands on Mars. Geophys. Res. Lett. 29, 1384. doi:10.1029/2001GL013832.
Hager, B.H., Clayton, R.W., 1989. Constraints on the structure of mantle convection using seismic observations, flow models, and the geoid. In: Peltier, W.R. (Ed.), Mantle Convection: Plate Tectonics and Global Dynamics. Gordon & Breach, New York, NY, pp. 675–763.
Hahn, B.C., McLennan, S.M., Taylor, G.J., Boynton, W.V., Dohm, J.M., Finch, M.J., Hamara, D.K., Janes, D.M., Karunatillake, S., Keller, J.M., Kerry, K.E., Metzger, A.E., Williams, R.M.S., 2007. Mars Odyssey Gamma Ray Spectrometer elemental abundances and apparent relative surface age: implications for Martian crustal evolution. J. Geophys. Res. 112 (E3), E03S11. doi:10.1029/2006JE002821.
Karunatillake, S., Squyres, S.W., Taylor, G.J., Keller, J.M., Gasnault, O., Evans, L.G., Reedy, R.C., Starr, R., Boynton, W., Janes, D.M., Kerry, K.E., Dohm, J.M., Sprague, A.L., Hahn, B.C., Hamara, D., 2006. Composition of northern low-albedo regions of Mars: insights from the Mars Odyssey Gamma Ray Spectrometer. J. Geophys. Res. 111(E3), E03S05. doi:10.1029/2006JE002675.
Kiefer, W.S., Richards, M.A., Hager, B.H., Bills, B.G., 1986. A dynamic model of Venus'

gravity field. Geophys. Res. Lett. 13, 14–17.
Lambeck, K., 1988. Geophysical Geodesy. Oxford Univ. Press, New York, NY.
Lognonné, P., 2005. Planetary seismology. Annu. Rev. Earth Planet. Sci. 33, 19.1–19.34.
Marinova, M.M., Aharonson, O., Asphaug, E., 2008. Mega-impact formation of the Mars hemispheric dichotomy. Nature 453, 1216–1219. doi:10.1038/nature07070.
McGovern, P.J., Solomon, S.C., Smith, D.E., Zuber, M.T., Simons, M., Wieczorek, M.A., Phillips, R.J., Neumann, G.A., Aharonson, O., Head, J.W., 2002. Localized gravity/ topography admittance and correlation spectra on Mars: implications for regional and global evolution. J. Geophys. Res. 107 (E12), 5136. doi:10.1029/2002JE001854.
McGovern, P.J., Solomon, S.C., Smith, D.E., Zuber, M.T., Simons, M., Wieczorek, M.A., Phillips, R.J., Neumann, G.A., Aharonson, O., Head, J.W., 2004. Correction to "Localized gravity/topography admittance and correlation spectra on Mars: implications for regional and global evolution". J. Geophys. Res. 109, E07007. doi:10.1029/2004JE002286.
McKenzie, D., Barnett, D.N., Yuan, D.N., 2002. The relationship between Martian gravity and topography. Earth Planet. Sci. Lett. 195, 1–16.
McSween, H.Y., Grove, T.L., Wyatt, M.B., 2003. Constraints on the composition and petrogenesis of the Martian crust. J. Geophys. Res. 108 (E12), 5125. doi:10.1029/ 2003JE002175.
Neumann, G.A., Zuber, M.T., Smith, D.E., Lemoine, F.G., 1996. The lunar crust: global structure and signature of major basins. J. Geophys. Res. 101 (E7), 16,841–16,843.
Neumann, G.A., Zuber, M.T., Wieczorek, M.A., McGovern, P.J., Lemoine, F.G., Smith, D.E., 2004. Crustal structure of Mars from gravity and topography. J. Geophys. Res. 109, E08002. doi:10.1029/2004JE002262.
Nimmo, F., Stevenson, D.J., 2001. Estimates of Martian crustal thickness from viscous relaxation of topography. J. Geophys. Res. 106, 5085–5098.
Nimmo, F., 2002. Admittance estimates of mean crustal thickness and density at the Martian hemispheric dichotomy. J. Geophys. Res. 107 (E11), 5117. doi:10.1029/ 2000JE001488.
Nimmo, F., Tanaka, K., 2005. Early crustal evolution of Mars. Annu. Rev. Earth Planet. Sci. 33, 3.1–3.29. doi:10.1146/annurev.earth.33.092203.122637.
Nimmo, F., 2005. Tectonic consequences of Martian dichotomy modification by lower crustal flow and erosion. Geology 33, 533–536. doi:10.1130/G21342.1.
Nimmo, F., Hart, S.D., Korycansky, D.G., Agnor, C.B., 2008. Implications of an impact origin for the Martian hemispheric dichotomy. Nature 453,1220–1223. doi:10.1038/ nature07025.
Okubo, C.H., McEwan, A.S., 2007. Fracture-controlled paleo-fluid flow in Candor Chasma, Mars. Science 315, 983–985. doi:10.1126/science.1136855.
Papanastassiou, D.A., Wasserburg, G.J., 1974. Evidence for late formation and young metamorphism in the achondrite Nakhla. Geophys. Res. Lett. 1, 23–26.
Pauer, M., Fleming, K., Čadek, O., 2006. Modeling the dynamic component of the geoid and topography of Venus. J. Geophys. Res. 111, E11012. doi:10.1029/2005JE002511.
Poulet, F., Bibring, J.P., Mustard, J.F., Gendrin, A., Mangold, N., Langevin, Y., Arvidson, R.E., Gondet, B., Gomez, C., OMEGA Team, 2005. Phyllosilicates on Mars and implications for early Martian climate. Nature 438, 623–627. doi:10.1038/nature04274.
Schott, B., Van den Berg, A.P., Yuen, D.A., 2001. Focused time-dependent martian volcanism from chemical differentiation coupled with variable thermal conductivity. Geophys.

Res. Lett. 28 (22), 4271–4274.
Schumacher, S., Breuer, D., 2006. Influence of a variable thermal conductivity on the thermochemical evolution of Mars. J. Geophys. Res. 111, E02006. doi:10.1029/ 2005JE002429.
Scott, D.H., Dohm, J.M., Rice, J.W., 1995. Map of Mars showing channels and possible paleolake basins. U. S. Geol. Surv. Misc. Inv. Series, Map I-2561, Scale: 1:30,000,000.
Simons, M., Solomon, S.C., Hager, B.H., 1997. Localization of gravity and topography: constrains on the tectonics and mantle dynamics of Venus. Geophys. J. Int. 131 (1), 24–44.
Smith, D., Zuber, M., Solomon, S., Phillips, R., Head, J., Garvin, J., Banerdt,W., Muhleman, D., Pettengill, G., Neumann, G., Lemoine, F., Abshire, J., Aharonson, O., Brown, C., Hauck, S., Ivanov, A., McGovern, P., Zwally, H., Duxbury, T., 1999. The global topography of Mars and implications for surface evolution. Science 284, 1495–1503.
Smrekar, S.E., Phillips, R.J., 1991. Venusian highlands: geoid to topography ratios and their implications. Earth Planet. Sci. Lett. 107, 582–597. doi:10.1016/0012-821X(91) 90103-O.
Spohn, T., Acuña, M.H., Breuer, D., Golombek, M., Greeley, R., Halliday, A., Hauber, E., Jauman, R., Sohl, F., 2001. Geophysical constraints on the evolution of Mars. Space Sci. Rev. 96, 231–262.
Sohl, F., Spohn, T., 1997. The interior structure of Mars: implications from SNC meteorites. J. Geophys. Res. E102, 1613–1635.
Sohl, F., Schubert, G., Spohn, T., 2005. Geophysical constraints on the composition and structure of the Martian interior. J. Geophys. Res. 110, E12008. doi:10.1029/ 2005JE002520.
Tanaka, K.L., Skinner Jr., J.A., Hare, T.M., Joyal, T.,Wenker, A., 2003. Resurfacing history of the northern plains of Mars based on geologic mapping of Mars Global Surveyor data. J. Geophys. Res. 108 (E4), 8043. doi:10.1029/2002JE001908.
Turcotte, D.L., Schubert, G., 2002. Geodynamics,, 2nd Edition. Cambridge University Press.
Turcotte, D.L., Shcherbakov, R., Malamud, B.D., Kucinskas, A.B., 2002. Is the Martian crust also the Martian elastic lithosphere. J. Geophys. Res. 107 (E11), 5091. doi:10.1029/ 2001JE001594.
Werner, S. C., 2005. Major aspects of the chronostratigraphy and geologic evolutionary history of Mars. Ph.D. thesis, Free University Berlin.
Wieczorek, M.A., 2007. The gravity and topography of the terrestrial planets. In: Schubert, G. (Ed.), Treatise on Geophysics. . Planets and Moons (Ed. T. Spohn), vol.10. Elsevier, pp. 165–206.
Wieczorek, M.A., Phillips, R.J., 1997. The structure and compensation of the lunar highland crust. J. Geophys. Res. 102 (E5), 10,933–10,943.
Wieczorek, M.A., Phillips, R.J., 1998. Potential anomalies on the sphere: application to the thickness of the lunar crust. J. Geophys. Res. 103 (E1), 1715–1724.
Wieczorek, M.A., Zuber, M.T., 2004. Thickness of the Martian crust: improved constraints from geoid-to-topography ratios. J. Geophys. Res. 109, E01009. doi:10.1029/ 2003JE002153.
Wise, D.U., Golombek, M.P., McGill, G.E., 1979. Tectonic evolution of Mars. J. Geophys. Res. 84, 7934–7939.
Zhong, S., Zuber, M.T., 2001. Degree-1 mantle convection and the crustal dichotomy on

Mars. Earth Planet. Sci. Lett. 189, 75–84. doi:10.1016/S0012-821X(01)00345-4.
Zuber, M.T., Smith, D.E., 1997. Mars without Tharsis. J. Geophys. Res. 102 (E12), 28,673–28,685.
Zuber, M.T., Solomon, S.C., Phillips, R.J., Smith, D.E., Tyler, G.L., Aharonson, O., Balmino, G., Banerdt,W.B., Head, J.W., Johnson, C.L., Lemoine, F.G., McGovern, P.J., Neumann, G.A., Rowlands, D.D., Zhong, S., 2000. Internal structure and early thermal evolution of Mars from Mars Global Surveyor Topography and Gravity. Science 287, 1788–1793.

C.3 Detectability of the ocean floor topography in the gravity field of Europa.

C.3.1 Abstract

Future missions to Jupiter's moon Europa will attempt to measure the gravity field of this planetary body. Here, we study the detectability of silicate shell density variations in the gravity field. The first step in the gravity processing will be to remove the gravity signal of the ice shell. The detection of the ice shell signal, however, can be technologically challenging depending on its thickness and compensation state since the predicted anomalies are only a few mGals or even smaller. For long-wavelength topography below degree 40, the signal of the silicate shell will likely dominate the gravity field. Assuming that the anomalies of the silicate shell are only caused by the ocean floor topography, thus neglecting possible density anomalies in the mantle, we should be able to detect the ocean floor signal even if its topographic variations are only a few hundred meters. When studying the gravity signal of isolated midsize topographic features like volcanoes, we find a good chance of detecting objects with a size of 75–200 km with measurement accuracy of 1 mGal. Owing to the large number of unknown parameters for the gravity inversion, the reconstruction of a global ice-water/silicate interface shape is uncertain, in particular, as possible contributions to the gravity field from a low-degree convecting mantle cannot be distinguished. The comparison between the standard measurement technique of Doppler tracking (detecting the gravity anomalies) and a microgradiometer (measuring gravity gradients) shows that the latter will not improve the detectability of the ocean floor structures.[3]

C.3.2 Introduction

The Galileo mission dedicated to the exploration of Jupiter and its satellites observed Europa, one of the four Galilean moons, during numerous flybys between 1996 and 2003. Data from the gravity measurements suggest the presence of an iron-rich core, a silicate mantle, and an outer ice/water layer. Owing to the ambiguity of gravity data, however, the thicknesses of the layers are not unequivocally determined. The water/ice layer, for instance, varies between 120 and 170 km depending on the assumed densities of the core and the

[3]published as: Pauer, M., S. Musiol, and D. Breuer (2010), Gravity signals on Europa from silicate shell density variations, J. Geophys. Res., 115, E12005, doi:10.1029/2010JE003595.

mantle [Sohl et al., 2002]. Gravimetric, geologic, and magnetometric data [e.g., Anderson et al., 1998; Pappalardo et al., 1999; Kivelson et al., 2000] as well as thermal modeling [e.g., Spohn and Schubert, 2003] suggest that a substantial part of this outer layer consists of a subsurface ocean hidden underneath the observed ice shell. This icy surface with its various tectonic and resurfacing features is geologically young [Pappalardo et al., 1999], presumably as a consequence of intense tidal deformation in the ice shell [e.g., Hussmann et al., 2002]. The geological activity of the silicate mantle, e.g., tectonism and volcanism, is basically unknown as direct observations of the ocean floor underneath the outer ice-water envelope are not possible. It is suggested from geophysical modeling that radiogenic heat sources in the silicate mantle could produce sufficient heat to run tectonic and volcanic processes, in particular during the early evolution of Europa [Hussmann and Breuer, 2007]. In the case that sufficient tidal energy is also dissipated in the silicate mantle [Thomson and Delaney, 2001; Tobie et al., 2005], the volcanic activity may even have existed until recent times [Hussmann and Breuer, 2007]. Thus any information about the ocean floor, such as the possible existence of volcanic and tectonic structures, could give us constraints on the internal dynamics of Europa. Without landing on the surface, one of possible ways to obtain this information is to measure and interpret the gravity field of Europa.

Gravity inversion is a procedure commonly used for the Earth and in planetary research to infer the subsurface distribution of the crust [e.g., Neumann et al., 1996; Wieczorek, 2007], to study variations in the effective elastic thickness [e.g., Simons et al., 1997; Belleguic et al., 2005] and to derive dynamic mantle properties [e.g., Richards and Hager, 1984; Pauer et al., 2006]. The input data for such studies consists of the surface topography and the global gravity field of a planetary body that have been measured to a certain maximum degree (in spherical harmonic representation). For future space probes orbiting Europa [e.g., Clarke, 2007; Blanc et al., 2007] it is anticipated both types of data will be collected to an adequate accuracy to allow not only for a study of the radial density structure [e.g., Anderson et al., 1998] but also to estimate lateral mass variations. However, the fact that the gravity field usually contains contributions from more than one source, together with the well known ambiguity of gravity field interpretation, i.e., the tradeoff between density and radial position [e.g., Wieczorek, 2007], makes any interpretation difficult. The main contribution to gravity anomalies usually comes from crustal thickness or density variations [e.g., Neumann et al., 1996, 2004] because of their vicinity to the surface. Other important sources can be underlying density inhomogeneities such as density variations connected with thermal convection in the silicate mantle [e.g., Richards and Hager, 1984] or in the case of icy satellites like Europa the ice/ocean floor topography and density anomalies in the ocean.

In the present paper we examine the strength of the gravity signal coming from synthetic topographic structures at the bottom of the ice-water layer to estimate their detectability. For simplicity, we assume an end-member model where a convecting silicate mantle does not contribute to the gravity signal. We combine these results with a modeled gravity signal of the overlying ice shell to see how that influences the detectability of the ocean floor features. We address questions concerning the size of the structures that can be resolved, to what degree do we need to measure the gravity and topography fields, and what should be the required sensitivity of future gravity experiments. An important input for the gravity interpretation is the topography of individual interfaces. However, the only topography that we will be able to quantify by means of either stereo-camera or/and laser altimeter

measurements [Blanc et al., 2007] will be the shape of the ice shell that is, at present, known only regionally [Greenberg et al., 2003; Moore et al., 2001; Nimmo et al., 2003a, 2003b; Pappalardo and Barr, 2004]. Thus, aside from a synthetic topography of the ocean floor, we create for our analysis also a global synthetic model of Europa's surface topography based on available information on local structures. The procedure of preparing synthetic topographies will be described first and based on those models the gravity field observable at different orbit heights will be examined. Finally, we examine the reduction of the ice shell signal and the properties of the gravity data inversion also with respect to the uncertainty in ocean floor depth.

C.3.3 Modeling Synthetic Topography and the Corresponding Gravity Field

To study the influence of the ocean floor on the gravity field, we first construct synthetic models of the topography at the ice-water/silicate interface and the ice surface that are then used for forward modeling of the gravity field. As a first order approximation, we generate a random ocean-floor topography represented by a set of spherical harmonic coefficients $t_{\ell m}$ (ℓ is harmonic degree and m harmonic order):

$$t(\theta, \phi) = \sum_{\ell,m} t_{\ell m} Y_{\ell m}(\theta, \phi) \tag{1}$$

where $Y_{\ell m}(\theta, \phi)$ is spherical harmonic function (for details on spherical harmonic formalism see e.g., Wieczorek [2007]) for which the power spectrum

$$S_\ell^{tt} = \sum_{m=-\ell}^{\ell} t_{\ell m}^2 \tag{2}$$

follows the power law (also known as Kaula's law [e.g., Kaula, 1966]) common for the silicate surface topography of terrestrial planets [Turcotte, 1997] with the single slope β of the power-law decay between -1.6 and -2.0 (the latter is a theoretical value emerging from a Brownian walk characteristics of topography distribution [Turcotte, 1997]). To create the synthetic model of the ice-water/silicate interface (Fig. 1a) we choose a representative value of β equal to -1.8. In this particular model, we use an amplitude range of the topography of less than ± 1250 m. For the study of the detected gravity signal, the available topographic information will be however limited to a certain maximum harmonic degree – Fig. 1b shows the reduction of details (and also amplitudes – by more than 20%) of this topographic model for a maximum degree $\ell_{\max} = 20$.

The topography of the ice surface is unknown with respect to its large scale structure but known locally within small regions [Greenberg et al., 2003; Moore et al. 2001; Nimmo et al., 2003a,b; Pappalardo and Bar, 2004]. To derive a global ice surface synthetic topography, we first construct a global model of small-scale features (including bands, craters, domes etc.) [Musiol, 2007] using available regional topographic information and a global geological map [Doggett et al., 2007]. In the second step we generate a synthetic topography (Fig. 1c) – as for the ocean floor shape by generating spherical harmonic coefficients obeying a single power spectrum decay slope – which has for degrees $\ell \sim$75–125 (i.e., a half-wavelength $\sim$40–65 km

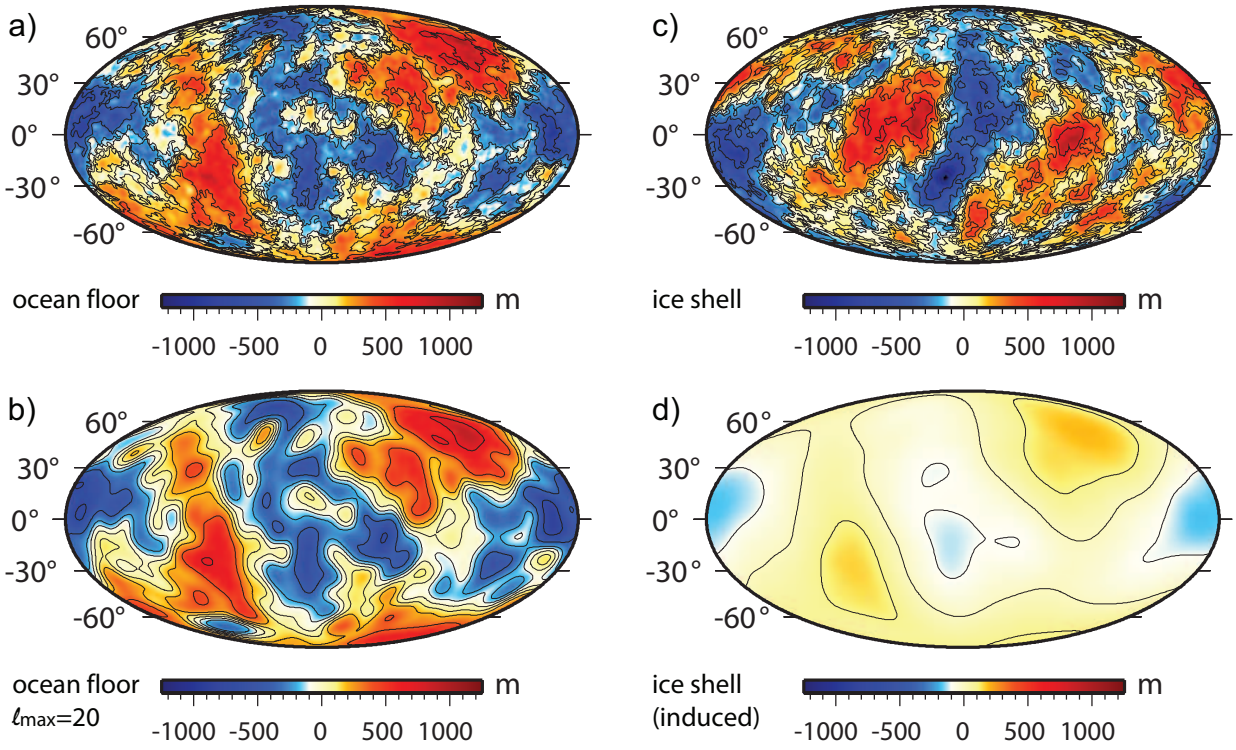

Figure C.3.1: *Synthetic topography of (a) the ocean floor and (c) the ice shell. Both were generated as a set of spherical harmonic coefficients complete to degree $\ell_{max} = 150$ using a topography power law with a fixed decay constant β. (b) Ocean floor topography but expanded only to degree $\ell_{max} = 20$ to demonstrate the possible resolution of the gravity inversion procedure. (d) An upper estimate of the ice shell topography induced by geoid undulations (for ocean floor topography where $R_s = 1450$ km, $\rho_s = 3100$ kg m^{-3}, $d_c^s = d_e^s = 50$ km, a combination of parameters which gives the strongest gravity signal). In all cases, degree 1 is not included since it does not influence gravity field models (those always originate in the center of mass; hence the signal at degree 1 is by definition zero).*

at the surface of Europa) similar values of the power spectrum as the observed small-scale global model derived by Musiol [2007]. Since the aim of our effort is to extrapolate for a global topography model we use a different approach than Blankenship et al. [1999], who constructed a local power spectrum for only one surface feature in order to extrapolate for a meter-scale surface topography. For our model, we use again peak amplitudes of ±1250 m, which is a factor of 3 higher than the observed small-scale geological features but roughly corresponds to the deviation of observed limb profiles from the hydrostatic ellipsoid (see Fig. 2 in Nimmo et al. [2007]). For both the topography of the ice shell and the ocean floor, we also test variations in the amplitude range to examine which topography is detectable depending on the particular compensation state. The latter depends on the crustal and elastic thicknesses, radial position, and density contrasts.

In addition to the global topography models, we also examine the detectability of isolated features at the ocean floor. As an example, we simulate the gravity signal of shield

Parameter	**Symbol**	**Value**	**Unit**
density of ice	ρ_{i}	900	kg m^{-3}
density of water ocean	ρ_{o}	1000	kg m^{-3}
density of silicate crust	ρ_{s}	$2700 - 3100$	kg m^{-3}
density of mantle	ρ_{m}	3500	kg m^{-3}
mean density of Europa	$\bar{\rho}_{\mathrm{avg}}$	3000	kg m^{-3}
thickness of ice crust	$d_{\mathrm{c}}^{\mathrm{i}}$	$5 - 30$	km
thickness of silicate crust	$d_{\mathrm{c}}^{\mathrm{i}}$	$5 - 50$	km
Poisson's ratio for ice	ν_{i}	0.3	–
Poisson's ratio for silicate crust	ν_{i}	0.25	–
Young's modulus for ice	E_{i}	10^9	Pa s
Young's modulus for silicate crust	E_{s}	10^{11}	Pa s
mean planetary radius	R_{i}	1561	km
ocean floor radius	R_{s}	$1400 - 1450$	km
mean gravitational acceleration	g_0	1.3	m s^{-2}

Table C.3.1: *Values of the parameters used for the gravity modeling.*

volcanoes, which are common features representing the volcanic activity as observed on Venus, Earth, Mars, and Io [e.g., Herrick et al., 2005; Schenk et al., 2004] and can have noticeable dimensions (diameter of tens of kilometers and more). To adequately approximate such a feature by a synthetic topography model, the important parameters are diameter, shape (both influence the wavelengths carrying the signal power), and height (determines the amplitude of a signal). To maintain a similarity to observed shield volcanoes we assume a shape similar to the volcano Ascraeus Mons on Mars and a conservative height/diameter ratio 1:25.

After generating the synthetic topography models, we calculate the corresponding geoid anomaly $g_{\ell m}$ (in meters), gravity anomaly $g_{\ell m}^{\mathrm{r}}$ (in mGal units – 1 Gal = 10^{-2} m s^{-2}), and gravity gradient signal $g_{\ell m}^{\mathrm{rr}}$ (in mE units – 1 E=10^{-7} Gal m^{-1} = 10^{-9} s^{-2}). All of them are an expression of the same physical quantity but can be measured with different techniques [e.g., Rio and Hernandez, 2004; Blanc et al., 2007; J. Bouman and R. Koop, Gravity gradients and spherical harmonics – A need for different GOCE products?, paper presented at 2nd International GOCE User Workshop, Eur. Space Agency, Paris, 2004]. We use a first approximation formula that relates an elastically supported topography to lateral gravity variations by means of a simple analytical admittance function Z_ℓ [e.g., Lambeck, 1988] resulting in a set of coefficients $g_{\ell m}$, $g_{\ell m}^{\mathrm{r}}$, and $g_{\ell m}^{\mathrm{rr}}$ [Wieczorek, 2007; Bouman and Koop, presented paper, 2004]. In case of a simple noncompressible boundary with topography t the resulting geoid coefficients are [e.g., Lambeck, 1988]

$$g_{\ell m}(r) = \left(\frac{R_0}{r}\right)^{\ell+1} Z_\ell t_{\ell m} = \left(\frac{R_0}{r}\right)^{\ell+1} \frac{4\pi G \Delta\rho R_0}{g_0(2\ell+1)} \left[1 - c_\ell \left(\frac{R_0 - d_\mathrm{c}}{R_0}\right)^{\ell}\right] t_{\ell m} \tag{3}$$

where $r = R_\mathrm{orb}$ is the evaluation radius (i.e., radius of the orbit), R_0 is the reference radius of the topography (radius of the moon R_i or of the ocean floor R_s), G is the gravitational constant, $\Delta\rho$ is the density change associated with the topography of the respective interface (density difference between ice and vacuum or between silicate crust and water), and d_c is the thickness of the ice or the silicate crust. The factor c_ℓ is an elastic compensation coefficient given by Turcotte et al. [1981]:

$$c_\ell = \frac{1 - f_\mathrm{self}}{\frac{\sigma[\ell^3(\ell+1)^3 - 4\ell^2(\ell+1^2)] + \tau[\ell(\ell+1)-2]}{\ell(\ell+1)-(1-\nu)} + 1 - f_\mathrm{self}} \tag{4}$$

with

$$f_\mathrm{self} = \frac{3\rho_\mathrm{m}}{(2\ell+1)\rho_\mathrm{avg}} \tag{5}$$

$$\tau = \frac{E d_\mathrm{e}}{R_0^2 g_0 (\rho_\mathrm{m} - \rho_\mathrm{c})} \tag{6}$$

$$\sigma = \frac{\tau}{12(1-\nu^2)} \left(\frac{d_\mathrm{e}}{R_0}\right)^2 \tag{7}$$

where f_self is the self-gravitational term, τ is the shell rigidity, σ is the bending rigidity, E is the Young's modulus, ν is the Poisson's ratio, ρ_avg is the mean density of planet, ρ_m is the mantle density, ρ_c is the crustal density, g_0 is the mean gravitational acceleration, and d_e is the elastic thickness. For small values of d_e and low harmonic degrees, c_ℓ approaches 1 (pure Airy compensation) and for the large values of d_e and high degrees, it approaches 0 (no compensation).

If used for calculation of an ocean floor gravity signal, the equation (3) neglects that the gravity anomaly caused by a seafloor edifice will generate topography at the ice-lwater interface and the surface, thus resulting in additional topography and gravity anomalies. To introduce this effect, equation (3) needs to be modified according to

$$g_{\ell m}(r) = \frac{1}{\gamma_\ell} \left(\frac{R_0}{r}\right)^{\ell+1} \frac{4\pi G \Delta\rho R_0}{g_0(2\ell+1)} \left[1 - c_\ell \left(\frac{R_0 - d_\mathrm{c}}{R_0}\right)^{\ell}\right] t_{\ell m} \tag{8}$$

$$\text{where } \gamma_\ell = 1 - \frac{4\pi G \rho_\mathrm{o} R_\mathrm{i}}{g_0(2\ell+1)} \text{ for ocean floor and}$$

$$\gamma_\ell = 1 \text{ for ice shell topography signal.} \tag{9}$$

Consider that this equation assumes instantaneous deformation of the ice shell as it is given for a pure water interface. The ice shell deformation is in fact time dependent. However, due to the expected thin thickness of the shell this will not introduce a significant error.

The factor $1/\gamma_\ell$ is a function of degree ℓ and causes in particular amplification of the low degrees signal. For degrees 2–5 the deformation of the ice shell induced by equipotential surface undulations increases the geoid amplitudes to 125-110%. Beyond degree 10 the

deformation of the ice shell by equipotential surface undulations and thus its influence on the geoid becomes negligible. To compare this induced ice topography with the "real" one (model depicted in Figure 1c), we show the geoid undulations (i.e., fluid body surface) at the reference level of Europa's surface (i.e., $r = R_\mathrm{i}$) in Figure 1d induced by "the best possible combination" of parameters (i.e., parameters that give the strongest gravity signal with $d_\mathrm{c}^\mathrm{s} = d_\mathrm{e}^\mathrm{s} = 50$ km, $R_0 = 1450$ km, and $r_\mathrm{c}^\mathrm{s} = 3100$ kg m^{-3}). The resulting shape of the ice shell is clearly dominated by the long wavelength structure and reaches amplitudes slightly smaller than ±200 m. For "the worst possible combination" of parameters (i.e., parameters that give the weakest gravity signal with $d_\mathrm{c}^\mathrm{s} = d_\mathrm{e}^\mathrm{s} = 5$ km, $R_0 = 1400$ km, and $r_\mathrm{c}^\mathrm{s} = 2700$ kg m^{-3}), we obtain undulations by an order of magnitude smaller (±50 m); it is obvious that in either case such an effect cannot be neglected and should be included in the gravitational anomaly computation. The same amplifying effect should be taken into account if one aims to consider also the gravity signal of a convecting mantle that is neglected in the present paper. For the above discussed models we have used formula (8) and parameters range from Table 1.

The equations for gravity anomaly $g_{\ell m}^\mathrm{r}$ and gravity gradient signal $g_{\ell m}^{rr}$, respectively, modified in a same way as the equation (8), are

$$g_{\ell m}^\mathrm{r}(r) = \frac{1}{\gamma_\ell}\left(\frac{R_0}{r}\right)^{\ell+2} Z_\ell^\mathrm{r} t_{\ell m} = \frac{1}{\gamma_\ell}\left(\frac{R_0}{r}\right)^{\ell+2} \frac{\ell+1}{2\ell+1} 4\pi G\Delta\rho\left[1 - c_\ell\left(\frac{R_0 - d_\mathrm{c}}{R_0}\right)^\ell\right] t_{\ell m} \qquad (10)$$

$$g_{\ell m}^\mathrm{rr}(r) = \frac{1}{\gamma_\ell}\left(\frac{R_0}{r}\right)^{\ell+3} Z_\ell^\mathrm{rr} t_{\ell m} = \frac{1}{\gamma_\ell}\left(\frac{R_0}{r}\right)^{\ell+3} \frac{(\ell+1)(\ell+2)}{2\ell+1} \frac{4\pi G\Delta\rho}{R_0}\left[1 - c_\ell\left(\frac{R_0 - d_\mathrm{c}}{R_0}\right)^\ell\right] t_{\ell m} \qquad (11)$$

We note that, while for modeling the gravity field of Moon and Mars finite relief modeling instead of first approximation approach is more appropriate [Wieczorek, 2007], in our case it gives no additional improvement in the modeled gravity signal since the synthetic topography of either the ice shell or the ocean floor satisfy the first approximation assumption $t \ll 2\pi R_0/\ell$ [e.g., Martinec, 1991]. For the case of high volcanic constructs this assumption no longer holds [Belleguic et al., 2005]; however, the difference in using the finite relief method in comparison to the used method (equations (8), (10), and (11)) is particularly pronounced for middle and high degrees, which are already strongly attenuated by the expected orbit heights 100-200 km above Europa's surface.

Equations (8), (10), and (11) show that the gravity signal depends not only on topography but also on input parameters like crustal thickness, (lithospheric) elastic thickness, and density contrast of the corresponding interface (see Table 1). Some parameters in the above mentioned equations are well known, whereas others are only educated estimates. Thus we examine, instead of single parameter value, a parameter range allowing to investigate both "the best" and "the worst" scenarios, i.e., the expected strongest and the weakest signal. It should be noted that some of the parameters (like ice shell thickness or rigidity) will be better constrained in the future with measurements that are complementary to gravity field detection, e.g., by laser altimeter crossovers [Wahr et al., 2006] or local tectonics analysis [e.g., Nimmo et al., 2003a]. For the ice layer, we can also decrease the number of free parameters by using a simple relation between the shell thickness d_c^i and the elastic thickness d_e^i. The elastic thickness is always smaller than the shell thickness because the water ocean

is below the surface ice layer. Moreover the ice layer exhibits elastic behavior only up to temperature $T_{\mathrm{elastic}} \approx 0.6 T_{\mathrm{melting}}$ [Garofalo, 1965; Ellsworth and Schubert, 1983; Hussmann et al., 2002]. If one further assumes that the melting temperature is given by hydrostatic pressure at the base of the ice shell [Chizhov, 1993; Hussmann et al., 2002]

$$T_{\mathrm{melting}} = 273.16\,\mathrm{K}\sqrt[9]{1 - \frac{\rho_{\mathrm{c}}^{\mathrm{i}} d_{\mathrm{c}}^{\mathrm{i}} g_0}{395.2\,\mathrm{MPa}}} \tag{12}$$

and that the temperature gradient toward the surface (with surface temperature $T_{\mathrm{s}} = 100$ K [e.g., Spencer et al., 1999]) is constant, then the elastic thickness for each shell thickness is given by

$$d_{\mathrm{e}}^{\mathrm{i}} \approx \frac{T_{\mathrm{elastic}} - T_{\mathrm{s}}}{T_{\mathrm{melting}} - T_{\mathrm{s}}} d_{\mathrm{c}}^{\mathrm{i}}. \tag{13}$$

This consideration is only valid for a conductive ice shell, which can accommodate a compensation process for the surface topography, and is not valid if part of the ice shell is convecting [Hussmann et al., 2002]. A convecting ice layer will influence the signal induced by the ice shell topography hence making the ocean floor topography signal either more or less pronounced. This point is discussed in more detail in section 4.

For the calculations throughout this paper, we confine the spherical harmonic analysis of the topography up to harmonic degree $\ell = 150$. This seems to be a maximum gravity field degree which will be possible to be obtained from a microgradiometer device on board a future Europa orbiting probe (R. Koop et al., Prospects for a gradiometry mission for high-resolution mapping of the Martian gravity field, paper presented at European Planetary Science Congress, Eur. Space Agency, Berlin, 2006). For geophysical interpretations, the radial-radial component of the gravity gradient measurements can then be easily converted to more commonly used gravity anomalies. If, however, a traditional Doppler tracking gravity recovery system will be used instead the maximum harmonic degree will be lower [Blanc et al., 2007; Koop et al., presented paper, 2006] with the maximum harmonic degree depending on the mission duration, e.g., for a 90 day mission this could be only $\ell_{\mathrm{max}} \sim 20$ (R. Greeley and T. V. Johnson, Jupiter Icy Moons Orbiter (JIMO) science forum compiled objectives, investigations and measurements, paper presented at Forum on Concepts and Approaches for Jupiter Icy Moons Orbiter, Lunar and Planet. Inst., Houston, Tex., 2003). This can have, in particular, an important influence on the recovery of the ice shell parameters from the admittance function analysis (see section 3 and Figure 5).

C.3.4 Results of the Synthetic Gravity Field Analysis

We first examine the strength of the gravity signal originating from the surface ice layer. A fundamental question for a future mission to Europa is whether we would be able to detect its signal with the anticipated detection sensitivity of 1 mGal or 100 mE [Blanc et al., 2007; Koop et al., presented paper, 2006] and how to reduce it from the measured gravity field. We calculate the gravity anomaly and the gravity gradient of an ice shell at an orbital height of 100 and 200 km (alternatives considered by Clarke [2007] and Blanc et al. [2007]) assuming the synthetic topography described in section 2. The used ice shell thicknesses are 5 and

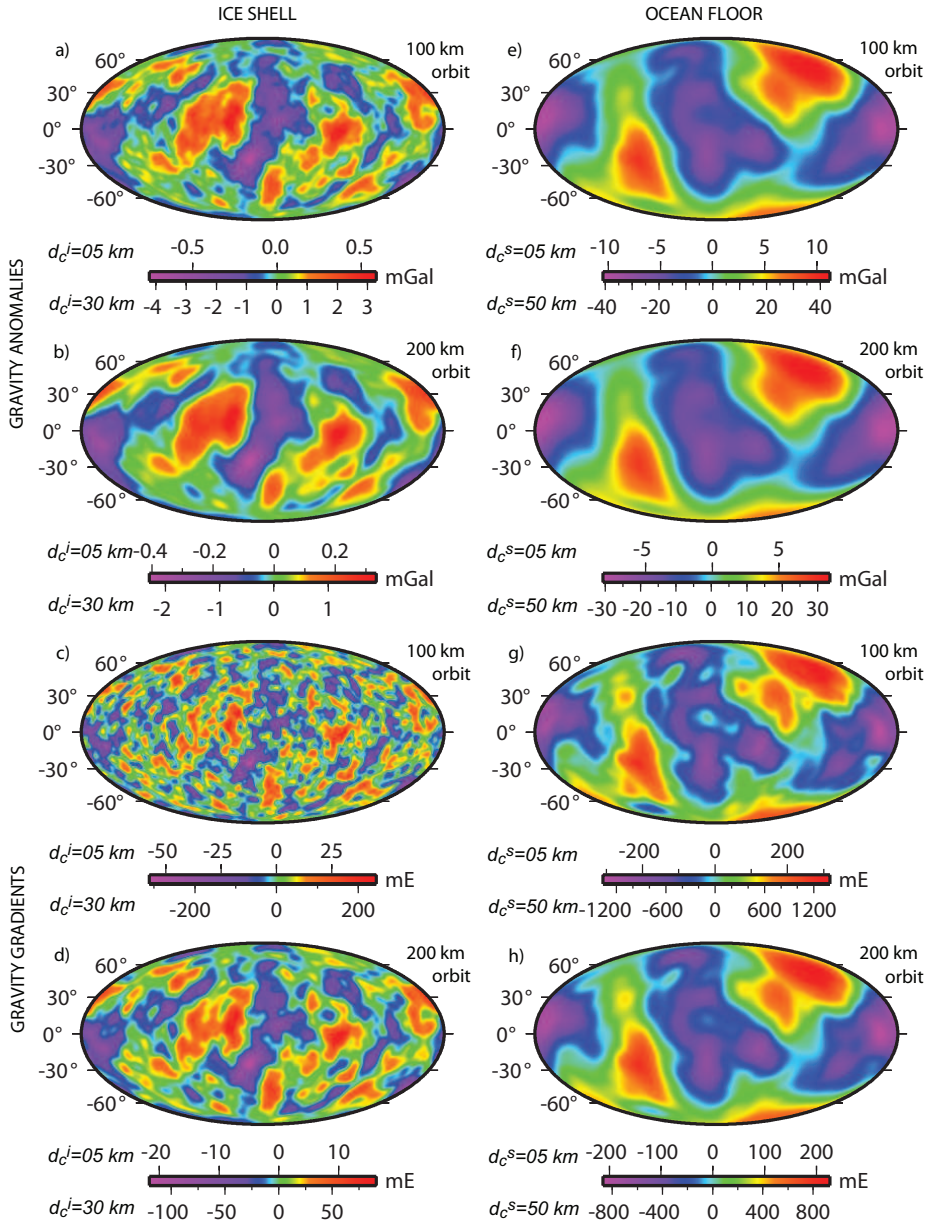

Figure C.3.2: *(ab) Simulated gravity anomalies and (cd) gravity gradients of the ice shell topography (Figure 1a) for two different compensation models (d_c^i = 5 km, d_e^i = 2 km and d_c^i = 30 km, d_e^i = 11 km) and for two different orbital heights (100 km and 200 km). (eh) The same is depicted for the ocean floor topography signal based on model depicted in Figure 1c with compensation parameters d_c^s = 5 km, d_e^s = 5 km and d_c^s = 50 km, d_e^s = 50 km (R_s = 1400 km, ρ_s = 2700 kg m^{-3} and R_s = 1450 km, ρ_s = 3100 kg m^{-3}, respectively). Results for thin and thick ice shell/silicate crust differ apart from the scale also by small lateral differences (because of factor $(R_0 - d_c)^\ell$ in equation (8)), which are for our purpose negligible. Hence we show them both in one panel.*

30 km and the corresponding elastic lithosphere thicknesses calculated using equations (12) and (13) are 2 and 11 km, respectively. The results in Figures 2a–2d show that for the thin ice model, irrespective of the orbit height, the gravity signal is below the anticipated detection sensitivity. The thick ice model on the other hand generates a sufficiently strong signal for detection. This is caused by two factors which appear in the equation (3): first, the thicker the elastic layer is the smaller is the level of compensation of the surface features, e.g., for a characteristic wavelength ~ 100 km the factor $c_\ell(d_{\mathrm{c}}^{\mathrm{i}} = 5 \text{ km}) = 0.988$ and $c_\ell(d_{\mathrm{c}}^{\mathrm{i}} = 30 \text{ km}) = 0.484$ and second, the deeper the subsurface interface of the ice shell is the more of its signal is attenuated. Thus the stronger is the surface signal, e.g., for the same characteristic wavelength of ~ 100 km is $(R_{\mathrm{i}} - 5 \text{ km}/R_{\mathrm{i}})^\ell = 0.851$ and $(R_{\mathrm{i}} - 30 \text{ km}/R_{\mathrm{i}})^\ell = 0.379$.

Studying the power spectra of the modeled gravity signal (Figures 3a and 3b), one can also see that with sufficient sensitivity the microgradiometer readings are in principle more suitable for detailed examination of the ice shell signal compared to standard Doppler technique. The microgradiometry method is obviously more sensitive to higher wavelengths for which the contribution over a certain harmonic interval ($\ell \sim$10–40 for 100 km and $\ell \sim$10–20 for 200 km orbit) is approximately of the same power. Beyond this harmonic interval the power spectra decay rapidly which indicate possible problems in obtaining data for these wavelengths.

There is, however, a tradeoff between topography amplitudes and ice shell thickness (see equations (10) and (11)). This tradeoff, calculated for both examined orbital heights, suggests that with maximum amplitude of ice shell topography at least $\pm$1000 m, we would be able to detect its gravity signal with the Doppler tracking method if the ice shell is thicker than 10–15 km (Figures 4a and 4b). If, however, the amplitudes of the ice shell topography are only $\sim \pm$500 m, then we will be able to measure a signal only for a shell thicker than 20–30 km given the anticipated sensitivity of the gravity experiments. Figures 4a and 4b show that with a measurement accuracy increased by a factor of 3 (achievable by current technical means [e.g., Iess and Boscagli, 2001]) the $\pm$500 m peak topography is even detectable for a shell thickness of 5–10 km depending on the actual orbit height.

Assuming a sufficiently strong signal from the ice shell that could be detected from orbit, it needs to be isolated from the overall measured gravity signal. The importance of this is twofold: first, it minimizes the error in the ocean floor gravimetric inversion and second it can give us some information about the ice shell, e.g., its thickness and elasticity. Figure 5a shows that with the assumed maximal ocean floor topography of $\pm$1250 m and a strong gravity signal from the ocean floor (the signal is in particular strong for a shallow ocean and topography supported by a thick elastic lithosphere) measurements beyond degree ~ 40 are needed to receive the signal only from the ice layer. For lower degrees, the gravity signal is influenced by the ocean floor contribution. Note that the signal beyond degree 40 (as discussed above) could already be too weak to be detected. The crossover, i.e., the degree above which the gravity signal is mostly influenced by the ice layer, depends strongly on the used synthetic topography model. If the real ocean floor has a substantially stronger signal at all wavelengths, then the gravity signal beyond degree 40 could also be influenced. To demonstrate how to separate the two signals, we compute the admittance $Z_\ell^{\mathrm{combine}}$ (for details on the method, see, e.g., Simons et al. [1997], Schubert et al. [2001], or Pauer et al. [2006]) between the "observed" gravity field (combining the field from ice shell and ocean floor) and the ice shell topography (Figure 5b, thick line). This admittance function can

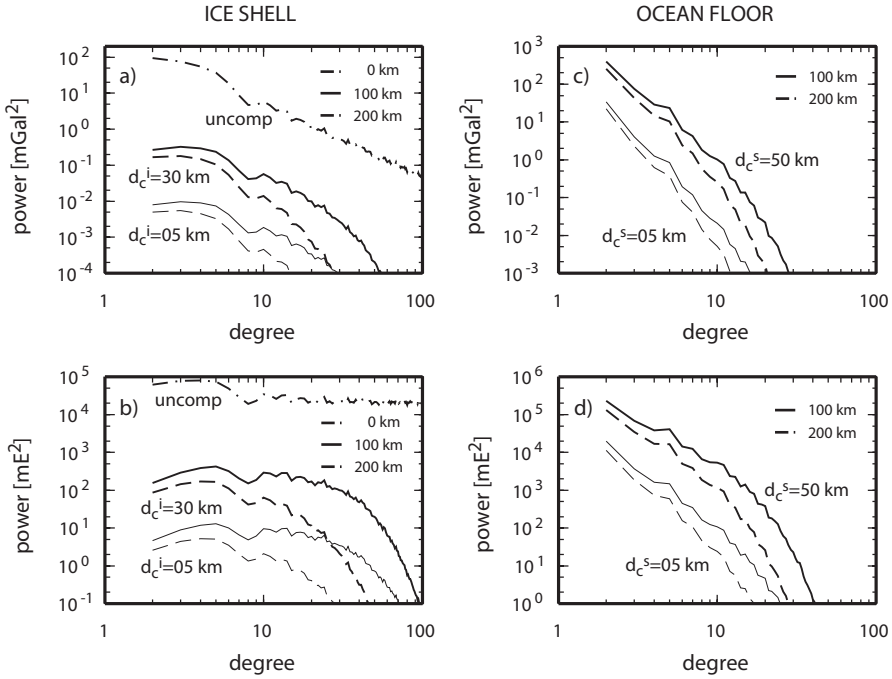

Figure C.3.3: *Power spectra of (a) gravity anomalies and (b) gravity gradients for the ice shell (d_c^i = 5 km case corresponds to d_e^i = 2 km and d_c^i = 30 km to d_e^i = 11 km) demonstrate that, especially for the lower orbit, the gradiometric method is out of these two in principle more sensitive at higher degrees (power decrease by less than one order of magnitude for degrees $\ell < 40$ and $\ell < 20$). To demonstrate an influence of both the compensation process and gravity signal attenuation with height, we plot also a power spectrum of uncompensated topography gravity at a zero height (dot-dashed line). The power spectra of (c) gravity anomalies and (d) gravity gradients for the ocean floor (d_c^s = 5 km case corresponds to d_e^s = 5 km and d_c^s = 50 km to d_e^s = 50 km from Figure 2) show that in this case the difference in measurements sensitivity is not so pronounced because of already strong height attenuation in both studied quantities.*

then be fitted for degrees higher than 40 by one of the theoretical admittance $Z_\ell(d_c^i)$ curves (see equation (10)) constructed for various ice shell thicknesses d_c^i (Figure 5b). As can be seen in Figure 5b, the lowermost degrees cannot be fitted by the ice topography admittance function since they are dominated by the gravity signal of the ocean floor. The results shown here demonstrate that for the combination of a weak ocean floor signal and a strong ice shell signal, the gravity experiment on board a future Europa orbiter might be able to recover the mean values of ice shell and its elastic thickness. If this is, however, not possible, we should take advantage of the results from other methods and experiments [e.g., Moore and Schubert, 2000; Nimmo et al., 2003a; Wahr et al., 2006] and remove the "probable" ice shell gravity field based on the observed topography and derived shell (elastic) thickness to minimize the error for the ocean floor gravimetric inversion. In the worst case, we simply reduce the signal of the ice topography and neglect any compensation of the ice shell. Such a procedure assumes a maximal signal reduction and underestimates the signal from the

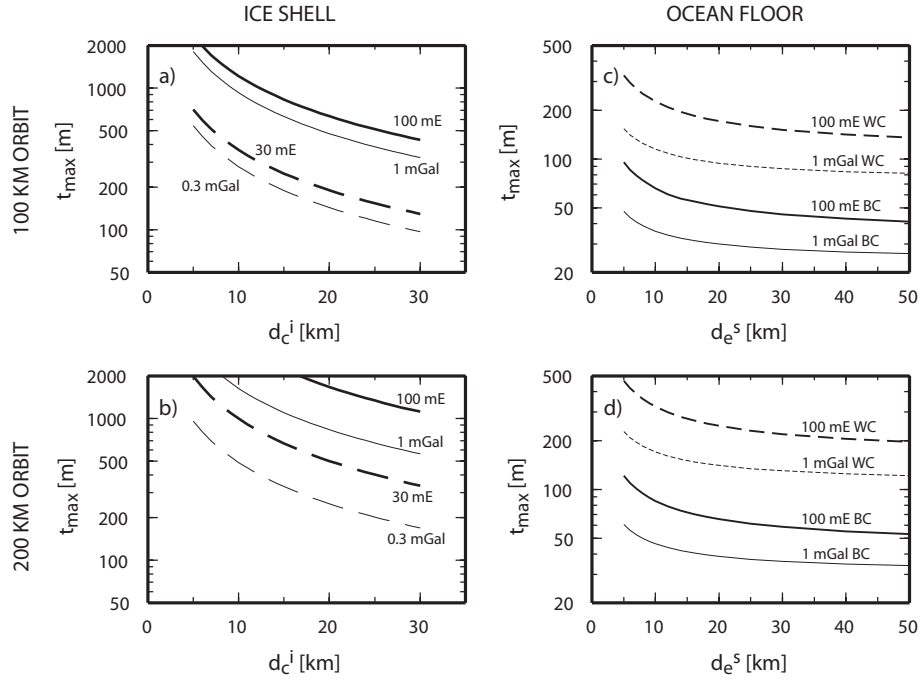

Figure C.3.4: *(a) Tradeoff between ice shell thickness dc i and minimum needed topography amplitudes range tmax to detect the gravity anomaly and gravity gradient signal due to the ice shell topography at 100 km above the Europa's surface. (b) The same but for orbit height 200 km. In both cases measurement accuracies of 0.3 and 1 mGal were investigated for the gravity anomaly and 30 and 100 mE were investigated for the gravity gradient. (cd) Similar study for the ocean floor topography showing the dependency of gravity anomaly/ gravity gradient detectability for orbital heights 100 km (Figure 4c) and 200 km (Figure 4d) and two different cases: "the worst case" WC (R_s = 1400 km and ρ_s = 2700 kg m^{-3}) and "the best case" BC (R_s = 1450 km and ρ_s = 3100 kg m^{-3}). In both cases, the crustal thickness was fixed to d_c^s = 20 km.*

silicate shell.

After reduction of the ice shell signal, the remaining signal is assumed to be caused by the ocean floor topography (the potential influence of other effects is discussed later). Figures 2e–2h shows the gravity field generated by our synthetic ocean floor model for two different sets of parameters. The first combination is chosen to give the presumably strongest gravity signal with $d_c^s = d_e^s = 50$ km, $R_0 = 1450$ km, and $\rho_c^s = 3100$ kgm^{-3}. The second combination gives the weakest gravity signal with $d_c^s = d_e^s = 5$ km, $R_0 = 1400$ km, and $\rho_c^s = 2700$ kgm^{-3}. The results show that the gravity signal for both extreme cases is well above the anticipated measurement accuracy at the assumed orbit heights. The tradeoff between a range of topography amplitude and an elastic thickness (Figure 4c) demonstrates that the likelihood of detecting gravity anomalies from the ocean floor is good even for unfavorable conditions, i.e., a thin elastic lithosphere and a small topography of only a few hundred meters. It is interesting to note that for any case of the ocean floor gravity signal there is no advantage in gradiometric measurements compared to gravity measurements due

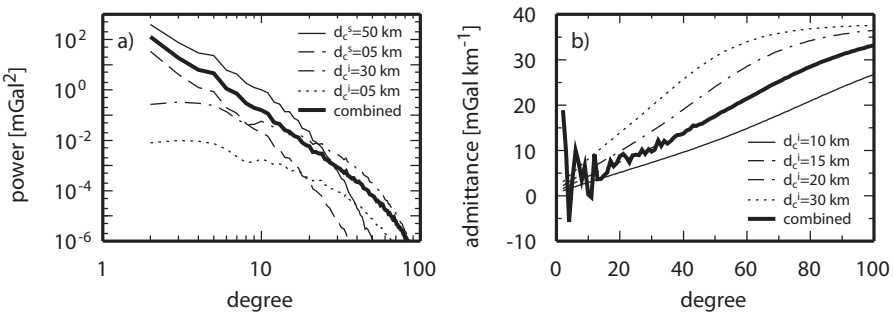

Figure C.3.5: *(a) Comparison of gravity anomaly power spectra for the ice shell signal (best d_c^i = 30 km and worst d_c^i = 5 km scenarios) and ocean floor topography (best case d_c^s = 50 km, d_e^s = 50 km, R_s = 1450 km, ρ_s = 3100 kg m^{-3} and worst case d_c^s = 5 km, d_e^s = 5 km, R_s = 1400 km, ρ_s = 2700 kg m^{-3} scenarios) using the same topographic models as for Figure 2, i.e., with maximum amplitudes ± 1250 m. Thick solid line shows an example of the combined signal (an intermediate ice shell model d_c^i = 15 km and ocean floor model d_c^s = 10 km, d_e^s = 10 km, R_s = 1425 km and ρ_s = 2900 kg m^{-3}). Note that the single contributions to the combined signal are not shown here. All the power spectra are evaluated at an orbit of 100 km. (b) Set of theoretical admittance curves for an ice shell with various shell thicknesses d_c^i; the elastic thickness is then computed using equation (13) (light lines). The curves are compared to a simulated admittance of the combined gravity signal (thick solid line). For this chosen model the fit beyond degree 30 constrains the crustal and elastic thickness of the simulated ice shell.*

to the stronger height attenuation of the gravity gradient (compare the attenuation factors in equations (10) and (11)), as one can see also from Figures 3c and 3d where there is no significant difference in characteristic decay of gravity anomaly and gravity gradient power spectra.

An admittance analysis as shown for the ice shell is not possible for the ocean floor since there will be no "observed" topography. Thus a gravimetric inversion of that interface is even more challenging as we have more unknown parameters in equations (10) and (11): topography, crustal and elastic lithosphere thickness, the crustal and mantle density, and the depth of the ocean. For the interpretation of the ocean floor signal we can, however, profit from the small radius of Europa. A small planetary radius makes the elastic support important even for relatively small values of the elastic thickness [Turcotte et al., 1981]. It is important to note that this is only true for the silicate shell and not for the ice shell, as the Young's modulus for silicate is 1–2 orders of magnitude larger than that for ice. Figure 6a shows that for expected values of E and ν, the gravity signal for elastic thicknesses of $d_e^s > 20$ km is already very close to the gravity signal of an uncompensated topography. Thus we can use for the inversion of the ocean floor gravity signal an uncompensated crustal structure model (i.e., we assume that the signal is coming solely from the topography undulations with no contribution from the crust-mantle interface), as a valid end member model. This model produces a minimum estimate of topography amplitudes since any compensated model requires higher topography. The other end member model for gravity signal inversion

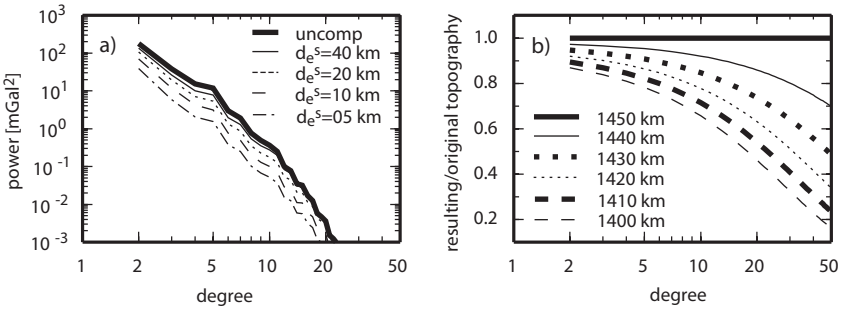

Figure C.3.6: *(a) Gravity anomaly power spectra caused by ocean floor topography for crustal thickness d_c^s = 20 km and different elastic thicknesses (light lines) and for an uncompensated topography model (thick line) (all cases are evaluated for a 100 km orbit). (b) Degree dependant factor modifying the result of recovered topography for radially misplaced gravity inversion, i.e., $R_s^{inv} \neq R_s^{orig}$ (original topography is referenced to radius 1450 km) while all other parameters are fixed to "real" values.*

would be an ocean floor topography solely supported by dynamic processes in the mantle, i.e., by mantle convection.

Another unknown parameter is, however, the depth of the ocean floor. This value has been fixed for the model calculations described above. In Figure 6b it is demonstrated that the unknown radial position influences not only the amplitude of the inverted topography but also the relative weight of each degree. Misplacement of the reference radius by 50 km causes then a relative artificial degree-dependent power decrease; the signal of degree 20 compared to the signal of degree 2 is reduced relatively by almost 50%. It should be noted that we will not be able to constrain the ocean depth with the gravimetric inversion method. If, however, the radial position can be determined with other methods, e.g., analysis of the moment of inertia [cf. Anderson et al., 1998], with a relatively small error of about ±10 lkm then the elastic thickness is the main factor influencing the uncertainty of the recovered topography.

In addition to global topographic variations, we test the possibility of detecting single volcanic/tectonic features like submarine volcanoes. The signal of the structure is again evaluated both in the form of gravity anomalies (Figure 7a) and gravity gradients (Figure 7b) in the two proposed orbit heights of 100 and 200 km. Additionally, the geoid anomaly above such features is studied (Figure 7c), which in case of a perfectly fluid body would create measurable deformation at the surface (this deformation could be recovered by a laser altimeter experiment with high accuracy [Wahr et al., 2006]). For all three cases again two end member states, the "best case" where the signal is strongest assuming deep compensation and a shallow ocean and the "worst case" where the signal is weakest assuming a shallow compensation and a deep ocean, are modeled to allow for an estimate on the range of the possible gravity signal strength. The results show that for the "best case" scenario, a volcano with a diameter of 75 km could be detected from a 100 km orbit whereas for the "worst case" scenario it should have a diameter of 200 km or more to allow detection at a 200 km orbit. Similar results are also obtained for synthetic submarine trenches where

the scaling parameter is the width. One should note, however, that because of a good localization in the spatial domain the signal of such an isolated feature is wide spread in the spectral domain [e.g., Wieczorek and Simons, 2005]. Therefore the detection limit up to a degree $\ell \sim 20$ will result in a strong underestimation of the feature's height, as demonstrated in Figure 7d. For instance, if we detect a volcano with diameter 200 km, we will obtain only about 20% of its peak signal. However, the larger the structure, the smaller the detection "error" caused by neglecting the intermediate and short wavelengths.

C.3.5 Summary and Discussion

The main aim of the present study is to determine the detectability of density anomalies in the silicate part of Europa for future missions. For simplicity, we assume that the anomalies of the ice/water shell are represented purely by ice surface topography and the density anomalies in the silicate shell by ocean floor structures. The following questions have been addressed: What minimum topography and size of structures at the ice surface and the ocean floor are we able to recover? Can we separate the gravity signal of the ice shell? What is the maximum degree to which we need to measure the gravity field? What can we learn from the remaining gravity signal and how important are other contributions to the gravity field?

Detectability of the Ice Shell and the Ocean Floor

The detection of the signal of the ice shell depends strongly on its thickness and the orbital height. For a thick ice shell of 20 to 30 km and an instrument accuracy of 1 mGal/ 100 mE, the maximum amplitude of the ice shell topography needs to be at least $\sim \pm 500$ m. With this instrument accuracy we will, however, not be able to detect gravity anomalies of a thin ice shell with a thickness of e.g., 5 km and any realistic topography. To detect gravity anomalies of a thin ice shell at all, we require a factor of 3 improvement in measurement precision. At present, the amplitudes of the ice surface topography, in particular for longer wavelengths, are unknown. From models of global ice shell thickness variations due to tidal dissipation and the assumption of isostatic compensation, Nimmo et al. [2007] suggested maximal 700m variations (i.e., approximately a topography of ± 350 m). If the "real" ice shell topography is indeed in that range, its signal will not be detected unless the measurement precision is again better than anticipated 1 mGal/100 mE. Gravity signal coming from the ocean floor topography should be relatively strong due to the large elastic support even for small elastic thicknesses (see Figure 6a). Thus the long wavelengths of the ocean floor undulations will be easier to detect and a topographic range of a few 100s meters should be sufficient even with an elastic thickness of $\sim$10–20 km. Small scale features like volcanoes or ocean trenches can be detected if they exceed a horizontal size of 75–200 km. Owing to the fact that most of the signal of the small features is not in the detectable spectral range (short wavelength gravity from ocean floor is strongly attenuated) the resulting topographic reconstruction will highly underestimate the original topography, depending on the actual size of the feature, more than 80% of its height may not be recovered from the observation.

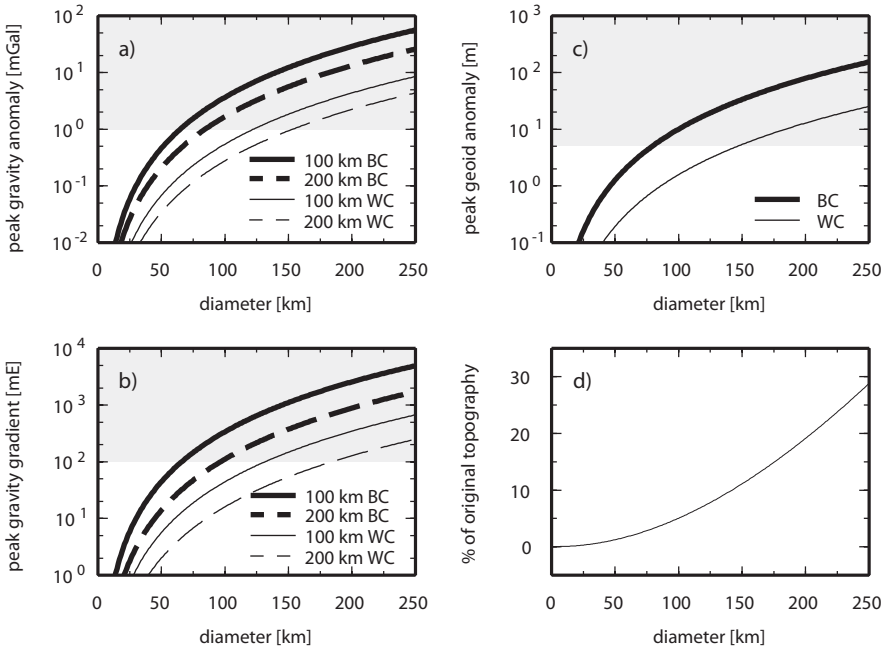

Figure C.3.7: *Detectability of a synthetic volcano's gravity signal: (a) peak gravity anomaly above the volcano's summit in mGals evaluated at 100 and 200 km above Europa's surface (best case scenario "BC":* $R_s = 1450$ *km,* $\rho_c^s = 3100$ *kg m*$^{-3}$, $d_c^s = d_e^s = 50$ *km and worst case scenario "WC":* $R_s = 1400$ *km,* $\rho_c^s = 2700$ *kg m*$^{-3}$, $d_c^s = d_e^s = 5$ *km). (b) The same but for gravity gradient changes in mE. (c) Equipotential surface deformation in meters evaluated at the outer radius of Europa. In all three cases the technological threshold for signal detection (1 mGal, 100 mE, 5 m) is depicted by a shaded area. (d) Percentage of theoretically possible recovered topography with spectral information complete only up to degree* $\ell = 20$ *(all the inversion parameters are adjusted to "true" values).*

Separation of the Gravity Signal of the Ice Shell From the Measured Data and Required Maximum Harmonic Degree

The present analysis shows that up to degree 40 the gravity signal can be influenced by both the ice layer and the ocean floor. For higher degrees, the signal of the ocean floor is strongly attenuated and consequently not measurable. Thus the separation of the signals would benefit if we measure the gravity field beyond degree 40. The technique of using a gravity microgradiometer (direct sampling of gravity gradient in orbit around Europa) would provide such a spectral resolution, especially for the ice shell gravity signal [Blanc et al., 2007; Koop et al., presented paper, 2006]. Measuring the higher degrees of the gravity field may allow an admittance study of the ice shell. Such a study permits a direct separation of the signal and in addition confirms/improves estimates of the global average thickness of the ice shell and its elastic thickness. If we only measure to about degree 20 with the standard method of Doppler radio tracking (e.g., Greeley and Johnson, presented paper, 2003), we may overestimate the signal from the ice shell by reducing only the measured surface topography and thereby neglecting the possible reduction of the signal by isostatic (or

partly isostatic) compensation. However, we may also use the results from other experiments (e.g., laser altimeter or subsurface radar) to estimate the shell/elastic thickness of the ice and thus the compensation state for a better separation of the signal of the shell. Furthermore, it is likely that the influence of an ice shell on the gravity signal in particular with a low topography and/or a thin shell is negligible (see previous paragraph) and thus not critical for interpreting the remaining signal. It is also important to note, that for the on-orbit strength of signal coming from the ocean floor the gravity micrograd iometer (i.e., the possibility of obtaining a gravity signal beyond degree ~ 20) cannot improve the measurements because of the strong height attenuation for the 100/200 km orbit, which diminishes the middle and short wavelength signal.

Interpretation of the Remaining Gravity Signal

As discussed above, it is likely that we will be able to detect gravity signals from the density variations in the silicate part of Europa with a future orbiter mission. The interpretation of the gravity signal, however, will be difficult due to the ambiguity in the data inversion and the large number of unknown parameters. Assuming that the density anomalies in the silicate part are represented purely by ocean floor structures, the recovery of actual ocean floor topography shape from the gravity signal requires knowledge of the crustal and elastic lithosphere thickness, the crustal and mantle density, and the depth of the ocean. Any uncertainty in these parameters will introduce an error in the inversion of the topography. However, since it has been shown that even a relatively thin elastic lithosphere gives a strong compensation support to the topographic load, we can use as a "realistic" end member model an uncompensated topography model for the gravimetric inversion. Such a model gives the minimum estimate of topography amplitudes. The uncertainty in the depth of the ocean (larger than ± 10 km) can introduce an additional error in the recovered topography, however mainly at shorter wavelengths which are not so important for the global shape determination.

Other Contributions to the Gravity Field

The present study is based on the simplification that our modeled synthetic gravity signal has contributions only from the gravity anomalies originating from the ice layer and the silicate crust at the ocean floor, with other contributions neglected. Other possible contributions of the outer ice and water layer to the signal could be warm ice convection [e.g., Hussmann et al., 2002; Tobie et al., 2003; Han and Showman, 2005], density anomalies in the ice shell [cf. Nimmo and Manga, 2009] and hydrothermal plumes in the subsurface ocean [e.g., Thomson and Delaney, 2001; Goodman et al., 2004; Vance and Brown, 2005]. Estimates of horizontal scales in all the above mentioned cases range up to about 50 km. At this scale, the gravity signal will be influenced mainly at higher degrees $\ell > 100$. Thus such contributions will not be detected and is not of relevance for the analysis. More problematic are signals at low degrees. Lateral surface temperature and tidal heating variations are assumed to lead to large scale shell thickness and topography variations [Ojakangas and Stevenson, 1989; Nimmo et al., 2007]. The gravity signal from the topography variations can be reduced from the signal. The contribution from the associated thermal anomalies in the convecting ice is not that easy to constrain and remove. Neglecting these contributions

will lead to an incorrect estimate of the remaining signal from the silicate shell. However, no such variations in the shell thickness and topography have been detected in existing limb profile data [Nimmo et al., 2007]. Two other effects connected to the existence of a subsurface ocean on Europa which may contribute to the gravity field are compositional (density) variations in the ocean and ocean currents-induced topography at the ice-water interface. The wavelengths of both these effects are expected to be small [e.g., Nimmo and Manga, 2009] and thus their influence on the gravity field interpretation is negligible since there will be no or very poor recovered gravity data at short wavelength (see discussion at the end of section 2) and moreover there is a strong attenuation at these degrees (e.g., equation (3)). It should be noted, however, that it has been also suggested that strong tidal dissipation in the liquid oceans may excite large-scale convection currents due to obliquity [Tyler, 2008].

Contributions to gravity anomalies of the silicate shell could be also related to the convecting silicate mantle in the same way as for the Earth [e.g., Richards and Hager, 1984] or as hypothesized for Venus [e.g., Pauer et al., 2006], i.e., directly to density anomalies in the mantle or indirectly through dynamically induced topography. Most likely there will be no way of distinguishing between the gravity signal coming from this source and the ocean floor topography. A first-order estimate of the gravity anomaly amplitudes caused by mantle convection that is not dominated by the lowermost degrees gives a peak gravity anomaly of only a few mGal at 100 km orbit, i.e., one order of magnitude smaller than our simulated gravity anomaly in Figure 2e. For this estimate we use internal structure models of Europa by Sohl et al. [2002] and the hybrid numerical method introduced by Zhong [2002] combining a viscous mantle flow with an elastic lithosphere. It has been shown, however, that tidal heating strongly influences the convection pattern and can result in low degree convection [e.g., Czechowski and Leliwa-Kopystynski, 2005]. Such a large-scale thermal (density) anomalies can induce in principle a stronger gravity signal. Although tidal effects in Europa most likely dominate in the ice shell, they might be also active in the silicate mantle [Hussmann et al., 2010]. Thus it will not be possible to distinguish between the gravity signal coming from the ocean floor topography and the convecting mantle. Any contribution from the silicate shell to the measured gravity field will most likely be a combination of both. To disentangle these contributions, it is necessary to study the characteristics of Europa's silicate mantle convection with 2-D and 3-D mantle convection codes including tidal effects, which is beyond the scope of the present paper. Furthermore, if tidal heating is important in the silicates, then the long-wavelength topography of the ice shell and the silicate mantle will likely be strongly correlated and any separation of the different interfaces will be even more challenging.

For completion, in addition to the internal sources, we must also separate the contributions from tides, i.e., dynamic gravitational tides, from the measured gravity field. The amplitudes of dynamic gravitational tides are expected to be several mGals at the 100/200 km orbital height depending on the moon's actual structure [Moore and Schubert, 2000]. This contribution is in fact comparable to the strongest expected signal of the ice shell. However, their periodical nature (one revolution of Europa around Jupiter takes only 3.55 days) permits their successful separation from the rest of the signal after 30 (Earth) days nominal mission [Wahr et al., 2006]. The dynamic gravitational tides can also be used to investigate the radial structure of Europa (amplitudes and phase lag of these tides depend

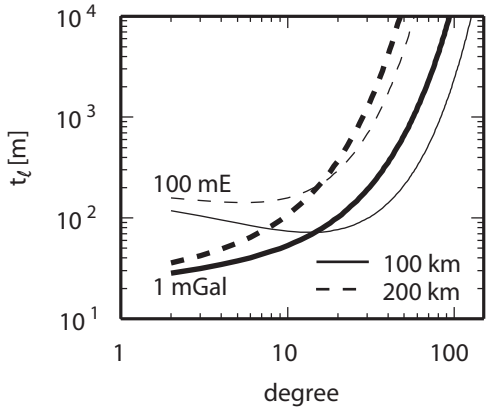

Figure C.3.8: *Topography t_ℓ, consisting of only degree ℓ structures, which is detectable for an uncompensated ice shell (i.e., the surface topography with no induced ice/water interface deformation) with measurements accuracy 1 mGal/100 mE. Its gravity anomaly/gravity gradient signal is evaluated at orbits 100200 km above the surface.*

on the thicknesses of the ice and water layers, rheological properties of ice etc.) [e.g., Moore and Schubert, 2000; Tobie et al., 2003] especially when combined with the surface tidal deformation observations [Wahr et al., 2006].

To model the synthetic topography of the ice surface, we assumed that the topography is supported by lateral variations of the ice shell thickness, including elastic support. This assumption neglects the influence on the ice/water compensation undulations by warm ice convection and/or the flow of the lower ice shell. Both processes tend to reduce the shell thickness variations and strongly depend on the shell thickness and the wavelength of the topography. In an ice shell of thickness 15–50 km, warm ice convection most likely occurs [e.g., McKinnon, 1998; Pappalardo et al., 1998; Tobie et al., 2003], which will effectively erase ice/water compensation undulations and results in topographic relaxation at long wavelengths. Even if there is no warm ice convection, lateral variations in the ice thickness can cause pressure gradients which drive the flow of ductile ice near the base of the shell [Stevenson, 2000]. Variations in the global ice shell thickness, such as those due to spatial variations in tidal heating [Ojakangas and Stevenson, 1989], cannot survive the observed surface age of Europa if the shell thickness is larger than 10 to 20 km, depending on the grain size of the ice. This is also valid for small-scale shell thickness variations. In fact, they are removed even more rapidly than longer wavelength topography [Nimmo, 2004]. It should be noted, however, that short-wavelength topography can be supported by the rigidity of the ice shell (such support is less effective at longer wavelength) and only the ice-water interface undulations are removed for small scale shell thickness variations. Considering the above, the assumptions used in our model are appropriate for an ice shell thinner than about 10 km. For an ice shell thicker than about 10–20 km, our results overestimate the influence of the ice shell on the measured gravity field for global topography. Here, only a small surface topography is expected for long-wavelengths and thus contributes only minimally to the gravity field. For small-scale topography that can be supported by the rigidity of the ice shell, however, we may have underestimated the influence of the ice shell because

the ice/water undulations are reduced for all wavelengths. This, on the other hand, would suggest a stronger gravity signal for these small-scale features. In Figure 8 the minimum degree topography height t_ℓ is studied for the case of an uncompensated ice shell topography. This, however, shows that unless the height of small-scale structures is ~ 1000 m their signal is still below the detection level.

C.3.6 Acknowledgments

We thank B. Giese who kindly provided us the topographic data on Europa's surface features derived from Galileo mission results by stereo reconstruction, O. Čadek and F. Sohl for inspiring discussions; K. Fleming, F. Nimmo, W. Moore and one anonymous reviewer of the original manuscript for their constructive comments. This work was financially supported through the European Community's Improving Human Potential Programme under contract RTN2-2001-00414, MAGE and the Charles University grant 280/2006/B-GEO/MFF.

C.3.7 References

Anderson, J. D., G. Schubert, R. A. Jacobson, E. L. Lau, W. B. Moore, and W. L. Sjogren (1998), Europa's differentiated internal structure: Inferences from four Galileo encounters, Science, 281, 2019–2022, doi:10.1126/science.281.5385.2019.

Belleguic, V., P. Lognonné, and M. Wieczorek (2005), Constraints on the Martian lithosphere from gravity and topography data, J. Geophys. Res., 110, E11005, doi:10.1029/2005JE002437.

Blanc, M., and the LAPLACE team (2007), LAPLACE: A mission to Europa and the Jupiter System for ESA's Cosmic Vision Programme, Exp. Astron., 23(3), 849–892.

Blankenship, D. D., et al. (1999), Feasibility study and design concept for an orbiting ice-penetrating radar sounder to characterize in threedimensions the European ice mantle down to (and including) any ice/ ocean interface, report, 184 pp., Jet Propul. Lab., Pasadena, Calif.

Chizhov, V. E. (1993), Thermodynamic properties and thermal equations of state of high-pressure ice phases, Prikl. Mekh. Tekh. Fiz., 2, 113–123.

Clarke, K. B. (2007), Europa Explorer – An exceptional mission using existing technology, Aerospace Conference, 2007 IEEE, doi:10.1109/ AERO.2007.352711.

Czechowski, L., and J. Leliwa-Kopystynski (2005), Convection driven by tidal and radiogenic heating in medium size icy satellites, Planet. Space Sci., 53(7), 749–769, doi:10.1016/j.pss.2005.01.004.

Doggett, T., P. Figueredo, R. Greeley, T. Hare, E. Kolb, K. Mullins, D. Senske, K. Tanaka, and S. Weiser (2007), Global geologic map of Europa, Lunar Planet. Sci. Conf., 38, 2296.

Ellsworth, K., and G. Schubert (1983), Saturn's icy satellites: Thermal and structural models, Icarus, 54, 490–510, doi:10.1016/0019-1035(83)90242-7.

Garofalo, F. (1965), The Fundaments of Creep and Creep-Rapture in Metals, Macmillan, New York.

Goodman, J. C., G. C. Collins, J. Marshall, and R. T. Pierrehumbert (2004), Hydrothermal plume dynamics on Europa: Implications for chaos formation, J. Geophys. Res., 109, E03008, doi:10.1029/2003JE002073.

Greenberg, R., M. A. Leake, G. V. Hoppa, and B. R. Tufts (2003), Pits and uplifts on Europa, Icarus, 161, 102–126, doi:10.1016/S0019-1035(02)00013-1.
Han, L., and L. P. Showman (2005), Thermo-compositional convection in Europa's icy shell with salinity, Geophys. Res. Lett., 32, L20201, doi:10.1029/2005GL023979.
Herrick, R. R., J. Dufek, and P. J. McGovern (2005), Evolution of large shield volcanoes on Venus, J. Geophys. Res., 110, E01002, doi:10.1029/2004JE002283.
Hussmann, H., and D. Breuer (2007), The thermo-chemical evolution of Europa: Constraints on silicate volcanism at Europa's ocean floor, Eos Trans. AGU, 88(52), Fall Meet. Suppl., Abstract P53B–1239.
Hussmann, H., T. Spohn, and K. Wieczerkowski (2002), Thermal equilibrium states of Europa's ice shell: Implications for internal ocean thickness and surface heat flow, Icarus, 156, 143–151, doi:10.1006/icar.2001.6776.
Hussmann, H., G. Choblet, V. Lainey, D. L. Matson, C. Sotin, G. Tobie, and T. van Hoolst (2010), Implications of rotation, orbital states, energy sources, and heat transport for internal processes in icy satellites, Space Sci. Rev., 153, 317–348, doi:10.1007/s11214-010-9636-0.
Iess, L., and G. Boscagli (2001), Advanced radio science instrumentation for the mission BepiColombo to Mercury, Planet. Space Sci., 49, 1597–1608, doi:10.1016/S0032-0633(01)00096-4.
Kaula, W. M. (1966), Theory of Satellite Geodesy, Blaisdell, Waltham, Mass.
Kivelson, M. G., K. K. Khurana, C. T. Russell, M. Volwerk, R. J. Walker, and C. Zimmer (2000), Galileo magnetometer measurements: A stronger case for a subsurface ocean at Europa, Science, 289, 1340–1343, doi:10.1126/science.289.5483.1340.
Lambeck, K. (1988), Geophysical Geodesy, Oxford Univ. Press, New York.
Martinec, Z. (1991), On the accuracy of the method of condensation of the Earth's topography, Manuscr. Geod., 16, 288–294.
McKinnon, W. B. (1998), Geodynamics of icy satellites, in Solar System Ices, edited by B. Schmitt et al., pp. 525–550, Kluwer Acad., Dordrecht, Netherlands.
Moore, J. M., et al. (2001), Impact features on Europa: Results of the Galileo Europa mission, Icarus, 151, 93–111, doi:10.1006/icar.2000.655 *Moore, W. B., and G. Schubert* (2000), NOTE: The Tidal Response of Europa, Icarus, 147, 317–319, doi:10.1006/icar.2000.6460.
Musiol, S. (2007), Influence of the ice/water layer on the gravity field of Jupiter's moon Europa (in German), diploma thesis, Univ. of Potsdam, Potsdam, Germany.
Neumann, G. A., M. T. Zuber, D. E. Smith, and F. G. Lemoine (1996), The lunar crust: Global structure and signature of major basins, J. Geophys. Res., 101(E7), 16,841–16,843, doi:10.1029/96JE01246.
Neumann, G. A., M. T. Zuber, M. A. Wieczorek, P. J. McGovern, F. G. Lemoine, and D. E. Smith (2004), Crustal structure of Mars from gravity and topography, J. Geophys. Res., 109, E08002, doi:10.1029/2004JE002262.
Nimmo, F. (2004), Non-Newtonian topographic relaxation on Europa, Icarus, 168, 205–208, doi:10.1016/j.icarus.2003.11.022.
Nimmo, F., and M. Manga (2009), Geodynamics of Europa's Ice Shell, in Europa After Galileo, edited by R. T. Pappalardo et al., pp. 381–404, Univ. of Ariz. Press, Tucson, Ariz.
Nimmo, F., B. Giese, and R. T. Pappalardo (2003a), Estimates of Europa's ice shell thickness from elastically supported topography, Geophys. Res. Lett., 30(5), 1233, doi:10.1029/2002GL016660.

Nimmo, F., R. T. Pappalardo, and B. Giese (2003b), On the origins of band topography, Europa, Icarus, 166, 21–32, doi:10.1016/j.icarus.2003.08.002.
Nimmo, F., P. C. Thomas, R. T. Pappalardo, and W. B. Moore (2007), The global shape of Europa: Constraints on lateral shell thickness variations, Icarus, 191, 183–192, doi:10.1016/j.icarus.2007.04.021.
Ojakangas, G. W., and D. J. Stevenson (1989), Thermal state of an ice shell on Europa, Icarus, 81, 220–241, doi:10.1016/0019-1035(89)90052-3.
Pappalardo, R. T., and A. C. Barr (2004), The origin of domes on Europa: The role of thermally induced compositional diapirism, Geophys. Res. Lett., 31, L01701, doi:10.1029/2003GL019202.
Pappalardo, R. T., et al. (1998), Geological evidence for solid-state convection in Europa's ice shell, Nature, 391, 365-368, doi:10.1038/34862.
Pappalardo, R. T., et al. (1999), Does Europa have a subsurface ocean? Evaluation of the geological evidence, J. Geophys. Res., 104(E10), 24,015–24,055, doi:10.1029/1998JE000628.
Pauer, M., K. Fleming, and O. Čadek (2006), Modeling the dynamic component of the geoid and topography of Venus, J. Geophys. Res., 111, E11012, doi:10.1029/2005JE002511.
Richards, M. A., and B. H. Hager (1984), Geoid anomalies in a dynamic Earth, J. Geophys. Res., 89(B7), 5987–6002, doi:10.1029/JB089iB07p05987.
Rio, M.-H., and F. Hernandez (2004), A mean dynamic topography computed over the world ocean from altimetry, in situ measurements, and a geoid model, J. Geophys. Res., 109, C12032, doi:10.1029/2003JC002226.
Schenk, P. M., R. R. Wilson, and A. G. Davies (2004), Shield volcano topography and the rheology of lava flows on Io, Icarus, 169, 98–110, doi:10.1016/j.icarus.2004.01.015.
Schubert, G., D. L. Turcotte, and P. Olson (2001), Mantle Convection in the Earth and Planets, Cambridge Univ. Press, New York, doi:10.1017/CBO9780511612879.
Simons, M., S. C. Solomon, and B. H. Hager (1997), Localization of gravity and topography: Constraints on the tectonics and mantle dynamics of Venus, Geophys. J. Int., 131, 24–44, doi:10.1111/j.1365-246X.1997.tb00593.x.
Sohl, F., T. Spohn, D. Breuer, and K. Nagel (2002), Implications from Galileo observations on the interior structure and chemistry of the Galilean satellites, Icarus, 157, 104–119, doi:10.1006/icar.2002.6828.
Spencer, J. R., L. K. Tamppari, T. Z. Martin, and L. D. Travis (1999), Temperatures on Europa from Galileo photopolarimeter-radiometer: Nighttime thermal anomalies, Science, 284, 1514–1516, doi:10.1126/science.284.5419.1514.
Spohn, T., and G. Schubert (2003), Oceans in the icy Galilean satellites of Jupiter?, Icarus, 161, 456–467, doi:10.1016/S0019-1035(02)00048-9.
Stevenson, D. J. (2000), Limits on the variations of thickness of Europa's ice shell, Lunar Planet. Sci. Conf., 31, 1506.
Thomson, R. E., and J. R. Delaney (2001), Evidence for a weakly stratified European ocean sustained by seafloor heat flux, J. Geophys. Res., 106(E6), 12,355–12,365, doi:10.1029/2000JE001332.
Tobie, G., G. Choblet, and C. Sotin (2003), Tidally heated convection: Constraints on Europa's ice shell thickness, J. Geophys. Res., 108(E11), 5124, doi:10.1029/2003JE002099.
Tobie, G., A. Mocquet, and C. Sotin (2005), Tidal dissipation within large icy satellites: Applications to Europa and Titan, Icarus, 177, 534–549, doi:10.1016/j.icarus.2005.04.006.

Turcotte, D. L. (1997), Fractals and Chaos in Geology and Geophysics, 2nd ed., 398 pp., Cambridge Univ. Press, New York.
Turcotte, D. L., R. J. Willeman, W. F. Haxby, and J. Norberry (1981), Role of membrane stresses in the support of planetary topography, J. Geophys. Res., 86(B5), 3951–3959, doi:10.1029/JB086iB05p03951.
Tyler, R. (2008), Strong ocean tidal flow and heating on moons of the outer planets, Nature, 456, 770–772, doi:10.1038/nature07571.
Vance, S., and J. M. Brown (2005), Layering and double-diffusion style convection in Europa's ocean, Icarus, 177, 506–514, doi:10.1016/j.icarus.2005.06.005.
Wahr, J. M., M. T. Zuber, D. E. Smith, and J. I. Lunine (2006), Tides on Europa, and the thickness of Europa's icy shell, J. Geophys. Res., 111, E12005, doi:10.1029/2006JE002729.
Wieczorek, M. A. (2007), The gravity and topography of the terrestrial planets, in Planets and Moons, Treatise on Geophys., vol. 10, edited by T. Spohn, pp. 165–206, Elsevier, New York.
Wieczorek, M. A., and F. J. Simons (2005), Localized spectral analysis on the sphere, Geophys. J. Int., 162, 655–675, doi:10.1111/j.1365-246X.2005.02687.x.
Zhong, S. (2002), Effects of lithosphere on the long-wavelength gravity anomalies and their implications for the formation of the Tharsis rise on Mars, J. Geophys. Res., 107(E7), 5054, doi:10.1029/2001JE001589